Theory of tunneling and transport in emerging narrow-gap semiconductor alloys

Sarita Das

Thesis submitted in partial fulfilment of the requirements
of the degree of Doctor of Philosophy

at the
School of Physics,
University College Cork,
National University of Ireland

Supervisors: Prof. Eoin P. O'Reilly
Dr. Christopher A. Broderick
Dr. Stefan Schulz

April 2024

Contents

Declaration of Authorship v

Dedication vi

Acknowledgements vii

Abstract viii

List of Publications x

List of Figures xi

1 Introduction 1
- 1.1 Background and motivation . . . 1
- 1.2 Dilute nitride and bismide alloys (InN_xAs_{1-x}, $InAs_{1-z}Bi_z$) . . . 3
- 1.3 Group-IV alloys . . . 4
- 1.4 Structure of the thesis and overview of primary results . . . 6

2 Theoretical background: Band to band tunneling current 9
- 2.1 Introduction . . . 9
- 2.2 Electronic band structure . . . 9
  - 2.2.1 Complex band structure (CBS) . . . 14
- 2.3 Introduction to tunneling . . . 15
- 2.4 tunneling through a 1D barrier . . . 16
  - 2.4.1 Analytic method . . . 17
  - 2.4.2 Transfer matrix method (TMM) . . . 20
  - 2.4.3 WKB approximation . . . 22
- 2.5 BTBT generation rate in a bulk semiconductor . . . 25
  - 2.5.1 Model Hamiltonian and CBS . . . 26
  - 2.5.2 BTBT transmission coefficient and generation rate . . . 27
    - 2.5.2.1 WKB approximation . . . 28
    - 2.5.2.2 Kane model . . . 29
- 2.6 Result and Discussion . . . 30
- 2.7 Conclusions . . . 32

3 Impact of band anti-crossing on band to band tunneling current in highly mismatched dilute nitride and bismide alloys (InN_xAs_{1-x}, $InAs_{1-z}Bi_z$) 34
- 3.1 Introduction . . . 34
- 3.2 Highly mismatched alloys and their electronic band structure . . . 36
  - 3.2.1 Band structure: BAC model . . . 37
- 3.3 Theoretical model . . . 40

3.3.1 Model Hamiltonians and complex band structure . . . 42
3.3.2 BTBT transmission coefficient and generation rate . . . 44
3.4 Results . . . 44
3.4.1 Fixed band gap ($E_g = 0.295$ eV, $\lambda = 4.2$ μm) . . . 45
3.4.2 Variable band gap: $InAs_{1-y}Sb_y$ vs. InN_xAs_{1-x}, $InAs_{1-z}Bi_z$ alloys . . . 48
3.5 Implications for practical applications . . . 51
3.5.1 Implications for APD applications . . . 51
3.5.2 Implications for TFET applications . . . 53
3.6 Conclusions . . . 54

4 Theoretical background - Electron transport fundamentals 57
4.1 Introduction . . . 57
4.2 Conduction band structure . . . 58
4.2.1 Density of states . . . 60
4.3 Boltzmann's transport equation . . . 60
4.3.1 Carrier distribution function . . . 60
4.4 Scattering mechanisms . . . 62
4.4.1 Formalism . . . 63
4.4.2 Conservation of energy and crystal momentum . . . 64
4.4.3 Polar optical phonon scattering (POS) . . . 67
4.4.4 Optical deformation potential scattering . . . 71
4.4.5 Intervalley scattering . . . 74
4.4.6 Acoustic phonon scattering . . . 75
4.4.7 Alloy scattering . . . 75
4.5 Field dependent transport for bulk GaAs by Boltzmann's transport equation . . . 76
4.6 Results and discussion . . . 80
4.7 Conclusion . . . 83

5 Theory of field-dependent electron transport in $Ge_{1-x}Sn_x$ alloys 84
5.1 Introduction . . . 84
5.2 Theoretical model . . . 85
5.3 Scattering mechanisms . . . 88
5.3.1 Selection of parameters . . . 89
5.3.2 Alloy scattering . . . 91
5.4 Low -field electron transport . . . 94
5.5 Field dependent electron transport . . . 100
5.5.1 Field-dependent electron transport in Ge . . . 100
5.5.2 Field-dependent electron transport in $Ge_{1-x}Sn_x$ alloys . . . 105
5.5.2.1 Carrier distribution function . . . 106
5.5.2.2 Electron drift velocity and mobility . . . 108
5.6 Conclusion . . . 114

6 Summary, conclusions and outlook 116
6.1 BTBT in InN_xAs_{1-x} and $InAs_{1-z}Bi_z$ alloys . . . 116
6.2 Electron transport in Ge and $Ge_{1-x}Sn_x$ alloys . . . 117
6.3 Outlook . . . 119

A Calculation of alloy scattering potentials 121

Bibliography 124

Declaration of Authorship

I, Sarita Das (student no. 117227346), hereby declare that, unless otherwise stated, this work is my own, and that it has not been submitted for another degree, either at University College Cork or elsewhere.

To my father (Mr. Umesh Chandra Das)

Acknowledgements

I still remember my first task, which Eoin gave me, from our first one-to-one meeting. When I showed him the solution the next day, it was completely wrong; unfortunately, I completely misunderstood it and felt quite stupid. However, Eoin responded with kindness and wisdom, saying, "No fear, Sarita; you are learning; in fact, we are all learning. I'm glad you gave it a try." Those words meant the world to me. They reminded me that making mistakes is part of learning. I'm so thankful for Eoin's patience, guidance, and belief in me. His mentorship has been a true inspiration, and I'm grateful for the opportunity to learn and work under his guidance. I wish Eoin a very happy and healthy life.

Thanks are also due to my co-supervisor, Dr. Christopher A. Broderick, who has helped me at every step during my PhD journey, starting with code debugging and helping me understand complex theoretical concepts to lessons on data organisation. I have learnt and am still learning so many things from him. He was always available to answer my queries, irrespective of how stupid they were. I wish Chris all the best in his future endeavours.

I thank the members of my progress review committee at Tyndall, Dr. Stefan Schulz and Michael Nolan, for their time and valuable input during my yearly reviews.

I sincerely thank my thesis examiners, Prof. Stephen Fahy from University College Cork and Prof. John P. R. David from the University of Sheffield, Sheffield, U.K., for their time in examining this thesis. I also thank Science Foundation Ireland for providing the funding that supported my PhD research under project 15/IA/3082, "Multiscale Simulation and Analysis of Emerging Group IV and III-IV Semiconductor Materials and Devices".

I want to thank my friends at the photonics theory group for helping me whenever needed, even during COVID time. Also, many thanks to Aman, Amit, and Heena, who made me feel at home in Ireland. I would like to thank my parents, my aunt, and my sisters for their incredible love and cheering during my PhD journey. Especially to my father, to whom I dedicate my thesis, who has always encouraged me to complete my thesis and has long hoped for me to obtain a foreign degree. Finally, I would like to thank my husband, Saroj, who has always been there for me.

Abstract

There is a high demand for narrow-band gap semiconductor alloys to support the development of advanced devices such as high-sensitivity photodiodes (PDs) and light sources (lasers and LEDs) for the application-rich wavelength range from 3 to 5 μm. These applications include environmental and industrial process monitoring, free-space optical communications, and imaging for aerospace and defence applications. Therefore, there is a need to access the electronic and optical properties of these alloys. For instance, the suppression of dark current is crucial to achieving high-sensitivity PDs to improve the detector signal-to-noise ratio. Leakage currents linked to band to band tunneling (BTBT) plays a substantial role in the dark current in PDs based on narrow-gap semiconductors. Determining the effectiveness of a device also involves looking into the electron transport properties of such alloys. Two types of emerging narrow-band gap alloys are investigated in this thesis, namely (i) highly mismatched dilute nitride and bismide alloys, and (ii) $Ge_{1-x}Sn_x$ alloys.

We first theoretically analyse BTBT in highly-mismatched, narrow-gap dilute nitride and bismide alloys. Replacing As by N (or Bi) introduces localised impurity states into the conduction (valence) band, whose impact on the band structure can be described by a band-anticrossing (BAC) interaction between the localised impurity states and the host conduction (valence) band. For this class of semiconductors, the assumptions underpinning the widely-employed Kane model of BTBT in an applied electric field break down, due to strong band edge nonparabolicity resulting from the BAC interactions. Via numerical calculations based on the Wentzel-Kramers-Brillouin approximation, we demonstrate that BAC leads, at a fixed band gap, to a reduced (increased) BTBT current at low (high) applied electric field compared to that in a conventional $InAs_{1-y}Sb_y$ alloy. Our analysis reveals that BTBT in InN_xAs_{1-x} and $InAs_{1-z}Bi_z$ is governed by a field-dependent competition between the impact of N (Bi) incorporation on (i) the dispersion of the evanescent Bloch band linking the valence and conduction band edges, which dominates at low field strengths, and (ii) the conduction (valence) band dispersion, which dominates at high field strengths. The implications of our results for applications in long-wavelength avalanche photodiodes (APDs) and tunneling field-effect transistors (TFETs) are discussed.

In addition to this study, we investigate the evolution of the electron transport properties of $Ge_{1-x}Sn_x$ alloys as a function of increasing Sn content, as the alloy goes from indirect-gap to direct-gap. $Ge_{1-x}Sn_x$ has attracted significant interest for applications in electronic and photonic devices as a (narrow-gap) direct-gap semiconductor compatible with existing CMOS processing. We use the Boltzmann transport equation to calculate as a function of Sn composition the evolution of the electron transport properties in an applied electric field. The intra and inter-valley alloy scattering rates are determined from tight-binding calculations. At extremely low electric field, we predict an increase of approximately two orders of magnitude in electron mobility in direct-gap alloys with higher Sn composition. However, our calculations predict that the electron mobility at these high Sn compositions decreases rapidly with increasing field, as the electrons are quickly accelerated to higher energy, where they can scatter from the Γ valley with low density of states

(DOS) to the L valleys, with their much higher DOS. We calculate that the contribution of alloy scattering causes the mobility to drop below that of Ge for all values of x considered once the field exceeds 50 V cm^{-1}.

List of Publications

Journal

- S Das, C A Broderick, E P O'Reilly, "Theory of alloy scattering and field-dependent electron transport in direct-gap group-IV $Ge_{1-x}Sn_x$ alloys", in preparation.
- S Das, C A Broderick, E P O'Reilly, "Impact of band anticrossing on band-to-band tunneling in highly mismatched semiconductor alloys", Phys. Rev. Applied 17, 014029, 2022.
- C A Broderick, S Das, E Pelucchi, B Corbett and E P O'Reilly, "Research Highlight: Routes to Ideal Telecom Lasers?"IEEE Photonics Society Newsletter, 34 (1), 4-9, 2020.

Conferences & Symposium

- C A Broderick, S Das, M D Dunne and E P O'Reilly, "Theory of electron transport in direct-gap Ge1-xSnx alloys ", Bulletin of the American Physical Society, Las Vegas, Nevada, 2023.
- S Das, C A Broderick, and E P O'Reilly, "Impact of band anticrossing on band-to-band tunneling in narrow-gap highly mismatched III-V semiconductor alloys", Photonics Ireland 2021.
- S Das, C A Broderick and E P O'Reilly, "Impact of band-anticrossing on band-to-band tunneling in highly-mismatched semiconductor alloys", 10th International Workshop on Bismuth-containing semiconductors, LAAS, Toulouse, France, 21-24 July 2019.
- C A Broderick, S Das and E P O'Reilly, "Theoretical analysis of band-to-band tunneling in highly-mismatched semiconductor alloys", NUSOD: 19th International Conference on Simulation of Optoelectronic Devices, Ottawa, Canada 8-12 July 2019.
- S Das, C A Broderick and E P O'Reilly, "Theoretical analysis of band-to-band tunneling in highly-mismatched, narrow-gap semiconductor alloys", UK Semiconductors 2019, Sheffield Hallam University, UK, 10-11 July 2019.
- S Das, C A Broderick, and E P O'Reilly, "Impact of band mixing on tunneling currents in dilute bismide avalanche photodiodes", Photonics Ireland 2018, Cork, Ireland, 4 September 2018

List of Figures

2.1 Band structure ($E_{n\mathbf{k}}$) of a direct gap cubic semiconductor solid. 11
2.2 CBS obtained by diagonalising the Hamiltonian matrix (2.23) where complex band links the CB and LH at the zone centre. Further calculation details are given in Sec. 2.5.1. 15
2.3 I-V characteristics for Esaki diode [92] (a) no net current flow at zero applied voltage (b) forward biased voltage with the peak current- due to tunneling of electrons (c) forward-biased voltage - minimum current obtained- due to non-availability of free states for tunneling into - creates NDR (d) at further forward-biased voltage, observation of diffusion current, and (e) at reverse-biased voltage, observation of tunneling current - due to tunneling of electrons from the VB of the p-type region to the CB of the n-type region. 17
2.4 Rectangular barrier having potential height, V_0 and width $(b-a)$. 18
2.5 Transmission coefficient for rectangular barrier, potential height, $V_0 = 0.05$ eV, width = 10 Å. 20
2.6 An asymmetrical barrier of energy V_0 and $\frac{V_0}{2}$ within the interval $a \leq z \leq c$ and $c \leq z \leq b$ respectively. 22
2.7 Transmission coefficient for asymmetrical barrier ($V_0 = 0.05$ eV, width = 10 Å). . 22
2.8 Arbitrary potential barrier having initial energy V_0. 23
2.9 Wave function of a tunneling electron through a rectangular barrier with position, z. 24
2.10 Transmission coefficient for rectangular barrier by analytic and WKB approximation, potential height, $V_0 = 0.5$ eV and width, w (a) 10 Å, and (b) 100 Å. 25
2.11 (a) Real-space schematic illustration of BTBT by an electron from the VB maximum to the CB minimum, in a semiconductor under the influence of an applied electric field, and (b) Reciprocal-space schematic illustration of the BTBT process of (a), in which the dashed lines denote the imaginary component of the wave vector describing the evanescent (complex) band linking the VB maximum and CB minimum. The evanescent band has the same real value of perpendicular wave vector $k_\perp$ as the states that it is linking, with the energy dependence of its imaginary component given by Eq. (2.62). 29
2.12 (a) CBS of InAs calculated using the 2-band $\mathbf{k}\cdot\mathbf{p}$ Hamiltonian of Eq. (2.58) (solid lines), and the simplified parabolic bands employed in the derivation of the Kane model of direct BTBT (dashed lines). (b) BTBT transmission coefficient T of InAs as a function of perpendicular wave vector $k_\perp$ calculated numerically using the 2-band complex dispersion of (a) in conjunction with the WKB approximation (solid lines), and using the analytical Kane model (open circles). Transmission coefficients are shown for applied electric fields F ranging from 0.1 MV cm^{-1} (yellow) to 1 MV cm^{-1} (black) in steps of 0.1 MV cm^{-1}. Inset: zone-centre ($k_\perp = 0$) transmission coefficient T as a function of applied electric field F, calculated numerically using the WKB approximation (solid line) and analytically using the Kane model (open circles). (c) BTBT generation rate G of InAs as a function of applied electric field F, calculated numerically using the WKB approximation (solid line) and analytically using the Kane model (open circles). 31

3.1 Conduction band structure of $InN_{0.05}As_{0.95}$ due to inclusion of N atoms ($x = 5\%$), computed using the BAC model (Eq. (3.3)). The BAC model describes that the InAs host matrix CB (dashed line) goes through a N composition-dependent anticrossing interaction with localized N-impurity related resonant states at energy E_N (dashed - dotted line), splitting the CB into two bands $E_\pm$(k)(solid lines). The zero of energy is taken at the InAs CB edge. 39
3.2 Valence band structure of $InBi_{0.05}As_{0.95}$ due to inclusion of Bi atoms ($x = 5\%$), computed using the BAC model (Eq. (3.4)). The BAC model describes that the InAs host matrix VB (dashed line) goes through a Bi composition-dependent anticrossing interaction with localized Bi-impurity related resonant states at energy E_{Bi} (dashed-dotted line), splitting the VB into two bands $E_\pm$(k)(solid lines). The zero of energy is taken at the InAs VB edge. 40
3.3 Calculated composition-dependent band gaps of (a) $InAs_{1-y}Sb_y$ (solid blue line), (b) InN_xAs_{1-x} (solid green line), and (c) $InAs_{1-z}Bi_z$ (solid red line). Open blue and green circles in (a) and (b) respectively denote the room temperature photoluminescence measurements of Refs. [152] and [140]. Open red circles in (c) denote the room temperature optical absorption measurements of Ref. [151]. 41
3.4 Calculated complex band structure of (a) $InAs_{1-y}Sb_y$ ($y = 7.85\%$), (b) InN_xAs_{1-x} ($x = 2.04\%$), and (c) $InAs_{1-z}Bi_z$ ($z = 0.85\%$) alloys having equal band gap $E_g = 0.295$ eV at $k_\perp = 0$. In each case, the left- (right-) hand panel shows the calculated imaginary (real) bands. The imaginary band $|\mathrm{Im}\{k_{z,-}(E, \mathbf{k}_\perp)\}|$ is shown for perpendicular wave vectors $k_\perp = 0.0$, 0.2, 0.4, 0.6, 0.8 and 1.0 nm^{-1} using solid black, dark purple, purple, red, orange and yellow lines respectively. Dashed lines and open circles highlight that, for a given perpendicular wave vector $k_\perp$, the imaginary band $|\mathrm{Im}\{k_{z,-}(E, \mathbf{k}_\perp)\}|$ links the CB and LH bands at energies $E_\pm(k_\perp)$. Note that the features associated with the N-related localised impurity state in (b) are out of scale, since $E_N = 1.386$ eV (cf. Table. 3.1). 45
3.5 Calculated relative BTBT transmission coefficient T at (a) $k_\perp = 0$, (b) $k_\perp = 0.2$ nm^{-1}, and (c) $k_\perp = 0.4$ nm^{-1} for $InAs_{1-y}Sb_y$ ($y = 7.85\%$; dashed blue lines), InN_xAs_{1-x} ($x = 2.04\%$, dash-dotted green lines), and $InAs_{1-z}Bi_z$ ($z = 0.85\%$; solid red lines) alloys having equal band gap $E_g = 0.295$ eV at $k_\perp = 0$. (d) Calculated relative BTBT generation rate G for $InAs_{1-y}Sb_y$ ($y = 7.85\%$; dotted blue lines), InN_xAs_{1-x} ($x = 2.04\%$, dash-dotted green lines), and $InAs_{1-z}Bi_z$ ($z = 0.85\%$; solid red lines) alloys. Relative values of T and G in (a) – (d) are computed at each applied electric field F by dividing the calculated value of T or G by that calculated for $InAs_{1-y}Sb_y$. 46
3.6 Calculated relative BTBT generation rate G as a function of the alloy band gap $E_g(x)$ for (a) InN_xAs_{1-x}, and (b) $InAs_{1-z}Bi_z$. Results are shown for applied electric fields $F = 50$ kV cm^{-1} (yellow), 0.1 MV cm^{-1} (orange), 0.2 MV cm^{-1} (red), 0.5 MV cm^{-1} (magenta), 1 MV cm^{-1} (purple), 2 MV cm^{-1} (dark purple), and 5 MV cm^{-1} (black). Relative values of G are computed at each alloy band gap $E_g(x)$ by dividing the value calculated for InN_xAs_{1-x} or $InAs_{1-z}Bi_z$ by that calculated for an $InAs_{1-y}Sb_y$ alloy having the same band gap. 49

4.1 Band structure of a two-atom GaAs primitive unit cell by tight binding approach (image taken from [87]). 59
4.2 Calculated acoustic phonon (dotted line), polar optical phonon (solid line), and Γ to L inter valley optical phonon (dashed line) scattering rates as a function of band energy E for parabolic Γ valley in GaAs. 78
4.3 Calculated acoustic phonon (dotted line), equivalent L to L (dash-dot line), and L to Γ (dashed line) inter valley optical phonon scattering rates as a function of band energy E for parabolic L valley in GaAs. 78

4.4 Steady state electron distribution functions in Γ and L valley for GaAs at different electric field strengths (a) $F = 0$, (b) $F = 1$ (c) $F = 2$, (d) $F = 5$, (e) $F = 10$, and (f) $F = 15$ kV cm^{-1}. 81
4.5 Drift velocity in GaAs as a function of applied electric field F, based on code presented here (magenta line), compared to previous experimental measurements from Ruch and Kino [191] (green plus symbol), Ashida et al. [192] (black dot symbol) and Houston et al. [193] (maroon square symbol) and the theoretical calculations [194] (dash-dot maroon line), [166] (dashed blue line). 82
4.6 Benchmarking of electron transport properties for GaAs [166]: (a) mobility, (b) drift velocity, (c) average energy, and (d) fraction of carriers. 82

5.1 Band structure of bulk Ge (image taken from thesis of O'Halloran [59]) 86
5.2 Schematic representation of the impact of Sn composition in the conduction band structure of Ge. The Sn composition where the transition from indirect to direct band gap occurs is denoted by x_c. The overall structure of the VBs remains unchanged within this composition range. 86
5.3 Comparison of different theoretical calculations for the band gap energies of the Γ and L valley (blue and red lines respectively) with Sn composition, x. Data are taken from Refs. [63, 85, 210, 212]. 89
5.4 Acoustic deformation potential scattering rate of Ge, and of $Ge_{1-x}Sn_x$ for Sn compositions $x = 4$, 8, 12 and 16%, for the (a) Γ, and (b) L valleys at room temperature (300 K). 92
5.5 (a) Optical deformation potential scattering rate in L valley, (b) and equivalent L-L scattering in Ge, and $Ge_{1-x}Sn_x$ for Sn compositions $x = 4$, 8, 12 and 16% at room temperature (300 K). 92
5.6 Inter-valley (Γ → L (a), (b) L → Γ) scattering rate in Ge, and $Ge_{1-x}Sn_x$ for Sn compositions $x = 4$, 8, 12 and 16 % at room temperature (300 K). 93
5.7 Alloy scattering rate in $Ge_{0.96}Sn_{0.04}$ due to $D_{al_{L\Gamma}}$, $D_{al_{LL}}$ and D_{al_L} at room temperature (300 K). 95
5.8 Alloy scattering rate in $Ge_{0.84}Sn_{0.16}$ due to $D_{al_{L\Gamma}}$, $D_{al_{LL}}$ and D_{al_L} at room temperature (300 K). 95
5.9 total scattering rate in Ge, and $Ge_{1-x}Sn_x$ for Sn compositions $x = 4$, 8, 12 and 16% for the (a) Γ, and (b) L valleys at room temperature (300 K). 96
5.10 Fractions of carriers in Γ and L valley as a function of Sn composition at room temperature (300 K). 98
5.11 Density of states in Ge, and $Ge_{1-x}Sn_x$ for Sn compositions $x = 4$, 8, 12 and 16% for the (a) Γ, and (b) L valleys at room temperature (300 K). 99
5.12 Zero-field mobility as a function of Sn composition (with and without alloy scattering) at room temperature (300 K). 99
5.13 Evolution of drift velocity as a function of electric field in Ge computed for different cut - off energies E_{max}, ($\hbar\omega = 38.25$ meV). 103
5.14 Calculated steady state distribution functions of electrons in Γ (solid line) and L valley (dotted line) at different fields, F. The number in parentheses on each line is the electric field strength F in kV cm^{-1}. 103
5.15 Drift velocity in Ge as a function of electric field F, based on the BTE model presented here (solid blue line), compared to previous experimental measurement by Gunn [232] (black circle), Sze [231] (red triangle up), and Smith et al. [230] (triangle left and right) and theoretical calculation by Jacboni et al [219](solid orange line), and by Gang et al. [233](solid green line). 104

5.16 Electron mobility in Ge as a function of electric field, F based on the BTE model presented here (solid blue line), compared to previous experimental measurement by Gunn (red circle) , Many (green star), Zucker (purple square) (data extracted from [195]) and the theoretical computation by Sanchez [222](dashed orange line). Normalised mobility data are available in all these references. Absolute mobility are obtained by multiplying our calculated zero field mobility (3987 cm^2 V^{-1} s^{-1}). . . 105
5.17 Distribution function in both L and Γ valley, for Sn composition $x = 0$, and 8% at various electric fields, F. The number in parentheses on each line is the electric field strength F in kV cm^{-1}. 107
5.18 Distribution function in both L and Γ valley, for Sn composition $x = 12$, and 16% at various electric fields, F. The number in parentheses on each line is the electric field strength F in kV cm^{-1}. 108
5.19 Fraction of electrons in Γ and L valleys, with respect to total electron density ($n_L + n_\Gamma$) as a function of applied electric field F, in Ge, $Ge_{1-x}Sn_x$ alloy at $x = 2$, 4, 6, 8, 10, 12 and 16%, (a) $\frac{n_\Gamma}{n_L+n_\Gamma}$ (b) $\frac{n_L}{n_L+n_\Gamma}$. The inset zoomed images in both the sub-figures show the corresponding properties within the range of low electric field up to 0.05 kV cm^{-1}. 109
5.20 average energy of electrons (a) Γ and, (b) L valley as a function of applied electric field F, Ge, $Ge_{1-x}Sn_x$ alloy at $x = 2$, 4, 6, 8, 10, 12 and 16%. The inset zoomed images in both the sub-figures show the corresponding properties within the range of low electric field up to 0.05 kV cm^{-1}. Results are shown for Ge (royal blue) and various Sn compositions $x = 2\%$ (navy), 4% (blue), 6% (cyan), 8% (orange), 10% (lime), 12% (olive), 14% (green), 16% (purple). 110
5.21 Evolution of drift velocity as a function of electric field F, in Ge, and $Ge_{1-x}Sn_x$ alloy at $x = 2$, 4, 6, 8, 10, 12 and 16%. 110
5.22 Evolution of mobility as a function of electric field F, Ge, $Ge_{1-x}Sn_x$ alloy at $x = 2$, 4, 6, 8, 10, 12 and 16%. 111
5.23 Comparison of the evolution of mobility in Ge, $Ge_{1-x}Sn_x$ alloy at $x = 2$, 4, 6, 8, 10, 12 and 16%, at very low electric field regime, (a) with alloy scattering, and (b) without alloy scattering. 111
5.24 Comparison of evolution of drift velocity in Ge, $Ge_{1-x}Sn_x$ at $x = 2$, 4, 6, 8, 10, 12 and 16%, at very low electric field regime, (a) with alloy scattering, and (b) without alloy scattering). 112

Chapter 1

Introduction

1.1 Background and motivation

Many environmentally and industrially important gases possess vibrational-rotational spectra which are characterised by strong absorption in the mid-infrared spectral range, particularly in the first atmospheric window at wavelengths between 3 and 5 μm. For instance, the vibrational-rotational spectra of greenhouse gases, such as methane (CH_4) and carbon dioxide (CO_2), show strong absorption signatures at wavelengths of 3.3 and 4.2 μm, respectively. As a result, developing photonic devices with these wavelengths for application in environmental monitoring is quite appealing. Aside from environmental monitoring, mid-infrared sensing has also a wide range of other applications, including chemical analysis of industrial processes, detection of biological markers in non-invasive medical diagnostics, free-space optical communications, and imaging for aerospace and defence. These applications require the development of highly sensitive mid-infrared photodetectors. In a number of these applications, when the input photon flux is low, gain-based devices such as avalanche photodiodes (APDs) are desired to amplify such low-intensity light and enable the requisite photoresponse. However, leakage in the form of dark current places a lower limit on the strength of a signal which can be unambiguously detected using a photodetector. It is therefore desirable to minimise the dark current in a given device, in order to maximise the detector signal-to-noise ratio (SNR). Dark current [1] in a p-i-n diode results from the generation of electron-hole pairs in the absence of external illumination, and is primarily associated with: (i) band to band tunneling (BTBT) of electrons from the valence band (VB) to the conduction band (CB) in the intrinsic region, (ii) thermally driven diffusion of carriers into, or thermal generation within, the intrinsic region, and (iii) avalanche breakdown (which occurs only in the presence of extremely large electric fields). The rate associated with each of these processes depends closely on the details of the band structure of the semiconductor materials constituting the photodetector suggesting the possibility to engineer the band structure of these materials in order to minimise dark current and maximise the SNR. There has recently been increasing interest in exploiting the strong band gap reduction, and modified band dispersion in dilute nitride [2] and bismide alloys [1] to provide access to mid-infrared wavelengths, which has proven challenging to achieve

using conventional semiconductor alloys. In particular optoelectronic devices such as LASERs [3–10] and highly-efficient multi-junction solar cells [11–14] based on dilute nitride and bismide alloys have been proposed and demonstrated. Additional research has also emphasised the potential of highly-mismatched alloys for applications in long-wavelength intermediate-band solar cells [15, 16], tunable low-frequency plasmonics [17], photodetectors [18] and APDs [19]. Adams et al. [19] studied the electron and hole impact ionisation coefficients, which are the essential elements that characterise the performance index of APDs, and proposed the use of nitride alloys as an improved low-noise medium for hole multiplication compared to conventional III-V alloys. Tan et al. [20] conducted an experimental investigation of impact ionisation in a dilute nitride diode. In a recent study, Liu et al. [21] demonstrated the potential of the valence band engineering of $GaAs_{1-z}Bi_z$ for a low noise APD. The narrow band gap nature of these alloys allows the tunneling effect to occur under a strong electric field with impact ionisation, increasing the dark current and noise levels and eventually degrading the device's performance. However, the modified band structure of these materials due to the inclusion of a dilute amount of N or Bi would also have an impact on the tunneling mechanism. Despite the possibility of employing these alloys as mid-infrared APDs and the effect of BTBT generation rate on the dark current, which reduces APD efficiency, this topic has yet to be thoroughly investigated. We shed more light onto this topic below in Sec. 1.2. The second topic addressed in this thesis relates to one of the most pressing issues confronting

today's world: the unprecedented increase in power consumption caused by the use of massive amounts of data. Global data consumption is increasing at an exponential rate, and this trend is being pushed by a range of applications, such as social and streaming media, cloud computing, data storage, artificial intelligence, machine learning, fintech, and an ever-increasing number of networked devices that compose the "Internet of Things". Although these new services and technologies enable people to connect, interact and benefit on a global scale, the required high usage of data comes at the expense of massive increases in power consumption. According to a 2022 report [22], the data centres at that time consumed approximately 1.7% of global electricity demand. Other sources [23, 24] claim even higher power consumption. One source of this tremendous power usage is the use of a staggeringly large number of transistors in a single chip. A solution to this challenge will demand the development of novel device designs for energy-efficient transistors, as well as the usage of high-mobility channel materials. Tunneling field effect transistors (TFETs) based on BTBT current are examples of such innovative devices, which outperform conventional transistors in terms of efficiency [25]. Furthermore, heating of the copper (Cu) interconnects, which are the passive components of integrated circuits (ICs), has also been discovered as a significant power dissipation carrier. An intriguing alternate approach to this problem is the fabrication of optoelectronic integrated circuits (OEIC), in which optical interconnects will replace the Cu electrical interconnects, which will simultaneously increase bandwidth and reduce power consumption. Significant progress has been made in recent years in the fabrication of numerous key passive components required for photonic integrated circuits, including APDs, modulators [26–28] and waveguides [29–31]. However, the indirect fundamental band gap of the group-IV semiconductor silicon (Si), makes it a poor light emitter and absorber. Hence manufacturing active photonic

components, such as electrically pumped LASERs and light-emitting diodes (LEDs), that employ silicon as light-emitting material remains problematic. As a result, the ultimate answer to reducing power consumption is to use a semiconductor material that (i) has a direct band gap to efficiently emit light for the fabrication of active photonic components for OEICs, (ii) is silicon compatible to be easily integrated with modern complementary metal-oxide-semiconductor (CMOS) chipsets and benefit from the existing CMOS fabrication infrastructure, (iii) has higher mobility to be used as a channel material for transistors, and (iv) provides novel device structures for energy-efficient computation such as TFETs and fin field effect transistors (FinFETs) [32]. The Group-IV alloy $Ge_{1-x}Sn_x$ has a direct band gap and is CMOS compatible and has therefore attracted significant interest for optoelectronic and novel device applications, as we discuss further below in Sec. 1.3.

1.2 Dilute nitride and bismide alloys (InN_xAs_{1-x}, $InAs_{1-z}Bi_z$)

The substitution of dilute concentrations of nitrogen (N) or bismuth (Bi) for group-V atoms in conventional group III-V semiconductor alloys such as InAs to form InN_xAs_{1-x} ($InAs_{1-z}Bi_z$), strongly modifies the CB (VB) structure of the host semiconductor. The unusual band structure evolution in InN_xAs_{1-x} ($InAs_{1-z}Bi_z$) can be described in terms of a band anti-crossing (BAC) interaction between the extended states of the host material CB (VB), and highly localised N- (Bi-) related impurity states [33, 34]. This BAC interaction leads to a strong reduction in band gap with increasing N (Bi) composition which, unusually, is accompanied by an increase in the CB (VB) edge effective mass, and hence the associated band edge density of states (DOS). Because of the strongly modified band gap and electronic band structure, band structure engineering provides a considerable opportunity to generate characteristics suitable for use in a variety of optoelectronic devices, specifically operating in mid-infrared wavelength region. For instance, the use of InN_xAs_{1-x} has been proposed as an active material for LASERs [35] and LEDs [36]. In this regard, Zhuang et al. [37] demonstrated room temperature photoluminescence emission at a wavelength of 4.5 μm. Furthermore, experimental investigation on hot electron transport and impact ionisation in the narrow band gap InN_xAs_{1-x} alloy were carried out by Makarovsky et al. [38]. Now coming to bismide alloys, Sandall et al. [1] have demonstrated the photoresponse and dark current characteristics of $InAs_{1-z}Bi_z$ photodiodes in the mid-infrared region. From the theoretical perspective recently Mal et al. [39] investigated the impact of Bi inclusion on optoelectronic and thermoelectric properties of InAs for long-wave infrared applications by employing the valence BAC model and density functional theory method. The same group [40] has also designed and simulated an $InAs_{1-z}Bi_z$-based p-i-n photodetector and investigated the dark current as a function of applied bias voltage and temperature for long wavelength infrared applications. Here, we address a topic that has yet received very little attention: the complex band structure (CBS), which extends the concept of Bloch states to evanescent states having complex-valued wave vectors, and its impact on BTBT in terms of the electronic characteristics of dilute nitride and bismide alloys. BTBT

can be a helpful enabling property or a negative loss mechanism, depending on the device application of interest. As already discussed, BTBT can contribute significantly to leakage currents in long-wavelength APDs [41–43], making suppression of the BTBT generation rate desirable for the realisation of detectors displaying high SNR. In addition, BTBT is the physical mechanism enabling the operation of TFETs [25, 44–46], making enhancement of the BTBT generation rate at fixed band gap and applied electric field desirable for the realisation of high on-state current to enable high-speed operation [47, 48]. Given the broad scope for applications of TFETs as an enabling platform for post-complementary metal-oxide semiconductor electronics, and of APDs for sensing at application-rich near- and mid-infrared wavelengths, it is of both fundamental and practical interest to investigate novel approaches to engineer BTBT in semiconductors. Chapter. 3 and 4 of this thesis specifically address this issue.

1.3 Group-IV alloys

The integration of III-V photonic devices with contemporary CMOS technology has been impeded due to integration challenges and high costs. Group-IV alloys compatible with the CMOS flow may be a superior solution. For Ge, the valence band maximum and the conduction band minimum are not located at the same wave vector thus making it an indirect band gap semiconductor. The conduction band minimum is at the L valley which lies approximately 0.145 eV below the direct band gap at the Γ valley. This small energy gap can be overcome by applying strain [49–53] or alloying Ge with other group-IV elements (tin (Sn) or lead(Pb) [54]) to create a direct band gap group-IV semiconductor. Theoretical calculations show that for significant biaxial tensile strains [51–53] of 2% or more, the band gap should transit from an indirect to a direct gap. From the experimental point of view, the direct band gap of Ge has been achieved by high tensile strain, and fabricated through multi-step lithography [55, 56], but, the application of these materials in practical applications remains challenging. However, the alloying of Ge has shown more promise. While Sn has gained the most attention, there is also interest in similar group-IV alloys incorporating Pb [54] and carbon (C) [57]. Kirwan et al. [58] presented hybrid density functional theory calculations for ordered $Ge_{1-x}C_x$ alloy supercells. O'Halloran et al. [59] have investigated the electronic and optical properties of both $Ge_{1-x}Sn_x$ and $Ge_{1-x}Pb_x$ alloys. For $Ge_{1-x}Sn_x$, Jenkins and Dow [60], predicted a direct band gap for $Ge_{1-x}Sn_x$, using a tight-binding model in the virtual crystal approximation in 1987. The interest in alloying of Ge with Sn was heightened following the experimental demonstrations of optically and electrically pumped lasing from $Ge_{1-x}Sn_x$ [61–64], providing proof of principle for its use as a CMOS-compatible active photonic material. Additional research also supports the direct band gap nature of $Ge_{1-x}Sn_x$ from both theoretical and experimental perspectives. The introduction of Sn in Ge reduces the Γ valley energy more rapidly than that of L valley. So, after a particular Sn composition, $x \lesssim 10\%$ where the energy of the direct CB edge state shifts below that of the indirect L CB minimum state, $Ge_{1-x}Sn_x$ becomes a direct gap material. There is a discrepancy between studies on the claimed Sn composition for switching from an

indirect to a direct band gap but it is generally accepted to lie in the Sn composition range $x = 6$ - 11% [65–68]. The most important aspect, however, is that the direct-band gap can be achieved, making it potentially valuable for Si-based optoelectronics devices [61, 62, 69–73]. Additionally, the reduction in band gap brought on by Sn also opens up potential applications in TFETs [74–77]. Recently Dunne [78] presented the current characteristics of $Ge_{1-x}Sn_x$ -based TFETs, indicating that otherwise overlooked atomic effects play a significant impact on improvement in BTBT current, hence influencing the electrical properties in such devices. $Ge_{1-x}Sn_x$ has been studied by Gupta et al. [66] as the channel material in n- and p- type FETs. Unlike other group-IV semiconductors such as Si, Ge, or SiGe, the Γ valley of the $Ge_{1-x}Sn_x$ alloy has a low effective mass and lies at the centre of the Brillouin zone, energetically below the L-valleys. Once the electrons start to populate conduction band states at the Γ valley, the electron mobility should improve significantly, potentially making $Ge_{1-x}Sn_x$ a high-mobility channel material for next-generation metal-oxide-semiconductor field-effect transistor (MOSFETs). In this regard, Sau et al. [79] have studied the influence of strain and Sn alloying on carrier mobilities in $Ge_{1-x}Sn_x$ alloys using a combination of ab-initio and empirical pseudo potential techniques, and predicted significantly higher mobility in $Ge_{1-x}Sn_x$ than in Ge. Mukhapadhay and colleagues [80] computed the electron mobility in strained and unstrained $Ge_{1-x}Sn_x$ alloys. They took into account alloy, impurity, and phonon scattering mechanisms. However, they didn't study the impact of applied electric fields on mobility. Liu et al. [81] calculated the electronic band structure by using a non-linear empirical pseudo potential method and derived the effective mass for the Γ and L valleys of $Ge_{1-x}Sn_x$ as a function of Sn composition. They demonstrated zero-field electron mobility and observed just a two-fold gain in mobility over Ge for increased Sn concentration at ambient temperature since the Γ valley contains fewer electrons than expected. They also employed a single-temperature model to illustrate the field-dependent drift velocity for high-range Sn compositions ($x = 0.17, 0.20, 0.24$). But we are yet to understand much about the transport properties in the low- and high-field regimes, and hence the associated potential for device applications. From a device perspective, we are interested in understanding the velocity vs. field properties of electrons. As such, we must undertake a quantitative analysis of the field-dependent carrier transport. However, most of the previous theoretical transport models investigate only the zero-field electron mobility and ignore the impact of the applied electric field. The previous study [81] only treated field-dependent transport via a simplified model, not taking account of the strong modification of the carrier distribution functions in response to an applied electric field. The previous zero-field mobility model [80] was based on band structure models for $Ge_{1-x}Sn_x$ that are now known to have shortcomings vs. experiments. Whereas, the model presented in this thesis incorporates band structure details coming from recent atomistic electronic structure calculations, which are in quantitative agreement with experiment. Given the requirement of the increase in sophistication in semiconductor devices and decrease in size, to fullfill the demand of modern-day technology, there is still a lack of a precise and comprehensive theoretical framework to define the composition and electric field-dependent carrier transport properties of $Ge_{1-x}Sn_x$ - this thesis addresses this problem.

1.4 Structure of the thesis and overview of primary results

The remainder of the thesis is structured as follows and principally focuses on the investigation of (i) band-to-band tunneling current in highly mismatched dilute nitride and bismide alloys, (Chapter. 2 and 3) and (ii) electron transport properties in $Ge_{1-x}Sn_x$ alloys (Chapter. 4 and 5).

Chapter. 2 discusses a number of key concepts relevant to the investigation of BTBT generation rate, beginning with a description of the electronic structure of a conventional III-V direct band-gap semiconductor, by constructing a $2-$band Hamiltonian to describe the band dispersion by using the $\mathbf{k}\cdot\mathbf{p}$ method and introducing the concept of CBS in a bulk semiconductor. After that, we detail the underlying theoretical framework to understand tunneling through a 1-D barrier by the transfer matrix and the WKB method and find that the latter method provides an approximate but far less expensive computing solution. Then we use all the relevant concepts to develop the tunneling model for a bulk semiconductor alloy, where we first compute the CBS from a previously derived $2-$band $\mathbf{k}\cdot\mathbf{p}$ Hamiltonian matrix and then from this CBS, we compute the field-dependent tunneling coefficient (T) and finally the generation rate (G), by employing a numerical implementation of the WKB approximation and the analytical Kane model. We show how utilising the WKB approach to explain the band structure of a conventional semiconductor alloy provides the same results as those obtained using the 2-band Kane model. However 3-band Hamiltonian models are required for describing the altered band dispersion in highly mismatched alloys such as InN_xAs_{1-x} and $InAs_{1-z}Bi_z$ alloys. Hence the analytical Kane model cannot be utilised to represent such alloys.

Chapter. 3 investigates the impact of band anti-crossing on band-to-band tunneling current in highly mismatched dilute nitride and bismide semiconductor alloys. To achieve this, we start with model $\mathbf{k}\cdot\mathbf{p}$ Hamiltonians that incorporate N- or Bi-related BAC interactions and analytically compute the CBS. We then use these perturbed CBSs to numerically calculate the BTBT transmission coefficient and, consequently, the BTBT generation rate in the WKB approximation. We compare the outcomes of our calculations for substantially mismatched InN_xAs_{1-x} and $InAs_{1-z}Bi_z$ to similar calculations for the traditional III-V alloy $InAs_{1-y}Sb_y$ in order to determine the impact of N- or Bi-related BAC. Our analysis reveals that BTBT in InN_xAs_{1-x} and $InAs_{1-z}Bi_z$ is governed by a field-dependent competition between the impact of N (Bi) incorporation on (i) the dispersion of the evanescent Bloch band linking the valence and conduction band edges, which dominates at low field strengths, and (ii) the conduction (valence) band edge density of states, which dominates at high field strengths. The implications of our results for applications in long-wavelength APDs and TFETs are discussed.

The theoretical framework for the field-dependent electron transport calculations in the case of a bulk semiconductor alloy is the subject of Chapter. 4, which provides a comprehensive solution to Boltzmann's transport equation. In this chapter, we describe the numerical solution of the coupled multi-valley Boltzmann transport equation in the relaxation time approximation. We begin with the electron energy distribution function at equilibrium conditions, which we assume to be the Maxwell-Boltzmann distribution for both sets of valleys. We then apply an external electric force ($\mathbf{F}$), through which the momentum of electrons is disrupted. The applied force plus the scattering

of electrons from one state to another, results in a change in the distribution function from the equilibrium distributions; we obtain two equations for the change in distribution function corresponding to each valley. Each equation represents the rate of change in the distribution function due to the applied force and scattering mechanisms. We apply explicit time-stepping methods using a uniform time grid by Euler's rule to solve these equations and determine the steady-state distribution functions. We then use these steady-state distribution functions to determine the corresponding electron transport properties as well as input to calculate the electron transport characteristics at the next electric field. Using this approach, we establish the electron transport properties for gallium arsenide (GaAs) at different electric fields. Here we take into account the scattering mechanisms due to acoustic phonons, inter and intra-valley optical phonons, and polar optical phonons. We validate our findings by comparing them to those of equivalent computations made in the literature, which also includes reproducing the well-known Gunn effect showing the negative differential resistance associated with the field-dependent electron transport in GaAs.

In Chapter. 5, we comprehensively investigate the effects of Sn concentration and applied electric field on the electron transport characteristics of $Ge_{1-x}Sn_x$. We do this work in two steps: first, we build the electron transport model for Ge by using the BTE approach as discussed in Chapter. 4. In this model, we take into account the acoustic deformation potential, optical phonon (which includes intervalley and optical deformation potential) scattering and calculate the field-dependent electron drift velocity and mobility. We validate our model by demonstrating that our results are consistent with earlier theoretical and experimental investigations of electron transport in Ge. In the second step, we then extend our model by incorporating alloy scattering due to the inclusion of Sn atoms, finding the alloy scattering potential using the tight binding method, and then examining how Sn content affects the electron transport characteristics. We begin our calculation by identifying appropriate band structure parameters by analysing different band structure calculations available in the literature. We use the bowing parameters, which are obtained by Gupta et al. [66] in fitting the experimental band gap with the band gap calculation carried out using a modified virtual crystal approximation which takes account of the effects of the alloy compositional and structural disorder. We then take the effective mass of Γ and L valley by interpolation of Ge and Sn effective mass, with a bowing parameter of 0.0128 and 0.042 respectively, which we find by equating $m_\Gamma(x) = 0$ for $x = 29.6\%$ i.e. the composition at which the Γ point band gap is equal to zero. Finally, we use all these parameters to find the impact of Sn composition on electron transport properties at both low ($0 < F < 0.1$ kVcm^{-1}) and high applied electric field ($0 < F < 10$ kVcm^{-1}). We find the Gunn effect for direct-gap $Ge_{1-x}Sn_x$ at a much lower electric field than in GaAs. As the Sn composition increases, the mobility in $Ge_{1-x}Sn_x$ increases, but up to a certain electric field; beyond which the mobility decreases to below that of Ge. With the increase in Sn composition and applied electric field, the alloy scattering plays a dominating role, making the mobility lower than Ge. We also analyse the zero-field mobility in a separate section. Our analysis suggests the use of $Ge_{1-x}Sn_x$ alloy as a high mobility channel can be beneficial for the fabrication of MOSFETs and FinFETs, but limited to very low voltage operation.

Finally, Chapter. 6 summarises and concludes the thesis. The final chapter also includes prospective future work. We review the key findings and conclusions of the research described in this thesis and provide a preview of prospective future research fields in group-IV and III-V optoelectronics that could be inspired by the work presented in this thesis.

Chapter 2

Theoretical background: Band to band tunneling current

2.1 Introduction

We introduce in this chapter several of the key concepts relevant to the investigation of band to band tunneling (BTBT) in Chapter. 3. We first provide an overview in Sec. 2.2 of the electronic structure of a conventional direct-gap semiconductor such as InAs [82] or InAsSb [83]. We introduce Bloch's theorem, which allows us to associate a real wave vector $\mathbf{k}$ with each energy state $E_{\mathbf{nk}}$ in the bulk semiconductor band structure. We describe how the $\mathbf{k}.\mathbf{p}$ method can be used to describe the band dispersion for energies in the vicinity of the semiconductor band gap. We then introduce the concept of evanescent states with complex wave vector, before turning in Sec. 2.3 to introduce tunneling across the energy gap in semiconductors and some of its applications. We then take the example in Sec. 2.4 of tunneling through a 1D barrier to introduce two of the main methods used to calculate the tunneling rate, namely the transfer matrix method, which provides an exact but computationally expensive solution for the tunneling rate, and the Wentzel-Kramers-Brillouin (WKB) method, which can provide an approximate and much cheaper computational solution. We turn in Sec. 2.5 to consider the calculation of the tunneling current generation rate in a bulk conventional semiconductor alloy, describing a $2-$band $\mathbf{k}.\mathbf{p}$ approximate model for the band dispersion introduced by Kane, and then describing how to calculate the band dispersion firstly using the Kane model. In Sec. 2.6, we take InAs as an example to illustrate the impact of the different tunneling models on the calculated current generation rates. Chapter. 3 will investigate the impact of band anti-crossing on BTBT current in highly mismatched dilute nitride and bismide semiconductor alloys. We wait until Chapter. 3 to introduce the models used to describe the band dispersion in such alloys.

2.2 Electronic band structure

The band structure of a semiconductor material plays a crucial role in defining its electronic and optoelectronic properties. In the simplest way, band structure defines the relation between

the wave function of an electron and the allowed energy states in a solid. It therefore plays a decisive role in determining the usefulness of these materials for applications in devices such as photodetectors, light-emitting diodes, etc. That's why there is a great amount of interest to engineer the band structure of the semiconductor materials used in such devices. For a typical solid, nearly 10^{23} valence electrons account for the bonding in each cubic centimetre. So, if we look at the band structure calculation, it seems like a complex many-body problem, as the energy and wave function of each electron depends on all of the others. However, the inclusion of the following factors significantly reduces the complexity of the band structure calculation. (i) "Independent electron approximation": this assumes that each electron experiences the same average potential due to all of the others, so that each electron then sees an identical crystal potential $V(\mathbf{r})$. (ii) Semiconductor materials are crystalline in nature with a periodic lattice; so, the potential $V(\mathbf{r})$ is periodic with $V(\mathbf{r}) = V(\mathbf{r}+\mathbf{R})$; where $\mathbf{R}$ can be defined as a vector which joins the same point of two neighbouring unit cells of atoms. (iii) The use of these two results then allows us to introduce Bloch's theorem.

Bloch's Theorem

According to Bloch's theorem, the wave function, $\psi_{n\mathbf{k}}(\mathbf{r})$ of an electron, with Hamiltonian, $H = \left(-\frac{\hbar^2}{2m_0}\nabla^2 + V(\mathbf{r})\right)$, associated with the n^{th} state of wave vector $\mathbf{k}$ can be defined as the product of a plane wave and a function, $u_{n\mathbf{k}}(\mathbf{r})$ having the lattice periodicity $\mathbf{R}$

$$\psi_{n\mathbf{k}}(\mathbf{r}) = e^{i\mathbf{k}.\mathbf{r}} u_{n\mathbf{k}}(\mathbf{r}) \tag{2.1}$$

where

$$u_{n\mathbf{k}}(\mathbf{r}+\mathbf{R}) = u_{n\mathbf{k}}(\mathbf{r}) \tag{2.2}$$

From Eqs. (2.1) and (2.2), we can also write another form of Bloch's theorem as follows

$$\psi_{n\mathbf{k}}(\mathbf{r}+\mathbf{R}) = e^{i\mathbf{k}.\mathbf{R}} \psi_{n\mathbf{k}}(\mathbf{r}) \tag{2.3}$$

Using Bloch's theorem, we can assign a wave vector $\mathbf{k}$ to each energy state $E_{n\mathbf{k}}$ in the case of a periodic solid. When atoms are in their free state, discrete energy levels corresponding to each principal quantum number n are produced. However, when atoms are brought into close proximity, as in a crystal lattice, regions of allowed and forbidden bands occur as a result of the interaction of atomic orbitals. The permissible bands are divided into two categories: valence bands (VB), which are energy levels that an electron occupies, and conduction bands (CB), which are energy levels that an electron does not occupy. The forbidden bands cause band gaps to form in the material. The band structure of the solid describes the study of the energy $E_{n\mathbf{k}}$, as a function of wave vector $\mathbf{k}$. In our calculation, we assume the band to be parabolic in nature, defined by $E_{n\mathbf{k}} = \frac{\hbar^2\mathbf{k}^2}{2m}$. Figure 2.1 shows a schematic diagram of the band structure for a direct gap semiconductor in the vicinity of the energy gap between the filled VB and empty CB. Here, the VBs are divided into

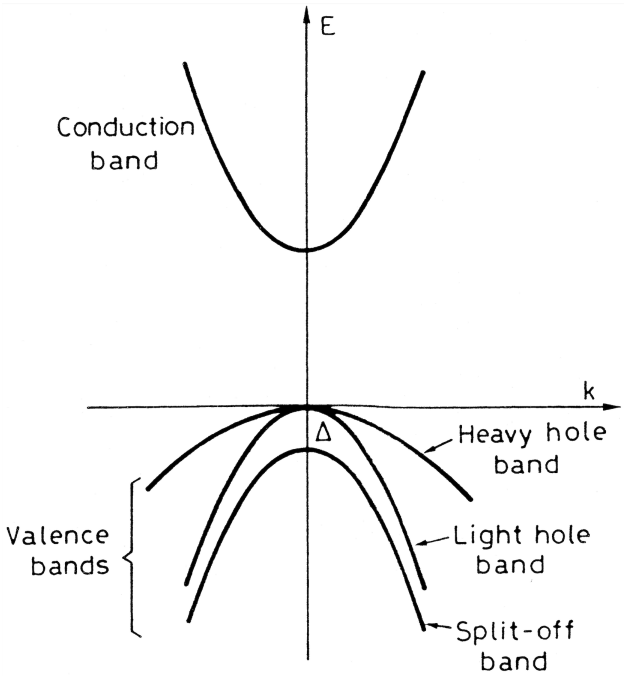

FIGURE 2.1: Band structure ($E_{n\mathbf{k}}$) of a direct gap cubic semiconductor solid.

three sub-bands: the highest band is known as the heavy hole (HH), the next is the light-hole (LH) and the bottom one is the spin-split-off (SO) band. There is an energy difference of Δ known as the spin-orbit splitting energy between the HH, (LH) and SO bands at the maximum point. As the lowest point of the CB and the highest point of the VB lie at the same $\mathbf{k}$ point, the electrons from VB can excite to CB without change in momentum, such semiconductor solids are known as a direct-band gap semiconductor. The materials in which the CB minimum and VB maximum don't lie at the same $\mathbf{k}$ point (e.g. Ge) are known as indirect-band gap materials. Such structures require the participation of an extra particle (e.g. phonon) to conserve both energy and momentum via process of light absorption or emission. In this thesis, we work with both direct and indirect band gap semiconductors.

Different methods such as density functional theory [84], the empirical tight-binding method [78], and empirical pseudopotentials [85] are used to study the electronic band structure of solids. We will be using a continuum empirical model, namely the $\mathbf{k}\cdot\mathbf{p}$ method [86], in our calculations, and therefore now discuss it in further detail.

The $\mathbf{k}\cdot\mathbf{p}$ method

The $\mathbf{k}\cdot\mathbf{p}$ method [87], based on perturbation theory, provides a simple and physically transparent approach to investigate semiconductor band structure. According to this model, if we know the exact energy value for a number of states at one wave vector ($\mathbf{k}_0$) in the Brillouin zone, then we can use perturbation theory [86] to find the band structure near the $\mathbf{k}_0$ point. Once we have different parameters such as band gap and effective mass from experimental data or any other analysis, we can implement the $\mathbf{k}\cdot\mathbf{p}$ theory to derive the Hamiltonian matrix, which will describe the band

structure. The time-independent Schrödinger equation for a single electron in a periodic crystal is

$$H_0\psi_{n\mathbf{k}}(\mathbf{r}) = E_{n\mathbf{k}}\psi_{n\mathbf{k}}(\mathbf{r}) \tag{2.4}$$

where,

$$H_0 = -\frac{\hbar^2}{2m_0}\nabla^2 + V(\mathbf{r}) \tag{2.5}$$

From Bloch's theorem (Eq. (2.1)) and Eq. (2.5), we find

$$H_0\psi_{n\mathbf{k}}(\mathbf{r}) = \left(-\frac{\hbar^2}{2m_0}\nabla^2 + V(\mathbf{r})\right)e^{i\mathbf{k}.\mathbf{r}}u_{n\mathbf{k}}(\mathbf{r}) = E_{n\mathbf{k}}\left(e^{i\mathbf{k}.\mathbf{r}}u_{n\mathbf{k}}(\mathbf{r})\right) \tag{2.6}$$

The Schrödinger equation at a specific value of $\mathbf{k}$, let's say at $\mathbf{k} = \mathbf{k}_0$ can be written as follows:

$$H_0\psi_{n\mathbf{k}_0}(\mathbf{r}) = \left(-\frac{\hbar^2}{2m_0}\nabla^2 + V(\mathbf{r})\right)e^{i\mathbf{k}_0.\mathbf{r}}u_{n\mathbf{k}_0}(\mathbf{r}) = E_{n\mathbf{k}_0}\left(e^{i\mathbf{k}_0.\mathbf{r}}u_{n\mathbf{k}_0}(\mathbf{r})\right) \tag{2.7}$$

We can rewrite Eq. (2.6) as:

$$H_0 e^{i(\mathbf{k}-\mathbf{k}_0).\mathbf{r}}\left(e^{i\mathbf{k}_0.\mathbf{r}}u_{n\mathbf{k}}(\mathbf{r})\right) = E_{n\mathbf{k}}e^{i(\mathbf{k}-\mathbf{k}_0).\mathbf{r}}\left(e^{i\mathbf{k}_0.\mathbf{r}}u_{n\mathbf{k}}(\mathbf{r})\right) \tag{2.8}$$

If we multiply $e^{-i(\mathbf{k}-\mathbf{k}_0).\mathbf{r}}$ from the left side on both sides of Eq. (2.8), we obtain

$$e^{-i(\mathbf{k}-\mathbf{k}_0).\mathbf{r}}H_0 e^{i(\mathbf{k}-\mathbf{k}_0).\mathbf{r}}\left(e^{i\mathbf{k}_0.\mathbf{r}}u_{n\mathbf{k}}(\mathbf{r})\right) = \left[e^{-i(\mathbf{k}-\mathbf{k}_0).\mathbf{r}}E_{n\mathbf{k}}e^{i(\mathbf{k}-\mathbf{k}_0).\mathbf{r}}\right]\left(e^{i\mathbf{k}_0.\mathbf{r}}u_{n\mathbf{k}}(\mathbf{r})\right) \tag{2.9}$$

Now, we can represent the above equation in terms of a $\mathbf{k}$ - dependent Hamiltonian $H_{\mathbf{k}'}$, where $\mathbf{k}' = \mathbf{k} - \mathbf{k}_0$

$$H_{\mathbf{k}'}\phi_{n\mathbf{k}}(\mathbf{r}) = e^{-i\mathbf{k}'.\mathbf{r}}\left(-\frac{\hbar^2}{2m_0}\nabla^2 + V(\mathbf{r})\right)e^{i\mathbf{k}'.\mathbf{r}}\phi_{n\mathbf{k}}(\mathbf{r}) \tag{2.10}$$

where, $\phi_{n\mathbf{k}}(\mathbf{r}) = e^{i\mathbf{k}_0.\mathbf{r}}u_{n\mathbf{k}}(\mathbf{r})$. If we expand the term $\nabla^2 e^{i\mathbf{k}'.\mathbf{r}}\phi_{n\mathbf{k}}(\mathbf{r})$, Eq. (2.10) becomes

$$H_{\mathbf{k}'}\phi_{n\mathbf{k}}(\mathbf{r}) = e^{-i\mathbf{k}'.\mathbf{r}}\left(-\frac{\hbar^2}{2m_0}\nabla^2 + \frac{\hbar^2\mathbf{k}'^2}{2m_0} - \frac{\hbar^2}{m_0}\mathbf{k}'.\mathbf{i}\nabla + V(\mathbf{r})\right)e^{i\mathbf{k}'.\mathbf{r}}\phi_{n\mathbf{k}}(\mathbf{r})\ . \tag{2.11}$$

If we replace the term $-i\hbar\nabla$ and $-\frac{\hbar^2}{2m_0}\nabla^2 + V(\mathbf{r})$ with the momentum operator P, (as $P\psi = -i\hbar\frac{\delta\psi}{\delta x}$) and H_0 (Eq. (2.5)) respectively, we get

$$H_{\mathbf{k}'}\phi_{n\mathbf{k}}(\mathbf{r}) = \left(H_0 + H'\right)\phi_{n\mathbf{k}}(\mathbf{r}) \tag{2.12}$$

where,

$$H' = \frac{\hbar^2\mathbf{k}'^2}{2m_0} + \frac{\hbar}{m_0}\mathbf{k}'.P \tag{2.13}$$

We can now focus in the vicinity of the Γ point, at $\mathbf{k}_0 = 0$ where we already know the energy value E_{n0}. Now we can treat the Hamiltonian H' as a perturbation to the Hamiltonian H_0 and from

standard second-order perturbation theory we can estimate E_{nk} as follows

$$E_{n\mathbf{k}} = E_{n0} + \frac{\hbar^2 k^2}{2m_0} + \frac{\hbar}{m_0} k.P_{nn} + \frac{\hbar^2}{m_0^2} \sum_{l \neq n} \frac{\left|\mathbf{k}.\mathbf{p}_{nl}\right|^2}{E_{n0} - E_{l_0}} \tag{2.14}$$

Here n accounts e.g. for the CB state, and all the other states are indexed by l; the matrix elements P_{nl} of the momentum operator are given by

$$\mathbf{P}_{ab} \equiv \langle u_{a\mathbf{k}_0} | \mathbf{P} | u_{b\mathbf{k}_0} \rangle = -i\hbar \int_s u^*_{a\mathbf{k}_0}(r) \nabla u_{b\mathbf{k}_0}(r)\, d\mathbf{r} \tag{2.15}$$

where $u_{a\mathbf{k}_0}$ and $u_{b\mathbf{k}_0}$ are the cell-periodic parts of the crystal eigenstates at $\mathbf{k}_0$ and s denotes integration over the volume of the unit cell. By symmetry, when $n = l$, the matrix elements P_{nn} is zero. So, if we rewrite the Eq. (2.14) for the CB state, we get

$$E_{CB}(\mathbf{k}) = E_{CB}(0) + \frac{\hbar^2 k^2}{2m_0} + \frac{\hbar^2}{m_0^2} \sum_{l \neq n} \frac{\left|\mathbf{k}.\mathbf{P}_{nl}\right|^2}{E_{n0} - E_{l0}} \tag{2.16}$$

where $E_{CB}(0)$ is the CB state energy at the Γ point. The effective mass can be defined as follows.

$$\frac{1}{m^*} = \frac{1}{m_0} + \frac{2}{m_0^2} \sum_{j \neq n} \frac{\left|\mathbf{P}_{nj}\right|^2}{E_{n0} - E_{j0}} \tag{2.17}$$

The dispersion of the lowest CB is determined primarily by its interaction with the LH and SO bands. If we presume that the spin-orbit splitting energy $\Delta_{so} = 0$, then the CB electron effective mass is to a good approximation given by

$$\frac{1}{m_{CB}} = \frac{1}{m_0} + \frac{2}{m_0^2} \frac{\mathbf{P}_{nj}.\mathbf{P}_{jn}}{(E_{CB} - E_0)} \tag{2.18}$$

$$\mathbf{P}_{nl}.\mathbf{p}_{ln} = \frac{m_0^2}{\hbar^2} P^2 \tag{2.19}$$

$$\frac{1}{m_{CB}} = \frac{1}{m_0} + \frac{2P^2}{\hbar^2 E_g} \tag{2.20}$$

If we set $E_P \equiv \frac{2m_0 P^2}{\hbar^2}$, where P is referred to as interband (Kane) momentum matrix element, then we have

$$\frac{1}{m_{CB}} = \frac{1}{m_0} + \frac{E_P}{m_0 E_g} \tag{2.21}$$

$$\implies \frac{1}{m_{CB}} = \frac{1}{m_0}\left(1 + \frac{E_P}{E_g}\right) \tag{2.22}$$

Because of the CB effective mass is determined primarily via the interaction of the CB with the LH VB , we can introduce a $2-$ band Hamiltonian to describe the CB and LH dispersion:

$$H = \begin{pmatrix} E_g + \frac{\hbar^2 k^2}{2m_0} & Pk \\ Pk & \frac{\hbar^2 k^2}{2m_0} \end{pmatrix}, \tag{2.23}$$

where E_g is the zone-centre ($\mathbf{k} = 0$) band gap. We shall employ this Hamiltonian in Sec. 2.5.1 to analyse BTBT. We exclude the HH bands because we focus on tunneling along the [001] direction, along which direction the HH VB is electronically decoupled from the CB. As a result, there does not exist a pathway for direct BTBT from the HH VB to the CB (i.e. in the context of what follows below, there does not exist a complex band linking the HH VB and CB at Γ). Consequently, no direct BTBT can occur across the band gap for electrons starting out in the HH VB. Hence a 2-band $\mathbf{k}\cdot\mathbf{p}$ Hamiltonian, describing the dispersion of the lowest energy CB and the LH VB can provide the necessary input to calculate the BTBT generation rate.

2.2.1 Complex band structure (CBS)

As a precursor to discussing the theory of BTBT, it is essential to consider the CBS [88]. Summarising the above: in a crystal, the potential energy is periodic, and via Bloch's theorem we can assign each energy state $E_{n\mathbf{k}}$ to a real wave vector $\mathbf{k}$; which defines the electronic band structure of the crystal. However, at crystal surface, the periodicity is lost along the direction perpendicular to the surface. In this situation, the component of the wave vector perpendicular to the surface is no longer restricted to be real-valued. The CBS is the solution of the Schrödinger equation in the presence of a wave vector $\mathbf{k}$ possessing one or more complex-valued components. Assuming we have a wave vector whose x and y components are real, but whose z component is complex-valued, we can write $k_z = k_z + i\kappa$; such that the single-electron wave function becomes

$$\psi_{n\mathbf{k}}(\mathbf{r}) = e^{i(k_z + i\kappa)\mathbf{r}} u_{n\mathbf{k}}(\mathbf{r}) = e^{-\kappa\mathbf{r}} e^{ik_z\mathbf{r}} u_{n\mathbf{k}}(r) \ . \tag{2.24}$$

While describing the wave function of an electron in a real Bloch state, $\kappa = 0$ is zero, otherwise, non-zero κ will introduce an exponential decaying or growth factor to the wave function, and hence the wave function can not be normalised. But at the surface of the crystal, the assumption of periodicity fails, so we can have an imaginary component (κ) of wave vector, giving what is known as an evanescent Bloch state, and for each wave vector ($\mathbf{k}$), the corresponding real energy $E_{n\mathbf{k}}$ can be obtained. Often people use the empirical pseudopotential method and the tight-binding method for the calculation of the CBS. The states having complex-valued wave vector can have energies lying within the energy gap (which are forbidden for Bloch states having real wave vector).

We can also compute it in the energy gap of a semiconductor by diagonalising the Hamiltonian matrix [89] and getting for each energy in the band gap the corresponding imaginary wave vector κ. The complex wave vector, κ is responsible for the exponential decaying of the wave function of an electron. complex bands lying within the band gap provide a pathway for BTBT, and this can be

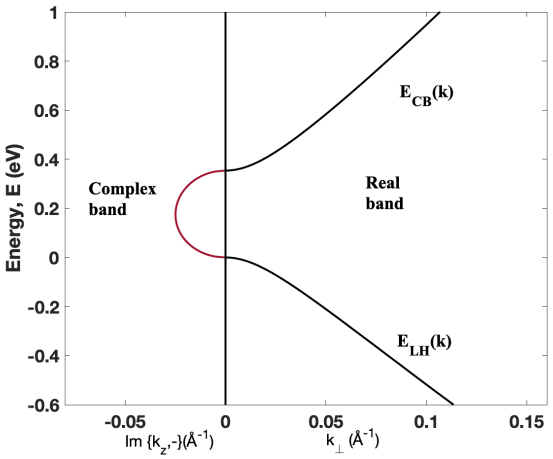

FIGURE 2.2: CBS obtained by diagonalising the Hamiltonian matrix (2.23) where complex band links the CB and LH at the zone centre. Further calculation details are given in Sec. 2.5.1.

understood qualitatively by considering the elementary quantum mechanical problem of tunneling through a potential energy barrier. Figure 2.2 shows an example CBS obtained by diagonalising the Hamiltonian matrix (2.23). Here, we see the presence of a complex band, having an imaginary wave vector, linking the LH VB to the CB and providing a pathway for direct BTBT. The use of this CBS as the basis to compute the BTBT generation rate G will be described in Sec. 2.5.1.

2.3 Introduction to tunneling

Tunneling [90] is a process where a particle having energy E can penetrate through a narrow-width, higher energy barrier, V_0 ($E < V_0$). But in classical physics, this mechanism is not allowed. That is why this barrier is known as the classically forbidden barrier. When an electron travels through such a barrier in a semiconductor, the associated tunneling current is known as leakage or dark current in a photodiode. In the case of semiconductor devices, when an electron tunnels through the potential barrier from the VB to the CB, the associated current is known as the BTBT current. As discussed in Sec. 2.2.1, a tunneling electron possesses a complex-valued wave vector having imaginary part κ. Both the magnitude of κ and the thickness of the barrier determine the transmission probability. The first device based on tunneling current was the tunneling diode, invented by Leo Esaki in 1957 [91] while studying the current-voltage properties of a heavily doped, narrow-width p-n diode. The I-V characteristic of the diode [92] is shown in Fig. 2.3. At zero voltage in Fig. 2.3(a) the Fermi level for both regions aligns with each other, and there is no net current flow at equilibrium condition. With the application of a forward-biased voltage, the Fermi-level for the n-region moves up in energy and makes free states available for the electrons of the n-region to tunnel directly into the p-region, as shown in Fig. 2.3(b). This tunneling of electrons creates a tunneling current. With the increase in applied voltage, the current increases up to a certain point; after that, it decreases. At a specific point, the current reaches its minimum value, where the Fermi-level aligns with the energy gap of the p-region, as shown in Fig. 2.3(c). This current decrease introduces what is referred to as a negative differential resistance (NDR).

After that, with a further increase in voltage, the current starts to increase again, as shown in Fig. 2.3(d) due to electrons diffusing over the barrier. Under reverse bias, the Fermi-level for the n-type region moves down in energy. Therefore, in the CB of the n-region free states are available for the electrons of the VB of the p-region to tunnel into and create the leakage current. This leakage or band-to-band tunneling current can decrease a photodiode's efficiency by reducing the signal to noise ratio.

The evolution of tunneling-based devices with different semiconductors has continued throughout the years. Tunneling has been investigated for a wide range of technologies, including the Esaki tunneling diode, resonant tunneling diodes (RTDs) [93], Zener tunneling [94], tunneling bipolar transistors [95], resonant hot electron transistors (RHETs) [96], solar cells [97] and many more. All these devices have applications in different domains: complementary metal-oxide-semiconductor [98], high-speed digital circuits [99], low power applications [100], and bio-sensing [101]. The NDR associated with some tunneling structures is of wide value for high-frequency applications [102]. A recent report [103] says a tunneling based memory selector is very fast, with low cyclic variation compared to conventional ones. In the early twenty-first century, tunneling field-effect transistors (TFETs) begun to attract attention as a route to produce subthreshold swing below the minimum $\sim$ 60 mV dec^{-1} limit in conventional metal-oxide-semiconductor field-effect transistors (MOSFETs). TFETs offer wide opportunities for applications including, bio-sensing [104], internet-of-things (IoT), gas-sensing [105], neuro-morphic [106] and low power [107] RF applications etc. Similarly, avalanche photodiodes (APDs) also contribute extensively to communication technology [108], 3-D imaging [109], space applications [110], etc. The performance of these widely used devices, mainly TFETs and photodiodes (PDs), depends directly on the characteristics of the tunneling current. The BTBT current drives the TFET operation at low voltage. BTBT current can have a negative impact on PDs, mainly in mid-infrared PDs; as for these devices, the band gap is very small, so the BTBT-enabled dark current can occur even under low reverse bias. Given the vast range of applications for these devices and the key role that BTBT plays in determining their performance, it is vital to investigate BTBT when engineering many semiconductor devices.

2.4 tunneling through a 1D barrier

We begin by considering the simple situation of tunneling through a 1D barrier [111] to examine the primary characteristics that contribute to the tunneling probability. First, we consider a rectangular barrier, for which we can determine the transmission coefficient analytically. We then generalise to a more complex barrier, for which we show that the analytical approach can be recast as a transfer matrix method, which becomes increasingly more complicated to solve as the complexity of the barrier increases. We therefore introduce the WKB method [112], which provides an approximate method to calculate the transmission coefficient. Calculations are undertaken to compare the results of the WKB and transfer matrix approaches, from which it can be seen that there are a wide range of problems for which the WKB method can provide a good estimate for the transmission coefficient.

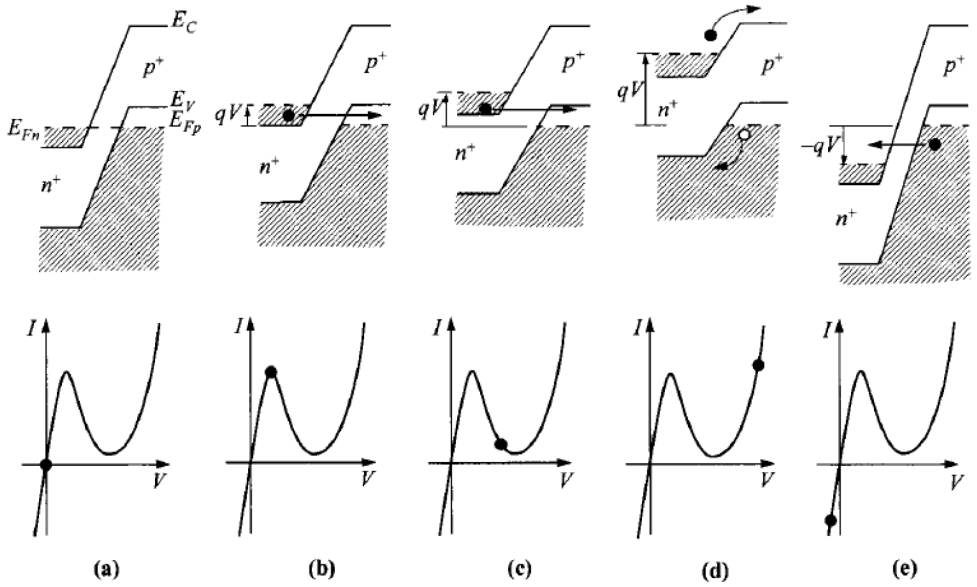

FIGURE 2.3: I-V characteristics for Esaki diode [92] (a) no net current flow at zero applied voltage (b) forward biased voltage with the peak current- due to tunneling of electrons (c) forward-biased voltage - minimum current obtained- due to non-availability of free states for tunneling into - creates NDR (d) at further forward-biased voltage, observation of diffusion current, and (e) at reverse-biased voltage, observation of tunneling current - due to tunneling of electrons from the VB of the p-type region to the CB of the n-type region.

2.4.1 Analytic method

Rectangular Barrier:

We outline here how to find the transmission coefficient [111] of the electron wave function for a 1D rectangular barrier as shown in Fig. 2.4. Because this is a two-boundary problem – with boundaries at $z = a$ and $z = b$ – we need to solve four equations, i.e. two for each boundary to obtain the transmission coefficient for a wave incident from one side onto the barrier.

When an electron with energy E tries to penetrate through the barrier ($V_0 > E$), the wave function of the electron within each of the three regions is given as follows.

In the region $z < a$, we can write

$$\psi(z) = A_+ e^{ikz} + A_- e^{-ikz}\,, \tag{2.25}$$

where A_+ and A_- are the incident and reflected coefficient of the wave function of the electron, and where

$$k = \sqrt{\frac{2mE}{\hbar^2}}\,. \tag{2.26}$$

For region $a < z < b$, E is less than V_0 and in this case, the wave vector k will be imaginary. Writing $k = i\kappa$ the wave function for $a < z < b$ can be written

$$\psi(z) = B_+ e^{\kappa z} + B_- e^{-\kappa z}\,, \tag{2.27}$$

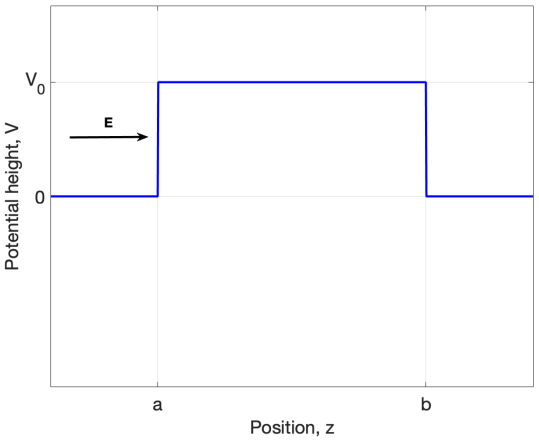

FIGURE 2.4: Rectangular barrier having potential height, V_0 and width $(b-a)$.

with

$$\kappa = \sqrt{\frac{2m\,(V_0 - E)}{\hbar^2}}\,. \tag{2.28}$$

Finally, for the region $z > b$, $\psi(z)$ is

$$\psi(z) = C_+ e^{ikz} + C_- e^{-ikz}\,, \tag{2.29}$$

where we will later set $C_- = 0$ because there is no reflected wave component in travelling in the direction of decreasing z for $z > b$.

If we apply the boundary conditions that the wave function and its derivative must be continuous at $z = a$ and $z = b$, then we can obtain four linear equations linking the coefficients: two linking the coefficients A_+ and A_- with B_+ and B_- at $z = a$ and two linking B_+ and B_- with C_+ and C_- at $z = b$. These boundary conditions can be written in matrix form as

$$\begin{bmatrix} A_+ \\ A_- \end{bmatrix} = \frac{1}{2}\begin{bmatrix} e^{-a(\kappa - ik)}\left(1 - \frac{i\kappa}{k}\right) & e^{a(\kappa+ik)}\left(1 + \frac{i\kappa}{k}\right) \\ e^{-a(\kappa+ik)}\left(1 + \frac{i\kappa}{k}\right) & e^{a(\kappa-ik)}\left(1 - \frac{i\kappa}{k}\right) \end{bmatrix}\begin{bmatrix} B_+ \\ B_- \end{bmatrix}\,, \tag{2.30}$$

$$\begin{bmatrix} B_+ \\ B_- \end{bmatrix} = \frac{1}{2}\begin{bmatrix} e^{b(\kappa - ik)}\left(1 + \frac{ik}{\kappa}\right) & e^{b(\kappa+ik)}\left(1 - \frac{ik}{\kappa}\right) \\ e^{-b(\kappa+ik)}\left(1 - \frac{ik}{\kappa}\right) & e^{-b(\kappa-ik)}\left(1 + \frac{ik}{\kappa}\right) \end{bmatrix}\begin{bmatrix} C_+ \\ C_- \end{bmatrix}\,. \tag{2.31}$$

Hence, from Eqs. (2.30) and (2.31), we can compute A_+, A_- as follows,

$$\begin{bmatrix} A_+ \\ A_- \end{bmatrix} = S\begin{bmatrix} C_+ \\ C_- \end{bmatrix}\,, \tag{2.32}$$

where S is given by

$$S = \begin{bmatrix} e^{-ik(a-b)}\left(\cosh\kappa\,(a-b) - i\frac{\epsilon}{2}\sinh\kappa\,(a-b)\right) & -i\frac{\alpha}{2}e^{-ik(a+b)}\sinh\kappa\,(a-b) \\ i\frac{\alpha}{2}e^{ik(a+b)}\sinh\kappa\,(a-b) & e^{ik(a-b)}\left(\cosh\kappa\,(a-b) + i\frac{\epsilon}{2}\sinh\kappa\,(a-b)\right) \end{bmatrix},$$

and $\epsilon = \frac{\kappa}{k} - \frac{k}{\kappa}$, $\alpha = \frac{\kappa}{k} + \frac{k}{\kappa}$.
We can also represent the coefficients C_+ and C_- in terms of coefficients A_+ and A_- as follows

$$\begin{bmatrix} C_+ \\ C_- \end{bmatrix} = M \begin{bmatrix} A_+ \\ A_- \end{bmatrix}, \tag{2.33}$$

where the matrix M, known as the transfer matrix, is given by

$$M = \begin{bmatrix} e^{-ik(b-a)}\left(\cosh\kappa\,(b-a) - i\frac{\epsilon}{2}\sinh\kappa\,(b-a)\right) & -i\frac{\alpha}{2}e^{-k(b+a)\sinh\kappa(b-a)} \\ i\frac{\alpha}{2}e^{-k(b+a)\sinh\kappa(b-a)} & e^{-ik(b-a)}\left(\cosh\kappa\,(b-a) - i\frac{\epsilon}{2}\sinh\kappa\,(b-a)\right) \end{bmatrix}.$$

In region 3, there is no reflection, so coefficient C_- is set to be zero. We can compute the transmission coefficient $T(E)$ – i.e. the probability that an electron having energy E tunnels through the barrier – as the ratio of the modulus squared of the coefficient C_+ and A_+ either from Eq. (2.32) or Eq. (2.33) as follows

$$T = \frac{|C_+|^2}{|A_+|^2} = \frac{1}{|S_{11}|^2} = \frac{det(M)}{M_{22}}, \tag{2.34}$$

where S_{11} and M_{22} correspond to the $(1,1)$ and $(2,2)$ element of matrix S (Eq. (2.32)) and M (Eq. (2.33)) respectively, $\det(M)$ denotes the determinant of matrix M.

The resulting expression for the transmission coefficient through a 1D rectangular barrier is obtained as

$$T = \frac{1}{\cosh^2\kappa(b-a) + \frac{\epsilon^2}{4}\sinh^2\kappa(b-a)}. \tag{2.35}$$

For the rectangular barrier having potential height, $V_0 = 0.05$ eV, and barrier width of 10 Å, we compute the transmission coefficient using Eq. (2.35) and plot it as a function of the electron energy E – expressed as a fraction of the barrier energy V_0 – in Fig. 2.5. As the electron energy increases, so does the transmission coefficient. However, even at greater electron energies, it is limited to less than one because there is a finite probability of reflection from the barrier. As a result, even when the ratio $(\frac{E}{V_0})$ of electron energy to barrier potential height equals one, the transmission coefficient remains < 1.

Asymmetrical Barrier:

We now take another example, the asymmetrical type of potential barrier depicted in Fig. 2.6. We can still calculate T analytically, i.e. by imposing the boundary conditions of continuity of the

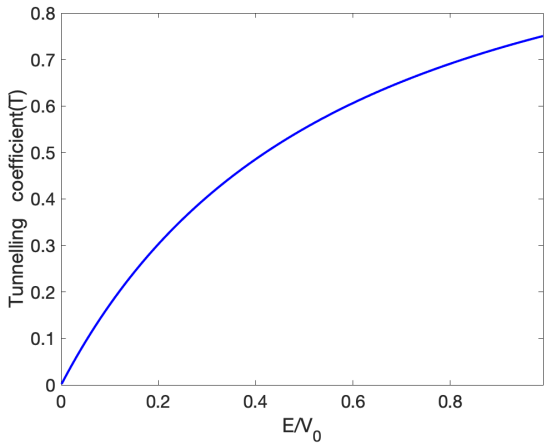

FIGURE 2.5: Transmission coefficient for rectangular barrier, potential height, $V_0 = 0.05$ eV, width = 10 Å.

wave function and its derivative at each of the three interfaces. However, in order to do so, we must solve six different equations, which is laborious. Suppose we have a barrier with even more number boundaries. The analytical approach will be significantly more complicated. In such cases, we can re-cast the problem as a matrix multiplication problem, referred to as the transfer matrix method, which we discuss in the following section.

2.4.2 Transfer matrix method (TMM)

As discussed above, we can obtain the transmission probability for the asymmetrical potential barrier as shown in Fig. 2.6 by the analytic method, directly solving six linear equations. Instead, the transfer matrix method [113, 114] provides a structured and readily implemented computational approach to determine T, extending the matrix approach introduced above for a single barrier. This method can be implemented for a piece-wise constant potential $V(z)$.

To demonstrate the TMM approach, we consider as an example an asymmetrical potential barrier as shown in Fig. 2.6. The coefficients of the electron wave function on the left and right side of the barrier are A_{as_+}, A_{as_-} and C_{as_+}, C_{as_-} respectively. In general, with the help of the transfer matrix, we can express the coefficients C_{as_+}, C_{as_-} in terms of A_{as_+}, A_{as_-}

$$\begin{bmatrix} C_{as_+} \\ C_{as_-} \end{bmatrix} = M_{as} \begin{bmatrix} A_{as_+} \\ A_{as_-} \end{bmatrix} , \tag{2.36}$$

where M_{as} is the transfer matrix.

This barrier can be divided into two rectangular barriers having amplitude V_0 and $\frac{V_0}{2}$ with width $c - a$ and $b - c$ respectively. Now, for the first region i.e. in interval a to c, we can define the transfer matrix $M1$ according to Eq. (2.36), given by

$$\begin{bmatrix} B_{as_+} \\ B_{as_-} \end{bmatrix} = M_1 \begin{bmatrix} A_{as_+} \\ A_{as_-} \end{bmatrix} , \tag{2.37}$$

where the coefficient B_{as_+}, B_{as_-} represent the output coefficient of the wave function of the electron for the 1^{st} segment within the interval $a \leq z \leq c$. The same coefficients are also input to the so-called second segment of the barrier having potential $\frac{V_0}{2}$ and width $b - c$.

So for the second segment of the barrier, we can have

$$\begin{bmatrix} C_{as_+} \\ C_{as_-} \end{bmatrix} = M_2 \begin{bmatrix} B_{as_+} \\ B_{as_-} \end{bmatrix} . \tag{2.38}$$

From Eq. (2.38) and (2.37), we can derive the following relation

$$\begin{bmatrix} C_{as_+} \\ C_{as_-} \end{bmatrix} = M_2 M_1 \begin{bmatrix} A_{as_+} \\ A_{as_-} \end{bmatrix} . \tag{2.39}$$

By comparing Eq. (2.39) with Eq. (2.36) , we get

$$M_{as} = M_2 M_1 . \tag{2.40}$$

The product of individual transfer matrices of the barrier from interval b to c and c to a defines the transfer matrix of the entire potential barrier for the full interval ranging from a to b. For a rectangular barrier having potential height V_0, and width $b-a$, the transfer matrix M is defined in Eq. (2.33). So, from Eq. (2.33), we can obtain these transfer matrices M_1 and M_2 for both segments of the barrier and can compute M_{as}. Now, from the transfer matrix M_{as}, we can compute the tunneling probability, T by using Eq. (2.35), as $T = \frac{det(M_{as})}{M_{as22}}$, where M_{as22} and $det(M_{as})$ represent the $(2, 2)$ element and determinant of the matrix M_{as} respectively.

In general, for any arbitrary barrier, we can find the tunneling probability through the barrier by dividing it into n different narrow segments, where each segment corresponds to a 1D rectangular potential problem having width w; where w tends to zero. We can compute numerically the transfer matrix M as $M_n M_{n-1} .... M_2 M_1$, where M_n represents the transfer matrix of the n^{th} segment of the full barrier and finally we apply Eq. (2.35) on the transfer matrix M to compute the tunneling probability.

We present the transmission coefficient obtained from both the methods, i.e. analytic and transfer matrix method, in Fig. 2.7. They perfectly match each other, reflecting that both are exact solutions of the same set of equations. So, we can directly implement the TMM approach and get an accurate result. However, for an arbitrary barrier, where the amplitude changes with position z, e.g. as shown in Fig. 2.8, the TMM approach might be very challenging. As amplitude changes, we need to divide the barrier into a large number of extremely narrow-width rectangular barriers. In doing so, the computational load can increase significantly, and the calculation can become unstable. In such a case, we can consider the WKB approximation/method to decrease the computation load, which we explore in the next segment. As the name suggests the solution for the tunneling barrier will not be an exact one but can be very close to the precise answer. We

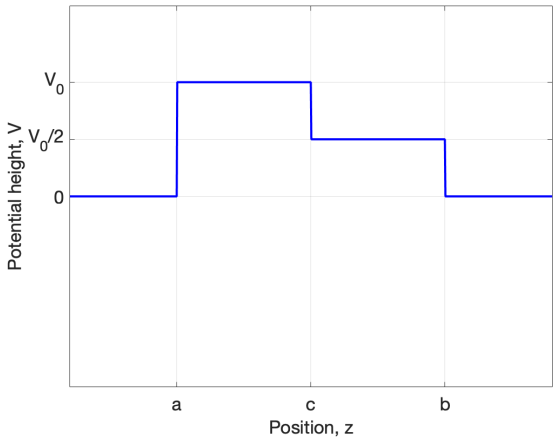

FIGURE 2.6: An asymmetrical barrier of energy V_0 and $\frac{V_0}{2}$ within the interval $a \leq z \leq c$ and $c \leq z \leq b$ respectively.

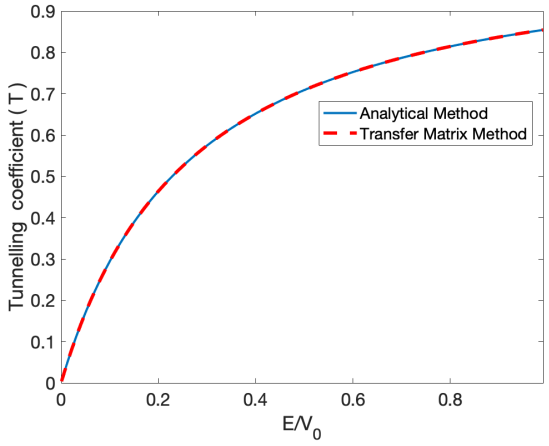

FIGURE 2.7: Transmission coefficient for asymmetrical barrier ($V_0 = 0.05$ eV, width = 10 Å).

will examine the method's accuracy for a rectangular barrier as a function both of barrier height and width.

2.4.3 WKB approximation

Here, we discuss the WKB [111] aproximation, developed by Wentzel, Kramers, and Brillouin, which provides an approximate solution for the Schrödinger equation. This method recognises that when the potential $V(z)$ is not constant but varies slowly with position z such that the local wavelength $\lambda(z)\frac{V^{'}(z)}{V(z)} \ll 1$ as shown in Fig. 2.8, then the analytical solution to the Schrödinger equation becomes very complicated. In such a scenario, an approximation is considered to find the solution to the equation. This approximation is known as the "WKB" approximation. Let us first consider the Schrödinger equation

$$\frac{\partial^2 \psi}{\partial z^2} + k^2(z)\,\psi = 0\,. \tag{2.41}$$

if $E > V(z)$,

$$k(z) = \sqrt{\frac{2m\,(E - V\,(z))}{\hbar^2}}\,, \tag{2.42}$$

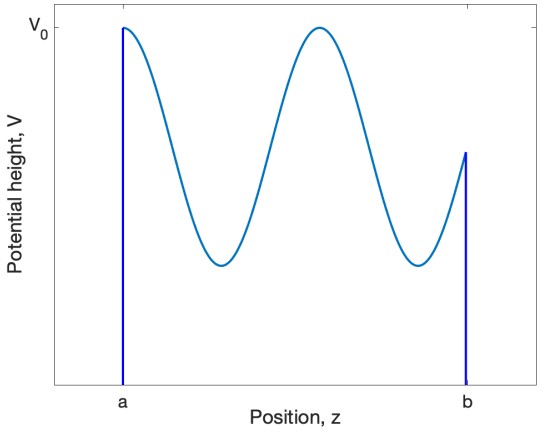

FIGURE 2.8: Arbitrary potential barrier having initial energy V_0.

if $E < V(z)$,

$$k(z) = i\sqrt{\frac{2m\left(V\left(z\right) - E\right)}{\hbar^2}} = i\kappa(z)\,. \tag{2.43}$$

We can express the solution to the wave function in exponential form as

$$\psi(z) = A(z)e^{i\phi(z)}\,, \tag{2.44}$$

where $\phi(z)$ is a real function. We can then calculate the first and second derivative of $\psi(z)$ as

$$\psi^{'}(z) = A^{'}e^{i\phi(z)} + iA\phi^{'}e^{i\phi(z)}\,, \tag{2.45}$$

$$\implies \psi^{''}(z) = A^{''}e^{i\phi(z)} + iA^{'}\phi^{'}e^{i\phi(z)} + iA^{'}\phi^{'}e^{i\phi(z)} + iA\phi^{''}e^{i\phi(z)} - A\phi^{'}\phi^{'}e^{i\phi(z)}\,. \tag{2.46}$$

When we substitute Eq. (2.46) into Eq. (2.41), we get

$$A^{''} + 2iA^{'}\phi^{'} + iA\phi^{''} - A\phi^{'}\phi^{'} + k^2(z)A = 0],\,, \tag{2.47}$$

separating the real and imaginary parts then gives

$$A^{''} = A(\phi^{'2} - k^2(z))\,. \tag{2.48}$$

Now, by taking the assumption that $A(z)$ varies slowly so that $A^{''}(z) \ll k(z)^2A(z)$

$$\phi^{'2} - k^2(z) = 0\,, \tag{2.49}$$

$$\implies \phi^{'}(z) = \pm k(z)\,, \tag{2.50}$$

$$\implies \phi(z) = \pm\int_0^z k(z)\,dz\,. \tag{2.51}$$

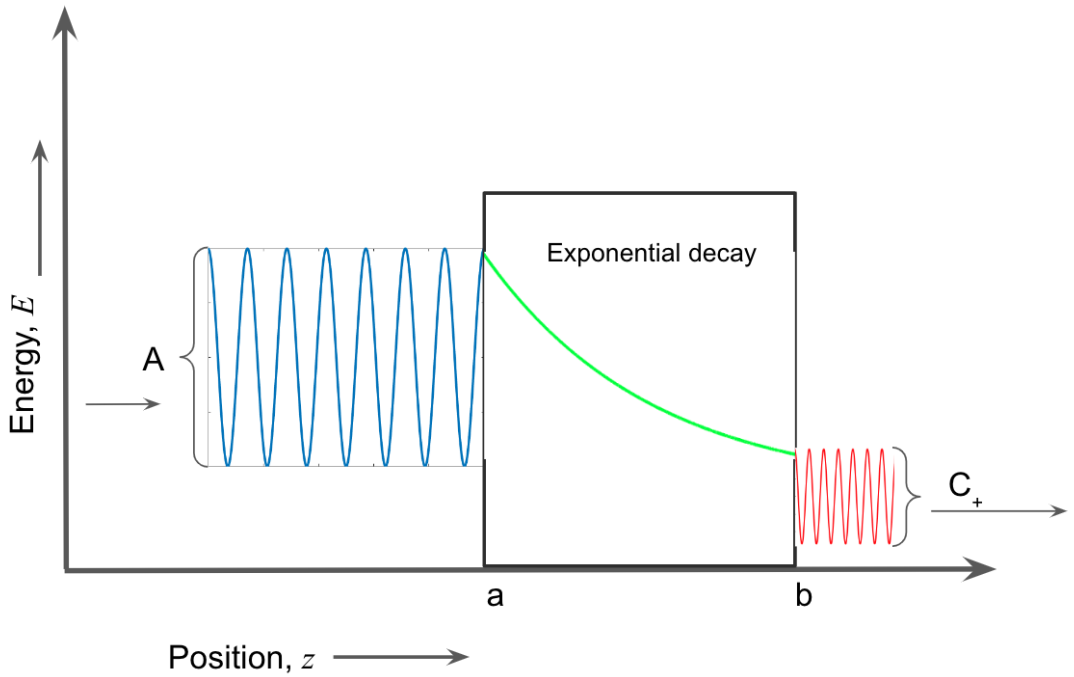

FIGURE 2.9: Wave function of a tunneling electron through a rectangular barrier with position, z.

Considering now the imaginary part of Eq. (2.47), we have

$$2A^{'}\phi^{'} + A\phi^{''} = 0 \implies \frac{\partial A^2\phi^{'}}{\partial z} = 0 \implies A = \frac{Const.}{\sqrt{\phi^{'}(z)}}\,. \tag{2.52}$$

In the forbidden region $k(z)$ is imaginary, so is replaced by $\kappa(z)$ and the wave function inside the forbidden region can be expressed as

$$\psi_2\,(z) = \frac{B_+}{\sqrt{\kappa(z)}}\exp^{\int_0^z \kappa(z)\,dz} + \frac{B_-}{\sqrt{\kappa(z)}}\exp^{-\int_0^z \kappa(z)\,dz}\,. \tag{2.53}$$

If we look at Fig. 2.9, it is not physically possible that the tunneling will increase exponentially for a high and/or wide barrier. Hence the coefficient B_+ is set to zero in Eq. (2.53). Now, the coefficient for the wave exiting the barrier at b can be approximated as

$$C_+ \approx A\exp\left(-\int_0^z \kappa(z)\,dz\right)\,, \tag{2.54}$$

from which, the probability of tunneling can be estimated as below.

$$T = \frac{|C_+|^2}{|A|^2}\,, \tag{2.55}$$

$$\implies T = \exp\left(-2\int_0^z \kappa(z)\,dz\right)\,. \tag{2.56}$$

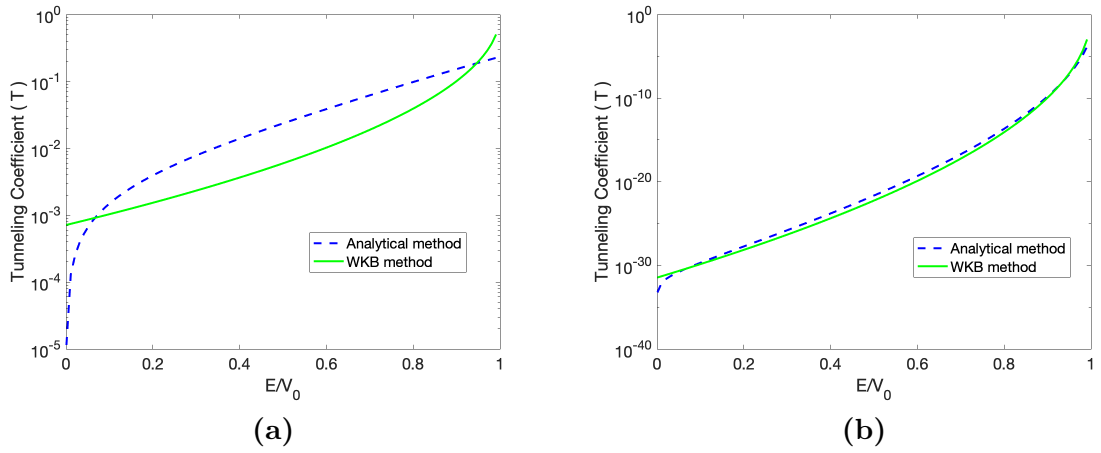

FIGURE 2.10: Transmission coefficient for rectangular barrier by analytic and WKB approximation, potential height, $V_0 = 0.5$ eV and width, w (a) 10 Å, and (b) 100 Å.

So, for a barrier defined between a and b, which are the start and end points of tunneling respectively, also known as classical turning points, the transmission probability using the WKB approximation, can be expressed as

$$T = \exp\left(-2\int_a^b \kappa(z)\,dz\right) = \exp\left(-2\int_a^b \mathrm{Im}\,(k_z)\;dz\right)\,. \tag{2.57}$$

In Fig. 2.10, we present the transmission coefficient for a rectangular barrier calculated using the analytic and WKB methods. Here we observe that, for a narrow-width barrier, the WKB approach is underestimating T compared to the analytic solution. But there is a much closer agreement between the WKB and exact solution for a wider width barrier. As the WKB tunneling approximation implicitly assumes a wide-width barrier, therefore, for a narrow-width barrier, it can give a poor approximation to the exact result. Nevertheless, it is a relatively easy, straightforward approach to calculating the transmission coefficient for any barrier. We want to study and compare the relative tunneling impact for both conventional semiconductor alloys and highly mismatched alloys so, in our analysis, we use the WKB method to find the transmission probability T. The next section discusses BTBT in a bulk semiconductor. To analyse BTBT, we first establish the InAs band structure before using the WKB approximation to calculate the transmission coefficient. We compare the results of these calculations to the well-known analytical model of Kane for the BTBT transmission coefficient and generation rate in a direct-gap semiconductor, demonstrating explicitly the close relationship between the two approaches.

2.5 BTBT generation rate in a bulk semiconductor

We outline in this section the different steps involved in the calculation of the BTBT generation rate (G) in a bulk semiconductor such as InAs. Given the CBS, there are several different approaches by which to compute the BTBT transmission coefficient and generation rate, including the semi-classical WKB approximation and quantum kinetic approaches based on non-equilibrium

Green's functions [115–117] or Wigner functions [118, 119]. Previous analysis has demonstrated that an appropriately parametrised **k·p** Hamiltonian employed in conjunction with the WKB approximation captures the key qualitative (and, for the most part, quantitative) physics of direct BTBT compared to full quantum kinetic calculations [112] while providing the benefits of theoretical simplicity and physical transparency.

2.5.1 Model Hamiltonian and CBS

Our description of the InAs band structure is based on the 2-band **k·p** Hamiltonian due to Kane [120, 121] which we have derived in Sec. 2.2. This describes the dispersion of the lowest energy CB and the LH VB in a direct-gap zinc-blende semiconductor as

$$H = \begin{pmatrix} E_g + \frac{\hbar^2}{2m_0}\left(k_\perp^2 + k_z^2\right) & P\sqrt{k_\perp^2 + k_z^2} \\ P\sqrt{k_\perp^2 + k_z^2} & \frac{\hbar^2}{2m_0}\left(k_\perp^2 + k_z^2\right) \end{pmatrix}, \tag{2.58}$$

where E_g is the zone-centre ($k = 0$) band gap, and P is the interband (Kane) momentum matrix element. While the band dispersion admitted by Eq. (2.58) is spherical – i.e. it depends only on the magnitude $k = \sqrt{k_\perp^2 + k_z^2}$ of the wave vector – in order to treat BTBT in the presence of an electric field applied along the [001] direction we have, for clarity, expressed the wave vector k in terms of its components parallel (k_z) and perpendicular ($k_\perp$) to [001].

The CB and LH dispersion is obtained by computing the roots of the characteristic equation associated with Eq. (2.58)

$$E_\pm(k) = \frac{E_g}{2} + \frac{\hbar^2 k^2}{2m_0} \pm \sqrt{\left(\frac{E_g}{2}\right)^2 + E_P\,\frac{\hbar^2 k^2}{2m_0}}\,, \tag{2.59}$$

where the $+$ and $-$ signs respectively describe the CB and LH dispersion, and $E_P = \frac{2m_0P^2}{\hbar^2}$ is the Kane parameter.

To obtain a description of the band structure suitable to compute the BTBT generation rate, it is critical that the CB and LH band edge effective masses $m_\pm^*$ are appropriately parametrised, so that the curvature of the complex band linking the VB and CB is accurately described. We therefore proceed by using Eq. (2.59) to compute the zone-centre CB and LH effective masses

$$\frac{m_\pm^*}{m_0} = \left|\frac{E_g}{E_g \pm E_P}\right|, \tag{2.60}$$

from which we note that the band edge effective masses are parametrisable via the choice of Kane parameter E_P. For InAs, we begin with the room temperature band gap $E_g = 0.354$ eV, [122] and adjust E_P to fit to the InAs CB edge effective mass $m_+^* = 0.026\,m_0$, [122] yielding $E_P = 13.261$ eV ($P = 7.108$ eV Å). Having determined the CB edge effective mass m_+^* in this manner, our choice of P then fixes the LH effective mass m_-^* (cf. Eq. (2.60)). In order to ascertain the suitability

of this approach, we have used the conventional 6-band Luttinger-Kohn **k·p** Hamiltonian [123] in conjunction with the spherical approximation [124] to estimate the LH DOS effective mass for comparison to our computed values of m^*_-. In the spherical approximation, the LH effective mass is given by $m^*_{\rm LH} = (\gamma_1 + 2\overline{\gamma})^{-1} m_0$, with $\overline{\gamma} = \frac{1}{5}(2\gamma_2 + 3\gamma_3)$, and where γ_1, γ_2 and γ_3 are the VB Luttinger parameters. [123] For InAs $\gamma_1 = 20.0$, $\gamma_2 = 8.5$ and $\gamma_3 = 9.3$, [122] giving $m^*_{\rm LH} = 0.0328\, m_0$, while for InSb $\gamma_1 = 34.8$, $\gamma_2 = 15.5$ and $\gamma_3 = 16.5$, [122] giving $m^*_{\rm LH} = 0.0149\, m_0$. We note that these values compare reasonably well with the values $m^*_- = 0.0274\, m_0$ and $0.0140\, m_0$ computed using Eq. (2.60) for InAs and InSb respectively – using the values of E_P fit to m^*_+ above – with Eq. (2.60) correctly describing that the LH band edge effective mass is greater than that associated with the CB edge (i.e. $m^*_- > m^*_+$).

To compute the CBS associated with Eq. (2.58) we re-cast the characteristic equation as a quartic equation in k_z, which can be solved analytically as a quadratic equation in k_z^2 to yield the E- and $k_\perp$-dependent dispersion

$$k^2_{z,\pm}(E, k_\perp) = \kappa^2_\pm(E) - k^2_\perp \,, \tag{2.61}$$

where the energy-dependent component $\kappa^2_\pm(E)$ is given by

$$\frac{\hbar^2 \kappa^2_\pm}{2m_0} = E + \frac{E_P - E_g}{2} \pm \sqrt{\left(E + \frac{E_P - E_g}{2}\right)^2 - (E - E_g)\, E} \,. \tag{2.62}$$

At fixed perpendicular wave vector $k_\perp$, the component $k_{z,\pm}$ of the wave vector parallel to the tunneling direction described by Eqs. (2.61) and (2.62) is purely real for $E \leq E_-(k_\perp)$ and $E \geq E_+(k_\perp)$, with $k_{z,-}$ reproducing the band dispersion of Eq. (2.59) in these energy ranges. For $E_-(k_\perp) < E < E_+(k_\perp)$ the band $k_{z,-}$ is purely imaginary. As such, $k_{z,-}(E, k_\perp)$ describes the evanescent Bloch band linking the VB and CB at energies $E_\pm(k_\perp)$. We note that $k_{z,+}(E, k_\perp)$ is a spurious solution of Eq. (2.58), describing unphysical states that possess large real wave vectors and lie energetically within the band gap [125].

2.5.2 BTBT transmission coefficient and generation rate

In this thesis we focus on the impact of perturbing the CBS on the BTBT generation rate in narrow-gap semiconductors and discuss its consequences for applications in APDs and TFETs. Direct (ballistic) BTBT proceeds without the absorption or emission of a phonon – i.e. when electrons near the VB maximum tunnels to the CB minimum without a change in in the real component of the wave vector **k** (Fig. 2.11(a)). For direct BTBT, the wave vector $k_\perp$, (k_x, k_y) in the plane perpendicular to the applied electric field is conserved, as illustrated schematically in Fig. 2.11(b), where the dashed line denotes the complex band linking the VB maximum and CB minimum. The band gap functions as a potential barrier through which the electron can tunnel.

2.5.2.1 WKB approximation

First, we use the WKB approximation of Eq. (2.57) to obtain the tunneling probability between the lowest conduction and highest valence state in a semiconductor in the presence of an applied electric field, **F**. In the expression (Eq. (2.57)), $\mathrm{Im}\{k_z(E)\}$ is a function of position z. If we assume constant electric field $F = |\mathbf{F}|$ directed along the tunneling direction z, the potential associated with which imparts the electron with energy $E = eFz$, where e is the electron charge. When the 2D wave vector $\mathbf{k}_\perp$ in the plane perpendicular to the tunneling direction is zero, i.e. $\mathbf{k}_\perp = 0$, then BTBT consists of the electron starting out a position z_i with energy $E = 0$ and tunneling to position z_f with energy equal to the band gap E_g, such that $z_f = \frac{E_g}{eF}$. Using these relations, we can re-express the WKB method of Eq. (2.57) as a function of energy E and the applied electric field F. We make the change of variables $z = E/eF$ and obtain the transmission coefficient between the lowest CB and highest VB for $\mathbf{k}_\perp = 0$, as follows

$$T(\mathbf{k}_\perp = 0) = \frac{\pi^2}{9} \exp\left(-\frac{2}{eF}\int_0^{E_g} \mathrm{Im}\{k_z(E)\}\,\mathrm{d}E\right), \tag{2.63}$$

where, for tunneling along [001], $\mathrm{Im}\{k_z(E)\}$ is the complex band linking the LH VB and CB at $\mathbf{k}_\perp = 0$. We introduce the pre-factor $\frac{\pi^2}{9}$ in Eq. (2.63), which is not present in Eq. (2.57). The origin of this prefactor is discussed in [90]. To compute the transmission coefficient $T(\mathbf{k}_\perp)$ at non-zero perpendicular wavevector $k_\perp$, (k_x, k_y), we modify the Eq. (2.63) by including the dependence of the real and imaginary bands on $\mathbf{k}_\perp$. The integrand follows from Eq. (2.62), while the limits on the integral are then determined by the (real) dispersion of the LH VB and CB. The resulting expression for the $\mathbf{k}_\perp$-dependent BTBT transmission coefficient $T(\mathbf{k}_\perp)$ is

$$T(\mathbf{k}_\perp) = \frac{\pi^2}{9} \exp\left(-\frac{2}{eF}\int_{E_{\mathrm{LH}}(k_\perp)}^{E_{\mathrm{CB}}(k_\perp)} |\mathrm{Im}\{k_{z,-}(E, k_\perp)\}|\,\mathrm{d}E\right). \tag{2.64}$$

Generally, the upward (downward) dispersion of the CB (LH VB) leads to an increase of the band gap at fixed $k_\perp = |\mathbf{k}_\perp|$, such that T reduces with increasing $\mathbf{k}_\perp$. We note that T does not depend explicitly on energy in the WKB approximation, unlike in more sophisticated quantum kinetic approaches. However, energy-averaged values of $T(\mathbf{k}_\perp)$ obtained from non-equilibrium Green's function calculations for bulk InAs have been demonstrated to be in good, quantitative agreement with Eq. (2.64), validating the application of the WKB approximation [112].

Given the BTBT transmission coefficient, the field-dependent BTBT generation rate (per unit volume) G is given by [126]

$$G(F) = \frac{eF}{2\pi^2\hbar}\int \frac{\mathrm{d}k_\perp}{(2\pi)^2}\, T(k_\perp)\,. \tag{2.65}$$

Recalling that the band structure admitted by Eq. (2.58) is spherical, we can write $\mathrm{d}\mathbf{k}_\perp = 2\pi k_\perp \mathrm{d}k_\perp$, so that computation of G requires numerical quadrature in only one dimension. The generation rate G is linked to the BTBT current density J via $eGV = JF$ [126, 127], where V is the applied

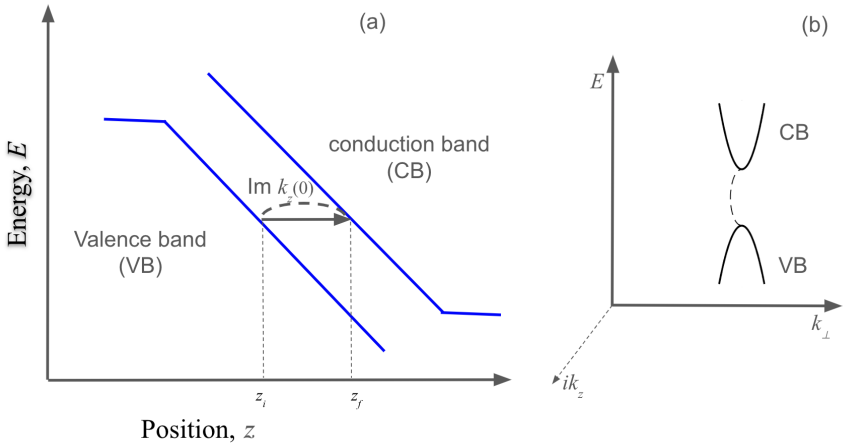

FIGURE 2.11: (a) Real-space schematic illustration of BTBT by an electron from the VB maximum to the CB minimum, in a semiconductor under the influence of an applied electric field, and (b) Reciprocal-space schematic illustration of the BTBT process of (a), in which the dashed lines denote the imaginary component of the wave vector describing the evanescent (complex) band linking the VB maximum and CB minimum. The evanescent band has the same real value of perpendicular wave vector $k_\perp$ as the states that it is linking, with the energy dependence of its imaginary component given by Eq. (2.62).

voltage generating the electric field F. Here, we focus solely on G as an intrinsic material property and simply note that defining a specific tunnel junction geometry and doping fixes the relationship between an applied voltage V and the resulting (local) electric field F, enabling the J-V relationship for the junction to be computed straightforwardly once G is known.

2.5.2.2 Kane model

In 1960, Evan O. Kane developed a model to find the tunneling probability of an electron from the VB to the CB in a uniform electric field F from a simple two-band Hamiltonian model as described in Eq. (2.66), known as the Kane model. In Kane's calculation, the field F acts as a perturbation that initiates the tunneling of electrons from the VB to the CB. We can see the link between Eqs. (2.64) and (2.65) and the widely employed Kane model for BTBT in a direct-gap semiconductor [90, 94]. Kane's use of a semi-classical wave function phase [128] in his analysis of BTBT, ensures that his approximate result for T (and hence G) is formally equivalent to Eqs. (2.64) and (2.65) [112]. Indeed, Kane's analytical result for T can be straightforwardly obtained from Eq. (2.64) via two simple approximations: (i) that only band states close to $k_\perp = 0$ contribute appreciably to BTBT, and (ii) that the dispersion of the CB and LH bands is purely parabolic[126]. The first of these approximations enables the integral of Eq. (2.64) to be computed analytically, while the second ensures that the growth of the energy gap between the CB and LH bands at fixed $k_\perp \neq 0$ can be described straightforwardly in terms of a reduced effective mass m_r^*. The resulting expression for the transmission coefficient is given by [126]

$$T(k_\perp) = \frac{\pi^2}{9} \exp\left(-\frac{\pi\sqrt{m_r^*}E_g^{\frac{3}{2}}}{2q\hbar F}\right) \exp\left(-\frac{\pi\hbar}{2qF}\sqrt{\frac{E_g}{m_r^*}}k_\perp^2\right), \tag{2.66}$$

where $(m_r^*)^{-1} = (m_+^*)^{-1} + (m_-^*)^{-1}$ is the reduced zone-centre effective mass of the CB ("+") and LH ("−") bands, given in the context of the 2-band Hamiltonian of Eq. (2.58) by $m_r^* = \frac{E_g}{2E_P} m_0$ (cf. Eq. (2.60)).

We note that Eq. (2.66) is comprised of a product of two exponential terms, which respectively describe field-dependent zone-centre ($k_\perp = 0$) and off-zone-centre ($k_\perp \neq 0$) contributions to direct BTBT. The physical interpretation of these terms is useful to recapitulate, as it describes features which apply generally to direct BTBT in narrow-gap semiconductors, and will therefore aid in our interpretation of the impact of BAC on BTBT in Sec. 3.4 below. The first of these terms, the zone-centre term, describes that T is a strong function of the $k_\perp = 0$ band gap E_g, increasing exponentially with decreasing E_g and with decreasing m_r^*. The second, off-zone-centre term describes that contributions to T from band states at $k_\perp \neq 0$ diminish rapidly with increasing $k_\perp$, due to the quadratic increase with $k_\perp$ of the energy gap between the (assumed parabolic) CB and LH bands, again encapsulated by the zone-centre band gap E_g and reduced effective mass m_r^*. We further note that the off-zone-centre term in Eq. (2.66) is $\propto -k_\perp^2 F^{-1}$, indicating that contributions to T from band states at larger perpendicular wave vector become more important not only in the presence of small zone centre band gap E_g and large reduced effective mass m_r^*, but also in the presence of high electric field strengths. As such, these two terms respectively encode the dependence of T, and hence G, on the band gap E_g and the CB and VB edge DOS.

In Kane's model, the integral of Eq. (2.65) can be computed analytically, yielding the BTBT generation rate [126]

$$G(F) = \frac{e^2 F^2}{18\pi\hbar^2} \sqrt{\frac{m_r^*}{E_g}} \exp\left(-\frac{\pi\sqrt{m_r^* E_g^{3/2}}}{2e\hbar F}\right), \tag{2.67}$$

which again displays exponential dependence on the zone centre band gap E_g and reduced effective mass m_r^*. In terms of nomenclature, we note that when we refer to the "Kane model" in the remainder of this thesis we are referring to the analytical treatment of the BTBT transmission coefficient and generation rate summarised by Eqs. (2.66) and (2.67), and not to the 2-band $\mathbf{k}\cdot\mathbf{p}$ Hamiltonian of Eq. (2.58).

2.6 Result and Discussion

In this section, we benchmark our numerical calculations of the BTBT coefficient T and generation rate G for InAs in the WKB approximation (Eqs. (2.64) and (2.65)) via comparison to the analytical Kane model (Eqs. (2.66) and (2.67)). The 2-band Hamiltonian matrix parameters for InAs, E_g, E_P and P are presented in Table. 2.1.

The results of these calculations are summarised in Fig. 2.12. Beginning with the CBS in Fig. 2.12(a), the left- and right-hand panels respectively show the complex band dispersion $\mathrm{Im}\{k_{z,-}(E,0)\}$ at perpendicular wave vector $k_\perp = 0$, and the real band dispersion in the $k_\perp$ plane. The dashed black line in Fig. 2.12(a) depicts the simplified CBS employed in the derivation of the Kane model, while

E_g (eV)	E_P (eV)	P(eV.Å)
0.354	13.261	7.108

TABLE 2.1: Parameters for the two-band Hamiltonian model for InAs.

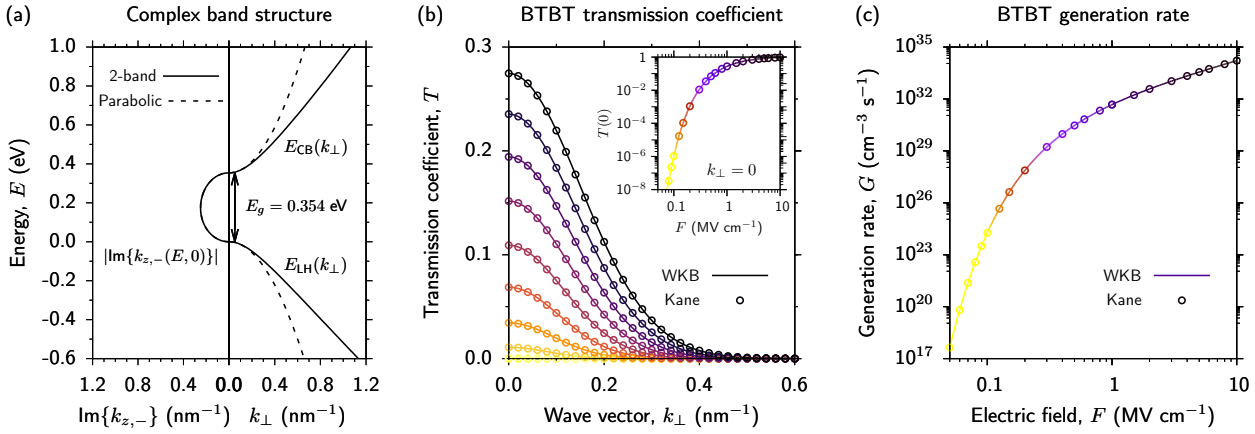

FIGURE 2.12: (a) CBS of InAs calculated using the 2-band **k**·**p** Hamiltonian of Eq. (2.58) (solid lines), and the simplified parabolic bands employed in the derivation of the Kane model of direct BTBT (dashed lines). (b) BTBT transmission coefficient T of InAs as a function of perpendicular wave vector $k_\perp$ calculated numerically using the 2-band complex dispersion of (a) in conjunction with the WKB approximation (solid lines), and using the analytical Kane model (open circles). Transmission coefficients are shown for applied electric fields F ranging from 0.1 MV cm^{-1} (yellow) to 1 MV cm^{-1} (black) in steps of 0.1 MV cm^{-1}. Inset: zone-centre ($k_\perp = 0$) transmission coefficient T as a function of applied electric field F, calculated numerically using the WKB approximation (solid line) and analytically using the Kane model (open circles). (c) BTBT generation rate G of InAs as a function of applied electric field F, calculated numerically using the WKB approximation (solid line) and analytically using the Kane model (open circles).

the solid black line shows the nonparabolic band structure described by the 2-band **k**·**p** Hamiltonian of Eq. (2.58) (cf. Eq. (2.62)). The simplified band structure employed in the derivation of the Kane model is assumed to be parabolic in $k_\perp$, with the CB and LH bands having respective effective masses m_+^* and m_-^* (cf. Eq. (2.60)). The assumption of parabolic CB and LH dispersion allows the $k_\perp$-dependent band gap to be described solely in terms of the reduced effective mass m_r^*. For consistency between our numerical WKB and analytical Kane model calculations we therefore set $m_r^* = \frac{E_g}{2E_P} m_0$ in Eqs. (2.66) and (2.67), using the same values of E_g and E_P for InAs employed in our 2-band **k**·**p** calculation of the CBS. This ensures that both the numerical and analytical calculations have equal band gap E_g and band edge (zone-centre) effective masses $m_\pm^*$. We note that the complex band dispersion assumed in the derivation of the Kane model is the same as that obtained by diagonalising Eq. (2.58) at $k_\perp = 0$ (cf. Eq. (2.62)). The key difference between the **k**·**p** band structure employed in our numerical WKB calculations and the simplified band structure employed in the derivation of the Kane model is then the nonparabolicity of the CB and VB in the former. Differences between the WKB and Kane model calculations of the BTBT transmission coefficient T and generation rate G are therefore expected to emerge only when band nonparabolicity is sufficiently pronounced to produce significant differences from the idealised parabolic band structure in the ranges of $k_\perp$ and E at which states contribute to BTBT. Given the narrow band gap and associated low band edge effective masses in InAs we expect the

impact of band nonparabolicity to be minimal. Hence, the results of our numerical WKB calculations should correspond closely to T and G computed using the Kane model. Figures 2.12(b) and 2.12(c) demonstrate that this is the case. Open circles in Fig. 2.12(b) show the analytical Kane model BTBT transmission coefficient T as a function of $k_\perp$ computed using Eq. (2.66), while solid lines show the corresponding numerical WKB calculations using Eq. (2.64). In Fig. 2.12(b) the colour denotes the strength F of the applied electric field, varying from 0.1 MV cm^{-1} (yellow) to 1 MV cm^{-1} (black) in steps of 0.1 MV cm^{-1}. The inset to Fig. 2.12(b) shows the dependence of T at $k_\perp = 0$ on the applied electric field, demonstrating that the transmission coefficient for zone-centre BTBT rapidly approaches unity for high fields $F \gtrsim 1$ MV cm^{-1}. We note excellent quantitative agreement between our numerical WKB calculations of T and the Kane model across the full ranges of $k_\perp$ and F considered.

Finally, Fig. 2.12(c) shows the numerical WKB-calculated BTBT generation rate G as a function of F (solid line) and the corresponding analytical Kane model calculation (open circles). The line colouring is as in Fig. 2.12(b). We again note excellent quantitative agreement between the two calculations. We also note that the calculated G continues to grow exponentially as F approaches 10 MV cm^{-1}. Recalling from the inset of Fig. 2.12(b) that the zone-centre transmission coefficient T saturates at high electric fields, we emphasise that the continued exponential growth of G at these high fields reflects that direct BTBT involving states at $k_\perp \neq 0$ constitutes an increasingly important contribution to G as F increases. As described in Sec. 2.5.2, this is driven by the strong growth of T away from $k_\perp = 0$ with increasing F (cf. Fig. 2.12(b) and Eq. (2.66)). Overall, these benchmark calculations indicate that band nonparabolicity plays a negligible role in influencing direct BTBT in InAs, while also verifying the validity of our numerical WKB calculations as a platform to investigate BTBT in highly mismatched alloys. Therefore all T and G calculations in Chapter. 3 are performed using the WKB approximation.

2.7 Conclusions

We presented here an overview of the theory of BTBT, which will be used in the next chapter to examine the BTBT current density in highly mismatched narrow-gap alloys. The use of different semi-classical models to calculate the tunneling coefficient is discussed and presented. Our objective is to calculate the BTBT transmission coefficient in such alloys, relevant to application in mid-infrared photodiodes and tunneling field-effect transistors. In this chapter, we showed how the WKB method gives results very similar to those obtained when using the 2−band Kane model to describe the band structure of a conventional semiconductor alloy. However, a 3−band Hamiltonian model is required for highly mismatched alloys such as InAsN and InBiAs. Hence, due to the change in band dispersion, the Kane model cannot be applied to such alloys. Therefore, we will use the WKB approach to examine the BTBT transmission coefficient for both conventional and highly mismatched semiconductor alloys as a function of external electric field and absorption wavelength. Because we are interested in quantifying direct BTBT, which is intrinsic to a given material, we do not consider a specific tunnel junction having defined dimensions. Rather, we instead compute

the BTBT generation rate $G = \frac{JF}{qV}$, which describes the rate at which carriers are generated in the CB, per unit volume, in an applied electric field of strength F.

Chapter 3

Impact of band anti-crossing on band to band tunneling current in highly mismatched dilute nitride and bismide alloys (InN_xAs_{1-x}, $InAs_{1-z}Bi_z$)

3.1 Introduction

Over the past two decades, highly-mismatched III-V semiconductor alloys containing nitrogen (N) and bismuth (Bi) have attracted significant research interest due to their unusual electronic properties. The impurity-like behaviour of substitutional N or Bi atoms in conventional III-V semiconductors strongly perturbs the electronic structure, providing significant opportunities for band structure engineering to obtain properties suitable for applications in a range of devices [34, 129]. Specifically, due to their large band gap reduction and modified band dispersion, near- and mid-infrared semiconductor lasers [3–10], as well as highly-efficient multi-junction solar cells [11–14] based on dilute nitride and bismide alloys have been proposed and demonstrated, while additional work has highlighted the potential of Highly mismatched alloys (HMAs) for applications in long-wavelength photodetectors [18] and avalanche photodiodes (APDs) [19], in intermediate-band solar cells [15, 16] and in tunable low-frequency plasmonics [17].

Here, we address an as yet unexplored aspect of the electronic properties of dilute nitride and bismide alloys: the complex band structure and its consequences for band to band tunneling (BTBT). Dependent on the specific device application of interest, BTBT can be either a desirable enabling property or a deleterious loss mechanism. For example, BTBT is the physical mechanism enabling the operation of tunneling field-effect transistors (TFETs) [25, 44–46], making enhancement of the BTBT generation rate at fixed band gap and applied electric field desirable for the realisation of high on-state current to enable high-speed operation. However, BTBT can contribute significantly

to leakage currents in long-wavelength APDs [41–43], making suppression of the BTBT generation rate desirable for the realisation of detectors displaying a high signal-to-noise ratio [47, 48]. Given the broad scope for applications of TFETs as an enabling platform for post-complementary metal-oxide semiconductor electronics, and of APDs for sensing at application-rich near- and mid-infrared wavelengths, it is of both fundamental and practical interest to investigate novel approaches to engineer BTBT in semiconductors.

Since BTBT is maximised in narrow-gap materials we focus on InN_xAs_{1-x} and $InAs_{1-z}Bi_z$ alloys, due to strong BTBT in the direct-gap host matrix semiconductor InAs. It is well established that the main features of the band structure of dilute nitride and bismide alloys can be described via the band-anticrossing (BAC) model [130–132] in which the extended Bloch states of the host matrix semiconductor – the conduction band (CB) edge in dilute nitrides [130, 133, 134], and the valence band (VB) edge in dilute bismides [135–137] – interact with and repel in energy the dispersionless localised impurity level associated with an isovalent substitutional N or Bi impurity.

Conventional analysis of direct ($\Delta\mathbf{k} = 0$) BTBT based on, e.g., the analytical Kane model [90, 94] and several popular modifications thereof [112, 116] implicitly assume parabolic CB and VB edge dispersion. Such models are therefore ill-suited to analyse BTBT in HMAs. As such, to allow explicit treatment of the strongly perturbed complex band structure, our analysis employs numerical calculation of the BTBT transmission coefficient and generation rate. To achieve this, we begin with model $\mathbf{k}\cdot\mathbf{p}$ Hamiltonians which include N- or Bi-related BAC interactions and which are parametrised directly via atomistic alloy supercell electronic structure calculations. We calculate analytically the complex band structure admitted by these model Hamiltonians, with these perturbed complex band structures then used to compute the BTBT transmission coefficient, and hence BTBT generation rate, numerically in the Wentzel-Kramers-Brillouin (WKB) approximation. To quantify the impact of N- or Bi- related BAC we compare the results of our calculations for highly-mismatched InN_xAs_{1-x} and $InAs_{1-z}Bi_z$ to equivalent calculations for the conventional III-V alloy $InAs_{1-y}Sb_y$.

In the semi-classical WKB approximation the BTBT transmission coefficient is a strong (exponential) function of the area bounded by the evanescent Bloch band linking the CB and VB in the plane defined by a carrier's energy and the imaginary part of its complex wave vector component along the tunneling direction. This area, and hence the BTBT transmission coefficient and generation rate, depends critically on the band gap and the CB and VB edge effective masses, which respectively determine the extent of this complex band in energy and in wave vector. The strong modification of these properties in response to N or Bi incorporation suggests significant implications for BTBT – where a reduction (increase) in band gap (band edge effective mass) is expected to strongly increase (decrease) the generation rate – and hence the potential to engineer BTBT for targeted device applications. Our analysis identifies that BAC-induced modification of the CB structure (in InN_xAs_{1-x}) or VB structure (in $InAs_{1-z}Bi_z$) impacts the BTBT generation rate. We

demonstrate that, at fixed band gap, this impact is manifested via a field-dependent competition originating in the increased band edge effective mass: at low applied electric field $F \lesssim 1$ MV cm^{-1} the increase in effective mass increases the area bounded by the complex band, reducing the generation rate, while at high applied electric field $F \gtrsim 1$ MV cm^{-1} the increased density of states (DOS) makes more states available to contribute to BTBT in a given energy range, increasing the generation rate. As such, in InN_xAs_{1-x} and $InAs_{1-z}Bi_z$ we find that BAC leads to reduced BTBT generation rate at a low applied electric field compared to that in a conventional $InAs_{1-y}Sb_y$ alloy having the same band gap, due to the increase in band edge effective mass. Conversely, at a high applied electric field, we find that BAC leads to an increased BTBT generation rate, due to contributions to BTBT from states having larger wave vectors in the plane perpendicular to the tunneling direction. Repeating this analysis as a function of the alloy band gap, we find that the relative BTBT generation rate in InN_xAs_{1-x} ($InAs_{1-z}Bi_z$) can be reduced by up to $\approx 20\%$ ($\approx 50\%$) compared to that in $InAs_{1-y}Sb_y$ at low applied field, while at high applied field it exceeds that in $InAs_{1-y}Sb_y$ by an amount dependent on the BAC-induced increase in the DOS close in energy to the N- or Bi-related localised impurity state in InN_xAs_{1-x} or $InAs_{1-z}Bi_z$ respectively. On this basis, we comment on the implications of our results for applications of narrow-gap HMAs in TFETs and in long-wavelength APDs.

3.2 Highly mismatched alloys and their electronic band structure

HMAs are those alloys, where the constituent element forming the alloy has significantly different physical and chemical properties from the host compound. For example, when a small amount x (z) of N (Bi) replaces arsenic (As) atoms to form InN_xAs_{1-x} and $InAs_{1-z}Bi_z$ alloys respectively, these N (Bi) atoms are significantly smaller (larger) and more electronegative (electropositive) than the As atoms. Therefore N (Bi) atoms act as an isovalent impurity resulting in a strong perturbation in the electronic band structure of the host material (InAs), mainly the CB (VB). As the concentration of N (Bi) increases, the material properties also change rapidly. Different experimental and theoretical investigations [129] for GaN_xAs_{1-x} and related alloys find that: (i) with increasing alloy composition, the magnitude of band gap (E_g) decreases rapidly, (ii) a large, composition-dependent bandgap bowing is observed, as well as (iii) large and strongly composition-dependent CB effective masses, (iv) significantly reduced pressure deformation potentials, and (v) a progression of sharp impurity lines in spectroscopic measurements, lying energetically within the band gap of the host matrix (GaAs or GaP). Based on atomistic tight-binding calculations [33] for these III-V alloys, the energy of the N-related impurity states (E_N) relative to the VB maximum energy, are 2.306, 1.706, and 1.386 eV for GaP, GaAs, and InAs respectively. By replacing a small fraction of the As atoms by N, the band gap in GaAs can be lowered by up to 150 meV [129] per percent N. When substituted for As in InAs, N produces a resonant impurity state lying ≈ 1 eV above the CB minimum, which couples to the extended (Bloch) CB edge state via a BAC interaction, driving a N composition-dependent band gap reduction in InN_xAs_{1-x} that is significantly weaker than in GaN_xAs_{1-x}. A reduced band gap of 0.12 eV at 6.1% N composition

was reported by Nai et al. [138]. This translates to a band gap decrease of 240 meV vs. pure InAs, or ≈ 39 meV per percent N. Photoluminescence measurements performed on InN_xAs_{1-x}/InGaAsP quantum wells [139] demonstrate a redshift of the emission peak with increasing N composition. At a temperature of 10 K, the photoluminescence peak energy is reduced by ≈ 31 meV with every 1% increase in N composition. When 1% of the As atoms are replaced with N, photoluminescence measurements on InN_xAs_{1-x} alloys grown via molecular beam epitaxy alloys [140] show a 29.6 meV reduction in band gap, again confirming the presence of a N-induced band gap reduction.
Similarly the substitution of a small fraction of Bi atoms for As in III-As group semiconductor alloys also results in strong composition-dependent band gap bowing. According to different studies (Ref. [34] and the references there in), in the case of $GaAs_{1-z}Bi_z$, (i) the band gap reduction is associated with a strong increase of the spin-orbit-splitting energy (Δ_{SO}) with increasing Bi composition, and (ii) the inclusion of higher Bi compositions ($z > 10\%$) in GaAs can lead to a band structure where the spin-orbit-splitting energy is greater than the band gap.
In the case of conventional semiconductor alloys, for example, $GaAs_{1-y}Sb_y$ or $InAs_{1-y}Sb_y$, where Sb atoms replace As atoms, with the increase in Sb composition, the material properties vary more smoothly. Here the Sb atom does not act as an impurity to the host compound. Hence for these conventional alloys, one can use the virtual crystal approximation (VCA) to study the material properties. But VCA fails due to the drastic change in properties in III-V nitride and bismide alloys. The theoretical modeling of these HMAs is quite complicated, due to their unique properties. Different atomistic models such as density functional theory (DFT) and empirical pseudo potential methods are able to demonstrate this band structure, but at the same time they are quite complex and computationally expensive. Shan et al. [130–132] introduced the idea of a simplest two-band model known as the BAC model which describes how the extended Bloch states of the InAs host matrix undergo a strong anticrossing interaction with localized N-impurity related states that are resonant with the (In)GaAs CB. One can obtain the CB structure by diagonalizing this BAC Hamiltonian matrix [130–132]. Using a similar approach, the VB structure of bismide alloys can also be found [34].

3.2.1 Band structure: BAC model

The main features of the band structure of dilute nitride and bismide alloys can be described via the BAC model [130–132], in which the extended Bloch states of the host matrix semiconductor – the CB edge in dilute nitrides [130, 133, 134], and the VB edge in dilute bismides [135–137] – interact with and repel in energy the dispersionless localised impurity level associated with an isovalent substitutional N or Bi impurity. In this manner, the BAC model describes (i) the strong reduction and composition-dependent bowing of the band gap due to N or Bi incorporation, and (ii) the increase in CB (VB) edge effective mass due to hybridisation of an extended band-edge state with a N- (Bi-) related localised impurity state [33, 133, 141] When we substitute a fraction of x (z) amount of As atoms by N (Bi) atoms, with As to form InN_xAs_{1-x} ($InAs_{1-z}Bi_z$), the resulting BAC Hamiltonian matrix is given by Eq. (3.1) and (3.2) respectively.

$$H_{\mathrm{N}}(x) = \begin{pmatrix} E_{\mathrm{N}} & \beta\sqrt{x} \\ \beta\sqrt{x} & E_{\mathrm{CB}}(k) \end{pmatrix}, \tag{3.1}$$

$$H_{\mathrm{Bi}}(z) = \begin{pmatrix} E_{\mathrm{VB}}(k) & \beta\sqrt{z} \\ \beta\sqrt{z} & E_{Bi} \end{pmatrix}, \tag{3.2}$$

where $E_{\mathrm{CB}}(k) = E_{\mathrm{CB}}(0) + \frac{\hbar^2 k^2}{2m_{\mathrm{CB}}}$, and $E_{\mathrm{VB}}(k) = E_{\mathrm{VB}}(0) - \frac{\hbar^2 k^2}{2m_{\mathrm{VB}}}$ describe the dispersion of the CB and VB of unperturbed InAs respectively. $E_{\mathrm{CB}}(0)$, $E_{\mathrm{VB}}(0)$, m_{CB} and m_{VB} are the CB, VB edge energy and electron effective mass of CB (VB) of the (unperturbed) InAs host matrix respectively, and E_N and E_{Bi} are the energy of the N (Bi)-related localized states. β is the BAC coupling parameter, which describes the strength $\beta\sqrt{x}$ ($\beta\sqrt{z}$) of the repulsive interaction between the E_{CB} (E_{VB}) and E_{N} (E_{Bi}) states, with the composition x (z). The CB structure for a dilute nitride alloy can then be obtained by diagonalizing the Hamiltonian matrix Eq. (3.1), the energy ($E_{c_\pm}(k)$) versus k relation is given by

$$E_{c_\pm}(k) = \frac{E_{\mathrm{N}} + E_{\mathrm{CB}}(k)}{2} \pm \sqrt{\left(\frac{E_{\mathrm{N}} - E_{\mathrm{CB}}(k)}{2}\right)^2 + \beta^2 x}\,. \tag{3.3}$$

Similarly, for dilute bismide alloys, the eigenenergy values for the VB, are given by

$$E_{v_\pm}(k) = \frac{E_{\mathrm{Bi}} + E_{\mathrm{VB}}(k)}{2} \pm \sqrt{\left(\frac{E_{\mathrm{Bi}} - E_{\mathrm{VB}}(k)}{2}\right)^2 + \beta^2 z}\,. \tag{3.4}$$

The N- and Bi-related parameters of Eqs. (3.1) and (3.2) have most often been estimated by fitting to experimental band gap data [130, 135, 142, 143]. However, this procedure is undesirable in general, because it typically relies on fitting two (or more) parameters to a single piece of experimental data (the band gap at a given N or Bi composition x (z)), requiring assumptions to be applied regarding unconstrained parameters and thereby introducing systematic uncertainty. To avoid this, our group have previously developed an approach to directly compute all of the N- and Bi-related parameters of Eqs. (3.1) and (3.2) via atomistic alloy supercell electronic structure calculations. Specifically, using the tight-binding method, we have explicitly constructed the localised states associated with an isolated substitutional N or Bi impurity in a series of ordered $2M$-atom $\mathrm{In}_M\mathrm{As}_{M-1}(\mathrm{N,\ Bi})_1$ ($x = M^{-1}$) alloy supercells, which are then used in conjunction with the $\mathrm{In}_M\mathrm{As}_{M-1}(\mathrm{N,\ Bi})_1$ alloy and $\mathrm{In}_M\mathrm{As}_M$ host matrix eigenstates to explicitly evaluate the associated BAC and virtual crystal matrix elements [33, 133, 134, 137, 144–147]. This removes the requirement to perform post hoc fitting to alloy experimental data, producing parameter sets that we have generally found to produce an excellent quantitative agreement with experiment. The N- and Bi-related parameters computed in this manner are listed in Table. 3.1. We note that the N and Bi localised state energies E_{N} and E_{Bi} are given relative to the InAs host matrix VB edge – which we maintain as our zero of energy throughout – so that, e.g., the N-related impurity level in InAs lies 1.032 eV ($= E_{\mathrm{N}} - E_g$) above the CB edge in energy.

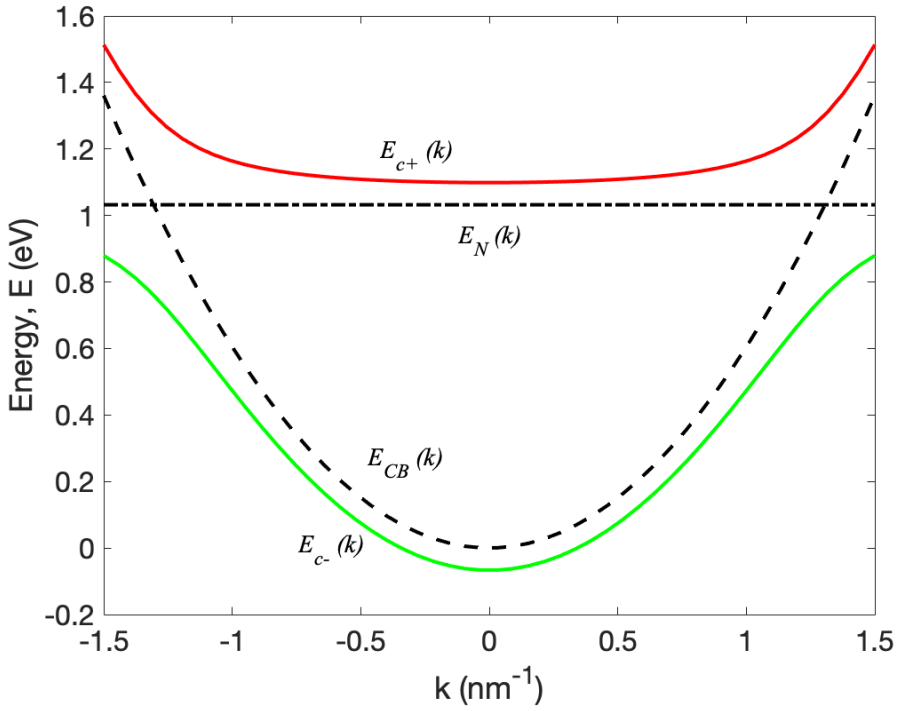

FIGURE 3.1: Conduction band structure of $InN_{0.05}As_{0.95}$ due to inclusion of N atoms ($x = 5\%$), computed using the BAC model (Eq. (3.3)). The BAC model describes that the InAs host matrix CB (dashed line) goes through a N composition-dependent anticrossing interaction with localized N-impurity related resonant states at energy E_N (dashed - dotted line), splitting the CB into two bands $E_{\pm}$(k)(solid lines). The zero of energy is taken at the InAs CB edge.

Parameter	InN_xAs_{1-x}	$InAs_{1-z}Bi_z$
E_N	1.386^a	—
E_{Bi}	—	-0.217^d
β	1.212^a	0.920^d
α	1.550^b	2.603^d
γ	0.000^c	1.027^d

TABLE 3.1: Parameters for the 3-band BAC Hamiltonians of InN_xAs_{1-x} and $InAs_{1-z}Bi_z$, Eqs. (3.1) and (3.2), including the N- and Bi-related resonant impurity state energies E_N and E_{Bi}, the BAC coupling strength β, and the CB and VB edge energy virtual crystal shifts α and γ (Eqs. (3.6) and (3.7)). E_N and E_{Bi} are given relative to the zero of energy at the InAs VB maximum. All parameters are listed in units of eV. (^{a}Ref. [33] ^{b}Ref. [148] ^{c}Ref. [149] ^{d}Ref. [150])

Using the N-related parameters of Table. 3.1, we have calculated the composition-dependent InN_xAs_{1-x} and $InAs_{1-z}Bi_z$ alloy band gaps $E_g(x)$ ($E_g(z)$) at $k = 0$, shown in Figs. 3.3(b) and 3.3(c) using solid green and red lines, respectively. Here, our calculations describe that N (Bi) incorporation in InAs produces a band gap reduction of approximately 29 (69) meV per % N (Bi) replacing As. Open green circles in Fig. 3.3(b) show the InN_xAs_{1-x} band gap determined via room temperature photoluminescence measurements [140], with which our calculations are in good, quantitative agreement. Open red circles in Fig. 3.3(c) show the $InAs_{1-z}Bi_z$ band gap determined via room temperature optical absorption measurements [151]. While our predicted band gap in Fig. 3.3(c) underestimates the measured band gap, we note that extrapolating the experimental data back to $y = 0$ produces an InAs band gap which is significantly in excess of that expected at room

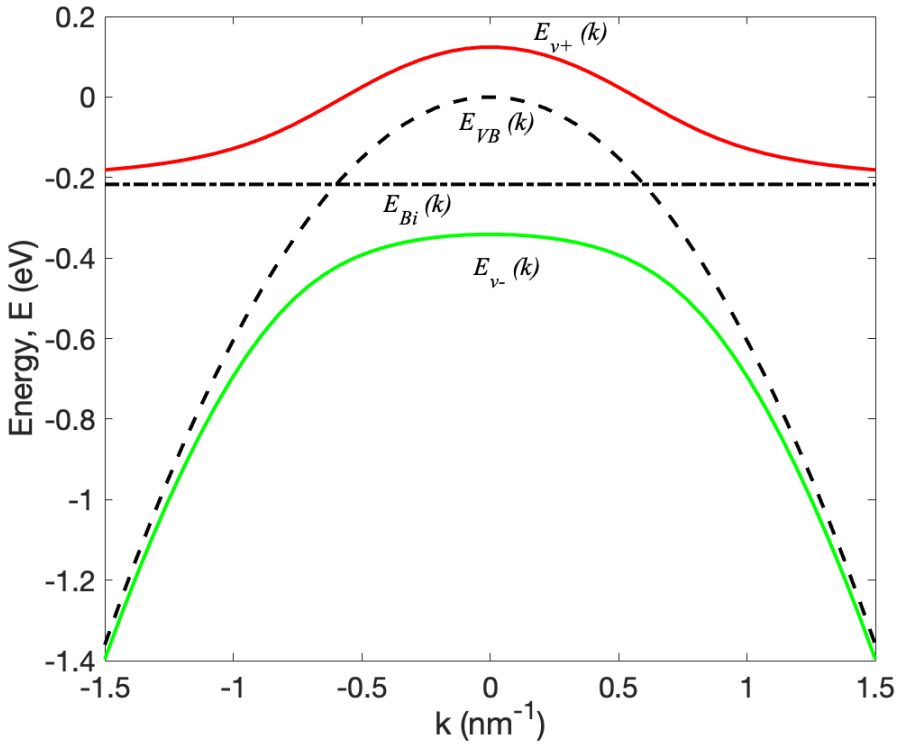

FIGURE 3.2: Valence band structure of $InBi_{0.05}As_{0.95}$ due to inclusion of Bi atoms ($x = 5\%$), computed using the BAC model (Eq. (3.4)). The BAC model describes that the InAs host matrix VB (dashed line) goes through a Bi composition-dependent anticrossing interaction with localized Bi-impurity related resonant states at energy E_{Bi} (dashed-dotted line), splitting the VB into two bands $E_{\pm}$(k)(solid lines). The zero of energy is taken at the InAs VB edge.

temperature (cf. open blue circle at $y = 0$ in Fig. 3.3(a)) [122]. We note that these measured $InAs_{0.9915}Bi_{0.0085}$ band gaps were obtained not by the conventional approach of exploiting the known energy dependence of the optical absorption edge in a direct-gap semiconductor, but rather as the energy at which the absorption reached a chosen fixed value (= 1000 cm^{-1}) [151]. This approach does not account for the strong, Bi composition-dependent spectral broadening observed in experiment, potentially introducing systematic uncertainty into the extraction of E_g. We emphasise that our parametrisation of Eq. (3.2) accurately describes the measured rate at which the $InAs_{1-z}Bi_z$ band gap reduces with increasing Bi composition z.

3.3 Theoretical model

We are interested in analysing the impact of BAC on BTBT due to modification of the complex band structure. It is simplest to employ a combined **k**·**p** and WKB approach to do so. While the WKB approximation has known quantitative shortcomings – e.g. underestimation of the low-field generation rate for larger band gaps [112] – we focus on the relative impact of BAC on BTBT by comparing results for highly-mismatched InN_xAs_{1-x} and $InAs_{1-z}Bi_z$ to those for conventional $InAs_{1-y}Sb_y$ alloys having equal band gap. In this manner, our analysis provides detailed insight into the impact of BAC on BTBT, with the implications for BTBT identified via this comparative

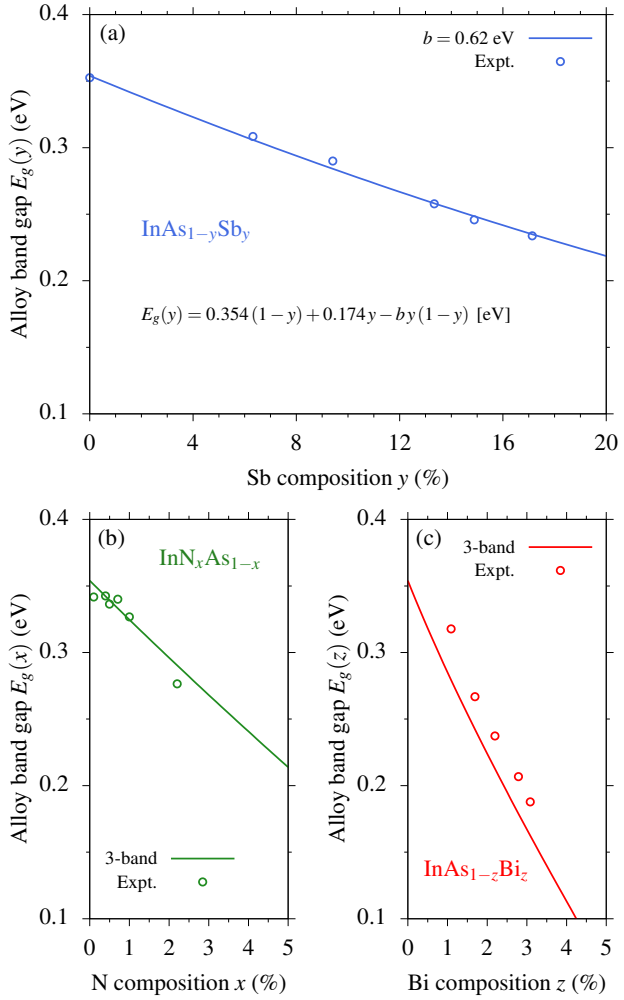

FIGURE 3.3: Calculated composition-dependent band gaps of (a) $InAs_{1-y}Sb_y$ (solid blue line), (b) InN_xAs_{1-x} (solid green line), and (c) $InAs_{1-z}Bi_z$ (solid red line). Open blue and green circles in (a) and (b) respectively denote the room temperature photoluminescence measurements of Refs. [152] and [140]. Open red circles in (c) denote the room temperature optical absorption measurements of Ref. [151].

analysis expected to hold in more sophisticated formalisms. We therefore began with a 2-band (Kane) **k·p** Hamiltonian for the band structure of InAs in Chapter. 2. The goal of the chapter was to provide a simple theoretical model to find the BTBT generation rate (G) which involved three main steps (i) To find the complex band structure (CBS) from the Hamiltonian matrix analytically (ii) then the numeric WKB analysis using the CBS to compute the transmission coefficient (T) and (iii) finally numerical evaluation of G from T. In that chapter, we also presented that the numerical WKB calculations produce results indistinguishable from the conventional Kane BTBT model. Having given a full description of how to calculate the BTBT generation rate from the Hamiltonian matrix in Chapter. 2, we now focus on the Hamiltonian matrix and the corresponding CBS for dilute nitride and bismide alloys InN_xAs_{1-x} and $InAs_{1-z}Bi_z$, for each of which the 2-band (Kane) **k·p** Hamiltonian is modified to an appropriate 3-band BAC Hamiltonian. This allows for the analytical calculation of the CBS associated with the BAC model. For $InAs_{1-y}Sb_y$ alloys, we retain the 2-band (Kane) model and obtain the interband momentum matrix element P via linear interpolation of the values determined for InAs and InSb.

3.3.1 Model Hamiltonians and complex band structure

As $InAs_{1-y}Sb_y$ is a conventional alloy, the Hamiltonian matrix describing its band structure is the same as that for InAs in Chapter. 2. The only difference is that here the band gap (E_g) and the interband (Kane) momentum matrix element P are functions of Sb composition y. The 2-band **k·p** Hamiltonian matrix due to Kane describes the dispersion of the lowest energy CB and the light-hole (LH) VB

$$H(y) = \begin{pmatrix} E_g(y) + \frac{\hbar^2}{2m_0}\left(k_\perp^2 + k_z^2\right) & P(y)\sqrt{k_\perp^2 + k_z^2} \\ P(y)\sqrt{k_\perp^2 + k_z^2} & \frac{\hbar^2\left(k_\perp^2 + k_z^2\right)}{2m_0} \end{pmatrix}, \tag{3.5}$$

where $E_g(y)$ is the zone-centre ($k = 0$) band gap, and $P(y)$ is the interband (Kane) momentum matrix element of $InAs_{1-y}Sb_y$ at a given Sb composition y. As previously discussed, the band dispersion admitted by Eq. (3.5) is spherical – i.e. it depends only on the magnitude $k = \sqrt{k_\perp^2 + k_z^2}$ of the wave vector, where in order to treat BTBT in the presence of an electric field applied along the [001] direction, k_z and $k_\perp$ are the components of wave vector parallel (k_z) and perpendicular ($k_\perp$) to the [001] direction.

We recall from Chapter. 2 that the band edge effective masses are parametrisable as $\frac{m_\pm^*}{m_0} = \left|\frac{E_g}{E_g \pm E_P}\right|$, via the choice of Kane parameter E_P, where $E_P = \frac{2m_0P^2}{\hbar^2}$. For $InAs_{1-y}Sb_y$ alloys we begin with the InAs room temperature band gap $E_g = 0.354$ eV, [122] and adjust E_P to fit to the InAs CB edge effective mass $m_+^* = 0.026\,m_0$ [122], yielding $E_P = 13.261$ eV ($P = 7.108$ eV Å). Repeating this procedure for InSb, with $E_g = 0.174$ eV and $m_+^* = 0.0135\,m_0$ [122], we obtain $E_P = 12.641$ eV ($P = 6.940$ eV Å). For $InAs_{1-y}Sb_y$ alloys, we obtain the interband momentum matrix element P via linear interpolation of the values determined for InAs and InSb. This choice of interpolation scheme imposes that the bowing of the Sb composition-dependent electron effective mass in $InAs_{1-y}Sb_y$ originates entirely from the bowing of the band gap. This is consistent with recent **k·p**-based analysis of experimental data [83], where linear interpolation of P was found to reproduce accurately the measured bowing of the $InAs_{1-y}Sb_y$ electron effective mass. Combined with our choice of band gap bowing parameter (described below), our linear interpolation of P in Eq. (3.5) produces a bowing parameter $0.046m_0$ for the $InAs_{1-y}Sb_y$ electron effective mass, which is close to the centre of the range $0.030m_0$ – $0.055m_0$ identified in Ref. [122].

For the alloy band gap of $InAs_{1-y}Sb_y$ we interpolate the alloy band gap between that of InAs (= 0.354 eV) and InSb (= 0.174 eV) using a bowing parameter b fit directly to experimental measurements. For the band gap range of interest in this study, which ranges from that of InAs down to ≈ 0.2 eV, we have obtained $b = 0.62$ eV for $InAs_{1-y}Sb_y$ by fitting to the room temperature photoluminescence measurements of Ref. [152] in the composition range $y \leq 20\%$. The result of this parametrisation is shown in Fig. 3.3(a), where we note that a composition-independent bowing parameter (solid blue line) is sufficient to quantitatively describe the measured alloy band gap (open blue circles) across the Sb composition range of interest.

Now from Eq. (3.5), we need to compute the CBS Im $\{k_{z,-}(E, \mathbf{k}_\perp)\}$, using which we can compute the corresponding transmission coefficient and generation rate for BTBT. The details regarding all these calculations were explained in Chapter. 2 where, using the 2-band Kane Hamiltonian matrix for InAs (Eq. (2.58)), we obtained the real CB and LH band dispersions, and the CBS, by using Eq. (2.59) and Eqs. (2.61) and (2.62) respectively. Finally, we computed the transmission coefficient and BTBT generation rate by implementing Eq. (2.64) and (2.65) respectively.

Having described the calculation of the CBS for conventional $InAs_{1-y}Sb_y$ alloys, we now turn our attention to highly-mismatched dilute nitride InN_xAs_{1-x} and bismide $InAs_{1-z}Bi_z$ alloys. As discussed in the previous section, when substituted in dilute concentrations in InAs to form dilute nitride InN_xAs_{1-x} or bismide $InAs_{1-z}Bi_z$ alloys, isolated N (Bi) atoms act as isovalent impurities, introducing N (Bi)-related localised impurity states that are resonant with the CB (VB) of the InAs host matrix semiconductor. We extend the Kane Hamiltonian of Eq. (3.5) via Eqs. (3.1) and (3.2) i.e. by inclusion of a N (Bi)-related localised impurity state, and including a N (Bi) composition-dependent BAC interaction between this state and the extended InAs CB (VB) edge state. Choosing the zero of energy to lie at the InAs VB edge, the resulting 3-band BAC Hamiltonian for $InN_{1-x}As_x$ and $InAs_{1-z}Bi_z$ at a given N and Bi composition x and z are given respectively by

$$H(x) = \begin{pmatrix} E_N & \beta\sqrt{x} & 0 \\ \beta\sqrt{x} & E_g - \alpha\, x + \frac{\hbar^2}{2m_0}\left(k_\perp^2 + k_z^2\right) & P\sqrt{k_\perp^2 + k_z^2} \\ 0 & P\sqrt{k_\perp^2 + k_z^2} & \gamma\, x + \frac{\hbar^2}{2m_0}\left(k_\perp^2 + k_z^2\right) \end{pmatrix}, \tag{3.6}$$

$$H(z) = \begin{pmatrix} E_g - \alpha\, z + \frac{\hbar^2}{2m_0}\left(k_\perp^2 + k_z^2\right) & P\sqrt{k_\perp^2 + k_z^2} & 0 \\ P\sqrt{k_\perp^2 + k_z^2} & \gamma\, z + \frac{\hbar^2}{2m_0}\left(k_\perp^2 + k_z^2\right) & \beta\sqrt{z} \\ 0 & \beta\sqrt{z} & E_{Bi} \end{pmatrix}, \tag{3.7}$$

where m_0 is the free electron mass, E_g is the InAs zone-centre ($k = 0$) band gap, P is the inter-band (Kane) momentum matrix element, E_N and E_{Bi} are the energy of the N and Bi -related localised state relative to the InAs VB edge respectively. β is the BAC coupling parameter describing the strength $\beta\sqrt{x}$ and $\beta\sqrt{z}$ of the N and Bi composition-dependent BAC interaction between the InAs extended CB(VB) edge and N (Bi)-related localised states and α and γ are virtual crystal-type terms respectively describing the N (Bi) -induced energy shifts to the host matrix CB and VB edge energies as a function of composition x [144, 148]. The parameters E_g and P are assigned the values given above for the InAs host matrix semiconductor.

The characteristic equations associated with Eqs. (3.6) and (3.7) are cubic in the energy E, with numerical diagonalisation for real wave vectors $\mathbf{k} = (\mathbf{k}_\perp, k_z)$ yielding the (real) band structure. However, since the N- (Bi-)-related impurity levels are dispersionless, the characteristic equations associated with Eqs. (3.6) and (3.7) can be cast as quartic equations in k_z, which can be factorised

analytically. It is therefore possible to compute the CBS associated with Eqs. (3.6), (3.7) analytically, yielding an expression for the CBS of the form of $k^2_{z,\pm}(E,k_\perp) = \kappa^2_\pm(E) - k^2_\perp$ (Eq. (2.61)) , where for the dilute nitride and bismide cases we obtain the respective expressions

$$\frac{\hbar^2\kappa^2_\pm}{2m_0} = E + \frac{E_P - E_g + (\alpha-\gamma)x}{2} + \frac{\beta^2 x}{2(E_\mathrm{N}-E)} \pm \sqrt{\left(E + \frac{E_P - E_g + (\alpha-\gamma)x}{2} + \frac{\beta^2 x}{2(E_\mathrm{N}-E)}\right)^2 - \left(E - E_g + \alpha x + \frac{\beta^2 x}{E_\mathrm{N}-E}\right)(E-\gamma x)}\,, \quad (3.8)$$

$$\frac{\hbar^2\kappa^2_\pm}{2m_0} = E + \frac{E_P - E_g + (\alpha-\gamma)z}{2} + \frac{\beta^2 z}{2(E_\mathrm{Bi}-E)} \pm \sqrt{\left(E + \frac{E_P - E_g + (\alpha-\gamma)z}{2} + \frac{\beta^2 z}{2(E_\mathrm{Bi}-E)}\right)^2 - \left(E - E_g + \alpha z + \frac{\beta^2 z}{E_\mathrm{Bi}-E}\right)(E-\gamma z)}\,, \quad (3.9)$$

which reduce to Eq. (2.62) for $x = 0$ and $z = 0$.

3.3.2 BTBT transmission coefficient and generation rate

In the previous chapter, we performed benchmark calculations which verified the validity of numerical WKB calculations as a platform to investigate BTBT in HMAs. We recall from Chapter. 2 that in the WKB approximation the transmission coefficient T associated with direct BTBT at applied electric field $F = |\mathbf{F}|$ and the generation rate (per unit volume) G [126] are computed as [112, 126]

$$T(\mathbf{k}_\perp) = \frac{\pi^2}{9}\exp\left(-\frac{2}{eF}\int_{E_\mathrm{LH}(\mathbf{k}_\perp)}^{E_\mathrm{CB}(\mathbf{k}_\perp)} |\mathrm{Im}\{k_{z,-}(E,\mathbf{k}_\perp)\}|\,\mathrm{d}E\right)\,, \quad (3.10)$$

$$G(F) = \frac{eF}{\pi\hbar}\int \frac{\mathrm{d}\mathbf{k}_\perp}{(2\pi)^2}\,T(\mathbf{k}_\perp)\,, \quad (3.11)$$

where, for tunneling along [001] $\parallel \mathbf{F}$, $k_{z,-}(E,\mathbf{k}_\perp)$ is the complex band linking the LH and CB at perpendicular wave vector $\mathbf{k}_\perp$ (cf. Eq. (2.61)), and the upper and lower limits on the integral are the energies of the (real) CB and LH bands at $\mathbf{k}_\perp$.

3.4 Results

In this section, we present our results based on the theoretical analysis. Analysis presented in Chapter. 2 showed that the field-dependent transmission coefficient depends on both complex and real band dispersion. The complex band dispersion dominates T at low field, but the evolution

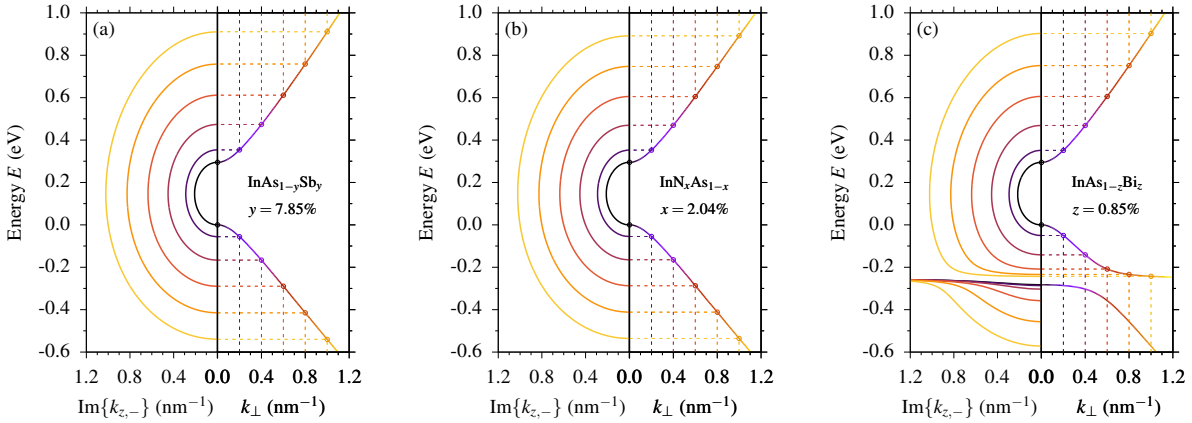

FIGURE 3.4: Calculated complex band structure of (a) $InAs_{1-y}Sb_y$ ($y = 7.85\%$), (b) InN_xAs_{1-x} ($x = 2.04\%$), and (c) $InAs_{1-z}Bi_z$ ($z = 0.85\%$) alloys having equal band gap $E_g = 0.295$ eV at $k_\perp = 0$. In each case, the left- (right-) hand panel shows the calculated imaginary (real) bands. The imaginary band $|\mathrm{Im}\{k_{z,-}(E, \mathbf{k}_\perp)\}|$ is shown for perpendicular wave vectors $k_\perp = 0.0$, 0.2, 0.4, 0.6, 0.8 and 1.0 nm^{-1} using solid black, dark purple, purple, red, orange and yellow lines respectively. Dashed lines and open circles highlight that, for a given perpendicular wave vector $k_\perp$, the imaginary band $|\mathrm{Im}\{k_{z,-}(E, \mathbf{k}_\perp)\}|$ links the CB and LH bands at energies $E_\pm(k_\perp)$. Note that the features associated with the N-related localised impurity state in (b) are out of scale, since $E_N = 1.386$ eV (cf. Table. 3.1).

of T for $F \gtrsim 1$ MV cm^{-1} is primarily governed by an interplay between the real and complex band dispersion away from $k_\perp = 0$. The substantial modification of the real and complex band dispersion in HMAs due to BAC interactions is then expected to modify BTBT compared to that in a conventional alloy having the same band gap. In the first part of this section, we target quantifying these effects and hence begin by analysing T and G in highly-mismatched InN_xAs_{1-x} and $InAs_{1-z}Bi_z$ alloys and in conventional $InAs_{1-y}Sb_y$ alloys at fixed band gap. In all three cases the alloy composition is chosen to ensure equal band gap $E_g = 0.295$ eV at $k_\perp = 0$. This exemplar band gap corresponds to a wavelength of 4.2 μm, chosen since it coincides with a strong absorption band of CO_2, and is hence a representative wavelength for mid-infrared sensing applications. Here, since we consider alloys having equal band gap, changes in T and G result solely from differences in the real and complex band dispersion, allowing to directly interrogate and quantify the impact of BAC on the BTBT transmission coefficient T and generation rate G. In the second part, we focus on studying the BTBT current generation rate as a function of zone-centred alloy band-gap at different electric field strengths.

3.4.1 Fixed band gap ($E_g = 0.295$ eV, $\lambda = 4.2$ μm)

We begin with the complex band structure of (a) $InAs_{1-y}Sb_y$ ($y = 7.85\%$), (b) InN_xAs_{1-x} ($x = 2.04\%$), and (c) $InAs_{1-z}Bi_z$ ($z = 0.85\%$) alloys having $E_g = 0.295$ eV as shown in Figure 3.4. The left- and right-hand panels respectively show the complex and real band dispersion, while the line colour denotes the magnitude $k_\perp$ of the perpendicular wave vector. Solid lines show the computed band structure calculated using Eq. (2.61) in conjunction with (a) Eq. (2.62), (b) Eq. (3.8), and $\kappa_\pm^2(E)$ computed via Eq. (3.7). The complex band dispersion $|\mathrm{Im}\{k_{z,-}(E, \mathbf{k}_\perp)\}|$ is shown in each case for perpendicular wave vectors $k_\perp = 0$ (black) to 1 nm^{-1} (yellow) in steps of 0.2 nm^{-1}.

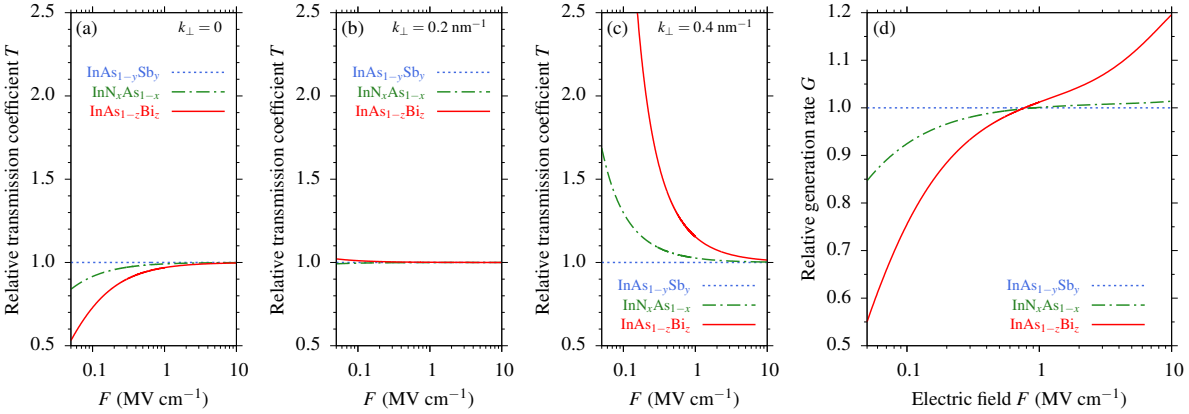

FIGURE 3.5: Calculated relative BTBT transmission coefficient T at (a) $k_\perp = 0$, (b) $k_\perp = 0.2$ nm^{-1}, and (c) $k_\perp = 0.4$ nm^{-1} for InAs$_{1-y}$Sb$_y$ ($y = 7.85\%$; dashed blue lines), InN$_x$As$_{1-x}$ ($x = 2.04\%$, dash-dotted green lines), and InAs$_{1-z}$Bi$_z$ ($z = 0.85\%$; solid red lines) alloys having equal band gap $E_g = 0.295$ eV at $k_\perp = 0$. (d) Calculated relative BTBT generation rate G for InAs$_{1-y}$Sb$_y$ ($y = 7.85\%$; dotted blue lines), InN$_x$As$_{1-x}$ ($x = 2.04\%$, dash-dotted green lines), and InAs$_{1-z}$Bi$_z$ ($z = 0.85\%$; solid red lines) alloys. Relative values of T and G in (a) – (d) are computed at each applied electric field F by dividing the calculated value of T or G by that calculated for InAs$_{1-y}$Sb$_y$.

Dashed lines and open circles indicate schematically the intersection between the real and complex bands at the CB and LH energies $E_\pm(k_\perp)$ – i.e. the limits of integration in Eq. (2.64) – obtained for InAs$_{1-y}$Sb$_y$ via Eq. (2.59), and for InN$_x$As$_{1-x}$ and InAs$_{1-z}$Bi$_z$ by diagonalising Eqs. (3.6) and (3.7) respectively. This figure highlights the growth of the area bounded by the complex band $|\mathrm{Im}\{k_{z,-}(E, \mathbf{k}_\perp)\}|$ linking the CB and VB with increasing $k_\perp$, which plays a critical role in determining the magnitude of T at high electric field.

Beginning with InN$_x$As$_{1-x}$, we note that the calculated complex band structure of Fig. 3.4(b) is minimally changed compared to that of InAs$_{1-y}$Sb$_y$ in Fig. 3.4(a). Recalling the parameters of Table. 3.1, we note that this is a consequence of InN$_x$As$_{1-x}$ representing a weakly perturbed, highly-mismatched alloy: the N-related localised impurity state lies 1.032 eV above the InAs CB edge in energy, a large energy difference which minimises the impact of N-related BAC on the band structure close in energy to the CB edge. This can be seen in Eq. (3.8), where the N composition-dependent terms at energy E are $\propto (E_\mathrm{N} - E)^{-1}$. We compute a minimal increase in CB edge effective mass for InN$_x$As$_{1-x}$, leading to a slight reduction in the band gap at fixed $k_\perp$ compared to InAs$_{1-y}$Sb$_y$. However, considering the complex band structure of dilute bismide InAs$_{1-z}$Bi$_z$ in Fig. 3.4(c), we note extremely strong modification compared to InAs$_{1-y}$Sb$_y$. This is a consequence of the close proximity in energy of the Bi-related localised impurity state in InAs to the VB edge (cf. Table. 3.1), resulting in a strongly perturbed VB structure. At small $k_\perp$ the BAC-induced increase in VB edge effective mass increases the area bounded by $|\mathrm{Im}\{k_{z,-}(E, \mathbf{k}_\perp)\}|$. However, at larger $k_\perp$ the growth of this area is strongly limited in the VB by BAC: the dispersion of the complex band flattens close in energy to the Bi impurity state at $E_\mathrm{Bi} = -0.217$ eV, at which energy the real band dispersion admitted by Eq. (3.7) possesses a singularity in the VB DOS.

Based on the complex band structures of Fig. 3.4 we therefore expect that BAC in InN$_x$As$_{1-x}$ (InAs$_{1-z}$Bi$_z$), compared to InAs$_{1-y}$Sb$_y$, will result in (i) reduced T and hence G at low F, where the

increase in CB (VB) edge effective mass will act to increase the area bounded by $|\mathrm{Im}\{k_{z,-}(E,\mathbf{k}_\perp)\}|$ close to $k_\perp = 0$, and (ii) increased T and hence G at high F, where BAC will act to limit the growth of the area bounded by $|\mathrm{Im}\{k_{z,-}(E,\mathbf{k}_\perp)\}|$ at larger $k_\perp$. The latter effect is expected to be minimal in InN_xAs_{1-x}, since the singularity in the CB DOS at energy E_N occurs at large values of $k_\perp$ – out of scale in Fig. 3.4(b) – at which the band gap is too large for states to contribute appreciably to BTBT. These expected trends are confirmed in Fig. 3.5, which shows T as a function of F calculated at (a) $k_\perp = 0$, (b) $k_\perp = 0.2$ nm^{-1}, and (c) $k_\perp = 0.4$ nm^{-1} for $InAs_{1-y}Sb_y$ (dashed blue lines), InN_xAs_{1-x} (dash-dotted green lines), and $InAs_{1-z}Bi_z$ (solid red lines). In each case T is shown relative to that calculated for $InAs_{1-y}Sb_y$ at a given electric field F, allowing to directly quantify the impact of the aforementioned modifications of the complex band structure on BTBT at fixed band gap.

At $k_\perp = 0$, in Fig. 3.5(a), we find that T in both $InN_{0.0204}As_{0.9796}$ and $InAs_{0.9915}Bi_{0.0085}$ is reduced compared to that in $InAs_{0.9215}Sb_{0.0785}$. For example, at $F = 0.1$ MV cm^{-1}, T in $InN_{0.0204}As_{0.9796}$ ($InAs_{0.9915}Bi_{0.0085}$) is reduced to 91.6% (72.9%) of that in $InAs_{0.9215}Sb_{0.0785}$, reflecting the stronger increase in band edge effective mass due to Bi incorporation, while at $F = 1$ MV cm^{-1} T in $InN_{0.0204}As_{0.9796}$ ($InAs_{0.9915}Bi_{0.0085}$) is 99.1% (96.9%) of that in $InAs_{0.9215}Sb_{0.0785}$, reflecting the saturation of T at high field (cf. Fig. 2.12(b)). At $k_\perp = 0.2$ nm^{-1}, in Fig. 3.5(b), we note minimal differences between the values of T calculated for the three alloys. We identify this value of the perpendicular wave vector as that corresponding to the boundary between "small" and "large" $k_\perp$, demarcating the crossover between the aforementioned portions of the complex band structure that govern the behaviour of G at "low" and "high" applied electric fields. Finally, at $k_\perp = 0.4$ nm^{-1}, in Fig. 3.5(c), we find that T in both $InN_{0.0204}As_{0.9796}$ and $InAs_{0.9915}Bi_{0.0085}$ is increased compared to that in $InAs_{0.9215}Sb_{0.0785}$, reflecting that BAC limits the growth of the area bounded by $|\mathrm{Im}\{k_{z,-}(E,\mathbf{k}_\perp)\}|$ at large $k_\perp$. Again, this effect is most pronounced for $InAs_{0.9915}Bi_{0.0085}$ due to the strength of the BAC-induced perturbation of the VB structure due to Bi incorporation (cf. Fig. 3.4(c)). We present the electric field-dependent BTBT transmission coefficient at three different $k_\perp$ (0, 0.2 , and 0.4 nm^{-1}). Finally we show the relative generation rate G in Fig. 3.5(d), for $InAs_{0.9215}Sb_{0.0785}$, $InN_{0.0204}As_{0.9796}$ and $InAs_{0.9915}Bi_{0.0085}$ using dashed blue, dash-dotted green and solid red lines, respectively. We present the relative G with respect to $InAs_{0.9215}Sb_{0.0785}$. Here, the calculated trends in the relative BTBT transmission coefficients of Figs. 3.5(a) – 3.5(c) are manifested. For $InN_{0.0204}As_{0.9796}$ we observe a reduction in G at low field, with the calculated generation rate at $F = 0.1$ MV cm^{-1} being 92.5% of that in $InAs_{0.9215}Sb_{0.0785}$. By $F = 1$ MV cm^{-1} the generation rate in $InN_{0.0204}As_{0.9796}$ is found to be within 0.1% of that in $InAs_{0.9215}Sb_{0.0785}$. At higher fields G in $InN_{0.0204}As_{0.9796}$ is calculated to exceed that in $InAs_{0.9215}Sb_{0.0785}$, but only minimally: at $F = 10$ MV cm^{-1} G in $InN_{0.0204}As_{0.9796}$ exceeds that in $InAs_{0.9215}Sb_{0.0785}$ by only 1.4%. Turning our attention to $InAs_{0.9915}Bi_{0.0085}$ we find, in line with the calculated transmission coefficients, that the impact on G due to Bi incorporation is enhanced compared to that associated with N incorporation. At low electric field G is suppressed, being only 75.5% of that in $InAs_{0.9215}Sb_{0.0785}$ at $F = 0.1$ MV cm^{-1}. We again find that G is approximately equal to that in

$InAs_{0.9215}Sb_{0.0785}$ for $F \approx 1$ MV cm^{-1}, beyond which it is enhanced in the high-field regime, with G at $F = 10$ MV cm^{-1} exceeding that in $InAs_{0.9215}Sb_{0.0785}$ by 19.6%.

This analysis demonstrates that incorporating N or Bi has the potential to significantly impact BTBT compared to a conventional semiconductor alloy having the same band gap. Generally, BAC acts to suppress (enhance) the BTBT generation rate G at low (high) electric field. Our analysis identifies that this behaviour is governed by a field-dependent competition between various aspects of the complex band structure. These effects are primarily governed by the strength of the impact of N- (Bi-) related BAC on the complex band structure close in energy to the CB (VB) edge, and are most pronounced when the associated N- (Bi-) related localised impurity state lies close in energy to the CB (VB) edge of the host matrix semiconductor.

3.4.2 Variable band gap: $InAs_{1-y}Sb_y$ vs. InN_xAs_{1-x}, $InAs_{1-z}Bi_z$ alloys

Having investigated the impact of BAC on BTBT at a single fixed band gap, we now turn our attention to trends as a function of the alloy band gap. The results of these calculations are summarised in Fig. 3.6, for (a) dilute nitride InN_xAs_{1-x}, and (b) dilute bismide $InAs_{1-z}Bi_z$. In each case the BTBT generation rate G is shown relative to that in an $InAs_{1-y}Sb_y$ alloy having the same band gap. Coloured solid lines in Fig. 3.6 show the variation of the relative G with the $k_\perp = 0$ alloy band gap $E_g(x), (E_g(z))$ for electric fields varying from 50 kV cm^{-1} (yellow) to 5 MV cm^{-1} (black). The dashed grey line in each case highlights the relative value $G = 1$ for the conventional (reference) $InAs_{1-y}Sb_y$ alloy.

In Fig. 3.6 we see more broadly the trends identified via our fixed band gap calculations above. For low fields $F \lesssim 1$ MV cm^{-1} (solid yellow, orange, red and magenta lines) the BTBT generation rate in InN_xAs_{1-x} and $InAs_{1-z}Bi_z$ is suppressed compared to that in $InAs_{1-y}Sb_y$. For the lowest electric field $F = 50$ kV cm^{-1} considered, we calculate that the relative G is minimised in InN_xAs_{1-x} ($InAs_{1-z}Bi_z$) for an alloy band gap of 0.254 eV (0.257 eV) – corresponding to a N (Bi) composition $x = 3.50\%$ (1.45%) – where it attains a value equal to 82.2% (50.0%) of that in $InAs_{1-y}Sb_y$. Again, we note that the reduction of G at low field is significantly more pronounced in $InAs_{1-z}Bi_z$ than in InN_xAs_{1-x}. The observed dependence of the calculated relative G values on alloy band gap can be understood in terms of the competing impacts of the BAC-induced band gap narrowing and increase in CB (VB) edge effective mass in InN_xAs_{1-x} ($InAs_{1-z}Bi_z$). In conventional $InAs_{1-y}Sb_y$ the decrease in E_g with increasing Sb composition is associated with a decrease in reduced effective mass m_r^* ($\propto E_g$), both of which then act to increase G at fixed electric field (cf. Eq. (2.67)) by reducing the area bounded by $|\mathrm{Im}\{k_{z,-}(E, \mathbf{k}_\perp)\}|$. However, in highly-mismatched dilute nitride (bismide) alloys the reduction in E_g is generally associated with an increase in CB (VB) edge effective mass, with the former and latter respectively acting to increase and decrease G. Since at low F contributions to G are dominated by states close to $k_\perp = 0$, the BAC-induced increase in band edge effective mass plays the decisive role and leads to an initial reduction in the relative G with decreasing E_g in InN_xAs_{1-x} and $InAs_{1-z}Bi_z$. As E_g decreases further, the band gap narrowing acts to increase G with sufficient strength that it counteracts the tendency of the increased band

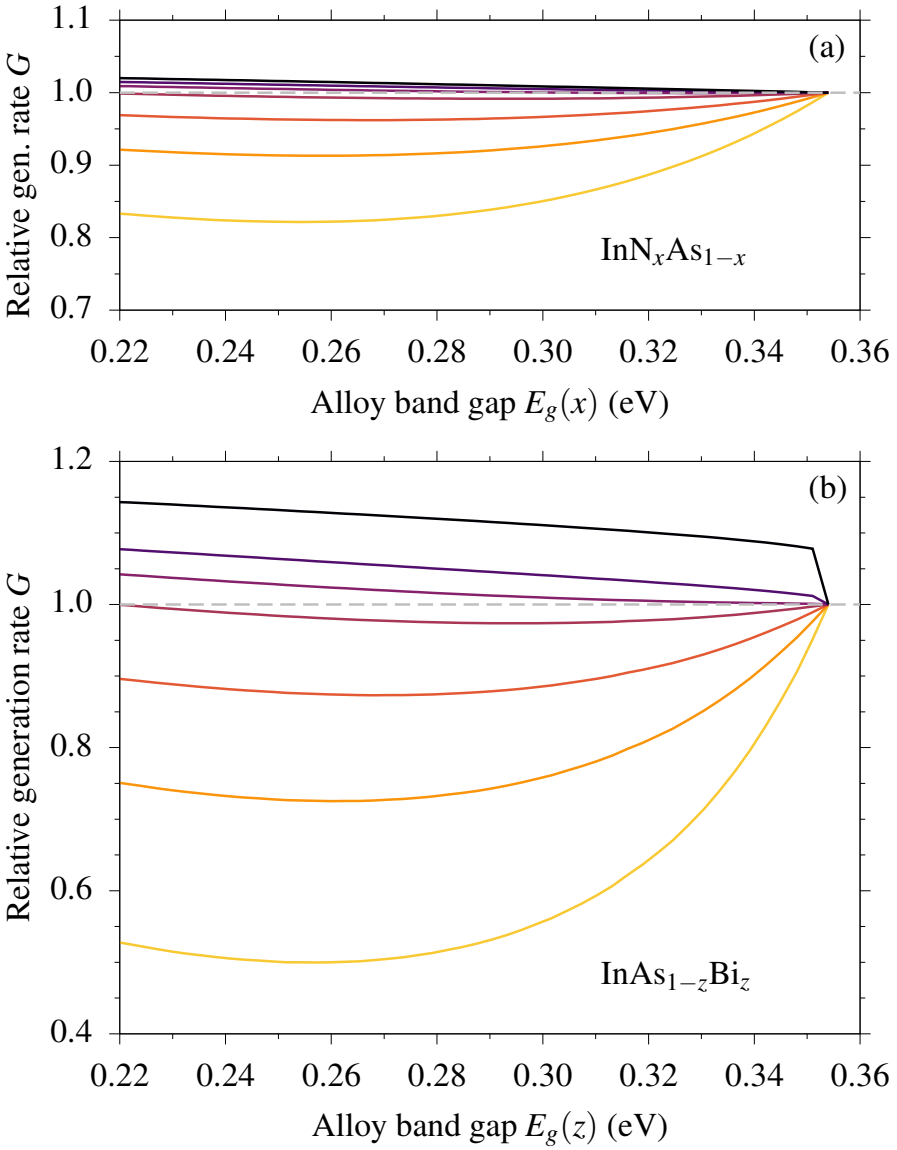

FIGURE 3.6: Calculated relative BTBT generation rate G as a function of the alloy band gap $E_g(x)$ for (a) InN_xAs_{1-x}, and (b) $InAs_{1-z}Bi_z$. Results are shown for applied electric fields $F = 50$ kV cm^{-1} (yellow), 0.1 MV cm^{-1} (orange), 0.2 MV cm^{-1} (red), 0.5 MV cm^{-1} (magenta), 1 MV cm^{-1} (purple), 2 MV cm^{-1} (dark purple), and 5 MV cm^{-1} (black). Relative values of G are computed at each alloy band gap $E_g(x)$ by dividing the value calculated for InN_xAs_{1-x} or $InAs_{1-z}Bi_z$ by that calculated for an $InAs_{1-y}Sb_y$ alloy having the same band gap.

edge effective mass to reduce G. This leads to the presence of a minimum in the calculated band gap dependence of the relative G at low field. However, we note overall that the calculated low-field values of G for InN_xAs_{1-x} and $InAs_{1-z}Bi_z$ in this $E_g \lesssim 0.25$ eV range remain lower than those calculated for $InAs_{1-y}Sb_y$ having equal band gap, confirming that the tendency of BAC to decrease low-field BTBT current holds across the full range of band gaps considered in our analysis.

For high fields $F \gtrsim 1$ MV cm^{-1} (solid dark purple and black lines), we see that the BTBT generation rate in InN_xAs_{1-x} and $InAs_{1-z}Bi_z$ exceeds that in $InAs_{1-y}Sb_y$. As described above, the amount by which G in InN_xAs_{1-x} exceeds that in $InAs_{1-y}Sb_y$ is limited by the weak impact of N-related BAC on the CB structure in the ranges of E and $k_\perp$ that contribute to BTBT. Our calculations in Fig. 3.6(a) reveal that this behaviour is approximately independent of the band

gap, so that high-field BTBT currents in InN_xAs_{1-x} are expected to be comparable to those in $InAs_{1-y}Sb_y$ across the range of dilute N compositions relevant to narrow-gap device applications. Turning to $InAs_{1-z}Bi_z$ in Fig. 3.6(b), we note here an unusual feature: at high fields $F \gtrsim 1$ MV cm^{-1} our calculations suggest an abrupt increase in G due to Bi incorporation. We note that this "jump" in G is a feature of the model employed rather than a true physical effect: it is a consequence of a well-known unphysical aspect of the BAC model. Specifically, the LH band dispersion described by Eq. (3.7) approaches the Bi localised impurity state energy E_{Bi} asymptotically with increasing $k_\perp$ (cf. Fig. 3.4(c)). This produces a singularity in the DOS at energy E_{Bi}, below which energy there exists a gap in the DOS. In the context of the present calculations, the origin of the calculated "jump" in G is the asymptotic dispersion of the LH band: the flattening of this band with increasing $k_\perp$ produces an artificially large number of states having energy close to E_{Bi} that can contribute to BTBT with increasing F. The magnitude of this "jump" in G is then a consequence of the cut-off value of $k_\perp$ employed in the numerical evaluation of Eq. (3.11).

These unphysical aspects of the BAC model have been understood via theoretical analysis of GaN_xAs_{1-x} and related dilute nitride alloys. The established approach to circumvent these issues has been to treat the BAC interaction via a Green's function solution of the Anderson impurity model [153, 154]. This approach assigns a complex energy broadening to the localised impurity state, removing the unphysical singularity and gap in the DOS predicted by the BAC model. Generally, this broadening has been treated phenomenologically, and assigned a constant value (which can be estimated using perturbation theory [154, 155]). More rigorous analysis of the Anderson impurity model has demonstrated that this localised state broadening is energy dependent, mandating a self-consistent computation of the Anderson model Green's function [156]. In a simple BAC model treating localised states having a single energy – such as the models employed in this work – this self-consistent Green's function approach removes the singularity in the DOS at the impurity energy, but the aforementioned gap in the DOS remains [155]. Rigorous self-consistent calculations for GaN_xAs_{1-x} demonstrate that this gap in the DOS is removed only when a full distribution of N-related localised (cluster) states is treated explicitly, producing a DOS which is in agreement with that obtained from large-scale atomistic supercell calculations [157]. To integrate such an approach into rigorous calculations of the BTBT generation rate is beyond the scope of this work. Therefore, while there is quantitative uncertainty in our prediction of the degree to which G in $InAs_{1-z}Bi_z$ exceeds that in $InAs_{1-y}Sb_y$, we emphasise that an increase is nonetheless expected at higher fields. This is because, even in the absence of an unphysical singularity in the DOS at the impurity state energy, Green's function solutions of the Anderson impurity model uniformly predict that the presence of BAC nonetheless produces a significant enhancement of the DOS close in energy to the impurity state. So, while our simple BAC model likely overestimates the magnitude of this increase in DOS, the fact that the DOS in $InAs_{1-z}Bi_z$ is expected to significantly exceed that of the InAs host matrix semiconductor close in energy to E_{Bi} indicates that our qualitative conclusions regarding the nature of high-field BTBT should hold.

Overall, our calculations reveal the existence of distinct low-field ($F \lesssim 1$ MV cm^{-1}) and high-field ($F \gtrsim 1$ MV cm^{-1}) regimes for BTBT in ideal HMAs. In the low-field regime, where tunneling

is dominated by states close to $k_\perp = 0$, the BAC-induced increase in band edge effective mass dominates and acts to reduce BTBT current compared to that in a conventional semiconductor having the same band gap. In the high-field regime, where tunneling is dominated by states at large $k_\perp$, the BAC-induced modification of the real DOS and complex band dispersion dominates and acts to increase the BTBT current. Additionally, our analysis highlights that careful theoretical treatment of BTBT is required in cases where localised impurity states lie close in energy to the CB or VB edge of the host matrix semiconductor. In this case, the unphysical prediction by the BAC model of a singular DOS at the impurity energy precludes fully quantitative prediction of the BTBT current when states close in energy to the impurity contribute to tunneling.

3.5 Implications for practical applications

As described in Sec. 3.1, for narrow-gap highly-mismatched III-V semiconductor alloys BTBT is most relevant to the operational characteristics of two classes of devices: (i) long-wavelength APDs, where BTBT contributes to leakage current, and (ii) TFETs, where BTBT provides the mechanism for current injection into the channel. Having elucidated the impact of BAC in HMAs on BTBT, we now describe the implications of our results for proposed practical applications in each of these classes of devices.

3.5.1 Implications for APD applications

Our results in Sec. 3.4.1 highlight that BTBT in HMAs is governed by a field-dependent interplay between the impact of (i) the BAC-induced increase in CB or VB edge effective mass, which dominates at field strengths $\lesssim 1$ MV cm^{-1} and acts to reduce the BTBT generation rate, and (ii) the BAC-induced increase in DOS close in energy to localised states, which dominates at field strengths $\gtrsim 1$ MV cm^{-1} and acts to increase the BTBT generation rate. Electric field strengths corresponding to APD operation are typically in the range of several MV cm^{-1}, where our calculations suggest that the BTBT generation rate can exceed that in a conventional III-V material of the same band gap. InAs-based APDs [158] possess a higher impact ionisation coefficient for electrons than for holes, and demonstrate electron-initiated impact ionisation for applied electric fields ~ 50 kV cm^{-1}. Similar III-V alloys, including materials such as $In_{0.53}Ga_{0.47}As$ [159] and GaAs-based APDs [160], respectively demonstrate electron-initiated for electric field strengths of 300 - 400 kVcm^{-1} [161]. In this context, our results demonstrate the potential of HMAs for APD applications. Our calculated BTBT generation rates for these alloys are lower at these field values than in a conventional alloy with the same band gap, suggesting that ideal HMAs could bring the advantage of reduced leakage current in long-wavelength APD applications.

However, of primary concern for the development of long-wavelength APDs are the electron and hole impact ionisation rates α and β. From this perspective, HMAs offer significant and as-yet little-explored opportunities.

The potential benefit of employing highly-mismatched III-V alloys to develop long-wavelength APDs was proposed by Adams in Ref. [19]. The excess noise factor of an APD is, at high multiplication, directly proportional to the ratio k of α and β, with $k = \frac{\beta}{\alpha}$ or $\frac{\alpha}{\beta}$ for electron or hole multiplication respectively. To achieve low-noise multiplication therefore requires $k \ll 1$ – i.e. that multiplication of one type of carrier via impact ionisation is, at fixed electric field, suppressed relative to multiplication of the other type of carrier [162]. This is the case, e.g., in Si ($E_g \approx 1.1$ eV), where $\alpha \gg \beta$ so that photo-generated electrons predominantly initiate electron-hole pair generation via impact ionisation. However, $k \sim 1$ in most conventional III-V semiconductors, limiting the ability to achieve high signal-to-noise ratio at longer wavelengths.

Adams proposed that this limitation could be overcome by exploiting the impact of N incorporation on the band structure of dilute nitride In(Ga)N_xAs_{1-x} – where N incorporation strongly perturbs the CB structure, while leaving the VB structure comparatively unchanged – to suppress electron multiplication. In In(Ga)N_xAs_{1-x}, N incorporation results in a reduction of the electron mobility by approximately an order of magnitude – e.g., from ≈ 8500 cm^2 V^{-1} s^{-1} at room temperature in GaAs to $\lesssim 500$ cm^2 V^{-1} s^{-1} in GaN_xAs_{1-x} [163, 164] – due to a combination of (i) the BAC-induced increase in CB edge effective mass, and (ii) strong alloy scattering by N-related localised impurity states [154, 165, 166]. This strongly suppresses the electron drift velocity in response to an applied electric field [166], so that N incorporation hinders electrons in acquiring sufficient energy to initiate carrier multiplication via impact ionisation. Dilute nitride alloys, therefore, present the opportunity to suppress α while leaving β unchanged, and hence achieve low-noise hole multiplication. However, initial experimental investigations suggested limited benefit to this approach [20], likely as it begins with an In(Ga)As semiconductor in which $\alpha > \beta$ and subsequently results, when N is incorporated, in a material which is closer to the unfavourable situation where $\alpha \approx \beta$ ($k \approx 1$).

Significantly more appealing is to exploit the same principle in dilute bismide In(Ga)$As_{1-z}Bi_z$ alloys, where Bi incorporation primarily impacts the VB structure while leaving the CB structure comparatively unchanged. Experimental investigations have demonstrated strong reduction in hole mobility in response to Bi incorporation [167] – with electronic structure calculations supporting suggestions based on experimental data of the presence of Bi-related localised impurity states that act as strong alloy scattering centres close in energy to the VB edge [137] – while the electron mobility remains close to that in GaAs [168]. The dilute bismide case then mirrors the dilute nitride case: in a dilute bismide alloy one begins with a material in which $\alpha > \beta$, and further suppresses β relative to α via Bi incorporation. This is a more desirable approach since it enables a reduced $k = \frac{\beta}{\alpha}$, with minimal reduction expected in the dominant electron impact ionisation rate, α. Indeed, new experimental evidence suggests strong suppression of the hole impact ionisation rate in $GaAs_{1-z}Bi_z$ alloys, such that $\beta \ll \alpha$ with reported $k = \frac{\beta}{\alpha}$ values as low as 0.01 [21].

Recent experimental work has demonstrated that prototypical telecom-wavelength APDs based on $AlAs_{1-y}Sb_y$ alloys offer significantly enhanced performance compared to conventional InP or $Al_xIn_{1-x}As$ devices, with high sensitivity operation demonstrated and impact ionisation rate ratio $k = \frac{\beta}{\alpha} \approx 0.005$ being significantly reduced compared to that in shorter wavelength Si APDs [47].

Here, beginning from a conventional $Al_xIn_{1-x}As$ material, replacement of As by large, electropositive Sb atoms – while simultaneously removing In to allow lattice matching to InP – is expected to have a comparable effect to that suggested above for Bi-containing alloys. On this basis, we suggest that dilute bismide alloys are a promising material system for the development of low-noise III-V APDs, with the additional benefit that the large band gap reduction associated with Bi incorporation allows the operating wavelength to be tuned across a broad range in the near- and mid-infrared on GaAs [4, 169], InP [9, 170] or InAs [18] substrates.

3.5.2 Implications for TFET applications

The tunneling field-effect transistor is an emerging semiconductor device with significant promise for low-power logic applications that uses BTBT as a carrier injection mechanism to achieve a subthermionic subthreshold swing of < 60 mV dec^{-1}. From the perspective of TFET applications, our results suggest three potential benefits of using narrow-gap HMAs as a channel material. Firstly, the ability to significantly alter the band gap E_g via N or Bi composition provides a critical additional degree of freedom in the design of ultra-thin body (UTB) or gate-all-around (GAA) TFETs, allowing, e.g., to circumvent the reduction in current associated with the increased band gap induced by quantum confinement effects in conventional nm scale structures. Here, N or Bi can be incorporated in order to reduce the bulk band gap of InAs (cf. Fig. 3.3), resulting in a tunable channel band gap in a UTB or GAA structure. Secondly, the suppression (enhancement) of the BTBT generation rate G at low (high) applied electric field F predicted above – compared to that in a conventional (non-highly-mismatched) alloy having the same band gap – indicates the possibility to achieve a higher ratio $\frac{I_{on}}{I_{off}}$ between the TFET on- and off-state currents I_{on} and I_{off}, allowing for high-speed operation. Thirdly, the enhanced difference between the low- and high-field BTBT generation rate in HMAs corresponds to an increased slope $\frac{dG}{dF}$ – i.e. a stronger increase in generation rate with increasing applied field compared to that in a conventional alloy having the same band gap. The BTBT generation rate is linked to the associated BTBT current density J via $eGV = JF$, where V is the applied voltage producing the effective local electric field F experienced by carriers in a TFET device structure. The enhanced $\frac{dG}{dF}$ in HMAs can therefore be expected to lead to enhanced $\frac{dJ}{dV}$, and hence to increased subthreshold slope (i.e. reduced subthreshold swing), allowing for low-power operation.

Based on our calculated dependence of G on F at fixed band gap (cf. Fig. 3.5(d)), we note that the second and third benefits described above are expected to be more pronounced for $InAs_{0.9915}Bi_{0.0085}$ than for InN_xAs_{1-x}. Atomistic quantum kinetic calculations for InAs TFETs suggest that while both GAA and UTB structures produce comparable $\frac{I_{on}}{I_{off}}$ as high as 10^2, the two classes of TFET structure differ markedly in terms of achievable subthreshold swing [127]. Specifically, GAA structures offer significantly reduced subthreshold swing compared to single- or double-gate UTB structures, but achieving < 60 mV dec^{-1} subthreshold swing is a sensitive function of channel diameter in GAA nanowire TFETs [127]. Here, incorporation of Bi to form an $InAs_{0.9915}Bi_{0.0085}$ channel in a GAA nanowire TFET offers clear benefits: the ability to tune the band gap at fixed nanowire

diameter relaxes constraints on the nanowire diameter required to achieve a < 60 mV dec^{-1} subthreshold swing, allowing to simultaneously engineer low subthreshold swing and increased $\frac{I_{on}}{I_{off}}$ ratio, due to the enhanced difference between the low- and high-field BTBT generation rate.

On this basis, our analysis suggests that $InAs_{1-z}Bi_z$ alloys are a potentially promising material for the design of low-power, high-speed III-V TFETs. In ideal (defect-free) structures, the performance of such devices is expected to be improved compared to the already impressive performance predicted for devices employing InAs as the channel material. However, it should be noted that the presence of native defects in HMAs is likely to generate deleterious trap-assisted BTBT, which has the potential to degrade the $\frac{I_{on}}{I_{off}}$ ratio and would be challenging to fully suppress in practice. Experimental investigations are therefore required in order to ascertain the degree to which the predicted enhanced BTBT characteristics of $InAs_{1-z}Bi_z$ alloys carry over to real devices, and hence the degree to which the performance of prototype $InAs_{1-z}Bi_z$-based TFETs can be enhanced over InAs-based TFETs.

3.6 Conclusions

In summary, we have presented a theoretical analysis of BTBT in narrow-gap, highly-mismatched III-V semiconductor alloys containing N and Bi. Specifically, by employing model BAC Hamiltonians derived and parametrised from atomistic alloy supercell electronic structure calculations, we analysed the impact of substitutional N or Bi impurities on the complex band structure, field-dependent BTBT transmission coefficient T, and field-dependent BTBT generation rate G. The impact of the impurity-like behaviour of substitutional N or Bi in InAs was emphasised via comparison of our calculations for highly-mismatched InN_xAs_{1-x} and $InAs_{1-z}Bi_z$ to those for the conventional alloy $InAs_{1-y}Sb_y$. Given the strong band gap dependence of T and G, the impact of BAC was firstly quantified by these alloys at fixed band gap, before trends as a function of alloy band gap were described.

Our analysis reveals that, at fixed band gap, the impact of BAC on BTBT is dominated by a field-dependent competition between the increased band edge effective mass (at low field), and the associated increased DOS close in energy to the N- or Bi-related impurity state (at high field). InN_xAs_{1-x} and $InAs_{1-z}Bi_z$ are alloys in which BAC effects are respectively weak and strong, due to the separation in energy between the relevant host matrix band edge and localised impurity state in each case. Correspondingly, Bi incorporation in InAs was observed to more strongly impact BTBT than N incorporation. At low field $F \lesssim 1$ MV cm^{-1}, the increased CB or VB edge effective mass increases the area bounded in energy and wave vector by the complex band linking the VB and CB, reducing G compared to that in $InAs_{1-y}Sb_y$ by $\approx 20\%$ and 50% in InN_xAs_{1-x} and $InAs_{1-z}Bi_z$, respectively. At high field $F \gtrsim 1$ MV cm^{-1}, the increased DOS close in energy to localised impurity states limits the growth of this area, reflecting that more states are available to contribute to BTBT in a given energy range and acting to increase G above that in $InAs_{1-y}Sb_y$.

From the perspective of device applications, our calculations indicate that ideal narrow-gap APDs based on HMAs should display reduced leakage currents compared to those based on conventional III-V alloys. As described for conventional III-V alloys, impact ionisation occurs at relatively low electric fields $\sim$ 50 kV cm^{-1}. At these field strengths, HMAs can provide reduced leakage current via BAC-induced suppression of BTBT compared to conventional III-V alloys. Additionally, the expected strong reduction in hole impact ionisation rate in dilute bismide alloys is highly promising, making dilute bismide alloys of continuing interest for low-noise, long-wavelength APD applications. Telecom-wavelength APD structures are generally grown on InP substrates, in which case we can start with lattice-matched $In_{0.53}Ga_{0.47}$ and obtain a lattice-matched HMA containing N - i.e. $In_xGa_{1-x}N_yAs_{1-y}$, where we increase $x > 0.53$ to keep the lattice parameter fixed - or containing Bi - i.e. $In_xGa_{1-x}As_{1-y}Bi_y$, where we decrease $x < 0.53$ to keep the lattice parameter fixed. Our initial results for Ga-free InNAs and InAsBi provide a crucial first step towards understanding BTBT in wider-gap Ga-containing materials for telecom-wavelength APDs. In $In_{0.53}Ga_{0.47}As$-based APDs (band gap $\approx$ 0.75 eV) [171] the BTBT current becomes significant at an electric field of $\sim$ 200 kV cm^{-1}. Here, it is of future interest to examine the impact of Bi incorporation at a larger band gap than considered in this work, to ascertain the potential suppression of BTBT-related leakage current in telecom-wavelength APDs.

Our calculations further indicate that HMAs possess greater contrast in low vs. high field BTBT generation rate compared to conventional alloys. This is promising from the perspective of TFET applications, suggesting a novel route to engineer the electrical characteristics via the complex band structure of the source and/or channel, and hence providing an new approach to employ in the design of TFETs displaying subthermionic subthreshold slope and high on-state current.

Investigations of the impact of BAC in HMAs have to date centred largely on modifications to the real band structure and their implications for applications in photonic or photovoltaic devices. Our analysis provides new insight into the properties of this interesting class of semiconductors by revealing that BAC interactions provide scope to modify the complex band structure and BTBT, thereby providing new opportunities for device applications. While calculations based on the WKB approximation provide significant insight into the key band structure features determining the nature of BTBT in HMAs, quantitative analysis for the design of devices in which tunneling currents are of importance should employ a more rigorous Green's function-based approach that allows computing the complex band structure self-consistently close in energy to localised states. Such models may also need to include contributions due to trap-assisted tunneling via defect states [172], due to the presence of native defects in HMAs arising from the low growth temperatures required to promote N and Bi incorporation [173, 174]. Atomistic calculations of the electronic structure of Bi-containing alloys suggest that Bi-Bi pairs (i.e. two Bi atoms sharing a common group-III nearest neighbour), and similar larger clusters of Bi atoms, generate bound localised impurity states that can lie energetically within the band gap. In this case, there is the possibility of trap-assisted BTBT via Bi-related localised states (in addition to trap-assisted BTBT associated with native

defects in the material). Probing these effects will require detailed atomistic calculations to capture the fine details of the InAsBi alloy VB structure in future work that builds upon this initial analysis.

Chapter 4

Theoretical background - Electron transport fundamentals

4.1 Introduction

The response of electrons to an applied external field and to scattering mechanisms governs the operation of a range of semiconductor optoelectronic devices [175]. It is highly essential for a device engineer to have a clear picture of carrier transport in different semiconductor structures and its consequences for semiconductor device applications. In this chapter, we outline the theoretical framework for field-dependent electron transport calculation in the case of a bulk semiconductor. This framework will be applied in the next chapter to analyse electron transport in Ge and $Ge_{1-x}Sn_x$ alloys. We introduce it here however by considering transport in gallium arsenide (GaAs) [10, 137, 176], a material which has been widely studied previously. GaAs is a III–V compound semiconductor where the constituents elements Ga and As belong to the third and fifth groups of the periodic table, respectively. Different experimental and theoretical techniques demonstrate the direct band gap nature of GaAs. Therefore, GaAs is an efficient light emitter and are widely employed in manufacturing of the light emitting diodes, lasers [148] etc. There are two primary reasons for selecting GaAs as a benchmark material for our investigation. Firstly, electron transport in GaAs has been heavily studied from both theoretical and experimental perspectives, providing suitable data against which to benchmark our field-dependent transport calculations. Secondly, our aim is to investigate field-dependent electron transport in direct-gap $Ge_{1-x}Sn_x$ alloys: in the direct-gap regime, $Ge_{1-x}Sn_x$ admits the same conduction band (CB) valley ordering as GaAs, with the zone-centre Γ-valley lying below the zone-edge L-valley in energy. In GaAs, this CB valley ordering gives rise to the well-known phenomenon of negative differential resistance (the Gunn effect) – driven by $\Gamma \rightarrow$ L intervalley scattering at high electric field – which has widespread practical applications in sensors, with emerging applications in collision avoidance systems in the automotive and aviation sectors. We wish to establish whether the indirect- to direct-gap transition in $Ge_{1-x}Sn_x$ alloys can be exploited to realise the Gunn effect in a group-IV semiconductor material, thereby requiring that we establish field-dependent transport calculations that accurately describe the well-known negative differential resistance in GaAs. In Sec. 4.2, we begin by discussing some of the important features of the CB structure of GaAs related to carrier transport theory.

After that, in Sec. 4.3 we turn our attention to several of the key concepts concerning the theoretical treatment of electron transport calculations such as Boltzmann's transport equation (BTE), distribution functions, and so on. Then we discuss different scattering mechanisms and the corresponding scattering rate and collision operators in Sec. 4.4. Having described the important factors related to transport calculation, in Sec. 4.2, 4.3 and 4.4, we dedicate Sec. 4.5 to outline the detailed explicit method of solving the BTE which we use to obtain the electron mobility and drift velocity for GaAs. To benchmark our results and models, we compare both theoretical and experimental results of equivalent calculations from the existing literature. The model developed here will then be used in the next chapter to investigate electron mobility in $Ge_{1-x}Sn_x$ alloys as a function of composition and applied electric field.

4.2 Conduction band structure

The CB structure is of fundamental importance in determining the qualitative character and quantitative nature of electron transport. Therefore it is crucial for us to know how the CB structure is modelled. Due to its widespread practical applications in photonics, the modelling of GaAs band structure has been undertaken using a range of theoretical techniques such as the tight binding (TB) approach [177, 178], empirical pseudopotential [179], first principles calculations [180–182] and the $\mathbf{k}\cdot\mathbf{p}$ method [183]. In Fig. 4.1, we show the band structure for GaAs, calculated using a tight-binding Hamiltonian [87]. The CB minimum and valence band maximum lie at the centre of the Brillouin zone, at the Γ point. In addition to the Γ point, the CB also has further minima at the L and X points at the edge of the Brillouin zone.

We can define the relation between the energy of an electron, near the bottom of the CB with the wave vector $\mathbf{k}$ as follows:

$$E_{CB}(k) = E_0 + \frac{\hbar^2 k^2}{2m_c^*}, \tag{4.1}$$

where the effective mass (m_c^*) describes the band dispersion near the CB minimum.

The following equation shows a generalised expression for effective mass [86], which can also be used for a non-parabolic band

$$\frac{1}{m^*} = \frac{1}{\hbar^2}\frac{\partial^2 E}{\partial k^2}. \tag{4.2}$$

Turning now to the L point, there are four equivalent L valleys, at the Brillouin zone edge along the (111) and three equivalent directions. The band dispersion is anisotropic at L, with different effective masses, m_l and m_t along the longitudinal and transverse directions. The band dispersion $E(\mathbf{k})$ near each L minimum is then given by

$$\gamma(E) = E = \frac{\hbar^2}{2}\left(\frac{k_l^2}{m_l} + \frac{k_t^2}{m_t}\right). \tag{4.3}$$

In the proximity of CB minima, we can assume a parabolic band dispersion, as given by Eq. (4.1). However, at higher energy, the band structure is usually represented by a non-parabolic [184]

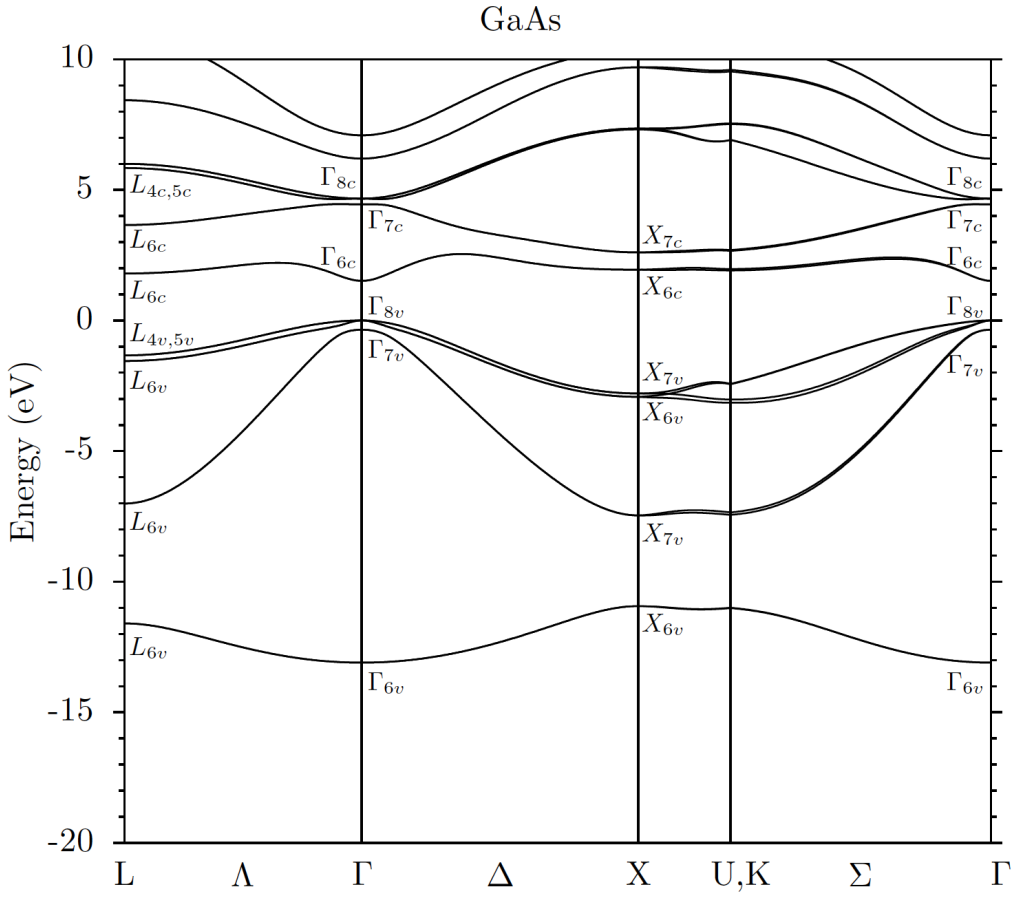

FIGURE 4.1: Band structure of a two-atom GaAs primitive unit cell by tight binding approach (image taken from [87]).

relation, $\gamma(E)$ which is given as follows

$$\gamma(E) = E(1 + \alpha E) = \frac{\hbar^2 k^2}{2m^*}, \tag{4.4}$$

where the value of α at the Γ point is usually taken as $\alpha = \frac{1}{E_g}\left(1 - \frac{m^*}{m_0}\right)^2$ and where the zero of energy is assumed at the band minimum.

A description of the full electronic band structure of GaAs can be found in [179, 182].

In our transport calculations, we consider a two-valley parabolic band model, including for both the low effective mass central Γ valley, and the four degenerate high effective mass L valleys. As the L valleys lie approximately 0.284 eV above the Γ valley, they are of significant importance for intervalley scattering, and hence in determining the nature of electron transport at the higher electric field. For the Γ valley, the electron effective mass is $m^*_\Gamma = 0.067 m_0$ where m_0 is the mass of a free electron. The L valley dispersion is ellipsoidal in nature, having different longitudinal ($\parallel \mathbf{k}_l$) and transverse ($\perp \mathbf{k}_t$) effective masses of $m^*_l = 1.66\, m_0$ and $m^*_t = 0.119\, m_0$ respectively. So, for the L valley, we compute the single-valley Density of states (DOS) effective mass as $m^*_L = (m^*_l (m^*_t)^2)^{1/3} = 0.286\, m_0$ [166].

At equilibrium, most of the electrons are in the Γ valley. Under the influence of a high electric field, the electrons may get excited to scatter into the L valley, where the larger electron-effective mass results in a decrease in mobility. We calculate electron transport without accounting for the X-valley. Electrons in the X-valley contribute significantly less to the low-field electron mobility compared to those in the Γ and L valleys, since the X-valleys lie significantly higher in energy. Furthermore, in the range of electric fields relevant to our investigation of the Gunn effect, electrons do not acquire sufficient energy to undergo scattering to the higher-lying X valleys. As we will demonstrate below, a two-valley model – including Γ- and L-valley states, but neglecting X-valley states – is sufficient to quantitatively describe experimental field-dependent transport data for both indirect-gap Ge and direct-gap GaAs, providing an appropriate starting point from which to analyse the impact on electron transport of the indirect- to direct-gap transition in $Ge_{1-x}Sn_x$.

4.2.1 Density of states

The DOS $D(E)$ is defined as the number of available energy state E_{nk} per unit volume at a given energy, E, which can be expressed as follows [166]:

$$D(E) = \frac{{m^*}^{\frac{3}{2}}}{\sqrt{2}\pi^2\hbar^3}\gamma^{\frac{1}{2}}(E)\gamma'(E)\,, \tag{4.5}$$

where $\gamma'(E)$ is the derivative of $\gamma(E)$ with respect to energy, E. We are going to use Eq. (4.5) in various instances when calculating scattering rates, as discussed further in Sec. 4.4. The detailed derivation of the DOS can be found in [185].

4.3 Boltzmann's transport equation

We introduce here the BTE, which we then use in this chapter and the following one to investigate the transport characteristics of bulk semiconductor materials.

4.3.1 Carrier distribution function

Electrons and holes are responsible for the current inside a semiconductor crystal, that's why they are known as carriers. At equilibrium condition, the distribution of carriers with the corresponding energy is arranged according to the Fermi-Dirac function. Here we focus on the electron transport problem, so we will only concentrate on the electron distribution function. The evaluation of electron transport properties of interest will be carried out from the electron distribution function, $f(E(\mathbf{k}))$ which defines the probability of finding an electron at an energy state E_k. We can find $f(E(\mathbf{k}))$ in a semi-classical approach, by solving the BTE. In the year 1872, the eminent Austrian physicist and philosopher, Ludwig Eduard Boltzmann proposed this popular transport equation to study the kinetic theory of ideal gases [186]. It is an integro - differential equation, widely used for solving different types of transport problems. The BTE for electron transport gives a

mathematical description of the change in the electron distribution function with time due to all possible collisions/scattering encountered by the electrons. Under the application of an external electric force (**F**), the momentum of electrons will be perturbed and also due to the scattering of electrons from one state to other will result in a change in the distribution function from the Fermi-Dirac distribution. The change in distribution function is given by,

$$\left(\frac{\partial f(E(\mathbf{k}))}{\partial t}\right) = \left(\frac{\partial f(E(\mathbf{k}))}{\partial t}\right)_F + \left(\frac{\partial f(E(\mathbf{k}))}{\partial t}\right)_S . \tag{4.6}$$

In Eq. (4.6), the field - dependent term [166] is defined as

$$\left(\frac{\partial f(E(\mathbf{k}))}{\partial t}\right)_F = -\frac{e\mathbf{F}}{\hbar}.\nabla_{\mathbf{k}} f_{\mathbf{k}} \,, \tag{4.7}$$

and the second term [175] is given by

$$\left(\frac{\partial f(E(\mathbf{k}))}{\partial t}\right)_S = \sum_{\mathbf{k}'} \left[\Big(S_+(\mathbf{k}',\mathbf{k}) + S_-(\mathbf{k}',\mathbf{k})\Big) f(E(\mathbf{k}')) - \Big(S_+(\mathbf{k},\mathbf{k}') + S_-(\mathbf{k},\mathbf{k}')\Big) f(E(\mathbf{k}))\right], \tag{4.8}$$

where the first and second terms $S_+(\mathbf{k}',\mathbf{k})$ and $S_-(\mathbf{k}',\mathbf{k})$ respectively describe scattering from all final states $|\mathbf{k}'\rangle$, having occupancy $f(E(\mathbf{k}'))$, into the initial state $|\mathbf{k}\rangle$, having occupancy $f(E(\mathbf{k}))$, and where we assume for now that scattering is just via phonon absorption and emission. The third and fourth terms $S_+(\mathbf{k},\mathbf{k}')$ and $S_-(\mathbf{k},\mathbf{k}')$ respectively describe scattering out of the initial state $|\mathbf{k}\rangle$ into all final states $|\mathbf{k}'\rangle$ via phonon absorption and emission. Equation (4.8) therefore describes the rate of change of the electron distribution function $f(E(\mathbf{k}))$ associated with the net scattering of electrons into state $|\mathbf{k}\rangle$. The solution of Eq. (4.6) gives the distribution function which can be evaluated by different approaches [175] such as Rode's iterative method, orthogonal polynomial expansion or a path integral solution. Following Conwell and Vassell [176], we expand the $f\left(E(\mathbf{k})\right)$ by a series of Legendre polynomials as follows

$$f\left(E(\mathbf{k})\right) = \sum_{i=0}^{\infty} f_i\left(E\right) P_i(\cos\theta) \,, \tag{4.9}$$

where P_i represent the i^{th} Legendre polynomial and θ is the angle between the wave vector **k** and the applied electric field **F**. The solution of Eq. (4.9) will have an infinite number of functions f_i. But considering Conwell and Vassell's [176] explanation and the maximum anisotropy approximation of Baraff [187], the function f_i can be assumed to be zero, for $i > 1$. We can therefore shrink Eq. (4.9) to only its first two terms, given by

$$f\left(E(\mathbf{k})\right) = f_0\left(E\right) + k_{\mathbf{F}} g\left(E\right) \,, \tag{4.10}$$

where $k_{\mathbf{F}}$ represents the component of wavevector **k** along the direction of the applied electric field, **F**. The rate of change of the distribution due to the electric field can be determined by employing

Eq. (4.7) and substituting $\frac{\hbar^2 k^2 F}{m}$ by its average $\frac{2\gamma}{3}$, and given by [166]

$$\left(\frac{\partial f\left(E(\mathbf{k})\right)}{\partial t}\right)_F = -\frac{e\mathbf{F}}{\hbar}\left(g + \frac{2}{3}\frac{\gamma}{\gamma'}g' + \frac{\hbar^2 k_F}{m^*\gamma'}f_0'\right), \tag{4.11}$$

where primes denote differentiation with respect to energy, E. We assume that the net effect of the collision processes is to cause $g(E)$ to relax with a time constant τ, within the relaxation time approximation:

$$\left(\frac{\partial f\left(E(\mathbf{k})\right)}{\partial t}\right)_S = \left(\frac{\partial f_0\left(E\right)}{\partial t}\right)_S - \frac{k_F g}{\tau}. \tag{4.12}$$

In light of this, it is possible to compute the asymmetric component of the distribution function from

$$g = -\frac{\hbar e F}{m^*}\frac{\tau}{\gamma'}f_0'. \tag{4.13}$$

As a result, the temporal rate of change of the distribution function's symmetric part due to the applied electric field is given by [166]

$$\left(\frac{\partial f\left(E(\mathbf{k})\right)}{\partial t}\right)_F = \frac{2e^2F^2}{3m^*\gamma'\left(E\right)\sqrt{\gamma\left(E\right)}}\frac{d}{dE}\left(\frac{\gamma^{3/2}\left(E\right)f'\left(E\right)}{\gamma'\left(E\right)\tau^{-1}(E)}\right), \tag{4.14}$$

where τ^{-1} is known as the total scattering rate which is the sum over all the scattering rates of interest, as will be discussed in more detail in Sec. 4.4. Equation (4.14) is the central focus in the electron transport model considering that it is associated to both perturbations i.e. the strength of applied electric field and the total scattering rate.

4.4 Scattering mechanisms

The motion of carriers can be perturbed due to several factors such as the presence of impurity atoms, crystal defects, phonons or other carriers etc. So the scattering of electrons plays a crucial role in finding the electron transport properties.

Below we describe some of the important scattering mechanisms and derive the energy-dependent scattering rate $\tau^{-1}(E)$ and collision operator $\frac{\partial f(E(\mathbf{k}))}{\partial t}$ associated with scattering of electrons by optical phonons. Polar-optical phonon scattering (POS) is the dominant scattering mechanism for CB electrons in III-V materials such as GaAs. This mechanism is, by symmetry, absent in the centrosymmetric group-IV semiconductors Si and Ge. As a result, we only consider this scattering mechanism in our transport calculations for GaAs. To achieve this we firstly follow Lundstrom's derivation [175] of the scattering rate due to POS, which is based on the integration of the transition rate $S(\mathbf{k}, \mathbf{k}')$ with respect to the phonon wave vector $\mathbf{q}$.

We then extend the same approach to derive the collision operator. This derivation of the collision operator is distinct from that presented by Conwell and Vassell, who instead performed integration with respect to the final (scattered) electron wave vector $\mathbf{k}'$ [176]. The approach presented here produces the same result for $\frac{\partial f(E(\mathbf{k}))}{\partial t}$, but avoids the complicated procedure employed by Conwell

and Vassell which involves a series expansion of $|\mathbf{k}-\mathbf{k}'|^{-1}$ in a basis of Legendre polynomials of the first and second kind. The approach adopted here more closely follows the earlier treatment by Howarth and Sondheimer [188], although we note that our integration over $\mathbf{q}$ follows Lundstrom insofar as the determination of the limits of integration are exact (under the commonly-employed assumption of dispersionless optical phonons). Once the derivation of $\frac{\partial f(E(\mathbf{k}))}{\partial t}$ is verified for POS, we apply the same general procedure to derive the scattering rate and collision operator associated with optical deformation potential scattering (ODS). While we only show the derivations for POS and ODS here, the same approach can be applied to compute $\tau^{-1}(E)$ and $\frac{\partial f(E(\mathbf{k}))}{\partial t}$ for different scattering mechanisms. Here, we assume throughout that we have a parabolic band with effective mass m^*, $E(\mathbf{k}) = \frac{\hbar^2 k^2}{2m^*}$.

4.4.1 Formalism

In a crystalline material normal (phonon) modes constitute a (periodic) time-dependent perturbation to the structure of the lattice. The transition rate for scattering of an electron from an initial state $|\mathbf{k}\rangle$, having wave vector $\mathbf{k}$ and energy $E(\mathbf{k})$, to a final state $|\mathbf{k}'\rangle$, having wave vector $\mathbf{k}'$ and energy $E(\mathbf{k}')$, by a time-dependent (phonon-related) perturbing potential $\widehat{H}'_{\pm}(t)$ is obtained via Fermi's Golden Rule as [175]

$$S_{\pm}(\mathbf{k},\mathbf{k}') = \frac{2\pi}{\hbar}|\langle\mathbf{k}'|\widehat{H}'_{\pm}(t)|\mathbf{k}\rangle|^2\,\delta(E(\mathbf{k}')-E(\mathbf{k})\mp\hbar\omega(\mathbf{q}))\,\delta(\mathbf{k}'-\mathbf{k}\mp\mathbf{q})\,, \tag{4.15}$$

where $\mathbf{q}$ is the phonon wave vector, so that $\hbar\omega(\mathbf{q})$ is the energy of the emitted or absorbed phonon. The Dirac delta distributions in Eq. (4.15) respectively enforce conservation of energy and crystal momentum, with the upper (lower) signs in Eq. (4.15) then corresponding to phonon absorption (emission).

The total scattering rate τ^{-1} from the initial state having wave vector $\mathbf{k}$ to all final states having wave vectors $\mathbf{k}'$ is computed by summing over all associated transition rates [175]

$$\tau^{-1}(\mathbf{k}) = \tau_+^{-1}(\mathbf{k}) + \tau_-^{-1}(\mathbf{k}) = \sum_{\mathbf{k}'}\Big(S_+(\mathbf{k},\mathbf{k}') + S_-(\mathbf{k},\mathbf{k}')\Big)\,. \tag{4.16}$$

In practice, conservation of crystal momentum produces a fixed relationship $\mathbf{k}' = \mathbf{k}\pm\mathbf{q}$ between the initial, final and phonon wave vectors. It is then in general more straightforward to write the transition rate of Eq. (4.15) as $S_{\pm}(\mathbf{k},\mathbf{q})$ and hence to evaluate Eq. (4.16) by summing over the phonon wave vector $\mathbf{q}$ instead of the final wave vector $\mathbf{k}'$, so that the total scattering rate out of the initial state $|\mathbf{k}\rangle$ is then given by [175]

$$\tau^{-1}(\mathbf{k}) = \sum_{\mathbf{q}}\Big(S_+(\mathbf{k},\mathbf{q}) + S_-(\mathbf{k},\mathbf{q})\Big) = \Omega\int\frac{d\mathbf{q}}{(2\pi)^3}\Big(S_+(\mathbf{k},\mathbf{q}) + S_-(\mathbf{k},\mathbf{q})\Big)\,, \tag{4.17}$$

where the conversion from a sum to an integral reflects the continuous nature of the phonon wave vector $\mathbf{q}$ in the Brillouin zone, and where the leading factor of the crystal volume Ω is inserted in order to preserve the dimension of the scattering rate.

Eqs. (4.15) and (4.17) summarise the procedure to compute the scattering rate associated with a given scattering process. Firstly, one determines the lattice perturbation $\widehat{H}'_{\pm}(t)$ associated with the phonon of interest, which is used to compute the transition rate $S_{\pm}(\mathbf{k},\mathbf{q})$ via Eq. (4.15). Secondly, using $S_{\pm}(\mathbf{k},\mathbf{q})$ one computes the scattering rate following Eq. (4.17), where the relationship $E(\mathbf{k}) = \frac{\hbar^2 k^2}{2m^*}$ describing the electron band dispersion allows to convert the expression $\tau^{-1}(\mathbf{k})$ for the total scattering rate in terms of the initial wave vector $\mathbf{k}$ into the desired energy-dependent expression $\tau^{-1}(E)$.

The computation of the collision operator $\frac{\partial f}{\partial t}$ is similar in spirit to that of the scattering rate, and is defined in terms of the transition rates $S_{\pm}(\mathbf{k},\mathbf{k}')$ [176] as stated in Eq. (4.8). We choose here to evaluate $\frac{\partial f(E(\mathbf{k}))}{\partial t}$ by integrating with respect to the phonon wave vector $\mathbf{q}$ as [188]

$$\frac{\partial f(E(\mathbf{k}))}{\partial t} = \Omega \int \frac{d\mathbf{q}}{(2\pi)^3} \left[\Big(S_+(\mathbf{q},\mathbf{k}) + S_-(\mathbf{q},\mathbf{k}) \Big) f(\mathbf{k}') - \Big(S_+(\mathbf{k},\mathbf{q}) + S_-(\mathbf{k},\mathbf{q}) \Big) f(\mathbf{k}) \right], \tag{4.18}$$

where, as for the scattering rate above, the known band dispersion $E(\mathbf{k})$ can be exploited to obtain the desired energy-dependent expression $\frac{\partial f(E)}{\partial t}$ for the collision operator.

In what follows we compute $S_{\pm}(\mathbf{k},\mathbf{q})$ for each scattering process of interest, which is then used to derive expressions for the scattering rate and collision operator, using Eqs. (4.17) and (4.18) respectively. The resulting energy-dependent scattering rates $\tau^{-1}(E)$ and collision operators $\frac{\partial f(E)}{\partial t}$ can then be employed in numerical solution of the BTE in the relaxation time approximation.

4.4.2 Conservation of energy and crystal momentum

The Dirac delta distributions in Eq. (4.15) respectively enforce the conservation of energy and crystal momentum conditions,

$$E(\mathbf{k}') = E(\mathbf{k}) \pm \hbar\omega(\mathbf{q}), \tag{4.19}$$

$$\mathbf{k}' = \mathbf{k} \pm \mathbf{q}, \tag{4.20}$$

where we recall that the upper (lower) signs correspond to phonon absorption (emission).

For evaluation of integrals with respect to phonon wave vector $\mathbf{q}$ in Eqs. (4.17) and (4.18) it is preferable to combine these two conditions into a single condition which simultaneously represents conservation of energy and crystal momentum, allowing to replace the two Dirac delta distributions in Eq. (4.15) by a single Dirac delta distribution which imposes a condition on $\mathbf{q}$ rather than $\mathbf{k}'$. We follow Lundstrom, where, for a parabolic band $E(\mathbf{k}) = \frac{\hbar^2 k^2}{2m^*}$, Eq. (4.19) becomes

$$\frac{\hbar^2 k'^2}{2m^*} = \frac{\hbar^2 k^2}{2m^*} \pm \hbar\omega(\mathbf{q})\,. \tag{4.21}$$

To remove k'^2 we obtain an expression in terms of $\mathbf{k}$ and $\mathbf{q}$ by taking the dot product of Eq. (4.20) with itself, giving [175]

$$\begin{aligned} k'^2 = \mathbf{k}'\cdot\mathbf{k}' &= (\mathbf{k}\pm\mathbf{q})\cdot(\mathbf{k}\pm\mathbf{q})\,, \\ &= \mathbf{k}\cdot\mathbf{k} + \mathbf{q}\cdot\mathbf{q} \pm 2\,\mathbf{k}\cdot\mathbf{q}\,, \\ &= k^2 + q^2 \pm 2\,kq\,\cos\theta\,, \end{aligned} \tag{4.22}$$

where θ is the angle between the initial wave vector $\mathbf{k}$ and the phonon wave vector $\mathbf{q}$.

Substituting Eq. (4.22) in Eq. (4.21) and rearranging yields

$$q^2 \pm 2kq\,\cos\theta \mp \frac{2m^*}{\hbar}\,\omega(\mathbf{q}) = 0\,, \tag{4.23}$$

or, equivalently,

$$\pm\cos\theta + \frac{q}{2k} \mp \frac{\omega(\mathbf{q})}{v(\mathbf{k})\,q} = 0\,, \tag{4.24}$$

where $v(\mathbf{k}) = \hbar^{-1}\frac{\partial E(\mathbf{k})}{\partial \mathbf{k}}$ is the electron group velocity, for our assumed parabolic band having effective mass m^*, $v(\mathbf{k})$ is given by $v(\mathbf{k}) = \frac{\hbar k}{m^*}$. Given $\pm$ ($\mp$) signs in Eq. (4.24) describe phonon absorption (emission).

From Eq. (4.15) we recall that conservation of energy is imposed by the Dirac delta distribution $\delta(E(\mathbf{k}') - E(\mathbf{k}) \mp \hbar\omega(\mathbf{q}))$. We can express the argument of this distribution using Eq. (4.22) as

$$\begin{aligned} E(\mathbf{k}') - E(\mathbf{k}) \mp \hbar\omega(\mathbf{q}) &= \frac{\hbar^2 k'^2}{2m^*} - \frac{\hbar^2 k^2}{2m^*} \mp \hbar\omega(\mathbf{q})\,, \\ &= \frac{\hbar^2 q^2}{2m^*} \pm \frac{\hbar^2}{m^*} kq\cos\theta \mp \hbar\omega(\mathbf{q})\,, \\ &= \hbar v(\mathbf{k})\,q\left(\pm\cos\theta + \frac{q}{2k} \mp \frac{\omega(\mathbf{q})}{v(\mathbf{k})\,q}\right)\,, \end{aligned} \tag{4.25}$$

allowing us to exploit the property $\delta(ax) = |a|^{-1}\,\delta(x)$ of the Dirac delta distribution to write [175]

$$\delta(E(\mathbf{k}') - E(\mathbf{k}) \mp \hbar\omega(\mathbf{q})) = \frac{1}{\hbar v(\mathbf{k})\,q}\,\delta\left(\pm\cos\theta + \frac{q}{2k} \mp \frac{\omega(\mathbf{q})}{v(\mathbf{k})\,q}\right)\,. \tag{4.26}$$

We note from Eq. (4.24) that the argument of Eq. (4.26) vanishes when both energy and crystal momentum are conserved, so that Eq. (4.26) encapsulates both of Eqs. (4.19) and (4.20), and can

hence be used to replace *both* the Dirac and Kronecker delta distributions of Eq. (4.15). Below, we will generally omit factors of $\delta(\mathbf{k}' + \mathbf{k} \mp \mathbf{q})$ when performing computations: since we are dealing with single-valued energy and phonon dispersions $E(\mathbf{k})$ and $\omega(\mathbf{q})$, the Dirac delta function imposing conservation of energy is tantamount to that enforcing conservation of crystal momentum.

When it comes to computing the integral over $\mathbf{q}$ in the calculation of the scattering rate or collision operator, we will have to evaluate integrals of the form

$$\begin{aligned}
\Omega \int \frac{d\mathbf{q}}{(2\pi)^3} S_{\pm}(\mathbf{k},\mathbf{q}) &= \frac{\Omega}{(2\pi)^3} \int_0^{2\pi} d\phi \int_0^{\pi} d\theta \, \sin\theta \int_0^{+\infty} dq \, q^2 \, S_{\pm}(k,q,\theta) \\
&= \frac{\Omega}{(2\pi)^2} \int_{-1}^{+1} d(\cos\theta) \int_0^{+\infty} dq \, q^2 \, S_{\pm}(k,q,\theta) \\
&\propto \frac{\Omega}{(2\pi)^2} \int_{-1}^{+1} d(\cos\theta) \int_0^{+\infty} dq \, q \, \delta\left(\pm\cos\theta + \frac{q}{2k} \mp \frac{\omega(\mathbf{q})}{v(\mathbf{k})\, q} \right) . \quad (4.27)
\end{aligned}$$

In order to evaluate this integral we must consider the nature of the "sifting" property of the Dirac delta distribution. Specifically, we are interested here in an integral of the form

$$\int_0^{+\infty} dy \int_{x_{\min}}^{x_{\max}} dx \, \delta(f(x,y) - x_0) \, . \quad (4.28)$$

If $x_{\min} < x < x_{\max}$ then the integral with respect to x evaluates to unity, and the two-dimensional integral yields a non-zero value. Otherwise, if $x < x_{\min}$ or $x > x_{\max}$, then the integral with respect to x vanishes and hence the entire two-dimensional integral vanishes. In the context of Eq. (4.27) $x \sim \cos\theta$ and $y \sim q$ so that the above therefore describes that the argument of the energy- and crystal momentum-conserving Dirac delta distribution will not achieve a value of zero – as it must in order to ensure that energy and momentum are conserved (cf. Eq. (4.24)) – if the magnitude q of the phonon wave vector $\mathbf{q}$ is either too large or small. Physically, this describes that absorption or emission of phonons which do not conserve both energy and crystal momentum do not contribute to the scattering rate or collision operator. Integration over the Dirac delta distribution with respect to $\cos\theta$ in Eq. (4.27) then places lower and upper bounds $q_{\pm,\min}$ and $q_{\pm,\max}$ on the wave vectors of phonons that can scatter an electron while simultaneously conserving energy and crystal momentum where, again, the upper (lower) signs in $q_{\pm,\min}$ and $q_{\pm,\max}$ refer to phonon absorption (emission). As such, performing the integration with respect to $\cos\theta$ in Eq. (4.27) yields

$$\frac{\Omega}{(2\pi)^2} \int_{q_{\pm,\min}}^{q_{\pm,\max}} dq \, q = \frac{\Omega}{2(2\pi)^2} \left(q_{\pm,\max}^2 - q_{\pm,\min}^2 \right) , \quad (4.29)$$

where our task is then to compute the minimum and maximum phonon wave vectors $q_{\pm,\min}$ and $q_{\pm,\max}$.

To achieve this we recall Eq. (4.23), which encapsulates conservation of energy and crystal momentum. We assume that optical phonons are dispersionless, so that $\omega(\mathbf{q}) = \omega_0$ is independent of $\mathbf{q}$, and hence Eq. (4.23) is a quadratic equation in q. We obtain $q_{\pm,\min}$ and $q_{\pm,\max}$ by solving

Eq. (4.23) for the cases of phonon absorption or emission which, when $\cos\theta$ assumes it extremum values of ± 1, provides expressions for the maximum and minumum wave vectors $\mathbf{q}$ of phonons that can scatter an electron having a given wave vector $\mathbf{k}$. We find

$$q_{\pm,\min} = k\left(-1+\sqrt{1\pm\frac{\hbar\omega_0}{E}}\right), \tag{4.30}$$

$$q_{\pm,\min} = k\left(\pm 1\pm\sqrt{1\pm\frac{\hbar\omega_0}{E}}\right), \tag{4.31}$$

where we recall that $E(\mathbf{k})=\frac{\hbar^2k^2}{2m^*}$ is the energy of an electron having wave vector $\mathbf{k}$.

4.4.3 Polar optical phonon scattering (POS)

Lundstrom derives the transition rates associated with scattering by polar optical phonons as [175]

$$\begin{aligned} S_\pm(\mathbf{k},\mathbf{q}) &= \frac{\pi e^2\omega(\mathbf{q})}{\epsilon_0\Omega q^2}\left(\frac{1}{\kappa_\infty}-\frac{1}{\kappa_0}\right)\left(n(\omega(\mathbf{q}))+\frac{1}{2}\mp\frac{1}{2}\right)\delta\left(E(\mathbf{k}')-E(\mathbf{k})\mp\hbar\omega(\mathbf{q})\right), \\ &= \frac{\pi e^2\omega(\mathbf{q})}{\hbar\epsilon_0\Omega v(\mathbf{k})q^3}\left(\frac{1}{\kappa_\infty}-\frac{1}{\kappa_0}\right)\left(n(\omega(\mathbf{q}))+\frac{1}{2}\mp\frac{1}{2}\right)\delta\left(\pm\cos\theta+\frac{q}{2k}\mp\frac{\omega_0}{v(\mathbf{k})q}\right) \end{aligned} \tag{4.32}$$

where the second equality follows from Eq. (4.26). Here, ω_0 is the (constant) phonon frequency, $v(\mathbf{k})$ is the electron group velocity, κ_0 and κ_∞ are respectively the static and high-frequency dielectric constant, and

$$n(\omega(\mathbf{q})) = \frac{1}{\exp\left(\frac{\hbar\omega(\mathbf{q})}{k_BT}\right)-1}, \tag{4.33}$$

is the phonon (Bose-Einstein) distribution function at temperature T.

Scattering rate

We compute the scattering rate via Eq. (4.17), where the transition rates $S_\pm(\mathbf{k},\mathbf{q})$ are given by Eq. (4.32)

$$\begin{aligned} \tau^{-1}(\mathbf{k}) &= \Omega\int\frac{d\mathbf{q}}{(2\pi)^3}\Big(S_+(\mathbf{k},\mathbf{q})+S_-(\mathbf{k},\mathbf{q})\Big) \\ &= \frac{\pi e^2}{\epsilon_0\hbar v(\mathbf{k})}\left(\frac{1}{\kappa_\infty}-\frac{1}{\kappa_0}\right)\int\frac{d\mathbf{q}}{(2\pi)^3}\frac{\omega(\mathbf{q})}{q^2}\Big[n(\omega(\mathbf{q}))\,\delta\left(E(\mathbf{k}')-E(\mathbf{k})-\hbar\omega(\mathbf{q})\right) \\ &+ (n(\omega(\mathbf{q}))+1)\,\delta\left(E(\mathbf{k}')-E(\mathbf{k})+\hbar\omega(\mathbf{q})\right)\Big], \end{aligned} \tag{4.34}$$

where the first and second terms respectively describe polar optical phonon absorption and emission. To proceed, we recall that we treat dispersionless optical phonons $\omega(\mathbf{q}) = \omega_0$, so that the distribution function $n(\omega(\mathbf{q})) = n(\omega_0)$ is independent of $\mathbf{q}$. So, factors of $\omega(\mathbf{q})$ and $n(\omega(\mathbf{q}))$ can be taken outside of the integration over $\mathbf{q}$. Next, we substitute the Dirac delta distributions following Eq. (4.26). The resulting integrand depends only on the magnitude q of the phonon wave vector $\mathbf{q}$, and the polar angle θ. To proceed, we choose to work in a spherical polar coordinate system, in which the polar (z) axis is chosen to lie parallel to the initial electron wave vector $\mathbf{k}$, so that the polar angle θ coincides with the angle θ between $\mathbf{k}$ and the phonon wave vector $\mathbf{q}$. We can then write the volume element $d\mathbf{q} = q^2 \sin\theta \, dq \, d\theta \, d\phi$. Performing the trivial integration over the azimuthal angle ϕ, and changing variables from θ to $\cos\theta$ for the integration over the polar angle, we obtain

$$\begin{aligned} \tau^{-1}(\mathbf{k}) &= \frac{e^2\omega_0}{4\pi\epsilon_0\hbar v(\mathbf{k})}\left(\frac{1}{\kappa_\infty}-\frac{1}{\kappa_0}\right)\left[n(\omega_0)\int_{-1}^{+1} d(\cos\theta)\int_0^{+\infty} dq\,\frac{1}{q}\,\delta\left(\cos\theta+\frac{q}{2k}-\frac{\omega_0}{v(\mathbf{k})\,q}\right)\right. \\ &+ \left.(n(\omega_0)+1)\int_{-1}^{+1} d(\cos\theta)\int_0^{+\infty} dq\,\frac{1}{q}\,\delta\left(-\cos\theta+\frac{q}{2k}+\frac{\omega_0}{v(\mathbf{k})\,q}\right)\right]. \end{aligned} \tag{4.35}$$

Recalling the discussion leading to Eqs. (4.30) and (4.31), we integrate with respect to $\cos\theta$ to obtain

$$\begin{aligned} \tau^{-1}(\mathbf{k}) &= \frac{e^2\omega_0}{4\pi\epsilon_0\hbar v(\mathbf{k})}\left(\frac{1}{\kappa_\infty}-\frac{1}{\kappa_0}\right)\left[n(\omega_0)\int_{q_{+,\min}}^{q_{+,\max}}\frac{dq}{q}+(n(\omega_0)+1)\int_{q_{-,\min}}^{q_{-,\max}}\frac{dq}{q}\right] \\ &= \frac{e^2\omega_0}{4\pi\epsilon_0\hbar v(\mathbf{k})}\left(\frac{1}{\kappa_\infty}-\frac{1}{\kappa_0}\right)\left[n(\omega_0)\,\ln\left(\frac{q_{+,\max}}{q_{+,\min}}\right)+(n(\omega_0)+1)\,\ln\left(\frac{q_{-,\max}}{q_{-,\min}}\right)\right], \end{aligned} \tag{4.36}$$

where $q_{\pm,\min}$ and $q_{\pm,\max}$ are the limiting phonon wave vectors of Eqs. (4.30) and (4.31).

Using Eq. (4.30) we write, for the first (phonon absorption) term,

$$\begin{aligned} \ln\left(\frac{q_{+,\max}}{q_{+,\min}}\right) &= \ln\left(\frac{1+\sqrt{1+\frac{\hbar\omega_0}{E}}}{-1+\sqrt{1+\frac{\hbar\omega_0}{E}}}\right) = \ln\left(\frac{\sqrt{\frac{E}{\hbar\omega_0}}+\sqrt{\frac{E}{\hbar\omega_0}+1}}{-\sqrt{\frac{E}{\hbar\omega_0}}+\sqrt{\frac{E}{\hbar\omega_0}+1}}\right) \\ &= \ln\left(\frac{\sqrt{x^2+1}+x}{\sqrt{x^2+1}-x}\right) = \ln\left(\sqrt{x^2+1}+x\right)-\ln\left(\sqrt{x^2+1}-x\right) = 2\sinh^{-1}(x), \end{aligned}$$

where $x = \sqrt{\frac{E}{\hbar\omega_0}}$, so that

$$\ln\left(\frac{q_{+,\max}}{q_{+,\min}}\right) = 2\sinh^{-1}\left(\sqrt{\frac{E}{\hbar\omega_0}}\right) . \tag{4.37}$$

Similarly,

$$\ln\left(\frac{q_{-,\max}}{q_{-,\min}}\right) = 2\sinh^{-1}\left(\sqrt{\frac{E}{\hbar\omega_0} - 1}\right) , \tag{4.38}$$

which is evaluated by defining $x = \sqrt{\frac{E}{\hbar\omega_0} - 1}$, so that $\sqrt{\frac{E}{\hbar\omega_0}} = \sqrt{x^2 + 1}$.

Substituting Eqs. (4.37) and (4.38) into Eq. (4.36) we obtain the following expression for the POS rate

$$\begin{aligned} \tau_{POS}^{-1}(\mathbf{k}) &= \frac{e^2\omega_0}{2\pi\epsilon_0\hbar v(\mathbf{k})}\left(\frac{1}{\kappa_\infty} - \frac{1}{\kappa_0}\right)\left[n(\omega_0)\sinh^{-1}\left(\sqrt{\frac{E(\mathbf{k})}{\hbar\omega_0}}\right)\right. \\ &+ \left.\theta(E(\mathbf{k}) - \hbar\omega_0)\,(n(\omega_0)+1)\sinh^{-1}\left(\sqrt{\frac{E(\mathbf{k})}{\hbar\omega_0} - 1}\right)\right] , \end{aligned} \tag{4.39}$$

where the Heaviside step function in the second term accounts for the fact that an electron having energy $E(\ \mathbf{k}\ ) < \hbar\omega_0$ cannot undergo scattering via polar optical phonon emission, because there are no states at energy $E < 0$ available to scatter into. Finally, we remove any explicit dependence on k by substituting in the expression for the electron group velocity $v(k) = \frac{\hbar k}{m^*} = \sqrt{\frac{2E}{m^*}}$, to obtain our desired energy-dependent scattering rate

$$\begin{aligned} \tau_{POS}^{-1}(E) &= \frac{e^2\omega_0}{4\pi\epsilon_0\hbar}\left(\frac{1}{\kappa_\infty} - \frac{1}{\kappa_0}\right)\sqrt{\frac{2m^*}{E}}\left[n(\omega_0)\sinh^{-1}\left(\sqrt{\frac{E}{\hbar\omega_0}}\right)\right. \\ &+ \left.\theta(E - \hbar\omega_0)\,(n(\omega_0)+1)\sinh^{-1}\left(\sqrt{\frac{E}{\hbar\omega_0} - 1}\right)\right] , \end{aligned} \tag{4.40}$$

which matches Eq. (2.94) of Ref. [175]. Or, equivalently,

$$\begin{aligned} \tau_{POS}^{-1}(E) &= \frac{e^2\omega_0}{4\pi\epsilon_0\hbar}\left(\frac{1}{\kappa_\infty} - \frac{1}{\kappa_0}\right)\sqrt{\frac{2m^*}{E}}\left[n(\omega_0)\coth^{-1}\left(\sqrt{1 + \frac{\hbar\omega_0}{E}}\right)\right. \\ &+ \left.\theta(E - \hbar\omega_0)\,(n(\omega_0)+1)\tanh^{-1}\left(\sqrt{1 - \frac{\hbar\omega_0}{E}}\right)\right] , \end{aligned} \tag{4.41}$$

which corresponds to Eq. (27) of Ref. [166] for a parabolic band.

Collision operator

We compute the collision operator via Eq. (4.18), where the transition rates $S_{\pm}(\mathbf{k},\mathbf{k}')$ are given by Eq. (4.32)

$$\begin{aligned}\left(\frac{\partial f(E(\mathbf{k}))}{\partial t}\right)_{POS} &= \frac{\pi e^2}{(2\pi)^3\epsilon_0}\left(\frac{1}{\kappa_\infty}-\frac{1}{\kappa_0}\right)\int d\mathbf{q}\,\frac{\omega(\mathbf{q})}{q^2}\Big[n(\omega(\mathbf{q}))\,f(E(\mathbf{k}'))\,\delta(E(\mathbf{k})-E(\mathbf{k}')-\hbar\omega(\mathbf{q}))\\ &+ (n(\omega(\mathbf{q}))+1)\,f(E(\mathbf{k}'))\,\delta(E(\mathbf{k})-E(\mathbf{k}')+\hbar\omega(\mathbf{q}))\\ &- n(\omega(\mathbf{q}))\,f(E(\mathbf{k}))\,\delta(E(\mathbf{k}')-E(\mathbf{k})-\hbar\omega(\mathbf{q}))\\ &- (n(\omega(\mathbf{q}))+1)\,f(E(\mathbf{k}))\,\delta(E(\mathbf{k}')-E(\mathbf{k})+\hbar\omega(\mathbf{q}))\Big]. \end{aligned} \tag{4.42}$$

We use $\delta(-x)=\delta(x)$ to re-write the Dirac delta distributions in the first and second terms, and then gather terms to obtain

$$\begin{aligned}\left(\frac{\partial f(E(\mathbf{k}))}{\partial t}\right)_{POS} &= \frac{\pi e^2}{(2\pi)^3\epsilon_0}\left(\frac{1}{\kappa_\infty}-\frac{1}{\kappa_0}\right)\int d\mathbf{q}\,\frac{\omega(\mathbf{q})}{q^2}\Big[\\ &\Big(n(\omega(\mathbf{q}))+1)\,f(E(\mathbf{k}'))-n(\omega(\mathbf{q}))\,f(E(\mathbf{k}))\Big)\,\delta(E(\mathbf{k}')-E(\mathbf{k})-\hbar\omega(\mathbf{q}))\\ &+ \Big(n(\omega(\mathbf{q}))\,f(E(\mathbf{k}'))-(n(\omega(\mathbf{q}))+1)\,f(E(\mathbf{k}))\Big)\,\delta(E(\mathbf{k}')-E(\mathbf{k})+\hbar\omega(\mathbf{q}))\Big]. \end{aligned} \tag{4.43}$$

Next, we use the fact that the optical phonons are assumed to be dispersionless, and Eq. (4.26), to replace the Dirac delta distributions and obtain

$$\begin{aligned}\frac{\partial f(E(\mathbf{k}))}{\partial t} &= \frac{\pi e^2\omega_0}{(2\pi)^3\epsilon_0\hbar v(\mathbf{k})}\left(\frac{1}{\kappa_\infty}-\frac{1}{\kappa_0}\right)\Big[(n(\omega_0)+1)\int d\mathbf{q}\,\frac{f(E(\mathbf{k}'))}{q^3}\,\delta\left(\cos\theta+\frac{q}{2k}-\frac{\omega_0}{v(\mathbf{k})q}\right)\\ &- n(\omega_0)\int d\mathbf{q}\,\frac{f(E(\mathbf{k}))}{q^3}\,\delta\left(\cos\theta+\frac{q}{2k}-\frac{\omega_0}{v(\mathbf{k})q}\right)\\ &+ n(\omega_0)\int d\mathbf{q}\,\frac{f(E(\mathbf{k}'))}{q^3}\,\delta\left(-\cos\theta+\frac{q}{2k}+\frac{\omega_0}{v(\mathbf{k})q}\right)\\ &- (n(\omega_0)+1)\int d\mathbf{q}\,\frac{f(E(\mathbf{k}))}{q^3}\,\delta\left(-\cos\theta+\frac{q}{2k}+\frac{\omega_0}{v(\mathbf{k})q}\right)\Big]. \end{aligned} \tag{4.44}$$

Recalling that the Dirac delta distributions enforce conservation of both energy and crystal momentum, and the assumed dispersionless nature of the optical phonons, fixes the ($\mathbf{q}$-independent) energy arguments of the distribution functions $f(E(\mathbf{k}))$ and $f(E(\mathbf{k}'))$, allowing to take them outside of the integration over $\mathbf{q}$. Integrating with respect to $\cos\theta$, as above, gives

$$\begin{aligned}\frac{\partial f(E(\mathbf{k}))}{\partial t} &= \frac{\pi e^2 \omega_0}{(2\pi)^2 \epsilon_0 \hbar v(\mathbf{k})}\left(\frac{1}{\kappa_\infty}-\frac{1}{\kappa_0}\right)\left[\Big(\big(n(\omega_0)+1\big) f(E(\mathbf{k})+\hbar\omega_0)\right.\\ &- \left. n(\omega_0) f(E(\mathbf{k}))\Big)\int_{q_{+,\min}}^{q_{+,\max}} \frac{dq}{q}\right.\\ &+ \left.\theta(E(\mathbf{k})-\hbar\omega_0)\Big(n(\omega_0) f(E(\mathbf{k})-\hbar\omega_0)-\big(n(\omega_0)+1\big) f(E(\mathbf{k}))\Big)\int_{q_{-,\min}}^{q_{-,\max}} \frac{dq}{q}\right].\end{aligned} \tag{4.45}$$

Evaluating the integrals as in the calculation of the scattering rate above, and substituting in the energy-dependent expression for the electron group velocity, gives the desired energy-dependent expression for the collision operator describing scattering of electrons by polar optical phonons

$$\begin{aligned}\left(\frac{\partial f(E(\mathbf{k}))}{\partial t}\right)_{POS} &= \frac{e^2\omega_0}{4\pi\epsilon_0\hbar}\left(\frac{1}{\kappa_\infty}-\frac{1}{\kappa_0}\right)\sqrt{\frac{2m^*}{E}}\left[\Big(\big(n(\omega_0)+1\big) f(E+\hbar\omega_0)\right.\\ &- \left. n(\omega_0) f(E)\Big)\sinh^{-1}\left(\sqrt{\frac{E}{\hbar\omega_0}}\right)+\theta(E-\hbar\omega_0)\Big(n(\omega_0) f(E-\hbar\omega_0)\right.\\ &- \left.\big(n(\omega_0)+1\big) f(E)\Big)\sinh^{-1}\left(\sqrt{\frac{E}{\hbar\omega_0}-1}\right)\right],\end{aligned} \tag{4.46}$$

or, equivalently,

$$\begin{aligned}\left(\frac{\partial f(E(\mathbf{k}))}{\partial t}\right)_{POS} &= \frac{e^2\omega_0}{4\pi\epsilon_0\hbar}\left(\frac{1}{\kappa_\infty}-\frac{1}{\kappa_0}\right)\sqrt{\frac{2m^*}{E}}\left[\Big(\big(n(\omega_0)+1\big) f(E+\hbar\omega_0)\right.\\ &- \left. n(\omega_0) f(E)\Big)\coth^{-1}\left(\sqrt{1+\frac{\hbar\omega_0}{E}}\right)\right)\\ &+ \left.\theta(E-\hbar\omega_0)\Big(n(\omega_0) f(E-\hbar\omega_0)-\big(n(\omega_0)+1\big) f(E)\Big)\tanh^{-1}\left(\sqrt{1-\frac{\hbar\omega_0}{E}}\right)\right],\end{aligned} \tag{4.47}$$

which is equal to Eq. (26) of Ref. [166] for the case of a parabolic band.

4.4.4 Optical deformation potential scattering

Lundstrom derives the transition rates associated with ODS as [175]

$$
\begin{aligned}
S_{\pm}(\mathbf{k},\mathbf{k}') &= \frac{\pi D_{\mathrm{op}}^2}{\rho\Omega\omega(\mathbf{q})}\left(n(\omega(\mathbf{q}))+\frac{1}{2}\mp\frac{1}{2}\right)\delta(E(\mathbf{k}')-E(\mathbf{k})\mp\hbar\omega(\mathbf{q})) \\
&= \frac{\pi D_{\mathrm{op}}^2}{\hbar\rho\Omega v(\mathbf{k})\omega(\mathbf{q})\,q}\left(n(\omega(\mathbf{q}))+\frac{1}{2}\mp\frac{1}{2}\right)\delta\left(\pm\cos\theta+\frac{q}{2k}\mp\frac{\omega(\mathbf{q})}{v(\mathbf{k})\,q}\right), \qquad (4.48)
\end{aligned}
$$

where D_{op} is the optical deformation potential, and ρ is the material's mass density.

Scattering rate

We compute the scattering rate via Eq. (4.17), where the transition rates $S_{\pm}(\mathbf{k},\mathbf{q})$ are given by Eq. (4.48)

$$
\begin{aligned}
\tau_{\mathrm{ODS}}^{-1}(\mathbf{k}) &= \frac{\pi D_{\mathrm{op}}^2}{\rho\hbar v(\mathbf{k})}\int\frac{d\mathbf{q}}{(2\pi)^3}\frac{1}{\omega(\mathbf{q})\,q}\Big[n(\omega(\mathbf{q}))\,\delta(E(\mathbf{k}')-E(\mathbf{k})-\hbar\omega(\mathbf{q}))\,\delta(\mathbf{k}'+\mathbf{k}-\mathbf{q})) \\
&+ (n(\omega(\mathbf{q}))+1)\,\delta(E(\mathbf{k}')-E(\mathbf{k})+\hbar\omega(\mathbf{q}))\,\delta(\mathbf{k}'+\mathbf{k}+\mathbf{q})\Big). \qquad (4.49)
\end{aligned}
$$

To proceed, we exploit the assumed dispersionless nature of the optical phonons to take factors of the phonon distribution function $n(\omega(\mathbf{q}))=n(\omega_0)$ outside of integrals over $\mathbf{q}$, and we replace the Dirac delta distributions according to Eq. (4.26), giving

$$
\begin{aligned}
\tau_{\mathrm{ODS}}^{-1}(\mathbf{k}) &= \frac{\pi D_{\mathrm{op}}^2}{(2\pi)^2\rho\hbar v(\mathbf{k})\,\omega_0}\Big[n(\omega_0)\int_{-1}^{+1}d(\cos\theta)\int_0^{\infty}dq\,q\,\delta\left(\cos\theta+\frac{q}{2k}-\frac{\omega_0}{v(\mathbf{k})\,q}\right) \\
&+ (n(\omega_0)+1)\int_{-1}^{+1}d(\cos\theta)\int_0^{\infty}dq\,q\,\delta\left(-\cos\theta+\frac{q}{2k}+\frac{\omega_0}{v(\mathbf{k})\,q}\right)\Big], \qquad (4.50)
\end{aligned}
$$

where the trivial integration over the azimuthal angle ϕ has been performed.

Integrating with respect to $\cos\theta$ we obtain

$$
\begin{aligned}
\tau_{\mathrm{ODS}}^{-1}(\mathbf{k}) &= \frac{\pi D_{\mathrm{op}}^2}{(2\pi)^2\rho\hbar v(\mathbf{k})\,\omega_0}\left[n(\omega_0)\int_{q_{+,\min}}^{q_{+,\max}}dq\,q+\theta(E(\mathbf{k})-\hbar\omega_0)\,(n(\omega_0)+1)\int_{q_{-,\min}}^{q_{-,\max}}dq\,q\right] \\
&= \frac{D_{\mathrm{op}}^2}{8\pi^2\rho\hbar v(\mathbf{k})\,\omega_0}\left[n(\omega_0)\,(q_{+,\max}^2-q_{+,\min}^2)+\theta(E(\mathbf{k})-\hbar\omega_0)\,(n(\omega_0)+1)\,(q_{-,\max}^2-q_{-,\min}^2)\right] \\
&= \frac{D_{\mathrm{op}}^2}{8\pi^2\rho\hbar v(\mathbf{k})\,\omega_0}\,\frac{4k\sqrt{2m^*}}{\hbar}\left[n(\omega_0)\,\sqrt{E+\hbar\omega_0}+\theta(E(\mathbf{k})-\hbar\omega_0)\,(n(\omega_0)+1)\,\sqrt{E-\hbar\omega_0}\right]. \qquad (4.51)
\end{aligned}
$$

Finally, we substitute $v(\mathbf{k})=\frac{\hbar k}{m^*}$ and $k=\frac{\sqrt{2m^*E}}{\hbar^2}$ to obtain the desired energy-dependent expression for the scattering rate

$$\tau_{\mathrm{ODS}}^{-1}(E) = \frac{\pi D_{\mathrm{op}}^2}{\rho\omega_0}\Big(n(\omega_0)\,D(E+\hbar\omega_0) + \theta(E-\hbar\omega_0)\,(n(\omega_0)+1)\,D(E-\hbar\omega_0)\Big)\,, \tag{4.52}$$

where, $D(E)$ is the DOS per unit volume (Eq. (4.5)) of the (non-degenerate) band $E(\mathbf{k}) = \frac{\hbar^2k^2}{2m^*}$. Note that Eq. (4.52) appears to differ by a factor of 2 compared to Lundstrom's Eq. (2.86) [175]. This is due to Lundstrom's definition of the DOS, which implicitly includes the electron spin degeneracy and is hence a factor of 2 larger than that employed here. As such, the two expressions are in direct agreement.

Collision operator

We compute the collision operator via Eq. (4.18), where the transition rates $S_{\pm}(\mathbf{k},\mathbf{k}')$ are given by Eq. (4.48)

$$\begin{aligned}\left(\frac{\partial f(E(\mathbf{k}))}{\partial t}\right)_{\mathrm{ODS}} &= \frac{\pi D_{\mathrm{op}}^2}{\rho}\int\frac{d\mathbf{q}}{(2\pi)^3}\frac{1}{\omega(\mathbf{q})}\Big[n(\omega(\mathbf{q}))\,f(E(\mathbf{k}'))\,\delta(E(\mathbf{k})-E(\mathbf{k}')-\hbar\omega(\mathbf{q}))\\ &+ (n(\omega(\mathbf{q}))+1)\,f(E(\mathbf{k}'))\,\delta(E(\mathbf{k})-E(\mathbf{k}')+\hbar\omega(\mathbf{q}))\\ &- n(\omega(\mathbf{q}))\,f(E(\mathbf{k}))\,\delta(E(\mathbf{k}')-E(\mathbf{k})-\hbar\omega(\mathbf{q}))\\ &- (n(\omega(\mathbf{q}))+1)\,f(E(\mathbf{k}))\,\delta(E(\mathbf{k}')-E(\mathbf{k})+\hbar\omega(\mathbf{q}))\Big]\,.\end{aligned} \tag{4.53}$$

Again, we apply $\delta(-x)=\delta(x)$ to the first and second terms, and then gather terms, giving

$$\begin{aligned}\left(\frac{\partial f(E(\mathbf{k}))}{\partial t}\right)_{\mathrm{ODS}} &= \frac{\pi D_{\mathrm{op}}^2}{(2\pi)^3\rho}\int d\mathbf{q}\,\frac{1}{\omega(\mathbf{q})}\;\times\\ &\Big[\Big((n(\omega(\mathbf{q}))+1)\,f(E(\mathbf{k}'))-n(\omega(\mathbf{q}))\,f(E(\mathbf{k}))\Big)\,\delta(E(\mathbf{k}')-E(\mathbf{k})-\hbar\omega(\mathbf{q}))\\ &+ \Big(n(\omega(\mathbf{q}))\,f(E(\mathbf{k}'))-(n(\omega(\mathbf{q}))+1)\,f(E(\mathbf{k}))\Big)\,\delta(E(\mathbf{k}')-E(\mathbf{k})+\hbar\omega(\mathbf{q}))\Big]\,.\end{aligned} \tag{4.54}$$

Next, we use the assumed dispersionless nature of the optical phonons to take factors of the phonon distribution function outside of integrals over $\mathbf{q}$, and replace the Dirac delta distributions following Eq. (4.26)

$$\left(\frac{\partial f(E(\mathbf{k}))}{\partial t}\right)_{\text{ODS}} = \frac{\pi D_{\text{op}}^2}{(2\pi)^3 \rho \hbar v(\mathbf{k})\,\omega_0}\Bigg[(n(\omega_0)+1)\int d\mathbf{q}\,\frac{f(E(\mathbf{k}'))}{q}\,\delta\left(\cos\theta+\frac{q}{2k}-\frac{\omega_0}{v(\mathbf{k})\,q}\right) - n(\omega_0)\int d\mathbf{q}\,\frac{f(E(\mathbf{k}))}{q}\,\delta\left(\cos\theta+\frac{q}{2k}-\frac{\omega_0}{v(\mathbf{k})\,q}\right) + n(\omega_0)\int d\mathbf{q}\,\frac{f(E(\mathbf{k}'))}{q}\,\delta\left(-\cos\theta+\frac{q}{2k}+\frac{\omega_0}{v(\mathbf{k})\,q}\right) - (n(\omega_0)+1)\int d\mathbf{q}\,\frac{f(E(\mathbf{k}))}{q}\,\delta\left(-\cos\theta+\frac{q}{2k}+\frac{\omega_0}{v(\mathbf{k})\,q}\right)\Bigg]. \tag{4.55}$$

Performing the integration with respect to (i) the azimuthal angle ϕ, and (ii) $\cos\theta$, which utilises the sifting property of the Dirac delta distributions, we obtain

$$\left(\frac{\partial f(E(\mathbf{k}))}{\partial t}\right)_{\text{ODS}} = \frac{\pi D_{\text{op}}^2}{(2\pi)^2 \rho \hbar v(\mathbf{k})\,\omega_0}\Bigg[\Big((n(\omega_0)+1)\,f(E+\hbar\omega_0)-n(\omega_0)\,f(E)\Big)\int_{q_{+,\max}}^{q_{+,\min}} dq\,q + \theta(E(\mathbf{k})-\hbar\omega_0)\Big(n(\omega_0)\,f(E-\hbar\omega_0)-(n(\omega_0)+1)\,f(E)\Big)\int_{q_{-,\max}}^{q_{-,\min}} dq\,q\Bigg]. \tag{4.56}$$

The remainder of the evaluation follows the computation of the scattering rate above, yielding the following energy-dependent expression for the collision operator associated with ODS

$$\left(\frac{\partial f(E(\mathbf{k}))}{\partial t}\right)_{\text{ODS}} = \frac{\pi D_{\text{op}}^2}{\rho\omega_0}\Bigg[\Big((n(\omega_0)+1)\,f(E+\hbar\omega_0)-n(\omega_0)\,f(E)\Big)D(E+\hbar\omega_0) + \theta(E-\hbar\omega_0)\Big(n(\omega_0)\,f(E-\hbar\omega_0)-(n(\omega_0)+1)\,f(E)\Big)D(E-\hbar\omega_0)\Bigg]. \tag{4.57}$$

4.4.5 Intervalley scattering

There exist constant energy surfaces of the CB structure for different semiconductor alloys, which consist of different valleys. When a high electric field is applied, electrons can get accelerated from an initial valley $'i'$ to a final valley $'f'$ resulting in a very large change in momentum associated with phonons. These phonons are known as intervalley phonons. As discussed in Sec. 4.2, for GaAs CB, the valleys are not energetically equivalent, there is a difference of 0.284 eV between the L and Γ valley minimum energy. At a higher electric field, when the electrons in the Γ valley acquire higher energy than this energy separation, the scattering of electrons from Γ to L is possible. Furthermore, the scattering of electrons within the L valleys (L-L) and from L to Γ (L - Γ) need to be considered. In the case of the intervalley scattering, optical phonons are involved and the associated scattering rate and collision operator bear resemblance to that of the optical phonon scattering as presented in Eqs. (4.52) and (4.57) respectively, but with the difference that the

DOS in the final valley i.e. the valley to which electrons are scattering, must be considered. The scattering rate and the associated collision operator due to the intervalley scattering are given by Eq. (4.58) and (4.59) respectively,

$$\tau_{if}^{-1}(E) = \frac{\pi N_f D_{if}^2}{\rho\omega_{if}}\Big(n(\omega_{if})\,D_f(E+\hbar\omega_{if}) + \theta(E-\hbar\omega_{if})\,(n(\omega_{if})+1)\,D_f(E-\hbar\omega_{if})\Big)\,, \tag{4.58}$$

$$\begin{aligned}\frac{\partial f(E)}{\partial t} &= \frac{\pi N_f D_{if}^2}{\rho\omega_{if}}\Big[\Big((n(\omega_{if})+1)\,f(E+\hbar\omega_{if}) - n(\omega_{if})\,f(E)\Big)\,D_f(E+\hbar\omega_{if}) \\ &+ \theta(E-\hbar\omega_{if})\Big(n(\omega_{if})\,f(E-\hbar\omega_{if}) - (n(\omega_{if})+1)\,f(E)\Big)\,D_f(E-\hbar\omega_{if})\Big]\,,\end{aligned} \tag{4.59}$$

where D_f corresponds to the DOS of the final valley f, and N_f is the number of available final valleys to which electrons can scatter,and D_{if} is the deformation potential for intervalley optical phonon scattering.

4.4.6 Acoustic phonon scattering

When the scattering of electrons is due to longitudinal mode acoustic phonons, then it is known as acoustic phonon scattering. At a given temperature T, the scattering rate due to acoustic phonons is given by

$$\tau_{APS}^{-1}(E) = \left(\frac{\pi D_{ac}^2 k_{\mathrm{B}}}{\hbar\rho v_s^2}\right) D(E)\,T\,, \tag{4.60}$$

where D_{ac} refers to the acoustic deformation potential, and ρ and v_s represent the mass density and sound velocity respectively. In our calculations, we consider this scattering as an elastic process.

4.4.7 Alloy scattering

The process of replacing host atoms with equivalent atoms from other materials with the goal of modifying the host material's electrical and optical properties is known as semiconductor alloying. Semiconductor alloys are widely useful in electronic and optoelectronic devices. As a result, extensive research is carried out to obtain the appropriate band gap, band offset, and lattice parameter properties for a given application. For example we saw in Chapter. 3 that when a very small amount (x) of nitrogen (bismuth) is introduced into III-V semiconductor alloys, there is a drastic change in the band gap properties, impacting their performance as field effect transistors, (FETs) and solar cells. These types of alloys are known as highly mismatched alloys. When Ge atoms are replaced with Sn atoms, the energy gap changes from being indirect to direct at a Sn composition (x) of $\sim 8\%$. Alloy scattering refers to the carrier scattering caused by the substitution of these atoms. First-principles calculations [189], tight binding [190] are used to investigate the composition-dependent scattering rate. In Chapter. 5, we will investigate the field-dependent electron transport characteristics of $Ge_{1-x}Sn_x$, taking into account the alloy scattering caused by

Parameter	Value
Mass density, ρ (g cm^{-3})	5.36
Lattice constant, a_0 (Å)	5.462
Sound velocity, v_s (cm s^{-1})	5.24 $\times 10^5$
Dielectric constant,	
High frequency, κ_∞	10.92
Low frequency, κ_0	12.90
Electron effective mass,	
Γ valley, m_Γ (m_0)	0.067
L valley, m_L (m_0)	0.286
Acoustic Deformation potential,	
Γ valley, $D_{ac,\Gamma}$ (eV)	7.01
L valley, $D_{ac,L}$ (eV)	9.2
Optical deformation potential,	
$\Gamma \rightarrow L$ scattering, $D_{\Gamma L}$ (eV m^{-1})	1 $\times 10^{10}$
$L \rightarrow$L scattering, D_{LL} (eV m^{-1})	1 $\times 10^{10}$
Inter valley phonon energy,	
$\hbar\omega_{\Gamma L}$, (meV)	27.8
$\hbar\omega_{LL}$, (meV)	29.0
Optical phonon energy ($\hbar\omega$)(meV)	35.36
Energy separation between Γ and L valley, Δ $E_{\Gamma L}$ (meV)	284

TABLE 4.1: Transport parameters for GaAs [166].

the presence of Sn atoms. The model used to determine the alloy scattering rate will be introduced in Sec. 5.3.2.

4.5 Field dependent transport for bulk GaAs by Boltzmann's transport equation

Now that the principles of electron transport and the scattering process have been discussed, we will implement these ideas to present the field-dependent electron transport model that we use to compute the electron drift velocity and mobility for GaAs.

Initial setup at zero field ($F = 0$)

The zero-field calculation is the first step, from which we can proceed to the field-dependent electron transport calculation. We specify our physical system at this stage, which includes the inclusion of specific scattering processes, the number of valleys to be considered, the electron temperature, the energy grid, and many more. For the present calculation, we have used the transport parameters [166] as listed in Table. 4.1. Based on previous two-valley analyses, which demonstrate that the key features of field-dependent electron transport in GaAs can be captured quantitatively using a model that incorporates the lowest energy Γ and L CB valleys, we include both the Γ and L valley in the CB in our calculation. Following that, we define the energy range of electrons over which we will do our calculation. To do so, we choose the zero of energy to lie at

the CB minimum and hence this corresponds, e.g., to the bottom of the Γ valley in GaAs, and to the bottom of the L valley in Ge. For GaAs, the L valley is taken to be 0.284 eV [166] above the Γ valley. Therefore the Γ valley energy starts from CB minimum, and the L valley energy begins beyond 0.284 eV. We then explicitly select the maximum energy E_{max} and an energy grid step size, which we take as $\Delta E = 0.1\,\hbar\omega$ [166], where $\hbar\omega$ is the optical phonon energy. The L valley energy grid begins beyond 284 meV. This produces an energy grid for each valley with which inelastic optical phonon scattering events are commensurate, allowing for accurate numerical evaluation of the associated scattering rates and collision operators. At zero field, we assume that the electron distribution is the Maxwell-Boltzmann distribution for both the Γ and L valleys, given by

$$f = \exp\left(-\frac{E}{k_{\mathrm{B}}T}\right), \tag{4.61}$$

where k_{B} is Boltzmann's constant and T is the temperature of the electron population, which at zero-field we assume to be equal to the lattice temperature. At equilibrium condition the electron distribution function for both the valleys are in Boltzmann's distribution.

We presume that $f_\Gamma = f_L = 0$ for energies greater than a maximum energy $E_{\max}$, which we set to be at least one eV above the CB minimum. The scattering mechanisms mentioned in Sec. 4.4 are now being recalled. In this case, however, we focus on the three most important mechanisms for determining field-dependent electron transport in intrinsic GaAs: polar optical phonon, acoustic deformation potential, and inter valley (Γ-L, L-Γ and L-L) optical phonon scattering. Using Eqs. (4.41), (4.60) and (4.58), we calculate the corresponding energy-dependent scattering rates for each of these mechanisms as shown in Fig. 4.2 and 4.3 for Γ and L valley respectively. Finally, we determine the total scattering rate for both Γ and L valley using Mattheisen's rule, per Eqs. (4.62) and (4.63) respectively. The total scattering rate associated with each valley is then used to compute the collision operator describing the acceleration of electrons by an applied electric field (see Eq. (4.14)).

$$\tau_\Gamma^{-1} = \tau_{APS}^{-1} + \tau_{POS}^{-1} + \tau_{\Gamma L}^{-1}\,. \tag{4.62}$$

$$\tau_L^{-1} = \tau_{APS}^{-1} + \tau_{LL}^{-1} + \tau_{L\Gamma}^{-1}\,. \tag{4.63}$$

Following the Boltzmann's transport equation ($\frac{\partial f(E(\mathbf{k}))}{\partial t}$) resulting from the applied electric field and scattering mechanism as stated in Eq. (4.6), the equivalent transport equations for Γ and L valley are given by Eq. (4.64) and (4.65) respectively.

$$\left(\frac{\partial f_\Gamma}{\partial t}\right) = \left(\frac{\partial f_\Gamma}{\partial t}\right)_{F_n} + \left(\frac{\partial f_\Gamma}{\partial t}\right)_{POS} + \left(\frac{\partial f_\Gamma}{\partial t}\right)_{\Gamma L}, \tag{4.64}$$

$$\left(\frac{\partial f_L}{\partial t}\right) = \left(\frac{\partial f_L}{\partial t}\right)_{F_n} + \left(\frac{\partial f_L}{\partial t}\right)_{POS} + \left(\frac{\partial f_L}{\partial t}\right)_{L\Gamma} + \left(\frac{\partial f_L}{\partial t}\right)_{LL}, \tag{4.65}$$

where f_Γ and f_L represent the symmetric part of the distribution functions in the Γ and L valleys respectively and the first term in both the expressions stands for the rate of change in distribution

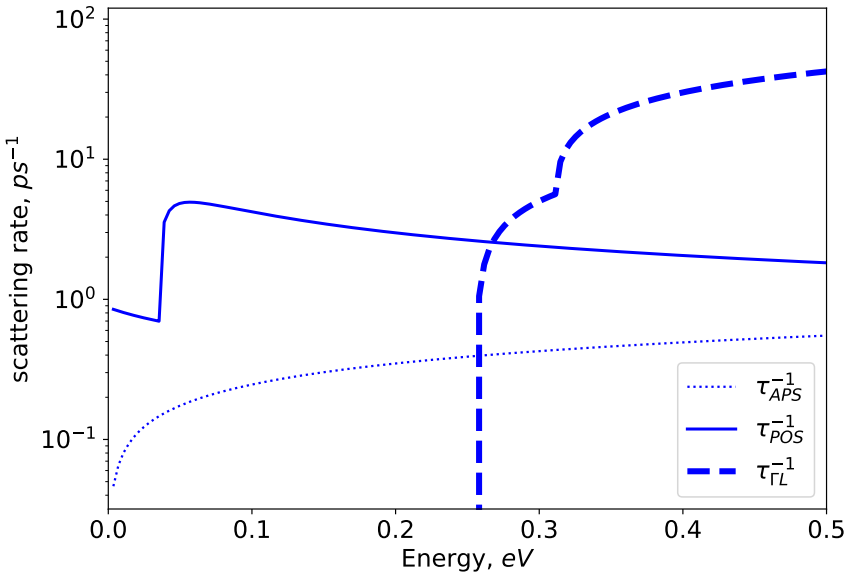

FIGURE 4.2: Calculated acoustic phonon (dotted line), polar optical phonon (solid line), and Γ to L inter valley optical phonon (dashed line) scattering rates as a function of band energy E for parabolic Γ valley in GaAs.

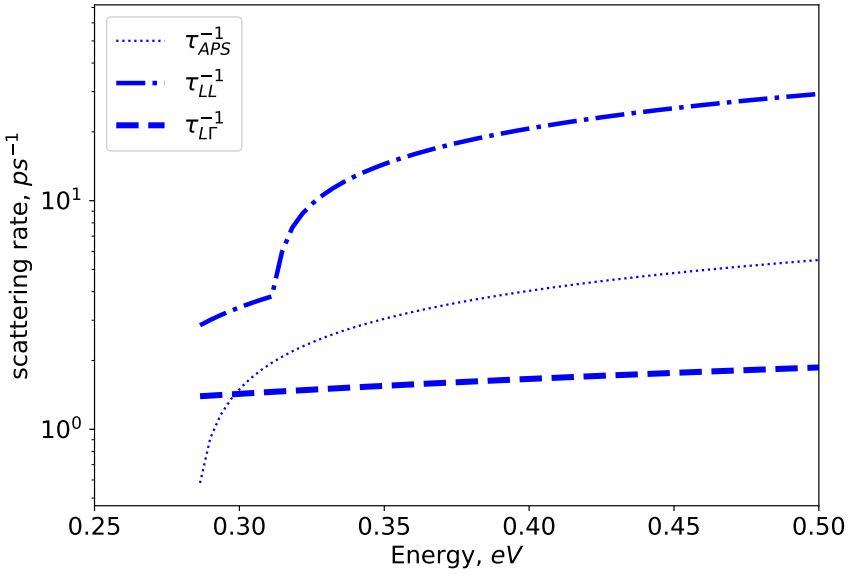

FIGURE 4.3: Calculated acoustic phonon (dotted line), equivalent L to L (dash-dot line), and L to Γ (dashed line) inter valley optical phonon scattering rates as a function of band energy E for parabolic L valley in GaAs.

function because of the applied electric field, which we calculate by using Eq. (4.14). The computations of the remaining collision operators due to polar optical and inter-valley scattering are carried out via Eq. (4.47) and (4.59) respectively.

At each electric field strength F_n, where n denotes the n^{th} index of the field strengths on a discrete grid of applied electric field strengths F, we use the steady state distribution functions that were obtained from the preceding field, F_{n-1} to obtain the corresponding time-dependent coupled transport equations (Eqs. (4.64) and (4.65)). In order to find the steady state distribution

functions, f_{Γ_n}, f_{L_n}, we then solve these equations (Eqs. (4.64) and (4.65)) via explicit time-stepping methods with a uniform time grid Δt employing Euler's rule given by,

$$f_\Gamma(E, t+\Delta t) = f_\Gamma(E,t) + \frac{\partial f_\Gamma}{\partial t}(E,t) \times \Delta t\,, \tag{4.66}$$

$$f_\mathrm{L}(E, t+\Delta t) = f_\mathrm{L}(E,t) + \frac{\partial f_\mathrm{L}}{\partial t}(E,t) \times \Delta t\,. \tag{4.67}$$

The above equations represent the relation between the initial and final distribution function within a very small increment in the time step Δt. This time step also changes with the variation in the applied electric field and scattering rate. To pull out the electrons from Boltzmann's distribution, we apply the first electric field F_1 ($F_1 = 1$ kV cm^{-1}). In order to find the new steady-state distribution function because of this applied electric field, F_1, we would first compute all the collision operators from the Boltzmann's distribution function ($F = 0$) by using Eqs. (4.64) and (4.65). The solution of these equations for the distribution function for both Γ and L valley start by updating the f_Γ and f_L by using Eq. (4.66) and (4.67) respectively. We start with a time step $\Delta t = 0.5$ fs and calculate $f_\Gamma(E, t+\Delta t)$ ($f_L(E, t+\Delta t)$) by substituting the right side of the Eq. (4.66) (Eq. (4.67)), with the previous distribution function, $f_\Gamma(E,t)$ ($f_L(E,t)$) and the corresponding collision operator $\frac{\partial f_\Gamma(E,t)}{\partial t}$ ($\frac{\partial f_L(E,t)}{\partial t}$) which is computed by using Eq. (4.64) (Eq. (4.65)). We repeat this procedure N number of times until we accomplish the steady state condition – i.e. until the change in distribution function, $\frac{\partial f_\Gamma}{\partial t} \times \Delta t$ ($\frac{\partial f_L}{\partial t} \times \Delta t$), becomes negligible compared to the magnitude of the distribution functions at all energies $0 \leq E \leq E_\mathrm{max}$. For the present calculation, we find the temporal evolution of distribution functions until 5 ps, which means N will be 5000, and find that the steady state condition is achieved within this time period. Now using the steady-state distribution function obtained at $F_1 = 1$ kV cm^{-1}, we proceed to determine the steady-state distribution function at the next electric field ($F_2 = 2$ kV cm^{-1}), and so on. For low electric fields $F \leq 1$ kV cm^{-1} we find that a time step $\Delta t = 0.5$ fs is sufficiently small to allow for stable temporal evolution of the coupled Γ and L valley BTEs. We note from Eq. (4.14) that the collision operator describing electron acceleration by the applied electric field is $\propto F^2$. This important contribution to the right-hand sides of Eqs. (4.66) and (4.67) increases strongly with increasing F, such that the product of the total collision operator and Δt can grow rapidly and introduce numerical instability. To control this behaviour, for applied electric fields $F > 1$ kV cm^{-1} we down sample the time step as $\Delta t \rightarrow \Delta t \times F^{-2}$, where F is the magnitude of the applied electric field in units of kV cm^{-1}. As a consequence of the time step down sampling, the number of repetitions required to determine the temporal dynamics of the distribution functions increases as $N \rightarrow N \times F^2$. The products of Δt and the collision operator on the right-hand sides of Eqs. (4.66) and (4.67) then remain "small", allowing for stable temporal evolution of the valley electron distribution functions. Now that the steady state electron distribution functions for the Γ and L valleys at each electric field have been established, we can utilise them to calculate the corresponding electron transport properties. The total carrier (n_{tot}) and current densities (J_{tot}) [166] associated with the electron distribution function f_v are given by

$$n_{tot} = \sum_v g_v \int f_v\left(E\right) D_v\left(E\right)\ dE\ , \tag{4.68}$$

$$J_{tot} = -\frac{2}{3} e^2 F \sum_v \frac{g_v}{m_v^*} \int \frac{\gamma_v(E) f_v^{'}\left(E\right) D_v\left(E\right)}{\left(\gamma^{'}\left(E\right)\right)^2 \tau_v^{-1}(E)} dE\,, \tag{4.69}$$

where v indexes the valleys, g_v is the valley degeneracy, m_v^* is the electron effective mass in valley v, D_v is the DOS of the single valley v (i.e. without spin or valley degeneracy), and τ_v^{-1} is the total electron scattering rate in valley v, which can be calculated from Eq. (4.62) and (4.63) for the Γ and L valleys respectively. The mobility μ and drift velocity v_d are computed as follows

$$\mu = \frac{J_{tot}}{eFn_{tot}}\,, \tag{4.70}$$

$$v_d = \mu F\,, \tag{4.71}$$

where J_{tot} and n_{tot} are the total current and carrier densities (i.e. summed over all valleys (Γ and L valleys)) respectively. Substituting the current density (J_{tot}) and carrier density (n_{tot}) in Eq. (4.70), we get mobility as follows

$$\mu = -\frac{2e}{3} \frac{\sum_v \frac{g_v}{m_v^*} \int \frac{\gamma_v(E) f_v^{'}(E) D_v(E)}{\left(\gamma^{'}(E)\right)^2 \tau_v^{-1}(E)} dE}{\sum_v g_v \int f_v\left(E\right) D_v\left(E\right)\ dE}\,. \tag{4.72}$$

4.6 Results and discussion

Having overviewed the BTE and its implementation, we now employ this model to benchmark our code by calculating the electronic transport properties of GaAs in the presence of an applied electric field. Figure 4.4 displays the calculated distribution of electrons in the Γ and L valleys at zero field and for five distinct field strengths (1, 2, 5, 10, 15 kV cm^{-1}). When the first electric field F = 1 kV cm^{-1} (Fig. 4.4 (b)) is applied, the electrons are pulled away from equilibrium; however, the electron distribution in the L valley remains close to the Boltzmann distribution function (Fig. 4.4 (a)). The electron distribution differs slightly from the preceding field at the next electric field F = 2 kV cm^{-1} (Fig. 4.4 (c)). Comparing the Γ valley distribution function to Boltzmann's distribution at lower energies, we can see a distinct difference. At field strength F = 5 kV cm^{-1} (Fig. 4.4 (d)), the electrons start to populate at higher energy levels. When the field strength further increases (Fig. 4.4 (e), (f)), the electrons scatter into the higher energy L valleys, at which point the electron mobility and drift velocity then start to be dominated by the transport characteristics of that valley.

Figure 4.5 shows the variation of electron drift velocity as a function of applied electric field strength F, where we also include the experimental measurements from Ruch and Kino [191], Ashida et al. [192], and Houston et al. [193], as well as theoretical computations using the Monte Carlo method [194] and from previous work in the Photonics Theory group [166]. The current calculation

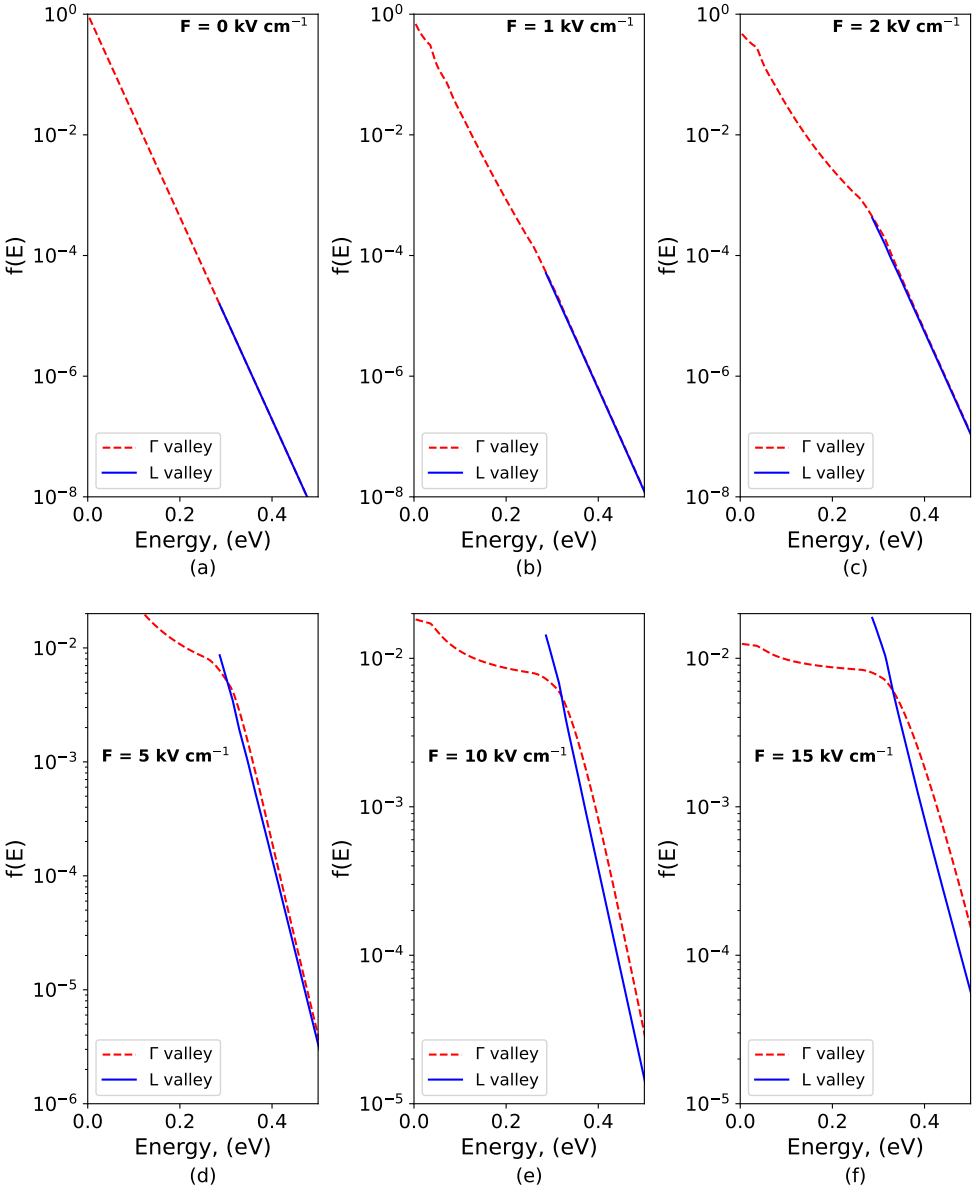

FIGURE 4.4: Steady state electron distribution functions in Γ and L valley for GaAs at different electric field strengths (a) $F = 0$, (b) $F = 1$ (c) $F = 2$, (d) $F = 5$, (e) $F = 10$, and (f) $F = 15$ kV cm^{-1}.

is depicted by a solid magenta line that demonstrates Gunn-effect-like behaviour. We find that the peak drift velocity is 7500 cm s^{-1} around an electric field of 3 kV cm^{-1}. The electric field at which the drift velocity is at its maximum value is known as the threshold electric field and the NDR region begins from this threshold electric field. This is because beyond the threshold electric field, the drift velocity decreases as a function of the electric field. So, for the current calculation, NDR starts around 3 kV cm^{-1}, after which the velocity decreases rapidly until 7-8 kV cm^{-1} beyond which it varies very slowly and tends to saturate. The computed threshold electric field is in good agreement with other calculations and experimental measurements. However, the magnitude of the peak drift velocity is underestimated in comparison to the experimental observation by Ruch and Kino [191], which are represented by green open circles in Fig. 4.5. These measurements are claimed to be the first-ever drift velocity versus field measurement.

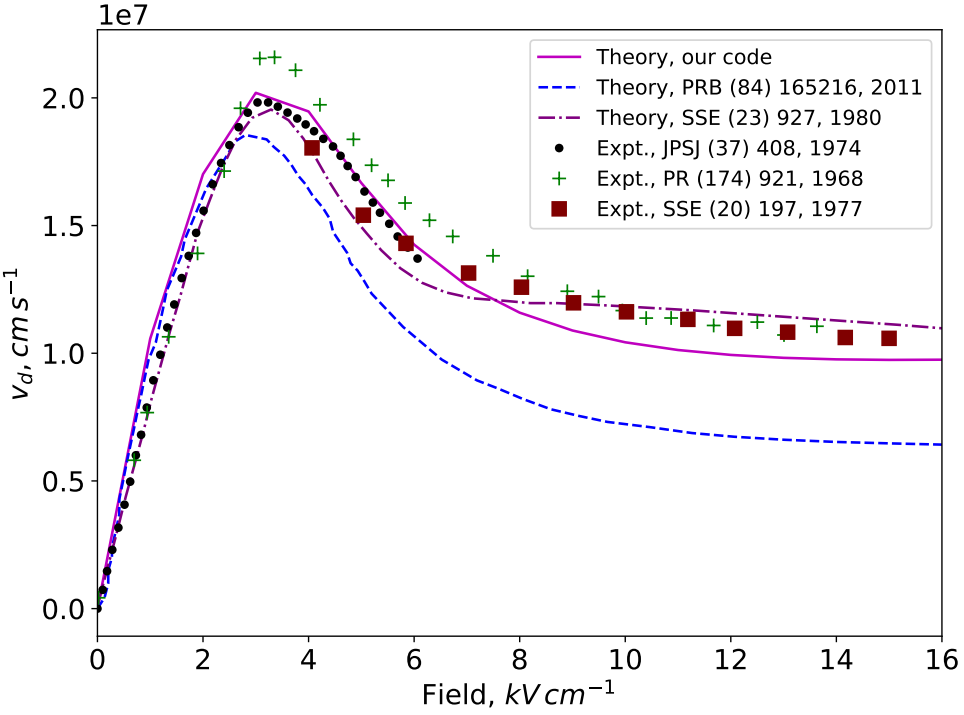

FIGURE 4.5: Drift velocity in GaAs as a function of applied electric field F, based on code presented here (magenta line), compared to previous experimental measurements from Ruch and Kino [191] (green plus symbol), Ashida et al. [192] (black dot symbol) and Houston et al. [193] (maroon square symbol) and the theoretical calculations [194] (dash-dot maroon line), [166] (dashed blue line).

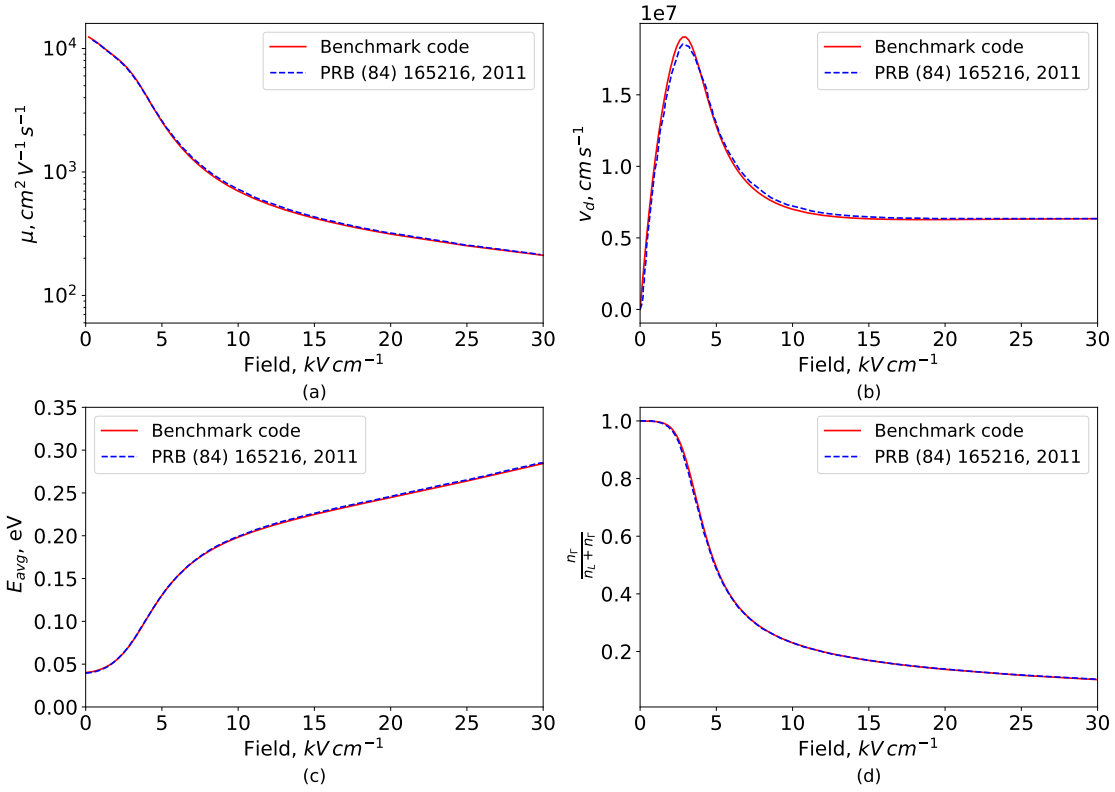

FIGURE 4.6: Benchmarking of electron transport properties for GaAs [166]: (a) mobility, (b) drift velocity, (c) average energy, and (d) fraction of carriers.

It can also be seen in Fig. 4.5 how the current result differs from the group's earlier findings [166], despite the fact that the transport model and the parameters are identical in both instances. From detailed testing and comparing all the equations with the reference paper [176] and with the previous code, we find that these differences are due to a number of minor errors in the previous code [166]. We observed three errors in the previous code. Firstly, there was improper handling of effective mass in the collision operator ($\frac{\partial f}{\partial t}$) for polar optical scattering in the L valley. Secondly, an incorrect energy was chosen for the onset of phonon absorption (emission) in the $\frac{\partial f}{\partial t}$ term for Γ to L (L to Γ) inter valley scattering. The phonon absorption (emission) term for this process - i.e. the first (second) of the two terms in curly brackets in Eq. (30) in Ref. [166] should switch on at energy $E = E_L - \hbar\omega_{\Gamma L}$ ($E = E_{L0}$) but instead switches on at energy $E = E_{L0}$ ($E = E_L + \hbar\omega_{\Gamma L}$). Finally, the L valley contribution to total current density J_{tot} is underestimated by a factor of $4^{1/3} \sim 1.59$, which means that there are associated errors in the mobility and drift velocity (which primarily manifest at high electric fields, when L valley states become populated due to inter valley scattering). For the purposes of benchmarking, we deliberately introduced these three errors into our code, and verified that this allows to exactly reproduce the relevant results in Ref. [166], as shown in Fig. 4.6. Following this explicit confirmation and benchmarking, we permanently removed these errors from our calculations.

Despite these errors, the conclusions of Ref. [166] all remain valid. Ref. [166] was primarily focused on investigating the electronic structure of the dilute nitride alloy GaN_xAs_{1-x} and the impact of nitrogen (N) incorporation on the alloy's transport properties. The incorporation of N strongly modifies the CB structure of GaAs, severely limiting the alloy mobility. The descriptions of all the relevant scattering mechanisms and collision operators and, most importantly, of the band dispersion ($\gamma(E)$) are all correctly incorporated in [166], so that its conclusions on how N incorporation strongly modify the band dispersion and electron mobility remain unchanged, despite the errors that were found in the code.

4.7 Conclusion

In this chapter, we presented the BTE as a means to calculate the electron transport properties of semiconductor materials. We first reviewed some of the key features of the band structure relevant to electron transport. We then gave an overview of the Boltzmann transport model and described some of the key scattering mechanisms that limit electron mobility in GaAs and in other semiconductor materials. Having outlined the method that we use to solve Boltzmann's equation, we then applied it to calculate electron mobility as a function of the applied electric field in GaAs. This calculation served both to illustrate the method and also to validate the code developed here compared to previous calculations. Having developed and established the code, we shall next apply it in Chapter. 5 to investigate the evolution of the electron transport properties of $Ge_{1-x}Sn_x$ alloys as the alloys evolve from an indirect to a direct gap semiconductor with increasing Sn composition x.

Chapter 5

Theory of field-dependent electron transport in $Ge_{1-x}Sn_x$ alloys

5.1 Introduction

$Ge_{1-x}Sn_x$ alloys are not only compatible with existing Si-based manufacturing processes, but they can also exhibit a direct fundamental band gap similar to that in III-V semiconductors such as GaAs [195, 196]. In addition, they also enable strain engineering and band gap engineering by regulating Sn composition and substrate lattice constant. Thus they have potential applications in Si-based optoelectronic devices such as lasers, photodetectors, and light emitting diodes (LEDs). An earlier publication [79] proposed the possibility of increased mobility in $Ge_{1-x}Sn_x$ alloys in comparison to Ge, which makes $Ge_{1-x}Sn_x$ an attractive candidate for electronic device applications. Si-based $Ge_{1-x}Sn_x$ photo-detectors [70, 197] offer better optical responsivity for mid-infrared imaging applications in comparison to Ge-based photodiodes. Liu et al. [198] have presented a vertical p-i-n heterojunction configured $Ge_{1-x}Sn_x$ waveguide photodetector, compatible with complementary metal-oxide semiconductor technology, which operates around 2 μm wavelength range with high optical responsivity at 5.28% Sn composition. A recent study [69] has presented the design of a homojunction $Ge_{1-x}Sn_x$ photodetector, which could be very useful in electronic-photonic integrated circuits. Lasing has also been demonstrated from direct-gap $Ge_{1-x}Sn_x$ structures. Wirth et al. [61] demonstrated the first optically pumped $Ge_{1-x}Sn_x$ laser, with a Sn composition of 12.6% and an operating temperature of up to 90 K. Using a commercial chemical vapor deposition reactor, Zhou et al. [62] fabricated electrically injected $Ge_{1-x}Sn_x/Si_yGe_{1-x-y}Sn_x$ heterostructure lasers on a Si wafer. They observed a lasing threshold of 598 A/cm^2 at 10 K and a 2300 nm peak wavelength; the maximum lasing temperature recorded was 100 K. A recent work [199] reports room-temperature optically pumped lasing in a heterostructure $Ge_{0.828}Sn_{0.172}$ microdisk. Now if we turn our attention to electronic devices, $Ge_{1-x}Sn_x$ has been proposed to be a very promising option. Because of its higher carrier mobility than equivalent Ge films, polycrystalline $Ge_{1-x}Sn_x$ (poly-$Ge_{1-x}Sn_x$) film [200] was proposed as an ideal channel material for high-performance thin film transistors. There is evidence of enhanced mobility in $Ge_{1-x}Sn_x$-based n-channel MOSFETs [201] fabricated under different strain conditions. Recently Junk et al. [202] have demonstrated top-down-fabricated vertical gate-all-around $Ge_{1-x}Sn_x$ nano wire nMOSFETs.

By using infrared spectroscopic ellipsometry and electrical measurements, Costa et al. [203] have studied the transport parameters of n- and p-type $Ge_{0.98}Sn_{0.02}$ alloys. In a recently published article, Harshvardhan and his colleagues [204] proposed the device structure and presented theoretical simulations of $Ge_{1-x}Sn_x$-based mid-infrared lateral waveguide-based phototransistors with improved optical responsiveness on a Si platform and a Sn composition of $x = 6\%$. They have investigated the Gummel and output properties in both dark and light environments, as well as the optical gain and responsivity by using finite element method simulation. However, they have simply employed two composition-dependent linear equations to compute the electron and hole mobility. However, for a device engineer, it is essential to have a quantitative understanding of carrier transport in different semiconductor structures and their associated consequences for semiconductor device applications, as the transport characteristics have a direct impact on the efficiency of all these electronic devices. Therefore, carrier transport in semiconductors is undoubtedly a topic of interest, both fundamentally and in terms of current and future electronic devices.

We present here the first detailed theoretical analysis of electron transport in $Ge_{1-x}Sn_x$ alloys as a function of Sn composition and of the applied electric field. In Sec. 5.2, we outline some of the key characteristics of the conduction band (CB) structure of Ge and $Ge_{1-x}Sn_x$. We also describe how the band gap energies and effective masses vary with Sn composition, and how this ultimately affects carrier transport. We then describe in Sec. 5.3, the evolution of alloy scattering and optical deformation potential with Sn composition. Following the descriptions of the band structure and scattering rates in Sec. 5.2 and Sec. 5.3 respectively, we move on to Sec. 5.4 to examine how the carrier transport and mobility change with Sn composition at very low field, while the electrons are still in the thermal equilibrium – i.e. with their statistics described by a Maxwell-Boltzmann distribution function. Then, we focus in Sec. 5.5 on solving the Boltzmann transport equation (BTE) to investigate the carrier transport characteristics of Ge and $Ge_{1-x}Sn_x$ alloys as a function of composition and applied electric field. We compare our results with previously reported data, including both theory and experiment and then summarise and present our conclusions.

5.2 Theoretical model

Figure 5.1 shows the band structure of bulk Ge where the valence band (VB) maximum and the CB minimum are not located at the same wave vector $\mathbf{k}$, thus making it an indirect band gap semiconductor. The lowest CB edge is at the four-fold degenerate L point, which is about 0.145 eV below the singly degenerate Γ point. This small offset between the Γ and L bands can be overcome by either applying tensile hydrostatic or axial strain which decreases the Γ valley energy relative to the L valley energy or through heavy doping which facilitates the radiative Γ_{7c}-Γ_{8v} transition. [205, 206]. Interestingly, the band gap of Ge can also be manipulated by incorporating Sn into Ge. Sn, a group-IV element, exists in two allotropic forms. In this section, we will restrict our discussion to α-Sn which has a diamond cubic lattice similar to Ge. In the case of α-Sn, the CB minimum and VB maximum are aligned at the Γ point in $\mathbf{k}$–space, giving a direct band gap material. α-Sn is a semimetal, exhibiting a "negative" band gap of ≈ 0.4 eV [205], i.e. the

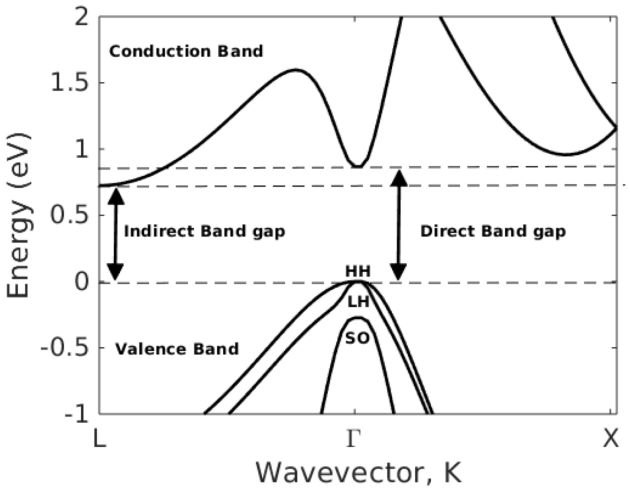

FIGURE 5.1: Band structure of bulk Ge (image taken from thesis of O'Halloran [59])

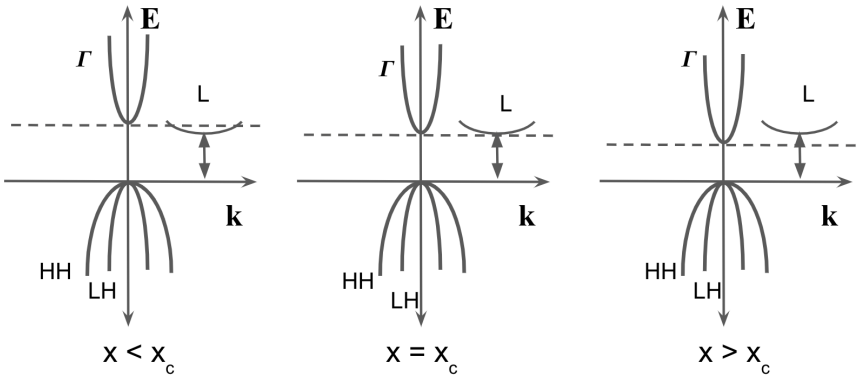

FIGURE 5.2: Schematic representation of the impact of Sn composition in the conduction band structure of Ge. The Sn composition where the transition from indirect to direct band gap occurs is denoted by x_c. The overall structure of the VBs remains unchanged within this composition range.

conduction minimum and VB maximum are overlapped at the Γ– point. Alloying Sn with Ge can then give a direct band gap semiconductor. With increasing Sn composition, the Γ valley energy decreases faster than the L valley energy and becomes the lowest CB minimum above a certain critical Sn composition. A schematic diagram showing the evolution of the band structure of $Ge_{1-x}Sn_x$ from indirect- to direct-gap is presented in Fig. 5.2. Several reports [207–209] exist of theoretical calculations of the $Ge_{1-x}Sn_x$ alloy electronic structure. However, there are conflicting reports regarding the critical Sn composition at which the indirect- to direct-gap transition occurs. According to early tight-binding simulations using the virtual crystal approximation, $Ge_{1-x}Sn_x$ was expected to become a direct gap material for Sn compositions > 20% [60]. Calculations with the supercell mixed-atom approach [68] predicted that the transition occurs at 17% Sn. A few reports such as first-principles calculations based on density functional theory (DFT) quote substantially lower Sn values of 8% [210] and 6.3% [211], for this transition. The band gap energies for the Γ

and L valley are obtained via a quadratic interpolation of the alloy band structure as presented in Eqs. (5.1) and (5.2) respectively

$$E_\Gamma(x) = (1-x)\,E_\Gamma^{Ge} + xE_\Gamma^{Sn} - b_\Gamma^{GeSn}x\,(1-x)\ , \tag{5.1}$$

$$E_L(x) = (1-x)\,E_L^{Ge} + xE_L^{Sn} - b_L^{GeSn}x\,(1-x)\ , \tag{5.2}$$

where b_Γ^{GeSn} and b_L^{GeSn} are the band gap bowing parameters for the Γ and L valley respectively. The variation in these bowing parameter values reported in different publications contributes to the deviation in the reported Sn compositions at which the indirect- to direct-gap transition occurs. Figure 5.3 exhibits the variation in these band energies as a function of Sn composition, as reported in some of the publications which include the bowing parameters, from Gupta et al. [210], Polak et al. [212], Rainko et al. [63] and the calculated band energy at the Γ and L valley by Galluccio [85]. Galluccio et al. employed the Synopsys Sentaurus Band Structure (S-Band) software, which computes the band structure in virtual crystal approximation using the empirical pseudopotential method (EPM). Polak et al. used DFT calculations to establish the composition dependence of lattice constants, band gaps, and band offsets in bulk $Ge_{1-x}Sn_x$ alloys over a wide range of Sn compositions. By implementing the non-local EPM, Gupta et al. [210] found the bowing parameters for the Γ and L valley to be 2.1 and 0.91 eV respectively; in good agreement with experimental data [213]. In our calculation, we choose the bowing parameters from Gupta et al. [210], since these bowing parameters produce an indirect- to direct-gap transition for $x \approx 8\%$, which is in agreement with the results of composition-dependent photoluminescence measurements [213]. Some previous work [80] focusing calculation of electron transport in $Ge_{1-x}Sn_x$ has also used these parameters. Furthermore, in their calculation, with the increase in Sn contribution the direct band gap decreases, and also the effective mass at Γ valley decreases. With these bowing parameters, the closing of the band gap occurs at Sn composition of $x = 29\%$, a value close to the recent DFT calculations of O'Donnell et al. [205].

If we now turn our attention to effective mass. Several publications [81, 85, 214–216] have examined how effective mass varies with Sn composition, despite the fact that effective mass is a key parameter to examine carrier transport properties. By using the band structure produced by the non-local EPM calculation, Liu et al. [81] computed the effective masses. Furthermore, by fitting their extracted composition-dependent effective masses, they reported effective mass-bowing parameters for electrons and holes. Prior to the publication of this work, Low et al. [214] researched the effective masses of the electron and the hole and also gave the corresponding bowing parameters. Their analysis shows that the effective mass of the CB at the Γ and L-point decreases along the transverse direction with an increase in Sn composition from 0 to 20%. The transverse direction within the L valley is perpendicular and the longitudinal direction is along the direction joining the Γ and L points. There are different masses along the longitudinal and the transverse directions. We use the density of states (DOS) mass in our transport calculations, which is the geometric average of the mass along the longitudinal and two orthogonal transverse directions. On the other hand, the composition of Sn has a relatively small impact on the effective mass

of the CB of the L valley along the longitudinal direction. Song et al. [215] calculated the electronic band structures for relaxed $Ge_{1-x}Sn_x$ as a function of Sn compositions and also extracted the composition-dependent bowing equations to determine the appropriate effective mass using a 30-band $\mathbf{k}\cdot\mathbf{p}$ model. Galluccio also computed the effective mass for $Ge_{1-x}Sn_x$ alloy using the EPM [85].

However, the behaviour of how the band gap, as well as the band edge effective masses, vary with Sn composition is of crucial importance from the perspective of carrier transport. With an increase in Sn contribution, the Γ valley energy decreases, and will eventually equal to zero at some Sn composition. At this composition, the effective mass of the Γ valley should become zero. Therefore, instead of considering the quadratic equations, which we discussed above, we build an expression in which the Γ valley mass begins at $0.037m_0$, the Γ-point effective mass at $x = 0$ (i.e. in pure Ge), which then decreases to zero when the alloy band gap reaches zero, and at $x = 1$, produces the Γ_{7c} effective mass of Sn, where we follow the double group notation of Refs. [205, 206]. As a result, we determine the effective masses for the Γ and L valley in $Ge_{1-x}Sn_x$ alloy by interpolating the respective effective masses of Ge and Sn using the following formula

$$m_\Gamma(x) = (1-x)\, m_\Gamma^{Ge} + x m_\Gamma^{Sn} - b_{m\Gamma}^{GeSn} x\,(1-x)\ , \tag{5.3}$$

$$m_L(x) = (1-x)\, m_L^{Ge} + x m_L^{Sn} - b_{mL}^{GeSn} x\,(1-x)\ , \tag{5.4}$$

where $b_{m\Gamma}^{GeSn}$ and b_{mL}^{GeSn} are the bowing parameters for the Γ and L valley effective mass. We obtain these parameters by equating $m_\Gamma(x) = 0$ for $x = 29.6\%$, i.e. the composition at which the Γ point band gap equals zero. In Table. 5.1, we present transport parameters for both Ge and Sn, which also include these bowing parameters. After finalising the bowing parameters for the Γ- and L-point band gaps and effective masses, we calculate the variation in the Γ and L valley energies and effective masses by using Eqs (5.1), (5.2), and Eqs (5.3), (5.4) respectively as a function of Sn composition. Exemplar values are listed in Table. 5.2.

5.3 Scattering mechanisms

In Chapter. 4, we explored various scattering mechanisms using Fermi's golden rule and presented the formalism of the corresponding scattering rates and collision operators. The BTE model for GaAs included the acoustic phonon (for both Γ and L valley), polar optical (only L valley), and inter-valley optical phonon (Γ L, L Γ, LL) scattering processes. We also presented these scattering rates as a function of electron energy. The BTE model of Ge includes two sets of valleys: Γ and L valleys, and thus we take into account the scattering processes that are associated with these two valleys, which are primarily driven by optical and acoustic phonons. Acoustic phonon scattering contributes to intra-valley scattering at both the Γ and L valleys. Optical phonons contribute inter-valley scattering from Γ to L, from L to Γ, and between equivalent L valleys, similar to GaAs. The non-polar crystal structure of Ge, in contrast to GaAs, does not allow for the inclusion of polar-optical scattering. Instead, we incorporate electron scattering by optical phonons in the L valley

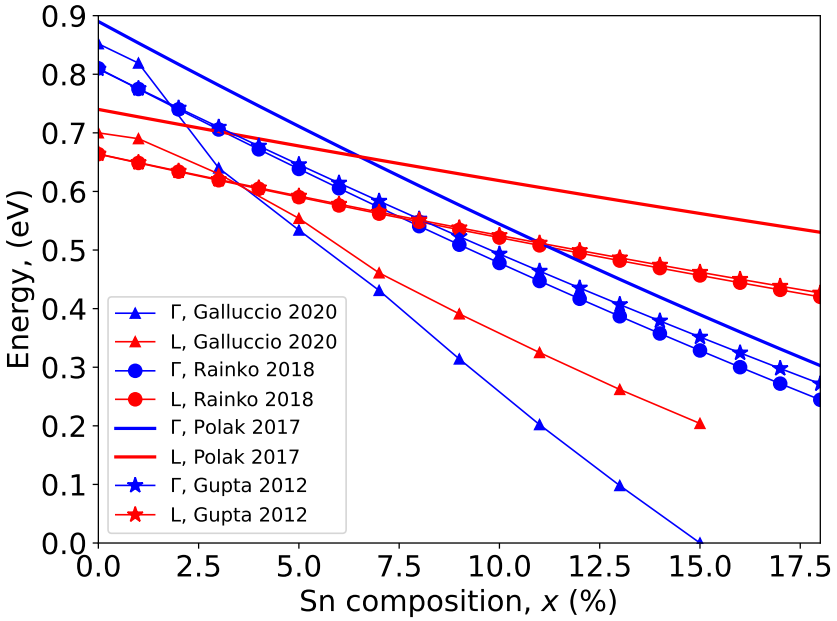

FIGURE 5.3: Comparison of different theoretical calculations for the band gap energies of the Γ and L valley (blue and red lines respectively) with Sn composition, x. Data are taken from Refs. [63, 85, 210, 212].

caused by the optical deformation potential. In addition to the scattering mechanisms present in Ge, the addition of Sn atoms to Ge contributes another major scattering pathway, namely alloy scattering, to the $Ge_{1-x}Sn_x$ electron transport model. This section focuses on how we select the deformation potential parameters for the dominant scattering mechanisms while building the BTE model for Ge and $Ge_{1-x}Sn_x$. We do not go into detail about these scattering mechanisms again, with the exception of alloy scattering, which was not covered in our previous chapter. Using the tight-binding method, which is also described in Appendix A, we determine the alloy scattering potentials. [1]

5.3.1 Selection of parameters

After determining which specific scattering mechanisms must be considered, the first step is to identify appropriate values of the associated deformation potentials. To do so, we review several sets of parameters from the literature [219, 222–224] and select the scattering potentials which produce results that are consistent with the experimental data. For example, from Ref. [222], we extract that the mean free path for L valley acoustic phonon scattering for Ge (l_{ac}) is 1.608×10^{-5} cm. The mean free path, l_{ac} and deformation potential, D_{ac}, are related as follows

$$l_{ac} = \frac{\pi \hbar^4 c_l}{m_L^2 2 D_{ac}^2 k_b T}, \tag{5.5}$$

[1] The tight-binding calculations of the alloy scattering deformation potentials were carried out by Co-Supervisor Dr. Christopher A. Broderick.

Parameter	Ge	Sn
Mass density, (g cm^{-3})	5.340 [217]	5.810 [205, 218]
Lattice constant, (Å)	5.655 [80]	6.473 [205]
Sound velocity, (cm s^{-1})	5.470×10^5 [219]	3.950×10^5 [220]
Effective mass (Γ valley), (m_0)	0.037 [80]	-0.079 [221]
Effective mass (L valley), (m_0)	0.220 [80]	0.212 [80]
Acoustic deformation potential (Γ valley), (eV)	5 [80] [219]	-6 [80]
Acoustic deformation potential (L valley), (eV)	9.36 [222]	-2.14 [80]
Optical deformation potential (L valley), (eV m^{-1})	3.63×10^{10} [223]	3.63×10^{10}
Deformation potential for $\Gamma \rightarrow L$ scattering, (eV m^{-1})	2×10^{10} [80, 217]	2×10^{10}
Deformation potential for $L \rightarrow L$ scattering, (eV m^{-1})	2×10^{10} [80]	2×10^{10}
Inter valley phonon energy $\hbar\omega_{\Gamma L}, \hbar\omega_{LL}$, (meV)	26.775 [220]	27.60 [220]
Optical phonon energy $\hbar\omega$(meV)	38.25 [220]	25.02 [220]
E_Γ (eV)	0.809 [205]	-0.413 [80]
E_L (eV)	0.664 [80]	0.092 [80]
Bowing parameter, Γ point band gap (b_Γ), (eV)	2.15 [80]	-
Bowing parameter, L point band gap(b_L), (eV)	0.91 [80]	-
Bowing parameter, Γ band effective mass ($b_{m\Gamma}$), (m_0)	0.0128	-
Bowing parameter, L band effective mass (b_{mL}), (m_0)	0.0402	-

TABLE 5.1: Transport parameters used for Ge & Sn in this thesis.

Sn composition (x)	$E_\Gamma(x)$, (eV)	$E_L(x)$, (eV)	$\Delta E(x)$, (eV)	$m_\Gamma(x)$, (m_0)	$m_L(x)$, (m_0)
0	0.8090	0.6640	0.1450	0.037	0.220
0.02	0.7424	0.6347	0.1077	0.0344	0.2191
0.04	0.6776	0.6062	0.0714	0.0319	0.2181
0.06	0.6144	0.5784	0.0361	0.0293	0.2173
0.08	0.5530	0.5513	0.0017	0.0268	0.2164
0.10	0.4933	0.5249	0.0316	0.0242	0.2156
0.12	0.4353	0.4993	0.0639	0.0217	0.2148
0.14	0.3791	0.4744	0.0953	0.0192	0.2140
0.16	0.3245	0.4502	0.1257	0.0167	0.2133

TABLE 5.2: Γ- and L-point band gaps (eV) and effective masses (m_0) for $Ge_{1-x}Sn_x$ as a function of Sn composition, x.

where, m_L and T denote the effective mass of the electron in L valley and lattice temperature respectively, and $c_l = \rho v_s^2$, is the average longitudinal module of crystal, with ρ and v_s being the mass density and sound velocity. At room temperature (T =300 K), when we plug in the value of all the parameters ρ, v_s and the effective mass, m_L of L valley from Table. 5.1, we compute the acoustic deformation potential for the L valley, $D_{ac_L} = 9.36$ eV. The Γ valley acoustic phonon scattering potential parameter and the inter (L- Γ and Γ- L) and intra (L-L) valley scattering rates are obtained from Jacoboni [219]. We use data from Murphy-Armando et al. [189, 223] to calculate the optical deformation potential scattering. By symmetry, Γ-valley electrons do not experience optical deformation potential scattering, hence this scattering rate only applies to the L valley electrons. All these scattering potentials and other parameters that are required for transport calculations are listed in Table. 5.1. We can utilise these scattering potentials to calculate the corresponding scattering rates and collision operators over a pre-selected range of CB energy using

the formulas presented in Sec. 4.4 of Chapter. 4.

Having described the scattering rates for Ge, we now move on to $Ge_{1-x}Sn_x$, where at each Sn composition, we obtain the associated band gap energy, and effective mass as shown in Table. 5.2. At each Sn composition x, the transport parameters, such as lattice constant and deformation potentials estimated via as a linear interpolation of the respective Ge and Sn parameters as Eq (5.6)

$$D_{GeSn}(x) = (1-x)\, D_{Ge} + x D_{Sn}\,, \tag{5.6}$$

where D_{Ge} and D_{Sn} represent a given parameter for Ge and Sn respectively. Using these modified parameters and the scattering rate calculations provided in Sec. 4.4 of Chapter. 4, we determine the scattering rate as a function of band energy for each Sn composition.

Figures 5.4, 5.5, and 5.6 show the acoustic, optical deformation potential , and intervalley scattering rate respectively for pure Ge and four different Sn compositions (x = 4, 8, 12 and 16%). We find that the acoustic scattering rate in the L valleys dominates over others, which could be in part ascribed to the higher effective mass of electrons there. As the Γ valley effective mass reduces with rising Sn composition, the acoustic scattering rate in the Γ valley and the Γ to L valley scattering both decrease significantly with increasing Sn composition. The scattering rate caused by optical deformation at L valley and the equivalent intra-valley L-L scattering have only a weak dependence on Sn composition, x, because of the slow variation in the L effective mass with x. Overall, these figures imply that as the band gap in $Ge_{1-x}Sn_x$ shifts from indirect to direct, the scattering rate of electrons decreases, potentially resulting in increased mobility. However, without investigating alloy scattering, we cannot draw any definitive conclusions about how the Sn composition influences total or overall scattering rate and, consequently, electron mobility. The following section discusses alloy scattering, followed by a discussion of the total scattering rate, which is a critical input to the electron transport model.

5.3.2 Alloy scattering

In addition to altering the band energy and effective masses, the presence of substitutional Sn atoms in Ge drives the composition-dependent alloy scattering, which includes inter-valley scattering (Γ → L, L → Γ), equivalent L to L scattering as well as intra-valley scattering in both the Γ and L valleys. We can use Fermi's golden rule to compute the alloy scattering rate [189]

$$\tau_{al}^{-1}(E) = N_f \frac{2\pi}{\hbar} x\,(1-x)\,\frac{a_0^3}{8} \sum_f D_{al_{if}}^2 D_f(E)\,, \tag{5.7}$$

where $D_f(E)$ is the DOS of the final valley f, N_f is the number of available final valleys to which electrons can scatter, and $D_{al_{if}}$ is the alloy scattering potential, which we calculate by using atomistic supercell electronic structure calculations. In the case of intra and equivalent L-L scattering, $D_f(E)$ and N_f change accordingly. We obtain the alloy scattering deformation potentials corresponding to intra and inter-valley scattering from tight-binding calculations performed on

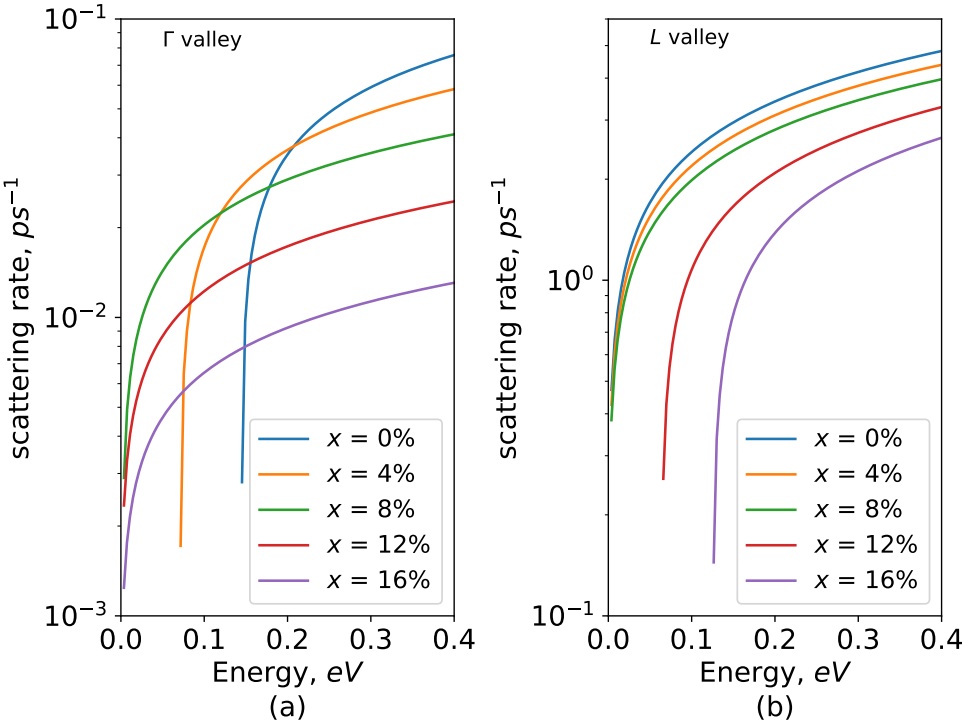

FIGURE 5.4: Acoustic deformation potential scattering rate of Ge, and of $Ge_{1-x}Sn_x$ for Sn compositions $x = 4$, 8, 12 and 16%, for the (a) Γ, and (b) L valleys at room temperature (300 K).

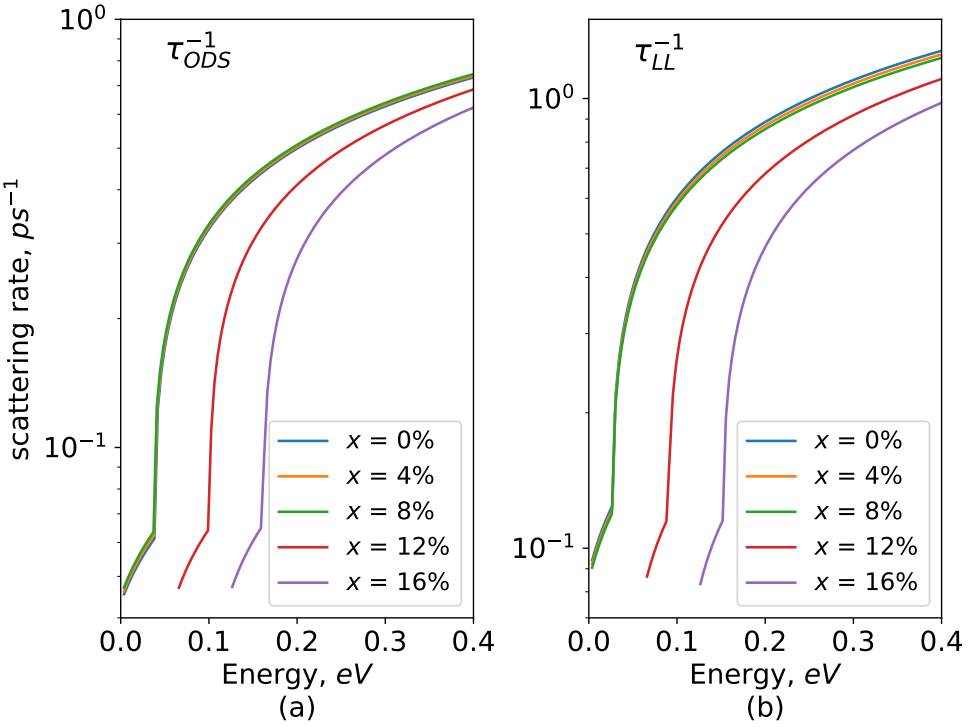

FIGURE 5.5: (a) Optical deformation potential scattering rate in L valley, (b) and equivalent L-L scattering in Ge, and $Ge_{1-x}Sn_x$ for Sn compositions $x = 4$, 8, 12 and 16% at room temperature (300 K).

N-atom ordered alloy supercells containing a single substitutional Sn impurity, with $N = 16, 64$ and 128 atoms ($x = 6.25$, 1.5625 and 0.78125%, respectively). The calculated alloy scattering

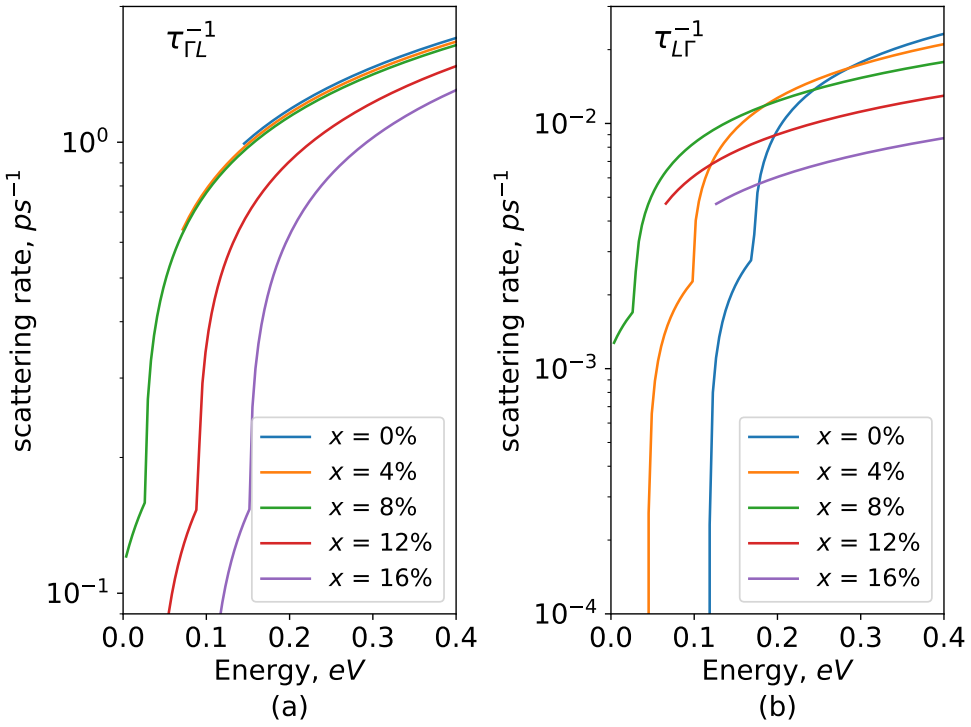

FIGURE 5.6: Inter-valley ($\Gamma \rightarrow$ L (a), (b) L $\rightarrow \Gamma$) scattering rate in Ge, and $Ge_{1-x}Sn_x$ for Sn compositions $x = 4$, 8, 12 and 16 % at room temperature (300 K).

deformation potentials are listed in Table. 5.3. The detailed calculation is given in Appendix A. In Refs. [189], [225], and [226] Murphy-Armando and Fahy developed a first principles approach to analyse carrier scattering in alloys, which they applied to successfully predict the experimentally measured composition-dependent electron mobility in $Si_{1-x}Ge_x$. Their analysis shows that the intra-valley alloy scattering deformation potentials for the Γ valley and the Γ to L scattering potential in $Si_{1-x}Ge_x$ are 1.28 and 0.82 eV, respectively. When comparing our calculated Γ to L scattering potential for $Ge_{1-x}Sn_x$ to that calculated by Murphy-Armando and Fahy for $Si_{1-x}Ge_x$, our calculation produces a higher value of 2.586 eV. Our calculated Γ to L inter-valley alloy scattering potential for $Ge_{1-x}Sn_x$ exceeds that in $Si_{1-x}Ge_x$ by a factor of approximately three. When squared, in the calculation of the corresponding alloy scattering rate (cf. Eq. (5.7), this indicates that Sn incorporation drives Γ to L inter-valley alloy scattering at a rate exceeding that in $Si_{1-x}Ge_x$ by close to one order of magnitude. Previous analysis of the $Ge_{1-x}Sn_x$ electronic structure indicates that this introduces strong Sn-induced hybridisation between the Γ- and L-point CB minima [221]. In $Si_{1-x}Ge_x$ alloy, the intra-valley scattering potentials for the L valley and equivalent L to L valley are 0.19 and 0.95 eV, respectively, where the former is equivalent to the characteristics of $Ge_{1-x}Sn_x$ alloy, and the latter is relatively lower.

Using Eq. (5.7) and the scattering potential values from Table. 5.3, we compute the energy-dependent alloy scattering rates for each valley for a given Sn composition x. To obtain more insight into alloy scattering, we show the individual alloy scattering rates for $x = 4$ and 16% $Ge_{1-x}Sn_x$ in Figs 5.7 and 5.8 respectively, with the band gap switching from indirect to direct as x increases from 4% to 16%. The calculated difference in Γ and L valley energy at $x = 4\%$ is quite

Alloy scattering process	Alloy scattering potential, eV
intra-valley (D_{al_Γ})	-1.368
intra-valley (D_{al_L})	-0.140
inter-valley, ($D_{al_{\Gamma L}}$)	2.586
equivalent-valley, ($D_{al_{LL}}$)	1.781

TABLE 5.3: Alloy scattering potential parameters for $Ge_{1-x}Sn_x$.

small, roughly 71 meV. As a result, as electrons exceed this energy, scattering from the L to Γ and from the Γ to L valley switches on. The scattering rates associated with the intra-valley alloy scattering potentials D_{al_Γ} and D_{al_L} are approximately in the range of 10^{-3} – 10^{-1} ps^{-1}, whereas the scattering rate associated with Γ to L valley is in the range of 10^{1} – 10^{2} ps^{-1}. With increasing Sn composition, the alloy band gap becomes direct, and the difference in energy between the Γ- and L-valley minima increase to 126 meV in $Ge_{0.84}Sn_{0.16}$. Above this energy, intervalley scattering from Γ to L is possible, and the increase in this alloy scattering rate depends mainly on two factors (i) with the increase in Sn composition within the range ($x < 50\%$), the alloy scattering rate increases, (ii) the DOS effective mass of the final valley. With those two factors dominating, the actual "shape" of the alloy scattering rate vs. energy is just a simple $\propto \sqrt{E}$ increase, following the DOS of the final valley. In both cases, the primary scattering mechanisms are Γ to L, L to L, and L to Γ. Except for L to Γ scattering, all of these scattering rates are relatively higher for $Ge_{0.84}Sn_{0.16}$ than for $Ge_{0.96}Sn_{0.04}$. We note however that the small change in L to Γ scattering is probably due to our assumption of a parabolic band dispersion in the calculations. In practice, the Γ band has a nonparabolic dispersion, which will increase the density of Γ states at higher energy, and therefore also increase the scattering rate above that which we have calculated. However, this underestimation of the L-Γ scattering rate will not significantly impact the conclusions of our analysis.

If we think back to the earlier scattering mechanisms, such as scattering due to an optical or acoustic phonon (Figs 5.4, 5.5 and 5.6), we can observe that as the Sn's composition grows, electron scattering tends to decrease. However, the outcome for alloy scattering is absolutely opposite. Following the discussion of each individual scattering process, the overall scattering rate for the Γ and L valleys for Ge and four distinct Sn compositions is shown in Fig. 5.9, which we utilise as the input to our electron transport model. Our results show that when Sn is added to Ge, the alloy scattering becomes the dominant scattering mechanism, and hence the total scattering rate increases for both valleys.

5.4 Low -field electron transport

We start our investigation of the electron transport properties by considering the zero-field mobility, i.e. the mobility when the field is sufficiently low that the electrons still thermalise into a Maxwell-Boltzmann $\left(f = \exp\left(-\frac{E}{k_b T}\right)\right)$. If we recall Chapter. 4, the expression for the field-dependent

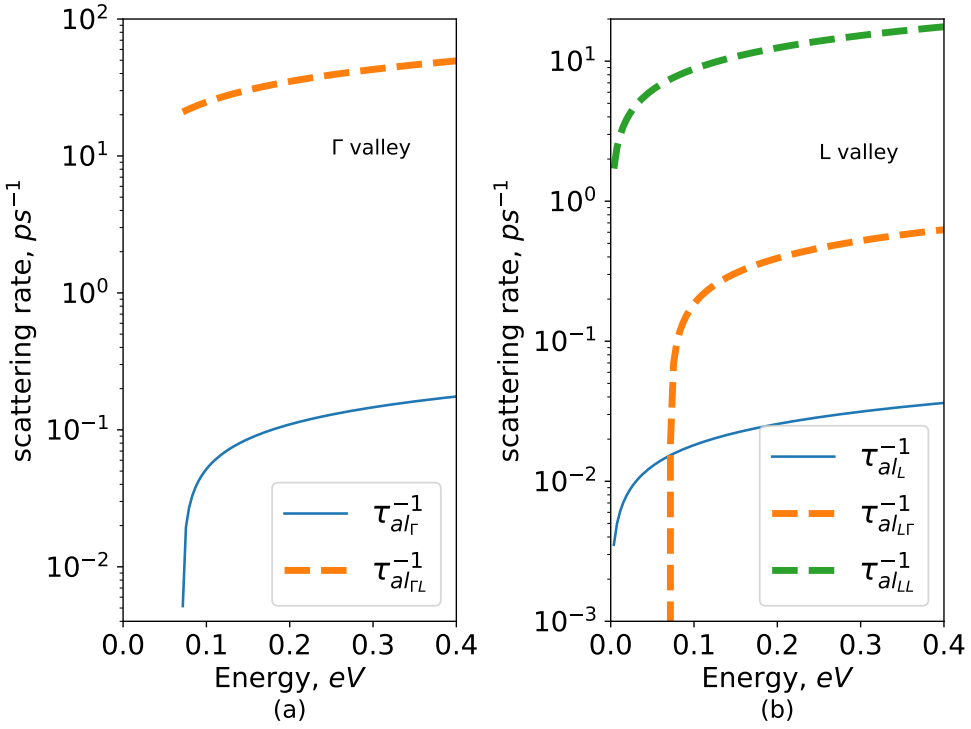

FIGURE 5.7: Alloy scattering rate in $Ge_{0.96}Sn_{0.04}$ due to $D_{al_{L\Gamma}}$, $D_{al_{LL}}$ and D_{al_L} at room temperature (300 K).

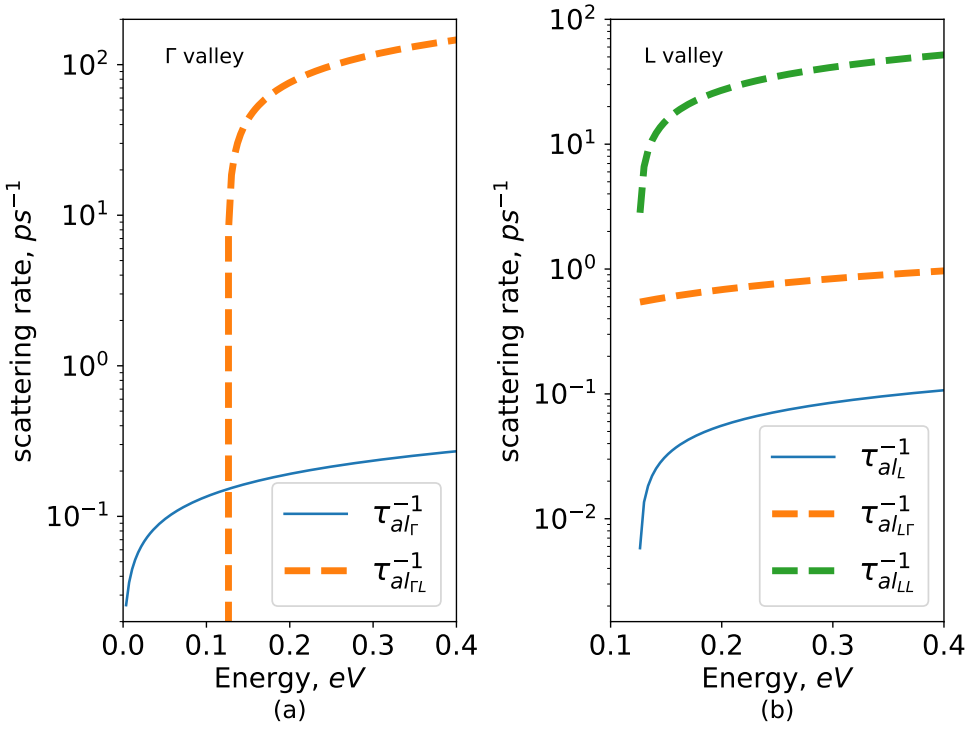

FIGURE 5.8: Alloy scattering rate in $Ge_{0.84}Sn_{0.16}$ due to $D_{al_{L\Gamma}}$, $D_{al_{LL}}$ and D_{al_L} at room temperature (300 K).

mobility, μ is as follows

$$\mu = -\frac{2e}{3}\frac{\sum_v \frac{g_v}{m_v^*}\int \frac{\gamma_v(E) f_b'(E) D_v(E)}{\left(\gamma'(E)\right)^2 \tau_v^{-1}(E)} dE}{\sum_v g_v \int f_v(E)\, D_v(E)\; dE}, \tag{5.8}$$

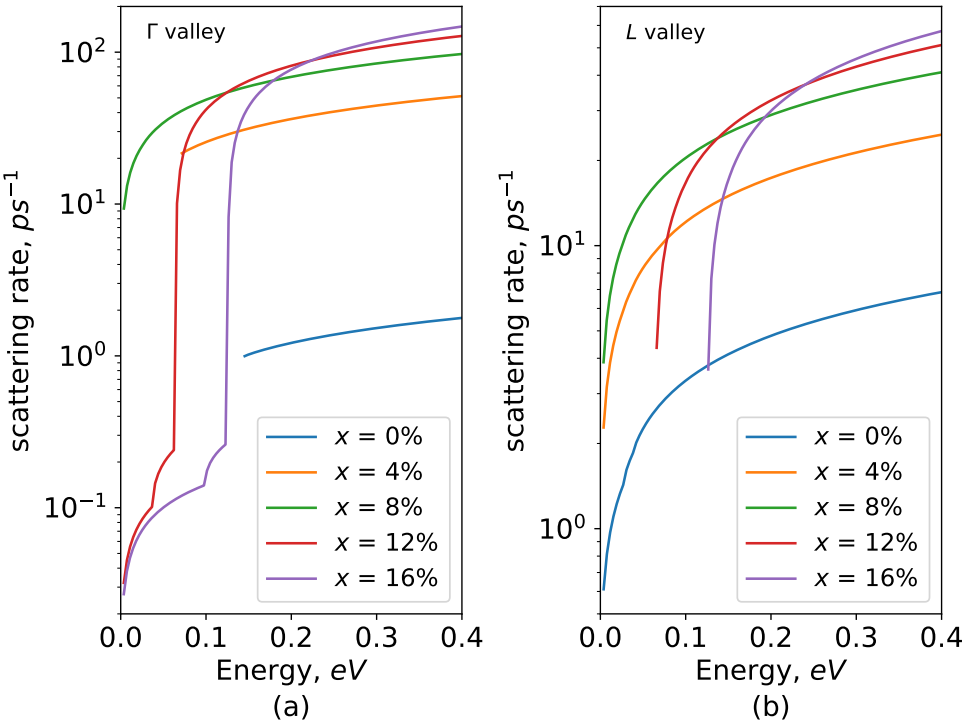

FIGURE 5.9: total scattering rate in Ge, and $Ge_{1-x}Sn_x$ for Sn compositions x = 4, 8, 12 and 16% for the (a) Γ, and (b) L valleys at room temperature (300 K).

where v indexes the valleys, g_v is the valley degeneracy, m_v^* is the electron effective mass, D_v is the DOS (i.e. without spin or valley degeneracy), and τ_v^{-1} is the total electron scattering rate in valley v, which can be calculated from Eq. (4.62) and (4.63) for the Γ and L valleys respectively. We compute the integrals in Eq. (5.8) numerically (using a trapezoidal rule) to determine zero-field mobility. When we substitute into the above expression an individual scattering rate, for example, acoustic phonon or inter-valley scattering, we can then compute the contribution to the total.

We take electron transport parameters from Jacboni et al. [219], Murphy-Armando et al. [189, 223], and Sanchez [222] for our analysis of electron transport properties of pure Ge. To determine at room temperature dependence of the electron mobility on the individual scattering mechanisms in Ge we compute the zero-field mobility in the following four cases (i) limited only by acoustic phonons scattering (μ_{APS}), (ii) limited only by intervalley optical phonon scattering ($\mu_{\Gamma L,LL}$), (iii) limited only by intravalley optical deformation potential scattering (μ_{ODS}), and (iv) the physically realistic case, in which all of these scattering mechanisms are included in the calculation of the mobility. The results of this analysis are presented in Table. 5.4. We note that the acoustic scattering of electrons in the L valley limits the overall mobility. This is mainly due to the large value of the scattering potential parameter and high DOS in the L valley. The blue solid line in Fig. 5.11 shows the DOS plotted as a function of energy for both valleys in Ge, showing that the DOS of the L valley is of order ≈ 100 times higher than that of the Γ valley. Finally, after accounting for all scattering mechanisms, we determine a room-temperature zero-field mobility of 3987 cm^2 V^{-1} s^{-1}, in good agreement with experiment [227–229]. This agreement underpins the selection

Scattering Process	μ_0, cm^2 V^{-1} s^{-1}
Inter and intra valley optical phonon scattering ($\Gamma \rightarrow L, L \rightarrow \Gamma$, $L \rightarrow L$)	29214
Acoustic phonon scattering (both Γ and L Valley)	5172
Optical deformation potential scattering (L Valley)	71683
All the above scattering mechanisms	3987

TABLE 5.4: Contributions to zero-field mobility in Ge due to individual scattering mechanism.

of our scattering parameters. We demonstrate in Sec. 5.5 below that the selected parameters also describe well the field-dependent electron mobility of Ge vs. a range of experimental data.

Following this analysis of mobility in pure Ge, we investigate how the zero-field electron mobility properties change as the Sn composition in $Ge_{1-x}Sn_x$ is increased. To evaluate electron mobility as a function of Sn composition, we first compute the composition-dependent parameters characterising the band structure and scattering rates for a given composition. Next, we compute the electron mobility by using Eq. (5.8) for Sn compositions in the range $x = 0$ – 16% using a composition step size of 0.5%.

To gain more insight into the expected electron transport properties, we begin our analysis by calculating the fraction of the thermalised free electron carrier density residing in the Γ and in the L valley as a function of Sn composition. Figure 5.10 shows the calculated fraction of carriers in the Γ and the L valleys as a function of Sn composition, based on the assumed composition dependence of the DOS, as shown for selected compositions in Fig. 5.11. We note from Fig. 5.10 that in the indirect-gap regime – i.e. for Sn compositions $x \leq 8\%$, the vast majority of the electrons occupy L-valley states due to the significantly higher L-valley DOS. As we increase Sn composition, the electrons start populating the Γ valley, as we transition to the direct-gap regime for $x \geq 8\%$ The band edge DOS in the Γ valley is ≈ 100 times lower than that in the L valley. As a consequence, it can be expected that the mobility will be significantly higher than that of pure Ge, when the overall mobility contribution is mainly due to the Γ valley electrons. As such, we expect that the zero-field electron mobility in $Ge_{1-x}Sn_x$ should increase strongly with increasing $x \geq 8\%$, due to the lower effective mass and overall scattering rate in the Γ valley. However, as we will demonstrate below, this mobility can decrease strongly in the presence of an applied electric field: Γ valley electrons accelerate rapidly in response to the field, gaining sufficient energy to rapidly scattering to the high effective mass (low mobility) L valleys.

Figure 5.12 shows the calculated zero-field electron mobility of $Ge_{1-x}Sn_x$ as a function of Sn composition x. The blue line shows the calculated mobility, including alloy scattering. For lower Sn compositions $x < 8\%$, below the indirect- to direct-gap transition, the mobility is less than that of pure Ge. To explain this limited mobility, we note from Fig. 5.10 that for $x < 8\%$, over 90% of the electrons are in the L valley with its higher DOS. Additionally, Sn incorporation results in alloy scattering, which acts to reduce the mobility. For $x > 8\%$, in the direct-gap regime, the zero-field mobility increases with increasing Sn composition. At $x = 16\%$, our calculated mobility is 4.315 $\times 10^5$ cm^2 V^{-1} s^{-1}, which is more than 100 times the mobility of pure Ge, and also significantly higher than that of GaAs, as computed in the previous chapter.

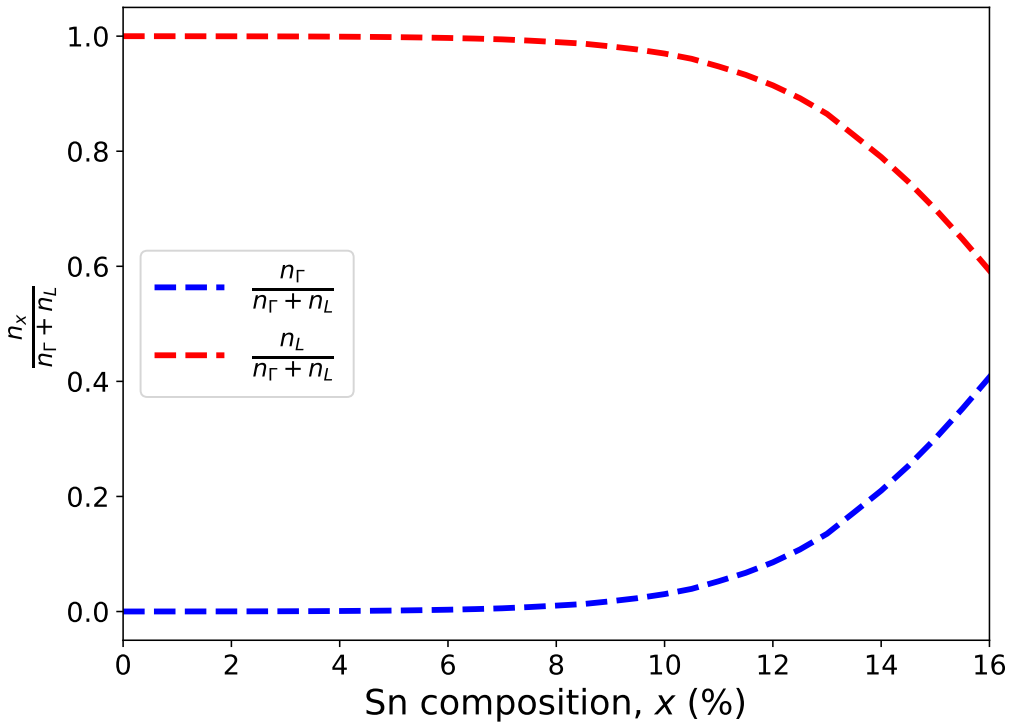

FIGURE 5.10: Fractions of carriers in Γ and L valley as a function of Sn composition at room temperature (300 K).

Despite using only intra valley alloy scattering , which may boost mobility, Mukhopadhyay et al. [80] reported an electron mobility of 2×10^5 cm^2 V^{-1} s^{-1} at $x = 20\%$, which is roughly half of our calculated mobility at $x = 16\%$. This could be because of higher values of the acoustic and optical deformation potential scattering parameters were used, as well as the inclusion of impurity scattering in their calculation. They did not, however, provide a quantitative explanation for the shift in effective masses and scattering parameters in both valleys as Sn composition rose. To understand the impact of alloy scattering on the overall mobility in our calculations, we have also calculated the mobility, with the alloy scattering rates set to zero (orange line in Fig. 5.12). When alloy scattering is set to zero, the mobility at lower Sn compositions also reaches higher values than that of Ge – a consequence of the decrease in the Γ and L valley DOS effective masses with increasing x – at higher Sn compositions, the mobility increases by a factor of order 20. To summarise, increasing Sn composition in Ge causes a shift from indirect to direct band gap and a decrease in the Γ valley band edge DOS, with the alloy and Γ to L valley inter-valley optical phonon scattering being the dominant scattering processes at higher Sn compositions. These scattering mechanisms set an upper limit on the low-field mobility at higher Sn compositions, but overall we calculate a strong enhancement of the low-field mobility in direct band gap $Ge_{1-x}Sn_x$ due to the significantly lower DOS in the Γ valley.

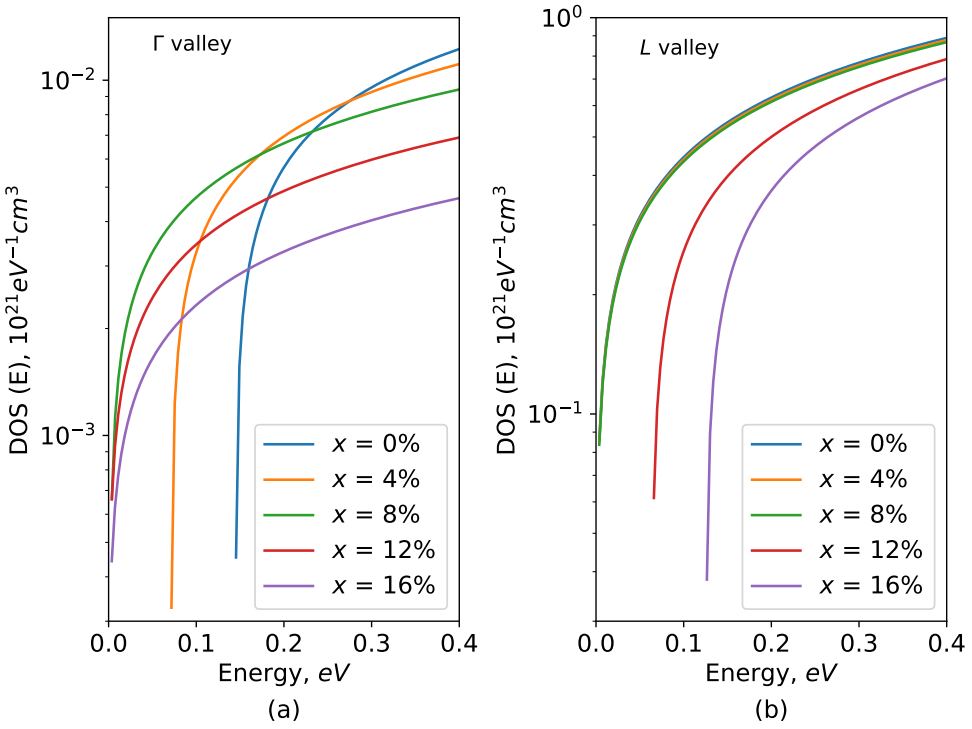

FIGURE 5.11: Density of states in Ge, and $Ge_{1-x}Sn_x$ for Sn compositions x = 4, 8, 12 and 16% for the (a) Γ, and (b) L valleys at room temperature (300 K).

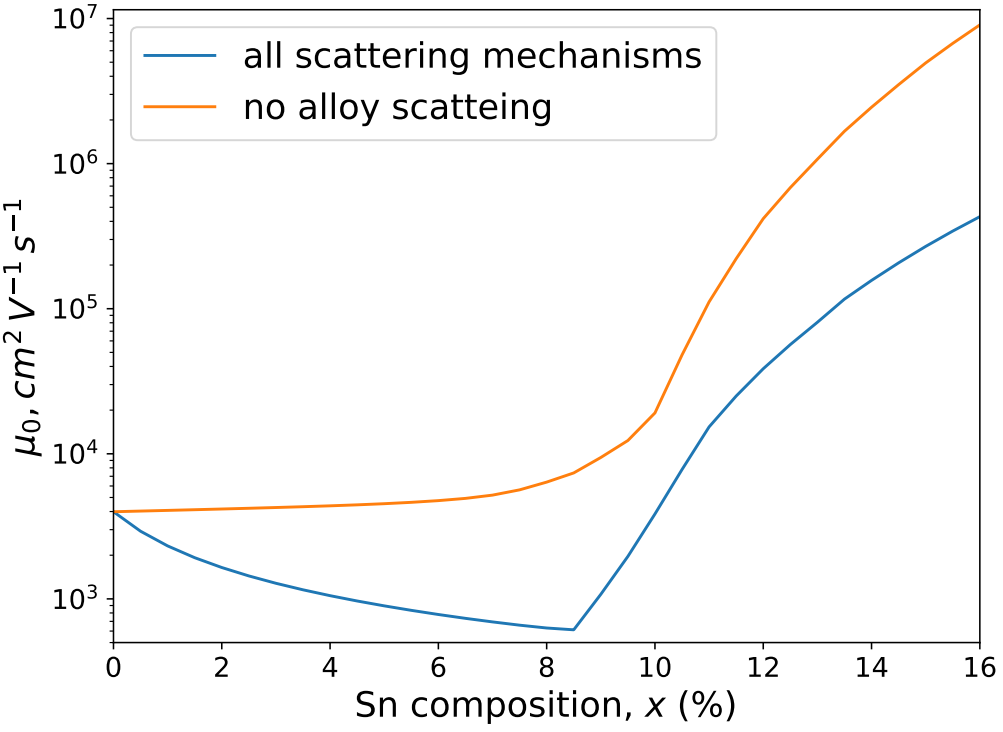

FIGURE 5.12: Zero-field mobility as a function of Sn composition (with and without alloy scattering) at room temperature (300 K).

5.5 Field dependent electron transport

We split this section into two parts. The first part discusses the room-temperature electron transport properties of Ge by calculating the electron drift velocity and mobility as a function of applied electric field, and compares them to experimental data and previous theoretical calculations. We explain the importance of choosing a suitable maximum cut-off energy and the total simulation time allow the numerical evolution of the distribution functions – described by the two-valley BTE model – to reach an accurate steady-state. After validating our results for pure Ge, we then investigate how Sn incorporation influences the electron transport properties in $Ge_{1-x}Sn_x$. For our calculations, we choose a range of Sn compositions between $x = 2$ and 16% and calculate the composition-dependent, steady-state electron distribution functions, average energy, electron occupancy, electron mobility, and drift velocity as a function of the applied electric field F, up to a maximum strength of 10 kV cm^{-1}.

5.5.1 Field-dependent electron transport in Ge

To investigate the field-dependent electron transport characteristics of Ge, we employ the BTE model, which we have discussed in detail in Chapter. 4. However, due to differences in scattering mechanisms, changes in the relative Γ and L valley energy, and other parameters, the implementation of the Ge-BTE model differs slightly from that of the prior GaAs-BTE model.

In the BTE approach, we start by defining the energy range over which we will evolve the valley distribution functions. To do so, we choose the zero of energy to lie at the CB minimum and explicitly select the maximum energy E_{max} and an energy grid step size, which we take as $\Delta E = 0.1\ \hbar\omega$ [2], where $\hbar\omega$ is the longitudinal optical phonon energy. For Ge, the CB minimum is at the L valley, and the Γ valley is taken to be 0.145 eV [221] above the L valley. Therefore the L valley energy starts from CB minimum, and the Γ valley energy begins beyond 0.145 eV. For both valleys we use the same maximum energy E_{max}. In our Ge-BTE model and as we describe below, we find that the choice of a sufficiently large E_{max} is crucial for an accurate description of the transport properties. After specifying the energy range, we calculate the energy-dependent scattering rates for each valley included in the model.

We include in our calculations the relevant scattering mechanisms described in Sec. 5.3, and for our initial calculations set $E_{max} = 60\,\hbar\omega$ (cf. Table. 5.1). We initiate the calculations by assuming that the electrons are thermalised into a Maxwell-Boltzmann distribution in each valley at zero field, $F = 0$. We then need to evaluate how the electron distribution function in both valleys changes as the field increases. To evaluate the steady state distribution function at field $F = F_n$, we need to solve the time-dependent coupled BTEs for the Γ and L valleys,

$$\left(\frac{\partial f_\Gamma}{\partial t}\right) = \left(\frac{\partial f_\Gamma}{\partial t}\right)_{F_n} + \left(\frac{\partial f_\Gamma}{\partial t}\right)_{\Gamma L}, \tag{5.9}$$

$$\left(\frac{\partial f_L}{\partial t}\right) = \left(\frac{\partial f_L}{\partial t}\right)_{F_n} + \left(\frac{\partial f_L}{\partial t}\right)_{ODS} + \left(\frac{\partial f_L}{\partial t}\right)_{L\Gamma} + \left(\frac{\partial f_L}{\partial t}\right)_{LL} . \tag{5.10}$$

These coupled equations are similar to those for GaAs, with the exception that the collision operator due to polar optical scattering is replaced by the optical deformation potential collision operator in the L valley. The formulation of all of these collision operators was discussed in Chapter. 4. We evolve the BTE for each valley using an explicit Euler method on a uniform temporal grid Δt,

$$f(E, t + \Delta t) = f(E, t) + \frac{\partial f}{\partial t}(E, t) \times \Delta t\,, \tag{5.11}$$

and integrate until we obtain steady-state distribution functions at a given field, $F = F_n$. The size of the time step and total integration time required to get a steady state distribution vary with the strength of the applied electric field, F_n, and the choice of maximum energy, E_{max}. Once we have the steady state distributions at field F_n, we use them as the starting distribution when determining the steady state distribution functions at the next electric field, F_{n+1}. We begin our calculations by taking $E_{max} = 60\,\hbar\omega$ (cf. Table. 5.1), and a time-step, $\Delta t = 0.25$ fs at electric field $F = 1$ kV cm^{-1}. As we proceed to the higher field, we down-sample the time step, as we did for GaAs. material parameters employed in our Ge transport calculations are listed Table. 5.1. To appropriately estimate the steady-state distribution functions, we run the simulations for a total time period of 200 ps. As the strength of the electric field increases, the number of time steps increases, and consequently so does the computation time. We determine the room temperature electron transport properties for Ge for electric field strengths up to 10 kV cm^{-1}. For each electric field strength, we found that the steady-state Γ- and L-valley distribution functions are attained after 75 ps. We find for $E_{max} = 60\,\hbar\omega$ (cf. Table. 5.1) that the drift velocity starts to decrease for fields above about 5 kV cm^{-1}. This is akin to the well-known Gunn (negative differential resistance) effect in GaAs, but in the case of Ge is unphysical since it is well known from experiment that the electron drift velocity saturates, but does not decrease, at high field [230, 231]. To test the origin of this decrease, we repeated the calculations for different upper cut-off energies (E_{max} = 60, 90, 120, 150 and 180 $\hbar\omega$) (cf. Table. 5.1). Figure 5.13 shows the calculated drift velocity as a function of electric field for the different values of E_{max}. Each of these calculations uses a total simulation time of 200 ps for each electric field. Our results unequivocally show that the drift velocity at higher field is reduced when the maximum energy limit is 60 $\hbar\omega$ ($\approx$ 2.29 eV) (blue diamond line in Fig. 5.13) for electric fields greater than 5 kV cm^{-1} compared to that calculated with higher cut-off energies. The drift velocity decreases for electric fields above 6 kV cm^{-1} for the next higher cut-off energy 90 $\hbar\,\omega$ ($\approx$ 3.4 eV) (squared orange line in Fig. 5.13), and so on. We finally eliminate this artificial high-field reduction of the drift velocity for electric fields up to 10 kV cm^{-1} at E_{max}= 180 $\hbar\omega$ ($\approx$ 6.8 eV) (circled purple line in Fig. 5.13). When we choose a "low" value of E_{max}, once the electric field gets high enough electrons reach the "top" (E_{max}) of the bands in our calculation. The electrons are then prevented from accelerating further because there are no higher energy states available in the calculations for them to accelerate into. Numerically we can say the distribution function starts to unphysically "pile up" at the top of the band, and this in turn then impacts the evaluation of $f^{'}(E)$, which impacts the calculation of collision operators

and pollutes the results of the calculation at higher electric field values. Therefore, the choice of cut-off energy for Ge is important, especially when working with larger electric fields. We note that this issue is not encountered in the GaAs calculations, because energy loss via strong polar optical phonon scattering prevents electrons from accelerating to the top of the calculational energy range, allowing to use smaller values of E_{max}.

After establishing the convergence of the Ge-BTE model, we now plot in Fig. 5.14 the steady-state electron distribution functions for various electric field strengths, ranging from zero field to $F = 10$ kV cm^{-1}, assuming parabolic Γ and L valleys and an upper cut-off energy of 180 $\hbar\omega$ ($\approx$ 6.8 eV). The solid and dotted lines represent the electron distribution for the Γ and L valley respectively. We normalise the distribution functions with respect to the value of f_L at energy (0.1 $\hbar\omega$) so that the L valley electron distribution functions for all electric field values begin at 1. The orange line represents the Boltzmann distribution function for field F =0. Up to the electric field strength of 0.1 kV cm^{-1}, the electron distribution function mostly follows the Boltzmann distribution line signifying that such low electric fields do not significantly pull the electron distribution from its equilibrium value. When the external electric force increases to 1 kV cm^{-1}, the change from the equilibrium distribution is noticeable, but at such a low electric field, the electron distribution remains similar to a higher temperature Boltzmann distribution. As the field increases further, electrons increasingly start to be accelerated to higher energy states. For the highest electric field (F = 10 kV cm^{-1}), the electron distribution becomes almost flat. We note however that at higher electric fields, the actual electron distribution is likely to be different in an actual Ge sample, due to two differences between our model and the true band structure of Ge. Firstly, at a higher field scattering of electrons can be expected to the higher energy X-point CB valleys, which we omit in our calculations, and secondly, at higher energy the Γ (and L) band dispersion quickly become non-parabolic. Our calculations assume a two-valley parabolic band dispersion model for the Γ and L valleys and ignore the X valley. While these issues impact the calculated high-field mobility of Ge, they will not affect our conclusions in the next section regarding carrier transport in $Ge_{1-x}Sn_x$.

Knowing the electron distribution function in both the Γ and L valleys for a specific electric field value F, we can then compute the drift velocity and mobility for that field as $v_d = \frac{J_\Gamma + J_L}{e(n_\Gamma + n_L)}$ and $\mu = \frac{v_d}{F}$ respectively, where J_Γ, J_L and n_Γ, n_L represent the current and carrier density for the Γ and L valleys respectively. Equations (4.69) and (4.68) provide the expressions used to determine the current and carrier density for a valley, v from the carrier distribution function, f_v.

The blue circles in Fig. 5.15 and 5.16 show the calculated room-temperature electron drift velocity and mobility as a function of applied electric field, computed with E_{max}= 6.8 eV. Figure 5.15 also includes theoretical results from the Monte Carlo calculations of Jacoboni et al. [219], and Gang et al. [233], as well as experimental data from Gunn [232], Sze [231], and from Smith et al. [230]. For the lower electric field strengths, up to 2 kV cm^{-1}, we find good agreement between our calculated drift velocity and the experimental data of Gunn [232]. Beyond this electric field, we calculate a higher drift velocity. However, even at the highest field, the difference is less than 20% and, over the full range of fields, our results match well with the earlier experimental measurement by Smith et al. [230]. Comparing to previous calculations, our velocity vs field curve lies between the

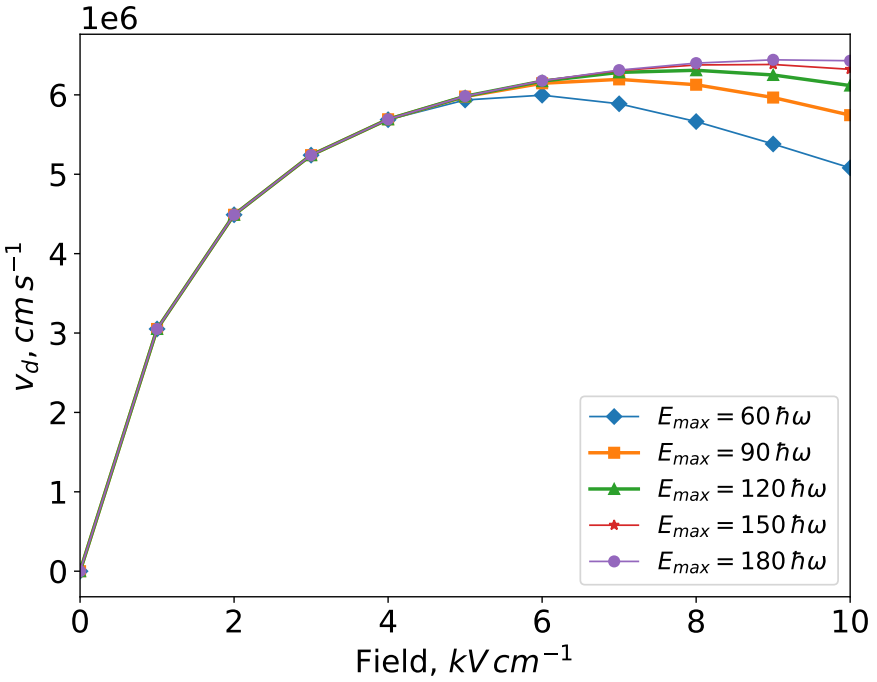

FIGURE 5.13: Evolution of drift velocity as a function of electric field in Ge computed for different cut - off energies E_{max}, ($\hbar\omega = 38.25$ meV).

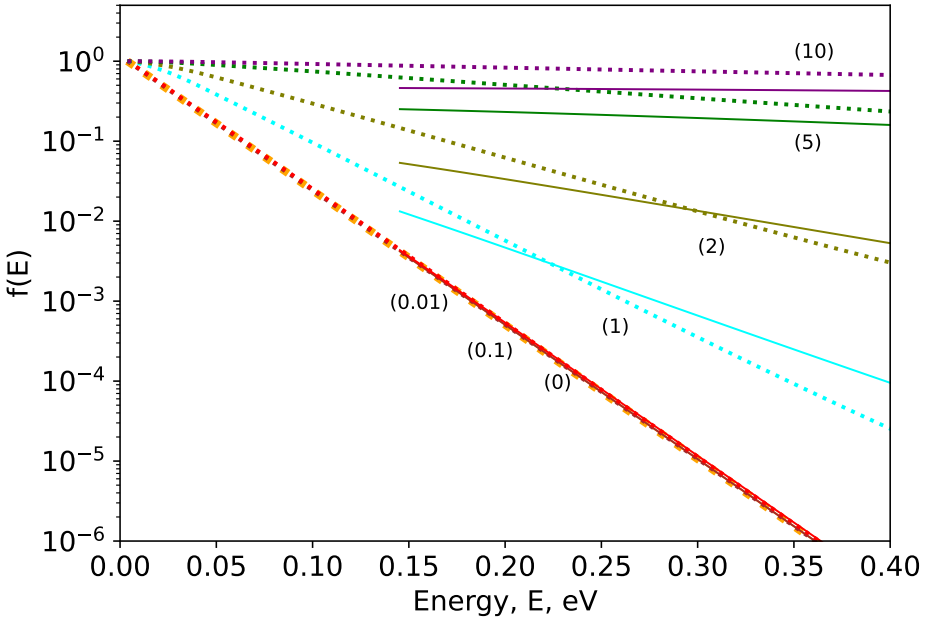

FIGURE 5.14: Calculated steady state distribution functions of electrons in Γ (solid line) and L valley (dotted line) at different fields, F. The number in parentheses on each line is the electric field strength F in kV cm^{-1}.

results of Gang et al. [233] and Jacboni et al. [219]. There is good agreement between our results and those of Gang et al. [233] up to an electric field of 2 kV cm^{-1}; at higher fields our calculated velocity is above their result but below that of Jacboni et al. [219].

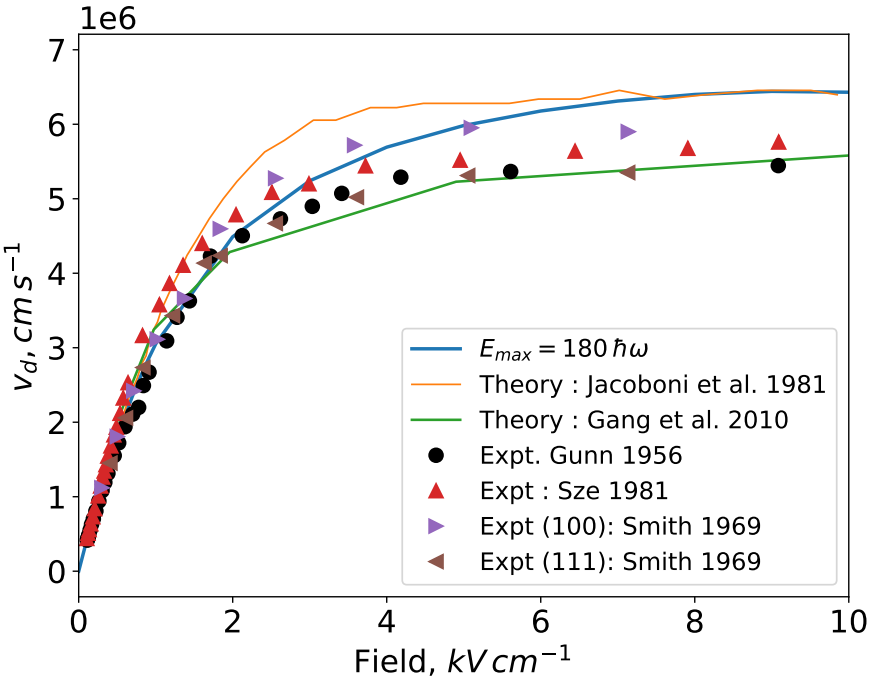

FIGURE 5.15: Drift velocity in Ge as a function of electric field F, based on the BTE model presented here (solid blue line), compared to previous experimental measurement by Gunn [232] (black circle), Sze [231] (red triangle up), and Smith et al. [230] (triangle left and right) and theoretical calculation by Jacboni et al [219](solid orange line), and by Gang et al. [233](solid green line).

Figure 5.16 compares the electric field dependence of our calculated mobility with the experimental data from Gunn, Many and Zucker [195] and the theoretical calculations of Sanchez [222]. We show very strong agreement between our projected mobility and the experimental data, as well as a similar decrease in mobility with increasing field strength vs. Sanchez's calculation. The absence of L to Γ and equivalent L to L scattering could explain the overestimation of the mobility vs. experiment in Sanchez's theoretical model.

The fact that our calculated drift velocity is higher than most other results is consistent with the absence of X valleys in our calculations, which introduce additional scattering pathways at higher energy and consequently at higher field values. In addition, our assumption of a purely parabolic band dispersion will underestimate the electron effective mass and scattering rates at higher energy, leading to an overestimation of the associated drift velocity. However, even with these simplifying assumptions, our calculated electron transport properties are in good quantitative agreement with previous theoretical and experimental analysis. Hence, we conclude that our two-valley BTE model for Ge provides a suitable foundation for studying the field-dependent electron transport in $Ge_{1-x}Sn_x$ alloys.

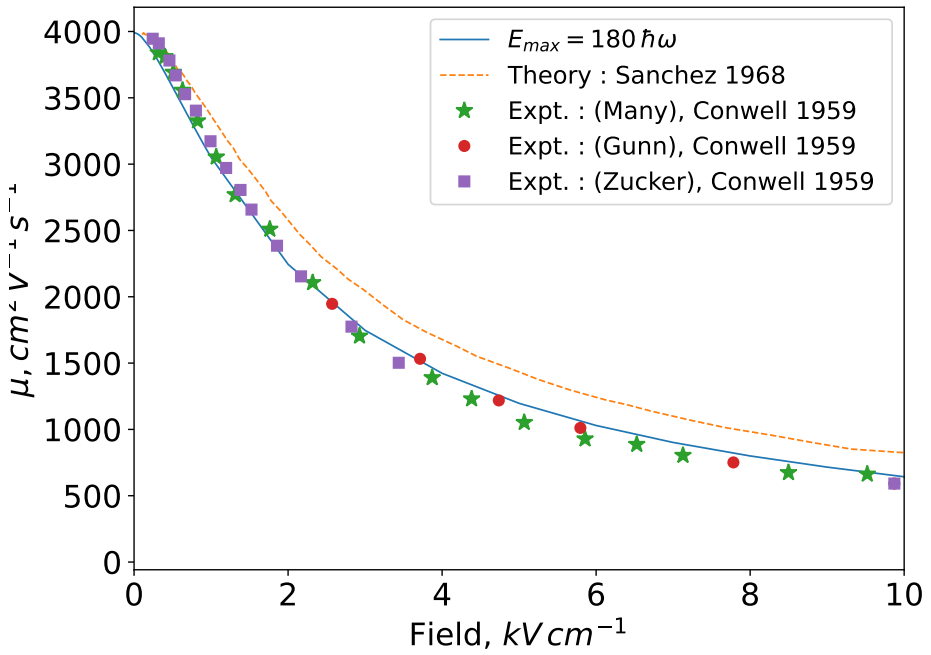

FIGURE 5.16: Electron mobility in Ge as a function of electric field, F based on the BTE model presented here (solid blue line), compared to previous experimental measurement by Gunn (red circle) , Many (green star), Zucker (purple square) (data extracted from [195]) and the theoretical computation by Sanchez [222](dashed orange line). Normalised mobility data are available in all these references. Absolute mobility are obtained by multiplying our calculated zero field mobility (3987 $cm^2\ V^{-1}\ s^{-1}$).

5.5.2 Field-dependent electron transport in $Ge_{1-x}Sn_x$ alloys

We turn now to investigate the impact of applied electric field on the electron transport properties of $Ge_{1-x}Sn_x$ alloys as a function of increasing Sn composition. We use the composition-dependent band structure parameters of Table. 5.2 as well as scattering potentials, lattice constants, and phonon energies as presented in Eq. (5.6). The BTE model is then used for each composition to determine the steady-state distributions as a function of the applied field. We assume that the alloy scattering is elastic [189], such that there are no non-zero collision operators corresponding to the alloy scattering rates described above. The transport properties are then derived from the resulting steady-state distribution functions, as described above. Due to the dependence of the scattering rates on Sn composition, the time-step in the BTE model changes for each composition. We again run our computations for a total time of 200 ps (for some electric fields 500 ps), repeating the procedure at the next higher cut-off energy, to ensure the convergence of the calculation. With the exception of the Sn composition $x = 2\%$, where steady-state distribution functions are acquired at the ensuing higher cut-off energy ($E_{max} = 90\,\hbar\omega$), steady-state distribution functions for all other compositions are achieved at a cut-off energy of $60\,\hbar\omega$, reflecting the impact of alloy scattering on the calculated electron distribution functions.

5.5.2.1 Carrier distribution function

$Ge_{1-x}Sn_x$ makes a transition in our calculations from an indirect gap to a direct gap at Sn composition $x = 8\%$. We therefore choose here four different Sn compositions, $x = 4$, 8, 12, and 16%, to investigate the composition dependence of the change in the distribution functions as a function of applied electric field. We chose these compositions to investigate the evolution of the field-dependent electron transport properties as the band gap changes from indirect to direct. We find for direct-gap alloys that we need to use very small electric field steps at low electric field in order to follow the evolution of the distribution function and carrier transport characteristics. Figure 5.17 displays the steady state distribution function obtained at various electric field values upto to 10 kV cm^{-1} for Sn composition $x = 4$, and 8%; we normalise the distribution functions in each case to the value at $f_L(0.1\ \hbar\omega)$, where $\hbar\omega$ is the phonon energy. The solid and dotted lines represent the Γ and L valley respectively.

At zero electric field, the steady-state distribution functions are Maxwell-Boltzmann, by construction. The bottom orange line in both figures represents the Boltzmann distribution. When a small electric field is applied (0.01 kV cm^{-1}), it is expected that this distribution will be slightly perturbed. The steady-state distribution functions for electric fields up to 0.1 kV cm^{-1} are effectively indistinguishable from the Maxwell-Boltzmann distribution for x =4, and 8%. As a result, we infer that the electron distribution in $Ge_{1-x}Sn_x$ is minimally perturbed at low electric fields ($F = 0.1$ kV cm^{-1}). Even when the electrons are driven out of thermal equilibrium at $F = 1$ kV cm^{-1}, out-of-equilibrium steady-state distribution functions remain Maxwell-Boltzmann-like, albeit, with carrier temperature elevated compared to the fixed lattice temperature of 300 K. As the field increases further, electrons begin to occupy higher energy states for both compositions. The steady-state distribution functions for the two compositions start to noticeably deviate from each other by $F = 5$ kV cm^{-1}, with stronger alloy scattering leading to fewer higher energy states being occupied in $x = 8\%$ alloy. At higher fields ($F = 10$ kV cm^{-1}), the electron function is approaching a flat distribution for $x = 4\%$, but more slowly than was observed in pure Ge.

Figure 5.18 shows the calculated distribution functions for the two direct gap alloys, (a) $x = 12\%$, and (b) $x = 16\%$. We find that even an electric field as low as 0.01 kV cm^{-1}, is sufficient to strongly perturb the electron distribution from equilibrium. There is already a significant difference between the Maxwell-Boltzmann distribution and the steady-state distribution for $F = 0.01$ kV cm^{-1} for both compositions. The solid and dotted lines in Fig. 5.18 represent the Γ and L valley respectively. At the next electric field shown ($F = 0.1$ kV cm^{-1}), there are for both compositions changes in the electron distribution functions with respect to the previous electric field electron distribution, with the changes being more pronounced for $x = 16\%$. Up to an electric field of 1 kV cm^{-1}, the relative electron population decreases in the direct gap DOS, with the electron distributions then following a Boltzmann distribution above the L valley band edge. As we increase the field strength further, more electrons start to populate states above the bottom of the L valley.

Understanding the quantitative evolution of electron concentration and average electron energy in both valleys is important for understanding the electron transport properties. The distribution

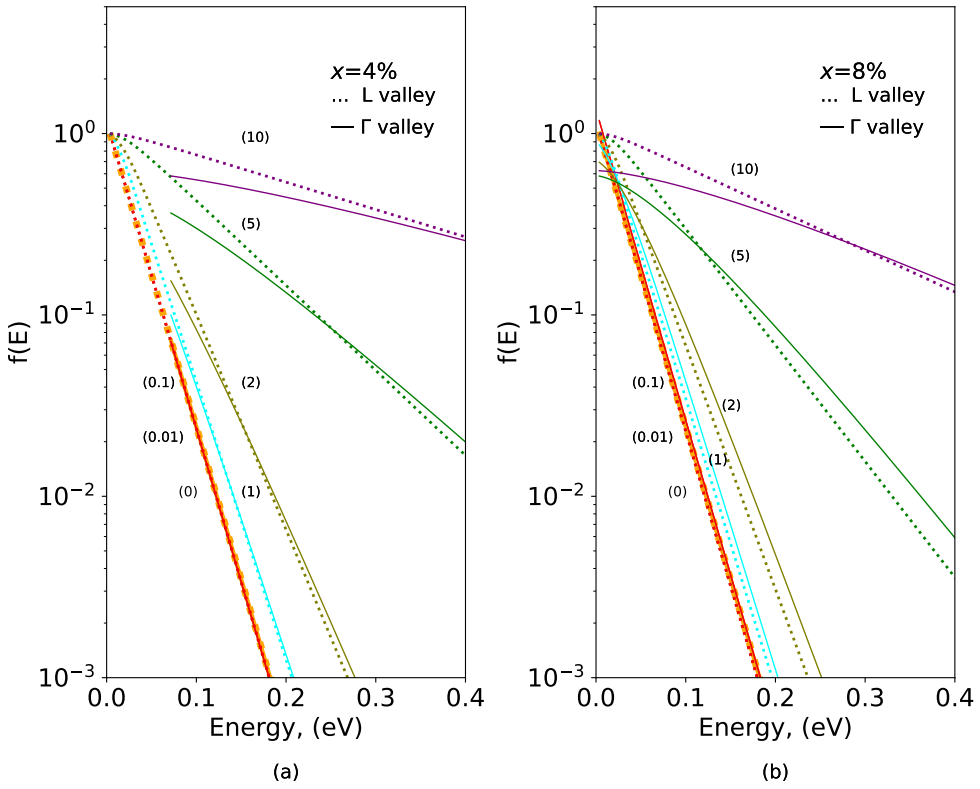

FIGURE 5.17: Distribution function in both L and Γ valley, for Sn composition $x = 0$, and 8% at various electric fields, F. The number in parentheses on each line is the electric field strength F in kV cm^{-1}.

functions allow us to calculate the fraction of individual electron occupancy, $\frac{n_\Gamma}{n_\Gamma+n_L}$ and $\frac{n_L}{n_\Gamma+n_L}$ in the Γ and L valleys as a function of the applied field. Figures 5.19 (a) and (b) show the calculated evolution of these ratios as a function of applied electric force for various Sn compositions. We insert in both cases a zoomed inset to highlight the rapid evolution of the carrier populations at very low fields. We can see that the electron population in the Γ valley at zero field increases with increasing Sn composition, as the energy of Γ valley minimum reduces relative to that of the L valley. However, an applied electric field then has a significant impact on the valley occupancy. Initially, 40% of the electrons are in the Γ valley at the highest Sn composition $Ge_{0.84}Sn_{0.16}$ (purple line). However, the transfer of electrons from the Γ to the L valley begins at a very small electric field. As shown in Fig. 5.19 (b) representing the fractional electron density for the L valley, the electron fraction quickly increases towards 90% by a field of order ≈ 0.02 kV cm^{-1}. The L valley then contains the vast majority of the electrons beyond this field. The zero-field maximum Γ valley occupancy at $x = 14\%$ is only 20% and again decreases rapidly with increasing applied electric field strength.

Figure 5.20 shows the average energies of electrons in the Γ and L valleys as a function of applied electric field for $Ge_{1-x}Sn_x$, as x increases from zero (pure Ge) to 16%, in steps of 2%. For each composition, the zero of energy is taken at the CB minimum, which is the L (Γ) valley minimum for $x \leq 8\%$ ($x > 8\%$). In all cases, the average energy of electrons in the Γ and L valleys increases with increasing electric field strength. The increase is largest for Ge where it is nearly quadratic.

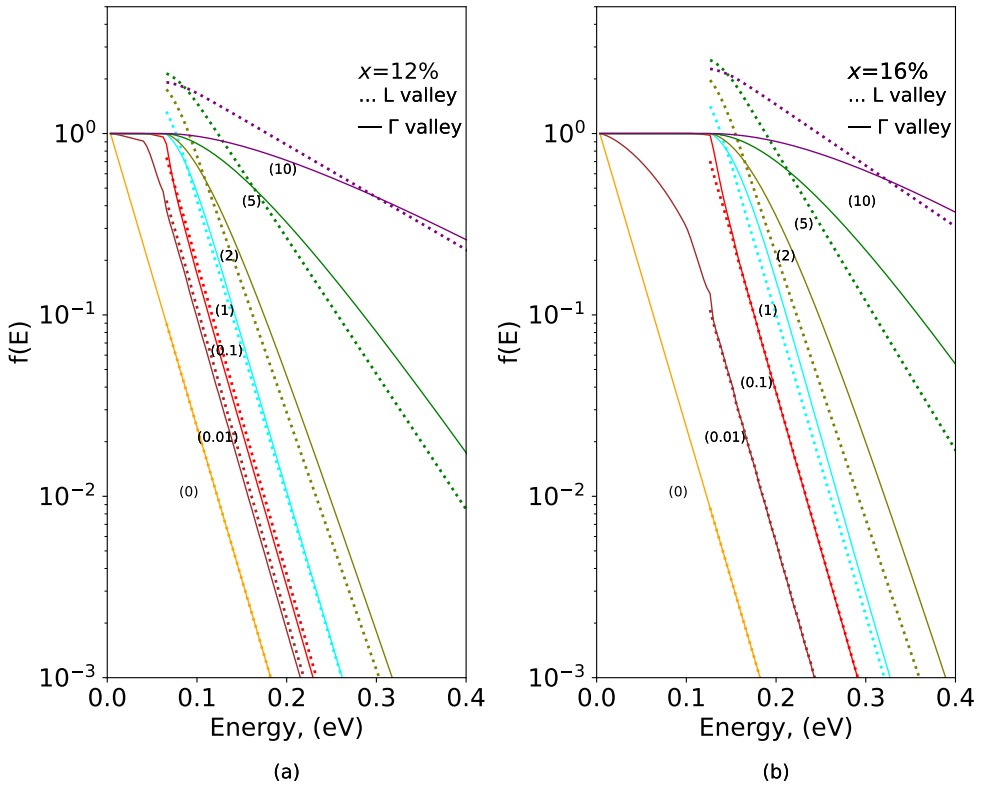

FIGURE 5.18: Distribution function in both L and Γ valley, for Sn composition $x = 12$, and 16% at various electric fields, F. The number in parentheses on each line is the electric field strength F in kV cm^{-1}.

A weaker field dependence is found at a higher field for increasing x, a consequence of the fact that stronger alloy scattering acts to limit the ability of electrons to accelerate in response to a given electric field. The variation of average energy in the Γ valley drops as x increases. However, a strong field dependence is observed at a very low field at higher Sn composition, as the Γ band edge moves further below the L band edge. The zoomed inset for $x = 16\%$ shows a close to linear increase of the average energy up to an electric field strength of 0.015 kV cm^{-1}, beyond which there is a much weaker variation in average energy. This trend is also observed for $x = 14\%$ and 12%. This behaviour reflects that electrons can rapidly accelerate to higher energies in the Γ valley, even in a small electric field until they become degenerate with L valley states, at which point strong Γ-L intervalley scattering limits the further acceleration of electrons in the Γ valley.

5.5.2.2 Electron drift velocity and mobility

Figures 5.21 and 5.22 depict for $Ge_{1-x}Sn_x$ the evolution of drift velocity v_d, and mobility μ with applied electric field, F in the range from 0 to 10 kV cm^{-1}, as the Sn composition is increased from $x = 2$ to 16%. These results are obtained from the calculated steady-state electron distribution functions using the same approach as we have already discussed for Ge. If we ignore the very low electric field regime for the time being, we find that there is a rapid increase in the magnitude of drift velocity up to an electric field value of $\approx$ 2 kV cm^{-1}, beyond which the drift velocity saturates. We also see that the magnitude of the drift velocity decreases with increasing Sn

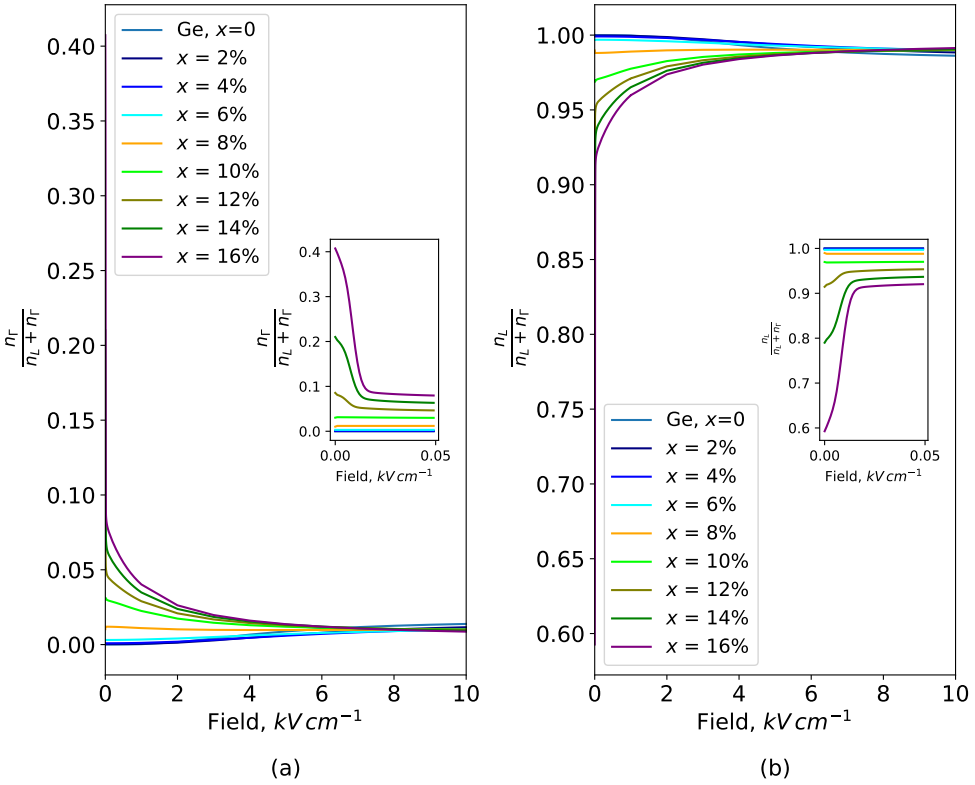

FIGURE 5.19: Fraction of electrons in Γ and L valleys, with respect to total electron density ($n_L + n_\Gamma$) as a function of applied electric field F, in Ge, $Ge_{1-x}Sn_x$ alloy at x = 2, 4, 6, 8, 10, 12 and 16%, (a) $\frac{n_\Gamma}{n_L+n_\Gamma}$ (b) $\frac{n_L}{n_L+n_\Gamma}$. The inset zoomed images in both the sub-figures show the corresponding properties within the range of low electric field up to 0.05 kV cm^{-1}.

composition x. Examining the mobility plot in Fig. 5.22, we see that, except close to $F = 0$ for higher Sn compositions, the magnitude of the mobility decreases both as the magnitude of the applied electric field increases and also with increasing Sn composition. Overall, except for the lowest field values at high Sn composition, we find that the incorporation of Sn significantly reduces the drift velocity and hence mobility in comparison to pure Ge.

To understand this behaviour at a very low field, we now present more detailed calculations over a considerably smaller range of electric fields close to $F = 0$. Figure 5.23 (a) presents the calculated evolution of electron mobility for electric field values ranging from 0 to 0.1 kV cm^{-1}, while Fig. 5.23 (b) depicts the calculated variation of electron mobility with alloy scattering set to zero. The calculated low-field mobility in $Ge_{0.84}Sn_{0.16}$ has a remarkable behaviour. The mobility decreases rapidly from its zero-field value for fields between 0 and 0.01 kV cm^{-1}, i.e. between 0 and 10 V cm^{-1}! At 0.1 kV cm^{-1}, the calculated mobility value has dropped to 10 ^{3} cm^2 V^{-1} s^{-1}, down by a factor of 400 from the zero-field mobility and already lower than that of Ge. Similar but less extreme behaviour is observed for all other Sn compositions with $x = 10\%$ and above. We attribute the rapid reduction in mobility within a very small electric field range to the early onset of scattering of electrons from the Γ to the L valley. The significant decrease in overall mobility is mostly brought on by alloy scattering, increases in strength with increasing x. The important role of alloy scattering is confirmed by the results in Fig. 5.23 (b) of the calculated field-dependent mobility in the absence of alloy scattering, where the peak mobility value for $Ge_{0.84}Sn_{0.16}$ reaches

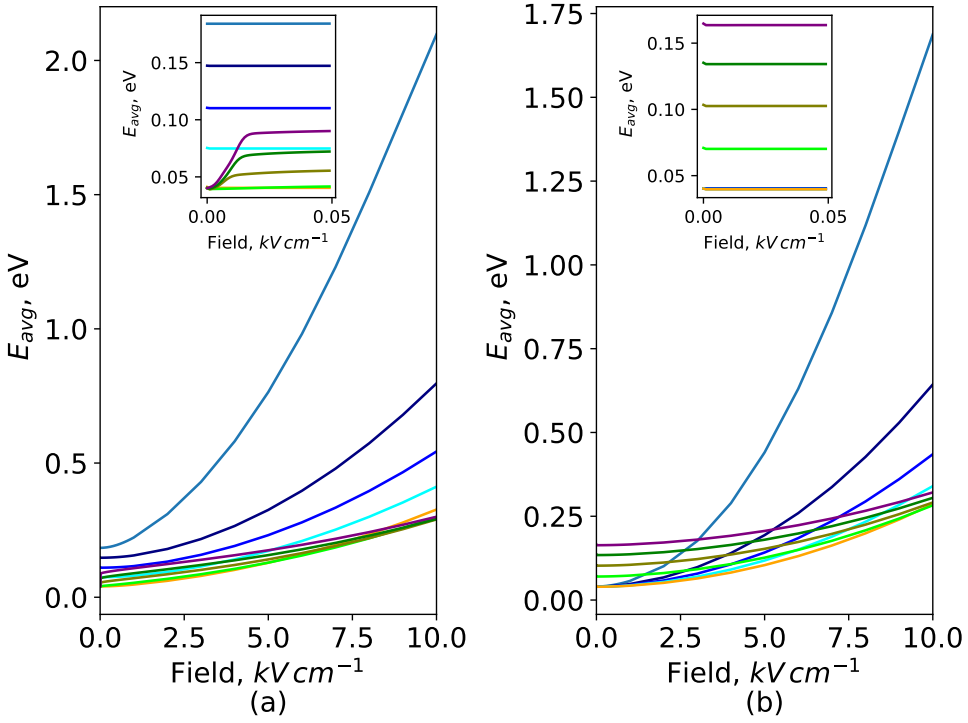

FIGURE 5.20: average energy of electrons (a) Γ and, (b) L valley as a function of applied electric field F, Ge, $Ge_{1-x}Sn_x$ alloy at x = 2, 4, 6, 8, 10, 12 and 16%. The inset zoomed images in both the sub-figures show the corresponding properties within the range of low electric field up to 0.05 kV cm^{-1}. Results are shown for Ge (royal blue) and various Sn compositions x = 2% (navy), 4% (blue), 6% (cyan), 8% (orange), 10% (lime), 12% (olive), 14% (green), 16% (purple).

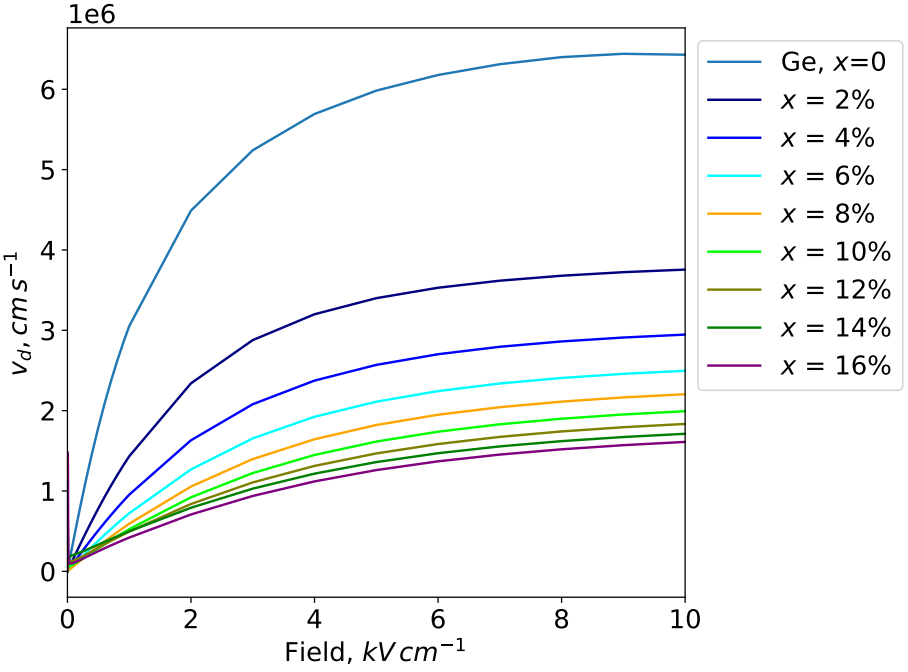

FIGURE 5.21: Evolution of drift velocity as a function of electric field F, in Ge, and $Ge_{1-x}Sn_x$ alloy at x = 2, 4, 6, 8, 10, 12 and 16%.

10^7 cm^2 V^{-1} s^{-1}, while the calculated mobility at 0.1 kV cm^{-1} is 2×10^4 cm^2 V^{-1} s^{-1}, up by over an order of magnitude compared to the value in Fig. 5.23 (a).

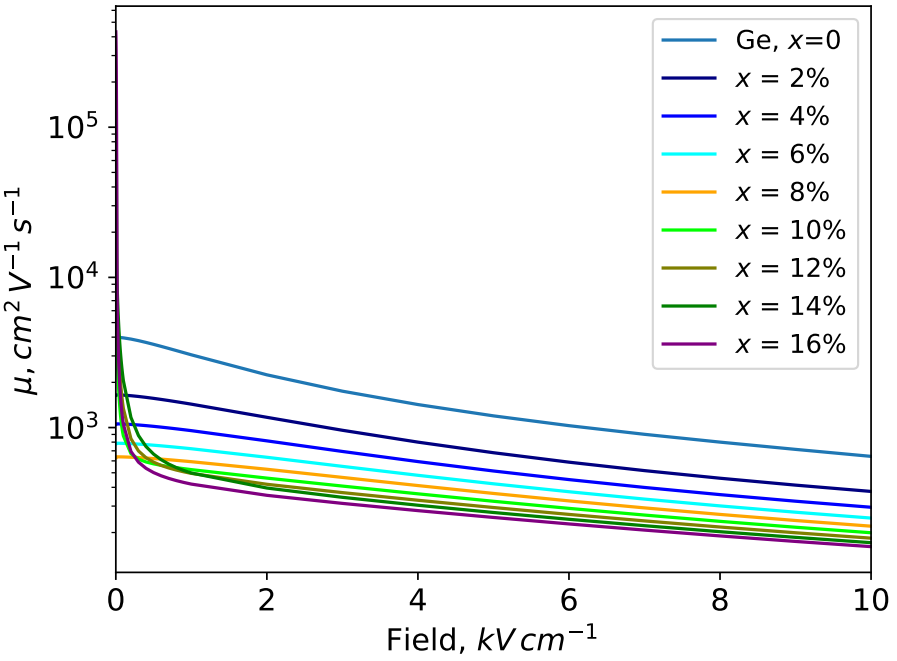

FIGURE 5.22: Evolution of mobility as a function of electric field F, Ge, $Ge_{1-x}Sn_x$ alloy at $x = 2$, 4, 6, 8, 10, 12 and 16%.

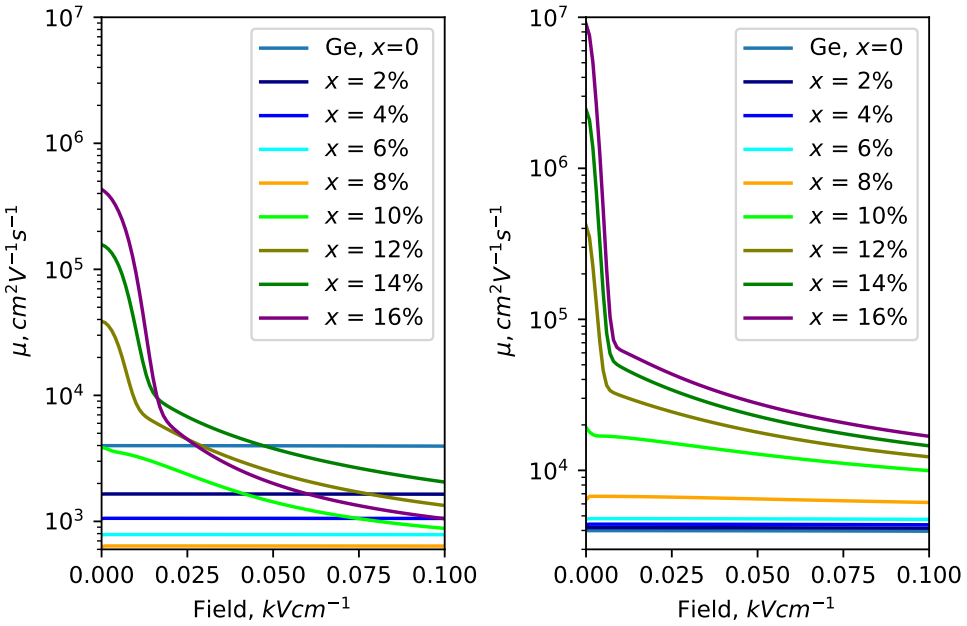

FIGURE 5.23: Comparison of the evolution of mobility in Ge, $Ge_{1-x}Sn_x$ alloy at $x = 2$, 4, 6, 8, 10, 12 and 16%, at very low electric field regime, (a) with alloy scattering, and (b) without alloy scattering.

Figure 5.24 (a) shows for various Sn compositions the calculated variation of electron drift velocity at low electric field strengths ranging from 0 to 0.1 kV cm^{-1}. The velocity-field curve for the highest Sn composition, $x = 16\%$ (purple line in Fig. 5.24) shows that the drift velocity increases linearly towards a peak of $\approx 1.4 \times 10^6$ cm s^{-1} at an electric field of 7×10^{-3} kV cm^{-1}, followed by a region of decreasing velocity until $F = 1.5 \times 10^{-2}$ kV cm^{-1}, resulting in negative differential

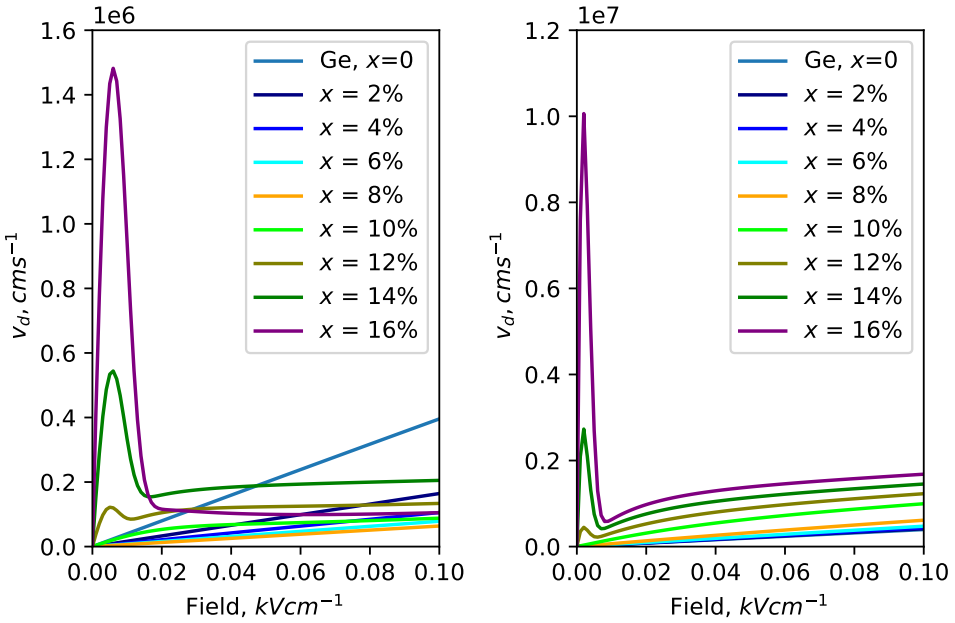

FIGURE 5.24: Comparison of evolution of drift velocity in Ge, $Ge_{1-x}Sn_x$ at x = 2, 4, 6, 8, 10, 12 and 16%, at very low electric field regime, (a) with alloy scattering, and (b) without alloy scattering).

resistance (NDR) – i.e. the Gunn effect – at these very low fields. As the electric field increases beyond 0.03 kV cm^{-1}, the drift velocity drops below that of Ge. The drift velocity gradually decreases further until it is only 6.7% of the peak velocity at F=7.4 $\times$ 10^{-2} kV cm^{-1}. Beyond this value, it then starts to increase with increasing field. For instance, at electric fields of 1 and 10 kV cm^{-1}, the drift velocities (Fig. 5.21) are $\approx$ 4.2 $\times$ 10^5 and 1.6 $\times$ 10^6 cm s^{-1} cm s^{-1} respectively, giving roughly a four times increase in drift velocity for a tenfold increase in the electric field. The results for Sn compositions of x = 14 and 12% follow the same pattern as that of x = 16%. For x = 14%, our calculations show a relatively lower peak velocity of $\approx$ 5.4 $\times$ 10^5 cm s^{-1}, at a very low electric field (6 $\times$ 10^{-3} kV cm^{-1}). $Ge_{0.86}Sn_{0.14}$ exhibits the NDR effect below a field of $\approx$ 1.8 $\times$ 10^{-2} kV cm^{-1}. The region and scale of NDR in $Ge_{0.88}Sn_{0.12}$ is extremely small. No NDR effect is observed for $Ge_{0.90}Sn_{0.10}$ in our calculations. $Ge_{1-x}Sn_x$ ($x \leq 8\%$), has an indirect band gap. In this range, the electron drift velocity decreases with increasing x, because of the increase in alloy scattering, but the overall field dependence remains similar to that of Ge. Again, the important role of alloy scattering is confirmed by comparing the results of Fig. 5.24 (a) with those of Fig. 5.24 (b), where the alloy scattering rates are set to zero.

Comparing the results for $Ge_{1-x}Sn_x$ with those for GaAs in the previous chapter, we find that at low field $Ge_{1-x}Sn_x$ has significantly higher mobility than GaAs for Sn compositions $x > 12\%$, but it does not maintain higher mobility with increasing electric field. For example, even at 0.2 $\times$ 10^{-3} kV cm^{-1}, the calculated electron mobility of GaAs is almost 18 times higher than that of $Ge_{0.84}Sn_{0.16}$. At F = 1 kV cm^{-1}, the ratio of predicted electron mobility of GaAs vs $Ge_{1-x}Sn_x$ is roughly 13%, 6.6%, and 6.6% for Sn compositions of 16%, 14%, and 12%, respectively. For an electric field of 10 kV cm^{-1}, these ratios are found to be 6.5%, 6.1%, and 5.6% respectively. In

GaAs, the onset of NDR is observed at approximately 3 kV cm^{-1}, whereas in $Ge_{1-x}Sn_x$ alloys ($x > 10$), we calculate the onset of NDR at a significantly lower electric field ($\approx 1.5 \times 10^{-2}$ kV cm^{-1}). Several factors play a role in explaining the marked difference between the two material systems. The presence of polar optical phonon scattering and the increased electron mass in GaAs both lead to reduced low-field mobility. As such electrons do not accelerate as rapidly in GaAs as in direct-gap $Ge_{1-x}Sn_x$. In addition, the energy separation between the Γ and L valleys is lower in $Ge_{1-x}Sn_x$ than in GaAs. All of these factors contribute to explaining the remarkably low field at which we predict onset of NDR velocity in direct-gap $Ge_{1-x}Sn_x$ alloys.

Although good quality $Ge_{1-x}Sn_x$ epitaxial layers have been grown with Sn composition up to 14% [61, 234] and beyond [199], there has, to the best of our knowledge, only been a limited amount of experimental investigation of electron mobility in $Ge_{1-x}Sn_x$ alloys. The work to date includes measurements on bulk [203, 235] and compressively stressed $Ge_{1-x}Sn_x$ alloy films [234].

D'Costa et al. [203] undertook transport measurements on $Ge_{0.98}Sn_{0.02}$ alloys with carrier concentrations of order 10^{18} cm^{-3} and above. The room temperature electron mobility for $n = 10^{19}$ cm^{-3} was of order 400 cm^2 V^{-1} s^{-1}, comparable to elemental Ge with an equivalent doping concentration. While this result is consistent with our calculations, we are more interested in direct-gap $Ge_{1-x}Sn_x$ alloys due to their potential to provide a CMOS-compatible group-IV semiconductor for electronic and photonic device applications.

Schulte-Braucks [235] undertook Hall experiments on n-type $Ge_{0.875}Sn_{0.125}$ samples. They found a maximal electron mobility of 4600 cm^2 V^{-1} s^{-1} at 50 K, a value much greater than bulk Ge at the comparable carrier concentration of 3 $\times 10^{17}$ cm^{-3}. They reported a 2-fold increase in mobility in $Ge_{0.875}Sn_{0.125}$ compared to Ge at 77 K, while the electron mobility of bulk $Ge_{0.875}Sn_{0.125}$ at ambient temperature was equivalent to that of pure Ge measured at the same carrier density. Their experimental results were significantly lower than their calculated mobilities which they attributed to a number of probable causes, including defect scattering and a high doping level.

Tao et al. [234] investigated compressively stressed $Ge_{1-x}Sn_x$ alloy sheets, where they found poorer mobility and electron concentration than Ge at 8% and 14% Sn composition. It should be noted however that the indirect- to direct-gap transition in compressively strained $Ge_{1-x}Sn_x$ occurs at higher Sn composition than in unstrained $Ge_{1-x}Sn_x$, so their results for 14% Sn are not directly comparable to ours at that composition. In summary, all of these results are consistent with our calculations but indicate that scattering mechanisms that we have omitted also play a part in determining the mobility, in particular in samples with higher doping levels. At higher doping levels, the fraction of carriers in the L valley will also increase.

Relatively few theoretical calculations have been undertaken to investigate the electron transport properties of $Ge_{1-x}Sn_x$. Mukhopadhyay et al. [80] showed a calculated increase in zero-field mobility with increasing x in direct-gap $Ge_{1-x}Sn_x$, but presented no analysis of the field dependence of drift velocity and mobility. Liu et al. [81] employed a simple single-temperature model to calculate the drift velocity versus electric field for three distinct compositions at room and low temperatures without solving the BTE. They did not observe NDR at room temperature, even at very high Sn

compositions. They demonstrated a twofold increase in electron mobility for a Sn composition of 20% in comparison to Ge. However, there is no mention of the specific scattering mechanisms considered in their analysis.

In comparison to the previous calculations, our analysis provides a fuller understanding of the electron transport properties, including detailed insight into scattering rates, distribution functions, electron occupancy, and the impact of alloy scattering on drift velocity and mobility as a function of electric field for Sn compositions covering the indirect- and direct-gap regimes.

5.6 Conclusion

The possibility of achieving enhanced electron mobility in direct-gap $Ge_{1-x}Sn_x$ alloys has been debated for the past several years. But, the majority of previous computations focused primarily on scattering mechanisms, ignoring the evolution of carrier distribution with applied electric field. However, understanding the electron transport properties of $Ge_{1-x}Sn_x$ alloys as a function of applied electric field not only helps fundamental understanding but also informs potential implementation in electronic devices. To determine the field-dependent electron transport properties, we first reviewed the fundamental features of the Ge and $Ge_{1-x}Sn_x$ CB structures, including how the band gap energies and effective masses change as a function of Sn composition. Following that, we analysed the evolution of scattering processes vs. electron energy at various Sn compositions, including the composition dependence of alloy scattering, as well as scattering due to acoustic phonons, inter- and intra-valley optical deformation potential. We then used these scattering rates to explore how variations in Sn composition affected the electron mobility while the electrons were still in the equilibrium Maxwell-Boltzmann distribution.

We calculated the zero-field mobility for Ge to be 3987 $cm^2\ V^{-1}\ s^{-1}$; in good agreement with experiment. For direct band gap $Ge_{0.84}Sn_{0.16}$, $Ge_{0.86}Sn_{0.14}$, and $Ge_{0.88}Sn_{0.12}$, our calculations predicted the zero-field electron mobility as 4.3×10^5, 1.6×10^5 and 3.9×10^4 $cm^2\ V^{-1}\ s^{-1}$ respectively, showing 100, 50, 10 times greater magnitude than that of pure Ge. Although $Ge_{0.90}Sn_{0.10}$ has a direct band gap, we found its calculated zero-field mobility to be comparable to that of pure Ge. Our analysis demonstrates that the Sn incorporation in Ge introduces two main factors that impact the zero-field electron mobility of $Ge_{1-x}Sn_x$: (i) the increase in alloy scattering, which raises the total scattering rate and limits the overall mobility; and (ii) the increase in electron population at the Γ valley, which has a significantly lower DOS than the L valley and thus enhances the overall mobility. Even if alloy scattering continues to limit the mobility at higher compositions ($x > 10\%$), it is expected that a significant proportion of the electrons will be in the lower DOS Γ valley at zero field. Therefore, at higher Sn compositions, the Γ lower DOS triumphs over alloy scattering, raising the zero-field mobility considerably above that of pure Ge. For lower Sn compositions, such as $Ge_{0.90}Sn_{0.10}$, the L valley with the greater DOS is still occupied by a majority of electrons. Overall mobility is constrained in this case by both alloy scattering and higher DOS.

Following the zero-field electron mobility calculation, we employed a multi-valley approach to solve the BTE in order to determine the electron transport properties of Ge and $Ge_{1-x}Sn_x$ as a function of the applied electric field. For the velocity-field curve, we calculate that the Gunn effect is exhibited in direct-gap $Ge_{0.84}Sn_{0.16}$ at a far lower electric field (≈ 0.015 kV cm^{-1}) than in GaAs (≈ 3 kV cm^{-1}), while the zero-field mobility of GaAs has a relatively lower value in comparison to $Ge_{0.84}Sn_{0.16}$. The origin of the Gunn effect at such a low electric field was due to the rapid acceleration of electrons in the Γ valley, enabling electron scattering from the Γ to L valley at very low fields. The very high DOS in the L valley and consequently higher scattering rates then account for the decreased mobility. The mobility of $Ge_{1-x}Sn_x$ then increases with increasing Sn composition in direct-gap $Ge_{1-x}Sn_x$ alloys, but only up to a very low electric field, beyond which it drops to levels below that in Ge.

Chapter 6

Summary, conclusions and outlook

This chapter describes the main findings of the thesis, and then presents a discussion of potential pathways for subsequent research on both group of alloys. Chapters 2 and 3 presented the theoretical analysis of the band-to-band tunneling (BTBT) current characteristics of group III-V (InN_xAs_{1-x}, $InAs_{1-z}Bi_z$) alloys. Chapter 4 focused on building an electron transport model for GaAs using the Boltzmann transport equation. Chapter. 5 presented an investigation of the field-dependent electron transport properties of Ge and $Ge_{1-x}Sn_x$ alloys.

6.1 BTBT in InN_xAs_{1-x} and $InAs_{1-z}Bi_z$ alloys

The goal of Chapter 2 was to introduce the relevant background theory behind our BTBT investigation of InN_xAs_{1-x} and $InAs_{1-z}Bi_z$ alloys. It began with a description of the electronic structure of InAs, a typical III-V direct band-gap semiconductor, and then presented a two-band Hamiltonian using the **k**.**p** method to represent the band dispersion. The concept of complex band structure (CBS) in a bulk semiconductor was then presented. Finally the BTBT generation rate model for InAs was presented based on these theories. In the BTBT model, first the CBS was constructed using the previously derived 2 band **k**.**p** Hamiltonian matrix. The field-dependent tunneling coefficient (T) was calculated using a numerical implementation of the Wentzel–Kramers–Brillouin (WKB) approximation and the analytical Kane model, and the generation rate was derived from the tunnelling coefficient. Our analysis found that the WKB approach produces the same results as the 2-band Kane model. However, 3-band Hamiltonian models are required to represent the altered band dispersion in highly mismatched alloys such as InN_xAs_{1-x} and $InAs_{1-z}Bi_z$. As a result, the analytical Kane model cannot represent such alloys.

Chapter. 3 aimed to present a theoretical analysis based on direct numerical implementation of the WKB approximation to investigate the impact of the band anti-crossing (BAC) interaction in narrow-gap, highly-mismatched dilute nitride and bismide alloys on BTBT in the mid-infrared spectral range, by employing model BAC Hamiltonians derived and parametrised from atomistic alloy supercell electronic structure calculations. By comparing the results of numerical calculations for highly mismatched InN_xAs_{1-x} and $InAs_{1-z}Bi_z$ to those with the conventional alloy $InAs_{1-y}Sb_y$,

we highlighted the impact of substitutional N or Bi atoms in InAs on the complex band structure, field-dependent BTBT coefficient T, and field-dependent BTBT generation rate G both at a fixed band gap and as a function of the zone-centre alloy band gap.

Our calculations at a fixed band gap demonstrated that the impact of BAC on BTBT was dominated by a field-dependent rivalry between the increased band edge effective mass (at low field) and the corresponding enhanced density of state (DOS) (at high field). While the first (second) of these contributions acts to decrease (increase) T, we found that the relative importance of these two effects was strongly field dependent.

For low field strengths ($F \lesssim 1$ MV cm^{-1}), our calculations demonstrate the potential to reduce BTBT by exploiting the impact of N or Bi on the complex band dispersion: the increased CB or VB edge effective mass increases the area bounded in energy and wave vector by the complex band linking the VB and CB, hence reducing G compared to that in $InAs_{1-y}Sb_y$ by $\approx 20\%$ and 50% in InN_xAs_{1-x} and $InAs_{1-z}Bi_z$, respectively. At high fields ($F \gtrsim 1$ MV cm^{-1}), the increased DOS due to interaction with the localised impurity states limits the growth of this area, reflecting that more states are available to contribute to BTBT in a given energy range and acting to increase G above that in $InAs_{1-y}Sb_y$.

Overall, we conclude that APDs and related devices – based on highly-mismatched alloys and operating in the mid-infrared spectral range – are unlikely to display significantly reduced leakage currents compared to equivalent devices based on conventional III-V semiconductor alloys. In practice, contributions to photodiode dark current associated with carrier leakage via BTBT are, at fixed wavelength, likely to be broadly comparable to those in devices based on conventional semiconductor alloys. Dilute bismide alloys are nevertheless of interest for low-noise, long-wavelength APD applications due to the projected strong reduction in hole impact ionisation rate.

The strong reduction and composition-dependent bowing of the band gap in InN_xAs_{1-x} and related highly-mismatched alloys provides access to longer wavelengths at fixed lattice mismatch compared to conventional alloys. It is possible therefore that highly-mismatched alloys can nonetheless play an important role in enabling the development of mid-infrared photodetectors at wavelengths which are challenging to access using conventional semiconductors.

The effects of the BAC interaction in highly mismatched alloys have largely been studied in terms of alterations to the real band structure and their implications for applications in photonic or photovoltaic devices. Our findings provide new light on the properties of this fascinating class of semiconductors by demonstrating that BAC interactions have the potential to modify the complex band structure and BTBT, opening up new avenues for potential device applications.

6.2 Electron transport in Ge and $Ge_{1-x}Sn_x$ alloys

The purpose of the second half of the thesis was to offer a detailed theoretical analysis of the electron transport properties of $Ge_{1-x}Sn_x$ alloys. There have been few theoretical studies of the electron transport properties of $Ge_{1-x}Sn_x$ alloys up to now. One previous study used a basic model

to calculate the drift velocity as a function of applied external field, and all subsequent research has considered only the zero-field electron mobility. Previous research anticipated that a direct-gap $Ge_{1-x}Sn_x$ alloy at higher Sn composition would have higher mobility than GaAs. But does it outperform GaAs when subjected to an applied electric field? Using the constant relaxation time approach, our work tried to answer this question and to provide a deeper understanding of the evolution of the electron transport properties in response to an applied field in $Ge_{1-x}Sn_x$. We first constructed and validated our field-dependent electron transport model for GaAs, as discussed in Chapter. 4 and then implemented the model to investigate the electron transport properties of Ge and $Ge_{1-x}Sn_x$ alloys in Chapter. 5.

The purpose of Chapter. 4 was to develop a field-dependent electron transport model for GaAs by solving the coupled multi-valley Boltzmann transport equation numerically using the relaxation time approximation. We began by presenting the relevant theoretical background for electron transport calculations in the case of a bulk semiconductor alloy, first by reviewing some of the important band structure characteristics that impact electron transport calculations, and then by outlining some of the important scattering mechanisms that restrict electron mobility in a semiconductor material such as GaAs. The electron transport model started at zero-field (in the equilibrium conditions) with the assumption that the electron energy distribution function followed a Maxwell-Boltzmann distribution in both sets of valleys (Γ and L). Then, we calculated the scattering rate due to the acoustic phonon, polar optical, and inter-valley optical phonons, which together have a significant influence on regulating the electron transport. By using a time-stepping method, we obtained the steady-state electron distribution functions and from these functions derived the associated electron transport properties at each electric field strength. Our calculations agreed well with a previous theoretical study that used the Monte Carlo approach, as well as showing good agreement with experimental results. This included replication of the well-known Gunn effect, demonstrating a negative differential resistance regime in the field-dependent electron transport properties. This computation was used to demonstrate the step-by-step theoretical framework as well as to validate the code, through comparison with earlier calculations.

Chapter. 5 used the BTE code developed to investigate the evolution of the electron transport properties in response to an applied electric field in $Ge_{1-x}Sn_x$ alloys as the alloys evolve from an indirect to a direct gap semiconductor with increasing Sn composition. Previous zero-field theoretical computations claimed an enhanced electron mobility in $Ge_{1-x}Sn_x$ for higher Sn compositions, x. However, these computations ignore the impact of the applied electric field, which is an important parameter when analysing electron transport properties.

For Ge, our predicted zero-field mobility value was 3987 $cm^2\ V^{-1}\ s^{-1}$; in good agreement with experimental data. We found acoustic phonon scattering to be the dominant scattering mechanism. The field-dependent electron transport calculations, i.e. the electron drift velocity and mobility vs. field, agreed well with previous theoretical and experimental results. Our calculation overestimated the drift velocity and mobility at higher fields. This is likely because the non-parabolicity

of the electron band energy and the X valleys were omitted from our model. Despite these simplifications, our model computed credible field-dependent electron transport parameters that are in good agreement with earlier research.

For $Ge_{1-x}Sn_x$, we first established from a literature review a model for the variation with Sn composition of the band gap energies and other relevant parameters for transport calculations. Then, we investigated the zero-field electron mobility (when the electrons still follow a Boltzmann distribution) as a function of Sn composition. We found that alloy scattering became the dominant scattering mechanism with increasing composition x in $Ge_{1-x}Sn_x$. Nevertheless, we calculated for the direct gap compositions $x = 16$, 14, and 12%, a 100, 50, and 10-fold increase respectively in electron mobility compared to that of pure Ge. The estimated electron mobility for Sn composition, ($x \leq 10\%$) was comparable to that of pure Ge.

Following the zero-field electron mobility calculation, we then employed the BTE model to evaluate electron transport properties of $Ge_{1-x}Sn_x$ in an applied electric field. From the velocity-field curve of $Ge_{0.84}Sn_{0.16}$, we found a very narrow region of negative differential resistance (NDR) at far lower electric field ($\approx$ 0.015 kV cm^{-1}) compared to GaAs ($\approx$ 3 kV cm $^{-1}$). We attributed the observation of the Gunn effect at such a low electric field to the rapid acceleration of electrons in the Γ valley, enabling electron scattering from the Γ to L valley at very low fields. The very high DOS in the L valley and consequently higher scattering rates then account for the decreased mobility. The mobility of $Ge_{1-x}Sn_x$ then increases with increasing Sn composition in direct-gap $Ge_{1-x}Sn_x$ alloys, but only up to a very low electric field, beyond which it drops to levels below that in Ge.

Test calculations that set the alloy scattering rate to zero showed an increase in electron mobility w.r.t the original computation, demonstrating that alloy scattering is the primary reason for the reduced mobility.

In conclusion, we have presented the first detailed theoretical analysis of electron transport as a function of applied electric field in $Ge_{1-x}Sn_x$ alloys as a function of Sn composition ($0 \leq x \leq 16\%$), over which range $Ge_{1-x}Sn_x$ evolves from an indirect-gap to direct-gap group-IV alloy. We conclude that $Ge_{1-x}Sn_x$ alloys can display very high mobility but only at very low fields, limiting any mobility advantage for application in devices such as MOSFETs and FinFETs.

6.3 Outlook

For the highly mismatched alloys InN_xAs_{1-x} and $InAs_{1-z}Bi_z$, our study identifies how BAC interactions modify the complex band structure and BTBT, thereby providing new insight into the opportunities for device applications. For APDs, we concluded that leakage currents in ideal dilute nitride and bismide devices are likely comparable to those in devices based on conventional III-V materials. For TFETs we described that Bi incorporation provides the potential to obtain both reduced subthreshold swing and increased on-state current, making $InAs_{1-z}Bi_z$ of interest for the development of low-power, high-speed devices. This is promising from the perspective of TFET

applications, suggesting a previously unexplored route to engineer the electrical characteristics via the complex band structure of the source and/or channel, and hence providing an additional approach to employ in the design of TFETs displaying subthermionic subthreshold slope and a high on-state current. We can consider this work as a future scope, where we could investigate the BTBT for nitride and bismide based TFETs structures. The role of BTBT could also form part of a wider study of impact ionisation in dilute bismide alloys, given the potential of these materials for use in low noise avalanche photodiodes.

For $Ge_{1-x}Sn_x$, our analysis predicts a very high mobility and Gunn effect at very low electric fields in direct-gap $Ge_{1-x}Sn_x$ alloys with high Sn composition $x = 16\%$. In practice, this may be very difficult to demonstrate experimentally given the challenges to grow high-quality $Ge_{1-x}Sn_x$ samples with such a high Sn composition. An alternative route to demonstrate the same effect could be to process structures where Ge is under high tensile strain [56, 236], of sufficient magnitude that the Ge Γ conduction band minimum drops below the L band minimum, giving a direct-gap Ge sample. Comparison of the transport characteristics of this structure and an unstrained piece of Ge from the same wafer would then allow to determine the impact of going from indirect to direct gap, while all other material parameters are nominally unchanged. A similar comparison could also be possible by varying the strain in high-quality $Ge_{1-x}Sn_x$ samples [63, 201, 234] with lower Sn composition, x. It would also be interesting in further calculations both to investigate the evolution of the predicted NDR as a function of temperature, and also to analyse how doping density would impact the results.

Overall, we found that the field-dependent electron mobility is limited by alloy scattering and by the small offset between the Γ and L valleys, even for Sn composition x as high as 0.16. Therefore when the electric field goes beyond 0.05 kV cm^{-1}, for all Sn compositions the mobility decreases and goes below that of pure Ge. Hence $Ge_{1-x}Sn_x$ will not be considered as a suitable high-mobility channel material for high voltage application. There has however also been interest in $Si_yGe_{1-x-y}Sn_x$ [62, 237–239] for CMOS compatible technology, and for photovoltaic technologies. It would be useful to know the electron transport properties in $Si_yGe_{1-x-y}Sn_x$. Hence future work could include an extension of the calculations carried out here to modify our existing BTE model to investigate the electron transport properties in such Si-Ge-Sn alloys.

Appendix A

Calculation of alloy scattering potentials

In this appendix, we give a description of the calculation of the alloy scattering parameters using the tight-binding method. The tight-binding calculations were undertaken by Dr. Christopher A. Broderick of the Photonics Theory group.

We denote the Hamiltonian of pure Ge by $\widehat{H}^{(0)}$. Substitutional incorporation of Sn to form $Ge_{1-x}Sn_x$ perturbs this Hamiltonian, giving rise to the alloy Hamiltonian $\widehat{H}(x) = \widehat{H}^{(0)} + \Delta\widehat{H}(x)$, where the impurity potential $\Delta\widehat{H}(x)$ encapsulates the chemical changes and structural relaxation associated with Sn incorporation. This impurity potential drives alloy scattering, such that to compute alloy scattering rates via Fermi's golden rule we must evaluate the matrix elements of $\Delta\widehat{H}(x)$. To describe alloy scattering involving the Γ and L point conduction band (CB) valleys in $Ge_{1-x}Sn_x$ we use ordered N atom $Ge_{N-1}Sn_1$ atomistic alloy supercells calculations to compute the Hamiltonian matrix $H_{mn}(x) = \left\langle m^{(0)}|\widehat{H}(x)|n^{(0)}\right\rangle$ explicitly, where superscripted " (0) " denotes the unperturbed Γ and L point CB edge eigenstates of Ge - i.e. $\widehat{H}^{(0)}\left|n^{(0)}\right\rangle = E_n^{(0)}\left|n^{(0)}\right\rangle$, so that $H_{mn}(x) = E_m^{(0)}\delta_{mn} + \left\langle m^{(0)}|\Delta\widehat{H}(x)|n^{(0)}\right\rangle$. We note that non-zero matrix elements $\Delta H_{mn}(x) = \left\langle m^{(0)}|\Delta\widehat{H}(x)|n^{(0)}\right\rangle$ of the impurity Hamiltonian describe (i) the shift in band energies, for $m = n$, or (ii) hybridisation between Ge host matrix eigenstates, for $m \neq n$. In what follows we neglect spin-orbit coupling, due to its minimal impact on the electronic structure close in energy to the CB edge of semiconducting $Ge_{1-x}Sn_x$.

We firstly compute the electronic structure of an unperturbed Ge_N supercell, from which we obtain the Γ point CB edge eigenstate $\left|\Gamma^{(0)}\right\rangle$, and the four degenerate L point states $\left|L_1^{(0)}\right\rangle$, $\left|L_2^{(0)}\right\rangle$, $\left|L_3^{(0)}\right\rangle$ and $\left|L_4^{(0)}\right\rangle$. Next, we set up and relax a series of ordered $Ge_{N-1}Sn_1$ alloy super cells and, using the aforementioned Ge eigenstates, explicitly compute the elements of the 5×5 Hamiltonian matrix $H_{mn}(x)$. Since we are interested here in interrogating only alloy scattering - which depends upon the eigenenergies of this reduced Hamiltonian, and only the moduli of the in general complex valued off diagonal matrix elements - we neglect differences in phase between our basis of L point Ge eigenstates and write

$$H(x) = \begin{pmatrix} E_\Gamma^{(0)} - \alpha x & V_{\Gamma L} & V_{\Gamma L} & V_{\Gamma L} & V_{\Gamma L} \\ V_{\Gamma L} & E_L^{(0)} + \gamma x & V_{LL} & V_{LL} & V_{LL} \\ V_{\Gamma L} & V_{LL} & E_L^{(0)} + \gamma x & V_{LL} & V_{LL} \\ V_{\Gamma L} & V_{LL} & V_{LL} & E_L^{(0)} + \gamma x & V_{LL} \\ V_{\Gamma L} & V_{LL} & V_{LL} & V_{LL} & E_L^{(0)} + \gamma x \end{pmatrix} \begin{matrix} |\Gamma^{(0)}\rangle \\ |L_1^{(0)}\rangle \\ |L_2^{(0)}\rangle \\ |L_3^{(0)}\rangle \\ |L_4^{(0)}\rangle \end{matrix} \tag{A.1}$$

where $V_{\Gamma L} = \beta_{\Gamma L} x$ and $V_{LL} = \beta_{LL} x$ respectively describe Sn-induced coupling between Ge Γ and L point eigenstates, and between distinct L point Ge eigenstates and where $E_\Gamma^{(0)}$ and $E_L^{(0)}$ are the respective unperturbed Ge Γ and L point CB edge energies.

The eigenvalues of Eq. (A.1) are

$$\begin{aligned} E_1 &= \frac{1}{2}\Bigg[E_\Gamma^{(0)} + E_L^{(0)} + (\gamma - \alpha)x + 3|V_{LL}| - \Bigg\{\left(E_\Gamma^{(0)} - \alpha x\right)^2 + \left(E_L^{(0)} + \gamma x\right)^2 \\ &- 2\left(E_\Gamma^{(0)} - \alpha x\right)\left(E_L^{(0)} + \gamma x - 3|V_{LL}|\right) + 3|V_{LL}|\left(2\left(E_L^{(0)} + \gamma x\right) + 3|V_{LL}|\right) - 16|V_{\Gamma L}|^2\Bigg\}^{1/2}\Bigg], \end{aligned} \tag{A.2}$$

$$E_2 = E_L^{(0)} + \gamma x - |V_{LL}|, \tag{A.3}$$

$$\begin{aligned} E_3 &= \frac{1}{2}\Bigg[E_\Gamma^{(0)} + E_L^{(0)} + (\gamma - \alpha)x + 3|V_{LL}| + \Bigg\{\left(E_\Gamma^{(0)} - \alpha x\right)^2 + \left(E_L^{(0)} + \gamma x\right)^2 \\ &- 2\left(E_\Gamma^{(0)} - \alpha x\right)\left(E_L^{(0)} + \gamma x - 3|V_{LL}|\right) + 3|V_{LL}|\left(2\left(E_L^{(0)} + \gamma x\right) + 3|V_{LL}|\right) - 16|V_{\Gamma L}|^2\Bigg\}^{1/2}\Bigg], \end{aligned} \tag{A.4}$$

where E_2 is threefold degenerate, describing alloy states corresponding to three orthogonal linear combinations of Ge L point states that possess purely p-like orbital character at the Sn atomic site, and which do not undergo hybridisation with $|\Gamma^{(0)}\rangle$. We note that $E_1(x)$ and $E_3(x)$ are the energies of a pair of hybridised alloy CB eigenstates of $H(x)$, resulting from Sn-induced coupling between two Ge eigenstates: $|\Gamma^{(0)}\rangle$ and a linear combination $|L^{(0)}(A_1)\rangle$ of the L point states possessing purely s-like orbital character at the Sn atomic site.

We can use the Hamiltonian in Eq. (A.1) and the eigenvalues in Eqs. (A.2) to (A.4) to extract the four alloy scattering parameters. We first use the value of the matrix element H_{11} in Eq. (A.1) to directly evaluate α. We then calculate γ by adding together the five eigenvalues Eq. (A.1), whose value equals the sum of the diagonal elements of the Hamiltonian. Knowing α and γ, we can then calculate V_{LL} from the value of the eigenvalues, E_2, given by Eq. (A.4). Finally we use the difference between E_3 and E_1 to determine $V_{\Gamma L}$.

$$\begin{aligned}\bar{E}_{\mathrm{L}}(x) - E_{\mathrm{L}}^{(0)} &= \frac{E_1(x) + 3E_2(x)}{4} - E_{\mathrm{L}}^{(0)} \\ &- \frac{1}{8}\Bigg[E_{\Gamma}^{(0)} - E_{\mathrm{L}}^{(0)} + (7\gamma - \alpha)x - 3\,|V_{\mathrm{LL}}| \\ &- \Bigg\{\left(E_{\Gamma}^{(0)} - \alpha x\right)^2 + \left(E_{\mathrm{L}}^{(0)} + \gamma x\right)^2 \\ &+ 3\,|V_{\mathrm{LL}}|\left(2\left(E_{\mathrm{L}}^{(0)} + \gamma x\right) + 3\,|V_{\mathrm{LL}}|\right) - 16\,|V_{\Gamma\mathrm{L}}|^2\Bigg\}^{1/2}\Bigg] \end{aligned} \tag{A.5}$$

The parameters α, γ, $\beta_{\Gamma\mathrm{L}}$, and β_{LL} were obtained from tight-binding calculations performed on ordered alloy supercells containing a single substitutional Sn impurity in $N = 16, 64$ and 128 atoms ($x = 6.25$, 1.5625 and 0.78125%, respectively), yielding: α= -1.3684 eV, γ=-0.1404 eV, $\beta_{\Gamma\mathrm{L}}$=2.5856 eV and β_{LL}= 1.7810 eV.

We rename the parameters α, γ, $\beta_{\Gamma\mathrm{L}}$ and β_{LL} as $\mathrm{D}_{al_{\Gamma}}$, $\mathrm{D}_{al_{L}}$, $\mathrm{D}_{al_{\Gamma L}}$ and $\mathrm{D}_{al_{LL}}$ respectively and use them in Chapter. 5 to compute the alloy scattering rate as a function of Sn composition.

Bibliography

[1] I. Sandall, F. Bastiman, B. White, R. Richards, D. Mendes, J. David, and C. Tan, "Demonstration of InAsBi photoresponse beyond 3.5 μm," Appl. Phys. Lett. **104** (2014).

[2] M. Seifikar, E. P. O'Reilly, and S. Fahy, "Theory of intermediate-and high-field mobility in dilute nitride alloys," Phys. Rev. B **84**, 165216 (2011).

[3] C. A. Broderick, M. Usman, S. J. Sweeney, and E. P. O'Reilly, "Band engineering in dilute nitride and bismide semiconductor lasers," Semicond. Sci. Technol. **27**, 094011 (2012).

[4] C. A. Broderick, P. E. Harnedy, and E. P. O'Reilly, "Theory of the electronic and optical properties of dilute bismide quantum well lasers," IEEE J. Sel. Topics Quantum Electron. **21**, 1503313 (2015).

[5] M. Gladysiewicz, R. Kudrawiec, and M. S. Wartak, "8-band and 14-band $\mathbf{k}\cdot\mathbf{p}$ modeling of electronic band structure and material gain in Ga(In)AsBi quantum wells grown on GaAs and InP substrates," J. Appl. Phys. **118**, 055702 (2015).

[6] J. Hader, J. V. Moloney, O. Rubel, S. C. Badescu, S. Johnson, and S. W. Koch, "Microscopic modelling of opto-electronic properties of dilute bismide materials for the mid-IR," Proc. SPIE **9767**, 976709 (2016).

[7] I. P. Marko and S. J. Sweeney, "Progress toward III–V bismide alloys for near- and mid-infrared laser diodes," IEEE J. Sel. Topics Quantum Electron. **23**, 1501512 (2017).

[8] O. Delorme, L. Cerutti, E. Luna, G. Narcy, A. Trampert, E. Tournié, and J.-B. Rodriguez, "GaSbBi/GaSb quantum well laser diodes," Appl. Phys. Lett. **110**, 222106 (2017).

[9] C. A. Broderick, W. Xiong, S. J. Sweeney, E. P. O'Reilly, and J. M. Rorison, "Theory and design of $In_xGa_{1-x}As_{1-y}Bi_y$ mid-infrared semiconductor lasers: type-I quantum wells for emission beyond 3 μm on InP substrates," Semicond. Sci. Technol. **33**, 094007 (2018).

[10] R. Arkani, C. A. Broderick, and E. P. O'Reilly, "Computational design of metamorphic In(N)AsSb mid-infrared light-emitting diodes," Proc. 18th IEEE International Conference on Nanotechnology (IEEE-NANO) (2018).

[11] D. B. Jackrel, S. R. Bank, H. B. Yuen, M. A. Wistey, and J. S. Harris Jr., "Dilute nitride GaInNAs and GaInNAsSb solar cells by molecular beam epitaxy," J. Appl. Phys. **101**, 114916 (2007).

[12] M. Wiemer, V. Sabnis, and H. Yuen, "43.5% efficient lattice matched solar cells," Proc. SPIE **8108**, 810804 (2011).

[13] V. Sabnis, H. Yuen, and M. Wiemer, "High-efficiency multijunction solar cells employing dilute nitrides," AIP Conf. Proc. **1477**, 14 (2012).

[14] N. Miyashita, N. Ahsan, and Y. Okada, "Generation and collection of photocarriers in dilute nitride GaInNAsSb solar cells," Prog. Photovolt. **24**, 28 (2016).

[15] Y. J. Kuang, K. M. Yu, R. Kudrawiec, A. V. Luce, M. Ting, W. Walukiewicz, and C. W. Tu, "GaNAsP: an intermediate band semiconductor grown by gas-source molecular beam epitaxy," Appl. Phys. Lett. **102**, 112105 (2013).

[16] R. Kudrawiec, A. V. Luce, M. Gladysiewicz, M. Ting, Y. J. Kuang, C. W. Tu, O. D. Dubon, K. M. Yu, and W. Walukiewicz, "Electronic band structure of $GaN_xP_yAs_{1-x-y}$ highly mismatched alloys: suitability for intermediate-band solar cells," Phys. Rev. Applied **1**, 034007 (2014).

[17] H. Allami and J. R. Krich, "Plasma frequency in doped highly mismatched alloys," Phys. Rev. B **103**, 035201 (2021).

[18] P. T. Webster, A. J. Shalindar, N. A. Riordan, C. Gogineni, H. Liang, A. R. Sharma, and S. R. Johnson, "Optical properties of InAsBi and optimal designs of lattice-matched and strain-balanced III-V semiconductor superlattices," J. Appl. Phys. **119**, 225701 (2016).

[19] A. R. Adams, "Band-structure engineering to control impact ionisation and related high-field processes," Electron. Lett. **40**, 1086 (2004).

[20] S. L. Tan, W. M. Soong, J. E. Green, M. J. Steer, S. Zhang, L. J. J. Tan, J. S. Ng, I. P. Marko, S. J. Sweeney, A. R. Adams, et al., "Experimental evaluation of impact ionization in dilute nitride GaInNAs diodes," Appl. Phys. Lett. **103**, 102101 (2013).

[21] Y. Liu, X. Yi, N. J. Bailey, Z. Zhou, T. B. O. Rockett, L. W. Lim, C. H. Tan, R. D. Richards, and J. P. R. David, "Valence band engineering of GaAsBi for low noise avalanche photodiodes," Nat. Commun. **12**, 4784 (2021).

[22] "Iea (2022), data centres and data transmission networks, iea, paris,", URL https://www.iea.org/fuels-and-technologies/data-centres-networks.

[23] "Datacentre,", URL https://datacentremagazine.com/articles/efficiency-to-loom-large-for-data-centre-industry-in-2023.

[24] "Engie,", URL https://www.engie.com/en/campaign/green-data-centers.

[25] A. M. Ionescu and H. Riel, "Tunnel field-effect transistors as energy-efficient electronic switches," Nature **479**, 329 (2001).

[26] A. Liu, R. Jones, L. Liao, D. Samara-Rubio, D. Rubin, O. Cohen, R. Nicolaescu, and M. Paniccia, "A high-speed silicon optical modulator based on a metal–oxide–semiconductor capacitor," Nature **427**, 615 (2004).

[27] L. Alloatti, R. Palmer, S. Diebold, K. P. Pahl, B. Chen, R. Dinu, M. Fournier, J.-M. Fedeli, T. Zwick, W. Freude, et al., "100 GHz silicon–organic hybrid modulator," Light Sci. Appl **3**, e173 (2014).

[28] D. Patel, A. Samani, V. Veerasubramanian, S. Ghosh, and D. V. Plant, "Silicon photonic segmented modulator-based electro-optic DAC for 100 Gb/s PAM-4 generation," IEEE Photonics Technology Letters **27**, 2433 (2015).

[29] G. T. Reed, W. R. Headley, and C. J. Png, in "Optoelectronic Integration on Silicon II" (SPIE, 2005), vol. 5730, pp. 1–18.

[30] R. Soref and J. Lorenzo, "Single-crystal silicon: a new material for 1.3 and 1.6 μm integrated-optical components," Electron. Lett. **21**, 953 (1985).

[31] A. Rickman, "The commercialization of silicon photonics," Nat. Photonics **8**, 579 (2014).

[32] W. Wang, D. Lei, Y.-C. Huang, K. H. Lee, W.-K. Loke, Y. Dong, S. Xu, C. S. Tan, H. Wang, S.-F. Yoon, et al., "High-performance GeSn photodetector and fin field-effect transistor (FinFET) on an advanced GeSn-on-insulator platform," Opt. Express **26**, 10305 (2018).

[33] E. P. O'Reilly, A. Lindsay, P. J. Klar, A. Polimeni, and M. Capizzi, "Trends in the electronic structure of dilute nitride alloys," Semicond. Sci. Technol. **24**, 033001 (2009).

[34] C. A. Broderick, I. P. Marko, E. P. O'Reilly, and S. J. Sweeney, "Chapter 10: Dilute Bismide Alloys, Handbook of Optoelectronic Device Modeling and Simulation, Vol. 1" (CRC Press, 2017).

[35] M. Osinski, "InNAs-a new optoelectronic material for mid-infrared applications," Opto-Electron. Rev. pp. 321–326 (2003).

[36] Q. Zhuang, A. Godenir, A. Krier, G. Tsai, and H. Lin, "Molecular beam epitaxial growth of InAsN: Sb for midinfrared Optoelectronics," Appl. Phys. Lett. **93** (2008).

[37] Q. Zhuang, A. Godenir, A. Krier, K. Lai, and S. Haywood, "Room temperature photoluminescence at 4.5 μm from InAsN," J. Appl. Phys. **103** (2008).

[38] O. Makarovsky, W. Feu, A. Patanè, L. Eaves, Q. Zhuang, A. Krier, R. Beanland, and R. Airey, "Hot electron transport and impact ionization in the narrow energy gap $InAs_{1-x}N_x$ alloy," Appl. Phys. Lett. **96** (2010).

[39] I. Mal and D. P. Samajdar, "Investigation of optoelectronic and thermoelectric properties of InAsBi for LWIR applications: A first principles and k dot p study," Mater. Sci. Semicond. Process. **137**, 106178 (2022).

[40] I. Mal, S. Singh, and D. P. Samajdar, "Design and simulation of InAsBi PIN photodetector for Long wavelength Infrared applications," Materials Today: Proceedings **57**, 289 (2022).

[41] A. Mahmoodi, H. D. Jahromi, and M. H. Sheikhi, "Dark current modeling and noise analysis in quantum dot infrared photodetectors," IEEE Sensor. J. **15**, 5504 (2015).

[42] J. C. Campbell, "Recent advances in avalanche photodiodes," J. Lightwave Tech. **34**, 278 (2016).

[43] S. J. Sweeney and J. Mukherjee, "Chapter 35: Optoelectronic Materials and Devices, Springer Handbook of Electronic and Photonic Materials" (Springer, 2017).

[44] U. E. Avci, D. H. Morris, and I. A. Young, "Tunnel field-effect transistors: prospects and challenges," IEEE J. Electron. Devices Soc. **3**, 88 (2015).

[45] E. Lind, E. Memišević, A. W. Dey, and L.-E. Wernersson, "III-V heterostructure nanowire tunnel FETs," IEEE J. Electron. Devices Soc. **3**, 96 (2015).

[46] C. Convertino, C. B. Zota, H. Schmid, A. M. Ionescu, and K. E. Moselund, "III–V heterostructure tunnel field-effect transistor," J. Phys.: Condens. Matter **30**, 264005 (2018).

[47] X. Yi, L. W. Lim, J. S. Cheong, C. H. Tan, J. P. R. David, S. Xie, D. L. Huffaker, B. Liang, and M. C. Debnath, "Extremely low excess noise and high sensitivity $AlAs_{0.56}Sb_{0.44}$ avalanche photodiodes," Nat. Photonics **13**, 683 (2019).

[48] A. H. Jones, S. D. March, S. R. Bank, and J. C. Campbell, "Low-noise high-temperature AlInAsSb/GaSb avalanche photodiodes for 2-μm applications," Nat. Photonics **14**, 559 (2020).

[49] M. V. Fischetti and S. E. Laux, "Band structure, deformation potentials, and carrier mobility in strained Si, Ge, and SiGe alloys," J. Appl. Phys. **80**, 2234 (1996).

[50] J. Liu, X. Sun, D. Pan, X. Wang, L. C. Kimerling, T. L. Koch, and J. Michel, "Tensile-strained, n-type Ge as a gain medium for monolithic laser integration on Si," Opt. Express **15**, 11272 (2007).

[51] P. H. Lim, S. Park, Y. Ishikawa, and K. Wada, "Enhanced direct bandgap emission in germanium by micromechanical strain engineering," Opt. Express **17**, 16358 (2009).

[52] M. El Kurdi, G. Fishman, S. Sauvage, and P. Boucaud, "Band structure and optical gain of tensile-strained germanium based on a 30 band $\mathbf{k}\cdot\mathbf{p}$ formalism," J. Appl. Phys. **107**, 013710 (2010).

[53] G. Pizzi, M. Virgilio, and G. Grosso, "Tight-binding calculation of optical gain in tensile strained [001]-Ge/SiGe quantum wells," Nanotechnology **21**, 055202 (2009).

[54] W. Huang, B. Cheng, C. Xue, and H. Yang, "The band structure and optical gain of a new IV-group alloy GePb: A first-principles calculation," J. Alloys Compd. **701**, 816 (2017).

[55] M. J. Süess, R. Geiger, R. Minamisawa, G. Schiefler, J. Frigerio, D. Chrastina, G. Isella, R. Spolenak, J. Faist, and H. Sigg, "Analysis of enhanced light emission from highly strained germanium microbridges," Nat. Photonics **7**, 466 (2013).

[56] J. R. Jain, A. Hryciw, T. M. Baer, D. A. Miller, M. L. Brongersma, and R. T. Howe, "A micromachining-based technology for enhancing germanium light emission via tensile strain," Nat. Photonics **6**, 398 (2012).

[57] C. Stephenson, W. O'Brien, M. Penninger, W. Schneider, M. Gillett-Kunnath, J. Zajicek, K. Yu, R. Kudrawiec, R. Stillwell, and M. Wistey, "Band structure of germanium carbides for direct bandgap silicon photonics," J. Appl. Phys. **120** (2016).

[58] A. C. Kirwan, S. Schulz, and E. P. O'Reilly, "Nature of the band gap of Ge:C alloys: insights from hybrid functional density functional theory calculations," Semicond. Sci. Technol. **34**, 075007 (2019).

[59] E. J. O'Halloran, "Theory of the electronic and optical properties of germanium-tin alloys" (University College Cork, 2020).

[60] D. W. Jenkins and J. D. Dow, "Electronic properties of metastable $Ge_{1-x}Sn_x$ alloys," Phys. Rev. B **36**, 7994 (1987).

[61] S. Wirths, R. Geiger, N. Von Den Driesch, G. Mussler, T. Stoica, S. Mantl, Z. Ikonic, M. Luysberg, S. Chiussi, J.-M. Hartmann, et al., "Lasing in direct-bandgap GeSn alloy grown on Si," Nat. Photonics **9**, 88 (2015).

[62] Y. Zhou, Y. Miao, S. Ojo, H. Tran, G. Abernathy, J. M. Grant, S. Amoah, G. Salamo, W. Du, J. Liu, et al., "Electrically injected GeSn lasers on Si operating up to 100 K," Optica **7**, 924 (2020).

[63] D. Rainko, Z. Ikonic, A. Elbaz, N. von den Driesch, D. Stange, E. Herth, P. Boucaud, M. El Kurdi, D. Grützmacher, and D. Buca, "Impact of tensile strain on low Sn content GeSn lasing," Scientific reports **9**, 259 (2019).

[64] K. P. Homewood and M. A. Lourenço, "The rise of the GeSn laser," Nat. Photonics **9**, 78 (2015).

[65] K. Lu Low, Y. Yang, G. Han, W. Fan, and Y.-C. Yeo, "Electronic band structure and effective mass parameters of $Ge_{1-x}Sn_x$ alloys," J. Appl. Phys. **112**, 103715 (2012).

[66] S. Gupta, "Germanium-tin (GeSn) technology" (Stanford University, 2013).

[67] B. Dutt, H. Lin, D. S. Sukhdeo, B. M. Vulovic, S. Gupta, D. Nam, K. C. Saraswat, and J. S. Harris Jr, "Theoretical analysis of GeSn alloys as a gain medium for a Si-compatible laser," IEEE J. Sel. Topics Quantum Electron. **19**, 1502706 (2013).

[68] P. Moontragoon, Z. Ikonić, and P. Harrison, "Band structure calculations of Si–Ge–Sn alloys: achieving direct band gap materials," Semicond. Sci. Technol. **22**, 742 (2007).

[69] S. Ghosh, R. Bansal, G. Sun, R. A. Soref, H.-H. Cheng, and G.-E. Chang, "Design and Optimization of GeSn Waveguide Photodetectors for 2-μm band silicon photonics," Sensors **22**, 3978 (2022).

[70] M. Oehme, M. Schmid, M. Kaschel, M. Gollhofer, D. Widmann, E. Kasper, and J. Schulze, "GeSn pin detectors integrated on Si with up to 4% Sn," Appl. Phys. Lett. **101**, 141110 (2012).

[71] H. Tran, T. Pham, J. Margetis, Y. Zhou, W. Dou, P. C. Grant, J. M. Grant, S. Al-Kabi, G. Sun, R. A. Soref, et al., "Si-based GeSn photodetectors toward mid-infrared imaging applications," ACS Photonics **6**, 2807 (2019).

[72] H. Kumar and R. Basu, "Design of mid-Infrared $Ge_{1-x}Sn_x$ Homojunction pin Photodiodes on Si Substrate," IEEE Sensors Journal **22**, 7743 (2022).

[73] L. Zhang and J. Dai, "$Ge_{1-x}Sn_x/Si_{1-y}Sn_y$ SLs lattice-matched to Ge for 1.55 μm lasers," Physics Letters A **466**, 128726 (2023).

[74] C. Schulte-Braucks, R. Pandey, R. N. Sajjad, M. Barth, R. K. Ghosh, B. Grisafe, P. Sharma, N. von den Driesch, A. Vohra, G. B. Rayner, et al., "Fabrication, characterization, and analysis of Ge/GeSn heterojunction p-type tunnel transistors," IEEE Trans. Electron. Devices **64**, 4354 (2017).

[75] J. Schulze, A. Blech, A. Datta, I. A. Fischer, D. Hähnel, S. Naasz, E. Rolseth, and E.-M. Tropper, "Vertical Ge and GeSn heterojunction gate-all-around tunneling field effect transistors," Solid-State Electron. **110**, 59 (2015).

[76] Y. Yang, G. Han, P. Guo, W. Wang, X. Gong, L. Wang, K. L. Low, and Y.-C. Yeo, "Germanium–tin p-channel tunneling field-effect transistor: Device design and technology demonstration," IEEE Trans. Electron. Devices **60**, 4048 (2013).

[77] G. Han, Y. Wang, Y. Liu, H. Wang, M. Liu, C. Zhang, J. Zhang, B. Cheng, and Y. Hao, "Relaxed germanium-tin P-channel tunneling field-effect transistors fabricated on Si: impacts of Sn composition and uniaxial tensile strain," AIP Advances **5**, 057145 (2015).

[78] M. D. Dunne, "Atomistic simulation and analysis of novel Group-IV semiconductor alloys and devices" (Ph.D. Thesis, University College Cork, 2023).

[79] J. D. Sau and M. L. Cohen, "Possibility of increased mobility in Ge-Sn alloy system," Phys. Rev. B **75**, 045208 (2007).

[80] B. Mukhopadhyay, G. Sen, R. Basu, S. Mukhopadhyay, and P. K. Basu, "Prediction of large enhancement of electron mobility in direct gap $Ge_{1-x}Sn_x$ alloy," Phys. Status Solidi B **254**, 1700244 (2017).

[81] L. Liu, R. Liang, J. Wang, and J. Xu, "Investigation on the effective mass of $Ge_{1-x}Sn_x$ alloys and the transferred-electron effect," Apple. Phys. Express **8**, 031301 (2015).

[82] Y. Zhou, Q. Lu, X. Chai, Z. Xu, J. Chen, A. Krier, and L. He, "InAs/GaSb superlattice interband cascade light emitting diodes with high output power and high wall-plug efficiency," Appl. Phys. Lett. **114**, 253507 (2019).

[83] S. Suchalkin, J. Ludwig, G. Belenky, B. Laikhtman, G. Kipshidze, Y. Lin, L. Shterengas, D. Smirnov, S. Luryi, W. L. Sarney, et al., "Electronic properties of unstrained unrelaxed narrow gap $InAs_xSb_{1-x}$ alloys," J. Phys. D: Appl. Phys. **49**, 105101 (2016).

[84] M.-H. Lee, P.-L. Liu, Y.-A. Hong, Y.-T. Chou, J.-Y. Hong, and Y.-J. Siao, "Electronic band structures of $Ge_{1-x}Sn_x$ semiconductors: A first-principles density functional theory study," J. Appl. Phys. **113**, 063517 (2013).

[85] E. Galluccio, "GeSn semiconductor for micro-nanoelectronic applications" (Ph.D. Thesis, University College Cork, 2020).

[86] E. P. O'Reilly, "Quantum Theory of Solids" (Taylor and Francis, London, 2002).

[87] C. A. Broderick, "Theory of the electronic and optical properties of dilute bismide alloys" (Ph.D. Thesis, University College Cork, 2015).

[88] I. Bolland, "Complex band structure calculations of the electronic structure of nitride quantum wells," (2003).

[89] M. G. Reuter, "A unified perspective of complex band structure: interpretations, formulations, and applications," J. Phys. Condens. Matter **29**, 053001 (2016).

[90] E. O. Kane, "Theory of tunneling," J. Appl. Phys. **32**, 83 (1961).

[91] L. Esaki, "Long Journey into Tunneling ," Proc. IEEE **62**, 825 – 831 (1974).

[92] S. Ma, "Silicon-germanium based tunnel field effect transistor for low power computation" (University of California, Los Angeles, 2014).

[93] T. A. Growden, D. F. Storm, E. M. Cornuelle, E. R. Brown, W. Zhang, B. P. Downey, J. A. Roussos, N. Cronk, L. B. Ruppalt, J. G. Champlain, et al., "Superior growth, yield, repeatability, and switching performance in GaN-based resonant tunneling diodes," Appl. Phys. Lett. **116**, 113501 (2020).

[94] E. O. Kane, "Zener tunneling in semiconductors," J. Phys. Chem. Solids **12**, 181 (1959).

[95] A. Seabaugh, A. Taddiken, E. Beam, J. Randall, Y.-C. Kao, and B. Newell, "Room-temperature resonant tunnelling bipolar transistor XNOR and XOR integrated circuits," Electron. Lett. **20**, 1802 (1993).

[96] N. Yokoyama, K. Imamura, H. Ohnishi, T. Mori, S. Muto, and A. Shibatomi, "Resonant-tunneling hot electron transistor (RHET)," Solid-State Electron. **31**, 577 (1988).

[97] G. S. Sahoo and G. P. Mishra, "Effect of wideband gap tunnel diode and thickness of the window layer on the performance of a dual junction solar cell," Proc. Technol **25**, 684 (2016).

[98] J. Liang and Y. Hu, "Design of an extreme low cutoff frequency highpass frontend for CMOS ISFET via direct tunneling principle," IEEE Trans. Biomed. Circuits Syst **15**, 210 (2021).

[99] G. Haddad and P. Mazumder, "Tunneling devices and applications in high functionality/speed digital circuits," Solid-State Electron. **41**, 1515 (1997).

[100] R. Molaei Imen Abadi and M. Saremi, "A resonant tunneling nanowire field effect transistor with physical contractions: a negative differential resistance device for low power very large scale integration applications," J. Electron. Mater **47**, 1091 (2018).

[101] Y. Liu, A. Offenhäusser, and D. Mayer, "Rectified tunneling current response of biofunctionalized metal–bridge–metal junctions," Biosens. Bioelectron. **25**, 1173 (2010).

[102] M. Asada and S. Suzuki, "Terahertz emitter using resonant-tunneling diode and applications," Sensors **21**, 1384 (2021).

[103] C.-H. Wang, V. Chen, C. J. McClellan, A. Tang, S. Vaziri, L. Li, M. E. Chen, E. Pop, and H.-S. P. Wong, "Ultrathin three-monolayer tunneling memory selectors," ACS Nano **15**, 8484 (2021).

[104] N. N. Reddy and D. K. Panda, "A comprehensive review on tunnel field-effect transistor (TFET) based biosensors: recent advances and future prospects on device structure and sensitivity," Silicon **13**, 3085 (2021).

[105] M. Dassi, J. Madan, R. Pandey, and R. Sharma, "Chemical modulation of conducting polymer gate electrode work function based double gate Mg_2Si TFET for gas sensing applications," J. Mater. Sci. Mater. Electron. pp. 1–10 (2022).

[106] J. W. Lee, J. S. Woo, and W. Y. Choi, "Tunneling field-effect transistors for neuromorphic applications," J. Semicond. Engg. **2**, 142 (2021).

[107] G. Nazir, A. Rehman, and S.-J. Park, "Energy-efficient tunneling field-effect transistors for low-power device applications: challenges and opportunities," ACS Appl. Mater. Interfaces **12**, 47127 (2020).

[108] M. Nada, F. Nakajima, T. Yoshimatsu, Y. Nakanishi, S. Tatsumi, Y. Yamada, K. Sano, and H. Matsuzaki, "High-speed III-V based avalanche photodiodes for optical communications—the forefront and expanding applications," Appl. Phys. Lett. **116** (2020).

[109] M. A. Itzler, M. Entwistle, M. Owens, K. Patel, X. Jiang, K. Slomkowski, S. Rangwala, P. F. Zalud, T. Senko, J. Tower, et al., in "Detectors and Imaging Devices: Infrared, Focal Plane, Single Photon" (SPIE, 2010), vol. 7780, pp. 387–401.

[110] J. Rothman, S. Pes, J. Abergel, S. Gout, A. Coquiard, G. Badano, G. Lasfargues, A. Vandeneyde, J.-A. Nicolas, J.-L. Santailler, et al., in "International Conference on Space Optics—ICSO 2022" (SPIE, 2023), vol. 12777, pp. 1858–1867.

[111] E. Merzbacher, "Quantum Mechanics" (Jones & Bartlett Publishers, 1961).

[112] A. Pan and C. O. Chui, "Modeling direct interband tunneling I: bulk semiconductors," J. Appl. Phys. **116**, 054508 (2014).

[113] B. Jonsson and S. T. Eng, "Solving the schrodinger equation in arbitrary quantum-well potential profiles using the transfer matrix method," IEEE J. Quantum Electron. **26**, 2025 (1990).

[114] J. S. Walker and J. Gathright, "A transfer-matrix approach to one-dimensional quantum mechanics using mathematica," Computers in Physics **6**, 393 (1992).

[115] M. Luisier and G. Klimeck, "Simulation of nanowire tunneling transistors: from the Wentzel–Kramers–Brillouin approximation to full-band phonon-assisted tunneling," J. Appl. Phys. **107**, 084507 (2010).

[116] H. Carrillo-Nuñez, A. Ziegler, M. Luisier, and A. Schenk, "Modeling direct band-to-band tunneling: from bulk to quantum-confined semiconductor devices," J. Appl. Phys. **117**, 234501 (2015).

[117] M. Luisier, A. Schenk, W. Fichtner, and G. Klimeck, "Atomistic simulation of nanowires in the $sp^3d^5s^*$ tight-binding formalism: from boundary conditions to strain calculations," Phys. Rev. B **74**, 205323 (2006).

[118] Y. Yamada, H. Tsuchiya, and M. Ogawa, "Quantum transport simulation of silicon-nanowire transistors based on direct solution approach of the Wigner transport equation," IEEE Trans. Electron. Devices **56**, 1396 (2009).

[119] O. Morandi, "Multiband Wigner-function formalism applied to the Zener band transition in a semiconductor," Phys. Rev. B **80**, 024301 (2009).

[120] E. O. Kane, "Band structure of indium antimonide," J. Phys. Chem. Solids **1**, 249 (2957).

[121] E. O. Kane, "Chapter 3: The $\mathbf{k}\cdot\mathbf{p}$ Method," Semicond. Semimet. **1**, 75 (1966).

[122] I. Vurgaftman, J. Meyer, and L. Ram-Mohan, "Band parameters for III-V compound semiconductors and their alloys," J. Appl. Phys. **89**, 5815 (2001).

[123] J. M. Luttinger and W. Kohn, "Motion of electrons and holes in perturbed periodic fields," Phys. Rev. **97**, 869 (1955).

[124] L. C. Andreani, A. Pasquarello, and F. Bassani, "Hole subbands in strained GaAs-$Ga_{1-x}Al_xAs$ quantum wells: exact solution of the effective-mass equation," Phys. Rev. B **36**, 5887 (1987).

[125] A. T. Meney, B. Gonul, and E. P. O'Reilly, "Evaluation of various approximations used in the envelope-function method," Phys. Rev. B **50**, 10893 (1994).

[126] D. Esseni, M. Pala, P. Palestri, C. Alper, and T. Rollo, "A review of selected topics in physics based modeling for tunnel field-effect transistors," Semicond. Sci. Technol. **32**, 083005 (2017).

[127] M. Luisier and G. Klimeck, "Atomistic full-band design study of InAs band-to-band tunneling field-effect transistors," IEEE Electron. Dev. Lett. **30**, 602 (2009).

[128] W. V. Houston, "Acceleration of electrons in a crystal lattice," Phys. Rev. **57**, 184 (1940).

[129] C. A. Broderick, M. Seifikar, E. P. O'Reilly, and J. M. Rorison, "Chapter 9: Dilute Nitride Alloys, Handbook of Optoelectronic Device Modeling and Simulation, Vol. 1" (CRC Press, 2017).

[130] W. Shan, W. Walukiewicz, J. W. Ager III, E. E. Haller, J. F. Geisz, D. J. Friedman, J. M. Olson, and S. R. Kurtz, "Band anticrossing in GaInNAs alloys," Phys. Rev. Lett. **82**, 1221 (1999).

[131] W. Shan, W. Walukiewicz, K. M. Yu, J. W. Ager III, E. E. Haller, J. F. Geisz, D. J. Friedman, J. M. Olson, S. R. Kurtz, H. P. Xin, et al., "Band anticrossing in III–N–V alloys," Phys. Status Solidi B **223**, 75 (2001).

[132] J. Wu, W. Shan, and W. Walukiewicz, "Band anticrossing in highly mismatched III–V semiconductor alloys," Semicond. Sci. Technol. **17**, 860 (2002).

[133] A. Lindsay and E. P. O'Reilly, "Theory of enhanced bandgap non-parabolicity in GaN_xAs_{1-x} and related alloys," Solid State Commun. **112**, 443 (1999).

[134] A. Lindsay, S. Tomić, and E. P. O'Reilly, "Derivation of a 10-band $\mathbf{k}\cdot\mathbf{p}$ model for dilute nitride semiconductors," Solid State Electron. **47**, 443 (2003).

[135] K. Alberi, J. Wu, W. Walukiewicz, K. M. Yu, O. D. Dubon, S. P. Watkins, C. X. Wang, X. Liu, Y.-J. Cho, and J. Furdyna, "Valence-band anticrossing in mismatched III-V semiconductor alloys," Phys. Rev. B **75**, 045203 (2007).

[136] K. Alberi, O. D. Dubon, W. Walukiewicz, K. M. Yu, K. Bertulis, and A. Krotkus, "Valence band anticrossing in $GaBi_xAs_{1-x}$," Appl. Phys. Lett. **91**, 051909 (2007).

[137] M. Usman, C. A. Broderick, A. Lindsay, and E. P. O'Reilly, "Tight-binding analysis of the electronic structure of dilute bismide alloys of GaP and GaAs," Phys. Rev. B **84**, 245202 (2011).

[138] H. Naoi, Y. Naoi, and S. Sakai, "MOCVD growth of InAsN for infrared applications," Solid-State Electron. **41**, 319 (1997).

[139] J.-S. Wang, H.-H. Lin, L.-W. Song, and G.-R. Chen, "Growth of InAsN/InGaAs (P) quantum wells on InP by gas source molecular beam epitaxy," J. Vac. Sci. Technol. B **19**, 202 (2001).

[140] M. Merrick, S. A. Cripps, B. N. Murdin, T. J. C. Hosea, T. D. Veal, C. F. McConville, and M. Hopkinson, "Photoluminescence of InNAs alloys: S-shaped temperature dependence and conduction-band nonparabolicity," Phys. Rev. B **76**, 075209 (2007).

[141] A. Lindsay and E. P. O'Reilly, "Unification of the band anticrossing and cluster-state models of dilute nitride semiconductor alloys," Phys. Rev. Lett. **93**, 196402 (2004).

[142] T. D. Veal, L. F. J. Piper, P. H. Jefferson, I. Mahboob, C. F. McConville, M. Merrick, T. J. C. Hosea, B. N. Murdin, and M. Hopkinson, "Photoluminescence spectroscopy of bandgap reduction in dilute InNAs alloys," Appl. Phys. Lett. **87**, 182114 (2005).

[143] R. Kudrawiec, J. Misiewicz, Q. Zhuang, A. M. R. Godenir, and A. Krier, "Photoreflectance study of the energy gap and spin-orbit splitting in InNAs alloys," Appl. Phys. Lett. **94**, 151902 (2009).

[144] E. P. O'Reilly, A. Lindsay, S. Tomić, and M. Kamal-Saadi, "Tight-binding and $\mathbf{k}\cdot\mathbf{p}$ models for the electronic structure of Ga(In)NAs and related alloys," Semicond. Sci. Technol. **17**, 870 (2002).

[145] C. A. Broderick, M. Usman, and E. P. O'Reilly, "Derivation of 12- and 14-band $\mathbf{k}\cdot\mathbf{p}$ Hamiltonians for dilute bismide and bismide-nitride semiconductors," Semicond. Sci. Technol. **28**, 125025 (2013).

[146] C. A. Broderick, M. Usman, and E. P. O'Reilly, "12-band $\mathbf{k}\cdot\mathbf{p}$ for dilute bismide alloys of (In)GaAs derived from supercell calculations," Phys. Status Solidi B **250**, 773 (2013).

[147] M. Usman, C. A. Broderick, and E. P. O'Reilly, "Impact of disorder on the optoelectronic properties of $GaN_yAs_{1-x-y}Bi_x$ alloys and heterostructures," Phys. Rev. Applied **10**, 044024 (2018).

[148] S. Tomić, E. P. O'Reilly, R. Fehse, S. J. Sweeney, A. R. Adams, A. D. Andreev, S. A. Choulis, T. J. C. Hosea, and H. Riechert, "Theoretical and experimental analysis of 1.3-μm InGaAsN/GaAs lasers," IEEE J. Sel. Topics Quantum Electron. **9**, 1228 (2003).

[149] S. B. Healy and E. P. O'Reilly, "Influence of electrostatic confinement on optical gain in GaInNAs quantum-well lasers," IEEE J. Quantum Electron. **42**, 608 (2006).

[150] G. M. T. Chai, C. A. Broderick, E. P. O'Reilly, Z. Othaman, S. R. Jin, J. P. Petropoulos, Y. Zhong, P. B. Dongmo, J. M. O. Zide, S. J. Sweeney, et al., "Experimental and modelling study of InGaBiAs/InP alloys with up to 5.8% Bi, and with $\Delta_{\mathrm{SO}} > E_g$," Semicond. Sci Technol. **30**, 094015 (2015).

[151] Z. M. Fang, K. Y. Ma, R. M. Choen, and G. B. Stringfellow, "Photoluminescence of InAsBi and InAsSbBi grown by organometallic vapor phase epitaxy," J. Appl. Phys. **68**, 1187 (1990).

[152] K. Murawski, E. Gomółka, M. Kopytko, K. Grodecki, K. Michalczewski, L. Kubiszyn, W. Gawron, P. Martyniuk, A. Rogalski, and J. Piotrowski, "Bandgap energy determination

of InAsSb epilayers grown by molecular beam epitaxy on GaAs substrates," Prog. Nat. Sci. **29**, 472 (2019).

[153] J. Wu, W. Walukiewicz, and E. E. Haller, "Band structure of highly mismatched semiconductor alloys: coherent potential approximation," Phys. Rev. B **65**, 233210 (2002).

[154] M. P. Vaughan and B. K. Ridley, "Electron-nitrogen scattering in dilute nitrides," Phys. Rev. B **75**, 195205 (2007).

[155] M. Seifikar, E. P. O'Reilly, and S. Fahy, "Analysis of band-anticrossing model in GaNAs near localised states," Phys. Status Solidi B **248**, 1176 (2011).

[156] A. P. Jauho and J. W. Wilkins, "Dilute resonant scatterers in a parabolic band: density of states as a function of scattering strength," Phys. Rev. B **28**, 4628 (1983).

[157] M. Seifikar, E. P. O'Reilly, and S. Fahy, "Self-consistent Green's function method for dilute nitride conduction band structure," J. Phys.: Condens. Matter **26**, 365502 (2014).

[158] A. R. Marshall, J. P. David, and C. H. Tan, "Impact ionization in InAs electron avalanche photodiodes," IEEE Trans. Electron. Devices **57**, 2631 (2010).

[159] W. Ng, C. Tan, J. David, P. Houston, M. Yee, and J. Ng, "Temperature dependent low-field electron multiplication in $In_{0.53}Ga_{0.47}As$," Appl. Phys. Lett. **83**, 2820 (2003).

[160] S. A. Plimmer, J. David, R. Grey, and G. Rees, "Avalanche multiplication in Al/sub x/Ga/-sub 1-x/As (x= 0 to 0.60)," IEEE Trans. Electron. Devices **47**, 1089 (2000).

[161] B. White, "Planar InAs avalanche photodiodes for infrared sensing: Towards a true solid state photomultiplier," (2016).

[162] J. P. R. David and C. H. Tan, "Material considerations for avalanche photodiodes," IEEE J. Sel. Topics Quantum Electron. **14**, 998 (2008).

[163] R. Mouillet, L.-A. Vaulchier, E. Deleporte, Y. Guldner, L. Travers, and J.-C. Harmand, "Role of nitrogen in the mobility drop of electrons in modulation-doped GaAsN/AlGaAs heterostructures," Solid State Commun. **126**, 333 (2003).

[164] J. Olea, K. M. Yu, W. Walukiewicz, and G. Gonzalez-Díaz, "Hall mobilities in GaN_xAs_{1-x}," Phys. Status Solidi C **7**, 1890 (2010).

[165] M. P. Vaughan and B. K. Ridley, "Solution of the Boltzmann equation for calculating the Hall mobility in bulk GaN_xAs_{1-x}," Phys. Rev. B **72**, 075211 (2005).

[166] M. Seifikar, E. P. O'Reilly, and S. B. Fahy, "Theory of intermediate- and high-field mobility in dilute nitride alloys," Phys. Rev. B **84**, 165216 (2011).

[167] D. A. Beaton, R. B. Lewis, M. Masnadi-Shirazi, and T. Tiedje, "Temperature dependence of hole mobility in $GaAs_{1-x}Bi_x$ alloys," J. Appl. Phys. **108**, 083708 (2010).

[168] R. N. Kini, L. Bhusa, A. J. Ptak, R. France, and A. Mascarenhas, "Electron Hall mobility in GaAsBi," J. Appl. Phys. **106**, 043705 (2009).

[169] S. J. Sweeney and S. R. Jin, "Bismide-nitride alloys: Promising for efficient light emitting devices in the near- and mid-infrared," J. Appl. Phys. **113**, 043110 (2013).

[170] S. R. Jin and S. J. Sweeney, "InGaAsBi alloys on InP for efficient near- and mid-infrared light emitting devices," J. Appl. Phys. **114**, 213103 (2013).

[171] S. Cao, Y. Zhao, S. Feng, Y. Zuo, L. Zhang, B. Cheng, and C. Li, "Theoretical analysis of InGaAs/InAlAs single-photon avalanche photodiodes," Nanoscale Res. Lett **14**, 1 (2019).

[172] G. A. M. Hurkx, D. B. M. Klaassen, and M. P. G. Knuvers, "A new recombination model for device simulation including tunneling," IEEE Trans. Electron. Devices **39**, 331 (1992).

[173] I. A. Buyanova, W. M. Chen, and C. W. Tu, "Defects in dilute nitrides," J. Phys.: Condens. Matter **16**, S3027 (2004).

[174] P. Ludewig, L. Nattermann, W. Stolz, and K. Volz, "MOVPE growth mechanisms of dilute bismide III/V alloys," Semicond. Sci. Technol. **30**, 094017 (2015).

[175] M. Lundstrom, "Fundamentals of Carrier Transport (2nd Ed.)" (Cambridge University Press, 2000).

[176] E. Conwell and M. Vassell, "High-field transport in n-type GaAs," Physical Review **166**, 797 (1968).

[177] Y. Tan, M. Povolotskyi, T. Kubis, Y. He, Z. Jiang, G. Klimeck, and T. B. Boykin, "Empirical tight binding parameters for GaAs and MgO with explicit basis through DFT mapping," J. Comput. Electron. **12**, 56 (2013).

[178] T. B. Boykin, G. Klimeck, R. C. Bowen, and F. Oyafuso, "Diagonal parameter shifts due to nearest-neighbor displacements in empirical tight-binding theory," Phys. Rev. B **66**, 125207 (2002).

[179] J. R. Chelikowsky and M. L. Cohen, "Electronic structure of GaAs," Phys. Rev. Lett. **32**, 674 (1974).

[180] F. Yao, M. Yang, Y. Chen, X. Zhou, and L. Wang, "First-principles calculations of the electronic, and optical properties of a GaAs/AlAs van der Waals heterostructure," Chem. Phys. Lett. **765**, 138194 (2021).

[181] G.-X. Qian, R. M. Martin, and D. Chadi, "First-principles calculations of atomic and electronic structure of the gaas (110) surface," Phys. Rev. B **37**, 1303 (1988).

[182] H. Ehrenreich, "Band structure and electron transport of GaAs," Physical Review **120**, 1951 (1960).

[183] S. Richard, F. Aniel, and G. Fishman, "Energy-band structure of Ge, Si, and GaAs: A thirty-band $\mathbf{k} \cdot \mathbf{p}$ method," Phys. Rev. B **70**, 235204 (2004).

[184] X. Marie and N. Balkan, "Semiconductor modeling techniques," **159** (2012).

[185] B. G. Streetman, S. Banerjee, et al., "Solid state electronic devices", vol. 10 (Pearson/Prentice Hall Upper Saddle River, 2006).

[186] L. Boltzmann, "Further studies on the heat balance among gas molecules" (knight, 1970).

[187] G. Baraff, "Maximum anisotropy approximation for calculating electron distributions; application to high field transport in semiconductors," Physical Review **133**, A26 (1964).

[188] D. Howarth and E. H. Sondheimer, "The theory of electronic conduction in polar semiconductors," Proceedings of the Royal Society of London. Series A. Mathematical and Physical Sciences **219**, 53 (1953).

[189] F. Murphy-Armando and S. Fahy, "First-principles calculation of carrier-phonon scattering in n-type $Si_{1-x}Ge_x$ alloys," Phys. Rev. B **78**, 035202 (2008).

[190] S. R. Mehrotra, A. Paul, and G. Klimeck, "Atomistic approach to alloy scattering in $Si_{1-x}Ge_x$," Appl. Phys. Lett. **98** (2011).

[191] J. G. Ruch and G. S. Kino, "Transport Properties of GaAs," Phys. Rev. **174**, 921 (1968).

[192] K. Ashida, M. Inoue, J. Shirafuji, and Y. Inuishi, "Energy relaxation effect of hot electrons in GaAs," J. Phys. Soc. Jpn. **37**, 408 (1974).

[193] P. Houston and A. Evans, "Electron drift velocity in n-GaAs at high electric fields," Solid-State Electron. **20**, 197 (1977).

[194] J. Požela and A. Reklaitis, "Electron transport properties in GaAs at high electric fields," Solid-State Electron. **23**, 927 (1980).

[195] E. Conwell, "Lattice mobility of hot carriers," J. Phys. Chem. Sol **8**, 234 (1959).

[196] S. Tomic, E. P. O'Reilly, and R. Fehse, "Theoretical and Experimental Analysis of 1.3 μm InGaAsN/GaAs Lasers," IEEE J. Sel. Topi Quantum Electron. **9**, 253507 (2003).

[197] H. Tseng, H. Li, V. Mashanov, Y. Yang, H. Cheng, G. Chang, R. Soref, and G. Sun, "GeSn-based pin photodiodes with strained active layer on a Si wafer," Appl. Phys. Lett. **103**, 231907 (2013).

[198] C.-H. Liu, R. Bansal, C.-W. Wu, Y.-T. Jheng, and G.-E. Chang, "GeSn waveguide photodetectors with Vertical p–i–n heterostructure for integrated photonics in the 2 μm wavelength band," Advanced Photonics Research p. 2100330 (2022).

[199] J. Chrétien, Q. Thai, M. Frauenrath, L. Casiez, A. Chelnokov, V. Reboud, J. Hartmann, M. El Kurdi, N. Pauc, and V. Calvo, "Room temperature optically pumped GeSn microdisk lasers," Appl. Phys. Lett. **120**, 051107 (2022).

[200] N. Uchida, T. Maeda, R. R. Lieten, S. Okajima, Y. Ohishi, R. Takase, M. Ishimaru, and J.-P. Locquet, "Carrier and heat transport properties of polycrystalline GeSn films on SiO_2," Appl. Phys. Lett. **107**, 232105 (2015).

[201] Y. Chuang, C.-Y. Liu, G.-L. Luo, and J.-Y. Li, "Electron Mobility Enhancement in GeSn n-Channel MOSFETs by Tensile Strain," IEEE Electron. Device Lett. **42**, 10 (2020).

[202] Y. Junk, M. Frauenrath, Y. Han, O. C. Diaz, J.-H. Bae, J.-M. Hartmann, D. Grützmacher, D. Buca, and Q.-T. Zhao, in "ESSDERC 2022-IEEE 52nd European Solid-State Device Research Conference (ESSDERC)" (IEEE, 2022), pp. 364–367.

[203] V. R. D'Costa, J. Tolle, J. Xie, J. Menéndez, and J. Kouvetakis, in "AIP Conference Proceedings" (American Institute of Physics, 2010), vol. 1199, pp. 57–58.

[204] H. Kumar, Q. Chen, and C. S. Tan, "Lateral GeSn waveguide-based homojunction phototransistor for next-generation 2000 nm communication and sensing applications," Semicond. Sci. Technol. (2023).

[205] C. O'Donnell, A. Sanchez-Soares, C. A. Broderick, and J. C. Greer, "Impact of stoichiometry and strain on $Ge_{1-x}Sn_x$ alloys from first principles calculations," J. Phys. D: Appl. Phys. **54**, 245103 (2021).

[206] C. Rödl, J. Furthmüller, J. R. Suckert, V. Armuzza, F. Bechstedt, and S. Botti, "Accurate electronic and optical properties of hexagonal germanium for optoelectronic applications," Physical. Rev. Mater. **3**, 034602 (2019).

[207] P. Moontragoon, Z. Ikonić, and P. Harrison, "Band structure calculations of Si–Ge–Sn alloys: achieving direct band gap materials," Semicond. Sci. Technol. **22**, 742 (2007).

[208] K. Lu Low, Y. Yang, G. Han, W. Fan, and Y.-C. Yeo, "Electronic band structure and effective mass parameters of $Ge_{1-x}Sn_x$ alloys," J. Appl. Phys. **112**, 103715 (2012).

[209] V. R. D'costa, C. S. Cook, A. G. Birdwell, C. L. Littler, M. Canonico, S. Zollner, J. Kouvetakis, and J. Menéndez, "Optical critical points of thin-film $Ge_{1-y}Sn_y$ alloys: a comparative $Ge_{1-y}Sn_y$/ $Ge_{1-x}Si_x$ study," Phys. Rev. B **73**, 125207 (2006).

[210] S. Gupta, B. Magyari-Köpe, Y. Nishi, and K. C. Saraswat, "Band structure and ballistic electron transport simulations in GeSn alloys," Proc. Simul. Semicond. Processes Devices **3** (2012).

[211] W.-J. Yin, X.-G. Gong, and S.-H. Wei, "Origin of the unusually large band-gap bowing and the breakdown of the band-edge distribution rule in the Sn_xGe_{1-x} alloys," Phys. Rev. B **78**, 161203 (2008).

[212] M. Polak, P. Scharoch, and R. Kudrawiec, "The electronic band structure of $Ge_{1-x}Sn_x$ in the full composition range: indirect, direct, and inverted gaps regimes, band offsets, and the Burstein–Moss effect," J. Phys. D: Appl. Phys. **50**, 195103 (2017).

[213] R. Chen, H. Lin, Y. Huo, C. Hitzman, T. I. Kamins, and J. S. Harris, "Increased photoluminescence of strain-reduced, high-Sn composition $Ge_{1-x}Sn_x$ alloys grown by molecular beam epitaxy," Appl. Phys. Lett. **99** (2011).

[214] K. Lu Low, Y. Yang, G. Han, W. Fan, and Y.-C. Yeo, "Electronic band structure and effective mass parameters of $Ge_{1-x}Sn_x$ alloys," J. Appl. Phys. **112**, 103715 (2012).

[215] Z. Song, W. Fan, C. S. Tan, Q. Wang, D. Nam, D. H. Zhang, and G. Sun, "Band structure of $Ge_{1-x}Sn_x$ alloy: a full-zone 30-band $\mathbf{k}\cdot\mathbf{p}$ model," New J. Phys. **21**, 073037 (2019).

[216] H. Hong, L. Zhang, K. Qian, Y. An, C. Li, J. Li, S. Chen, W. Huang, J. Wang, and S. Zhang, "Limitation of bulk GeSn alloy in the application of a high-performance laser due to the high threshold," Opt. Express **29**, 441 (2021).

[217] V. Aubry-Fortuna and P. Dollfus, "Electron transport properties in high-purity Ge down to cryogenic temperatures," J. Appl. Phys. **108**, 123706 (2010), https://doi.org/10.1063/1.3520656, URL https://doi.org/10.1063/1.3520656.

[218] T. B. Coplen, N. E. Holden, T. Ding, H. A. Meijer, J. Vogl, and X. Zhu, "The table of standard atomic weights—An exercise in consensus," Rapid Communications in Mass Spectrometry **36**, e8864 (2022).

[219] C. Jacoboni, F. Nava, C. Canali, and G. Ottaviani, "Electron drift velocity and diffusivity in germanium," Phys. Rev. B **24**, 1014 (1981).

[220] D. S. Tanner, C. A. Broderick, A. C. Kirwan, S. Schulz, and E. P. O'Reilly, "Fully analytic valence force fields for the relaxation of group-IV semiconductor alloys: elastic properties of group-IV materials calculated from first principles," arXiv preprint arXiv:2110.11888 (2021).

[221] E. J. O'Halloran, C. A. Broderick, D. S. Tanner, S. Schulz, and E. P. O'Reilly, "Comparison of first principles and semi-empirical models of the structural and electronic properties of $Ge_{1-x}Sn_x$ alloys," Opt. Quantum Electron. **51**, 1 (2019).

[222] S. M., "Mobility of hot carriers in germanium at 300°K," Zeitschrift für Naturforschung A **23**, 2035 (1968).

[223] F. Murphy-Armando and S. Fahy, "Giant enhancement of n-type carrier mobility in highly strained germanium nanostructures," J. Appl. Phys. **109**, 113703 (2011).

[224] V. Aubry-Fortuna and P. Dollfus, "Electron transport properties in high-purity Ge down to cryogenic temperatures," J. Appl. Phys. **108**, 123706 (2010).

[225] F. Murphy-Armando and S. Fahy, "First-principles calculation of alloy scattering in Ge_xSi_{1-x}," Phys. Rev. Lett. **97**, 096606 (2006).

[226] F. Murphy-Armando and S. Fahy, "First principles calculation of electron-phonon and alloy scattering in strained SiGe," J. Appl. Phys. **110** (2011).

[227] D. Rode, "Electron mobility in Ge, Si, and GaP," Phys. Status Solidi B **53**, 245 (1972).

[228] M. Prince, "Drift mobilities in semiconductors. I. Germanium," Physical Review **92**, 681 (1953).

[229] J. Haynes and W. Shockley, "The mobility and life of injected holes and electrons in germanium," Physical Review **81**, 835 (1951).

[230] J. JOHN E SMITH, "Longitudinal anisotropy of the high-field conductivity of n-type germanium at room temperature," Physical Review **178**, 1364 (1969).

[231] S. Sze, "Physics of Semiconductor Devices", Wiley-Interscience publication (Wiley, 1981).

[232] J. Gunn, "VI. The field-dependence of electron Mobility in germanium," Int. J. Electron. **2**, 87 (1956).

[233] D. Gang, L. Xiao-Yan, X. Zhi-Liang, Y. Jing-Feng, and H. Ru-Qi, "Effect of interface roughness on the carrier transport in germanium MOSFETs investigated by Monte Carlo method," Chinese Physics B **19**, 057304 (2010).

[234] P. Tao, W. Tang, Y. Wang, J. Shi, H. H. Cheng, and X. Wu, "Optoelectronic properties for the compressively strained $Ge_{1-x}Sn_x$ films grown on Ge (004)," Mater. Res. Express **7**, 035902 (2020).

[235] C. Schulte-Braucks, "Investigation of GeSn as novel group IV semiconductor for electronic applications" (Dissertation, RWTH Aachen University,, 2018).

[236] J. Liu, D. D. Cannon, K. Wada, Y. Ishikawa, S. Jongthammanurak, D. T. Danielson, J. Michel, and L. C. Kimerling, "Tensile strained Ge p-i-n photodetectors on Si platform for C and L band telecommunications," Appl. Phys. Lett. **87**, 011110 (2005).

[237] Z. Chen, Z. Ikonic, D. Indjin, and R. W. Kelsall, "Design considerations of intra-step SiGeSn/GeSn quantum well electroabsorption modulators," J. Appl. Phys. **130**, 153103 (2021).

[238] P. M. Pearce, C. A. Broderick, M. P. Nielsen, A. D. Johnson, and N. J. Ekins-Daukes, "Electronic and optical properties of $Si_xGe_{1-x-y}Sn_y$ alloys lattice-matched to Ge," Physical. Rev. Mater. **6**, 015402 (2022).

[239] S. Wirths, D. Buca, and S. Mantl, "Si–Ge–Sn alloys: From growth to applications," Prog. Cryst. Growth Charact **62**, 1 (2016).